LES of Rotating Detonation Engines : sensitivity and Physics

Patrick Strempfl

RÉPUBLIQUE FRANÇAISE
Liberté Égalité Fraternité

Université de Toulouse

Doctorat de l'Université de Toulouse

préparé à Toulouse INP

LES des moteurs à détonation rotative: Sensibilité et physique

Thèse présentée et soutenue, le 4 septembre 2024 par

Patrick STREMPFL

École doctorale
MEGEP - Mécanique, Energétique, Génie civil, Procédés

Spécialité
Dynamique des fluides

Unité de recherche
CERFACS

Thèse dirigée par
Thierry POINSOT et Omar DOUNIA

Composition du jury
M. Marc BELLENOUE, Président et rapporteur, ISAE-ENSMA
M. Antonio ANDREINI, Rapporteur, Università degli Studi di Firenze
M. Myles D. BOHON, Examinateur, Technische Universität Berlin
Mme Ratiba ZITOUN, Examinatrice, ISAE-ENSMA
M. Thierry POINSOT, Directeur de thèse, CNRS Occitanie Ouest
M. Omar DOUNIA, Co-directeur de thèse, CERFACS

Membres invités
M. Davide LAERA, Politecnico di Bari

Abstract English

To increase the efficiency of thermal engines, new pressure-gain combustion systems are the subject of extensive studies over the last years. Rotating Detonation Engines (RDE) constitute an example of such systems, where a self-sustained detonation continuously consumes fuel in a typically annular combustion chamber. Experimental investigation of these engines is extremely difficult, hence numerical methods are used to further explore the processes governing these types of engines. A powerful tool to analyse the flow in Rotating Detonation Engines are Large Eddy Simulations (LES), but literature has shown that their implementation is not straightforward. Various groups use simplifications (e.g. perfect premixing, geometrical 2D representations of the chamber) and numerical high-fidelity analysis comparing mixing assumptions, numerical schemes or chemical schemes in full scale configurations are not commonly found in literature. This thesis investigates strategies for 3D LES of a full RDE tested at TU Berlin and the influence of various modelling parameters on the simulation results. This is done by first deriving a reliable 1-step chemical scheme for the correct prediction of detonation and deflagration properties. Second a reliable initialization procedure is developed and two postprocessing indices for evaluating the mixture quality (I_{mix}) and the detonation efficiency (I_{det}) are introduced to further quantify the results of the simulations. Results confirm that mixing plays a significant role in the performance of RDEs and must be accurately reproduced in LES the capture the essential features of RDEs. The manuscript also highlights the impact that the chemical and numerical schemes can have on the detonation dynamics inside RDEs. Finally, the simulations show the importance of deflagration in the overall RDE combustor, implying that chemistry models need to account for deflagration properties as well as for detonation to capture the efficiency of RDEs and reveal that all cases lose a high amount of fuel to non-detonative combustion.

Based on the sensitivity study, a numerical master setup is designed and simulations are performed. The results are validated by comparing the experimental detonation wave speed and estimated pressure gain. The LES overpredicts the experimental detonation wave speed by 21%. The LES also confirms the absence of pressure gain in the TUB configuration.

This thesis shows that LES can be used to understand the dynamics and stabilization mechanisms as well as overall performance of RDE systems. However, it also highlights the current limitations of the method and the many areas where the LES community has to shift the focus on for predictive LES of RDEs.

Abstract Français

Afin d'accroître l'efficacité des moteurs thermiques, de nouveaux systèmes de combustion à gain de pression ont fait l'objet d'études approfondies au cours des dernières années. Les moteurs à détonation rotative (RDE) constituent un exemple de ces systèmes, où une détonation auto-entretenue consomme continuellement du carburant dans une chambre de combustion typiquement annulaire. L'étude expérimentale de ces moteurs est extrêmement difficile, c'est pourquoi des méthodes numériques sont utilisées pour explorer davantage les processus régissant ces types de moteurs. Les simulations de grandes turbulences (LES) constituent un outil puissant pour analyser l'écoulement dans les moteurs à détonation rotatifs, mais la littérature a montré que leur mise en œuvre n'est pas simple. Différents groupes utilisent des simplifications (par exemple, prémélange parfait, représentations géométriques en 2D de la chambre) et l'analyse numérique de haute fidélité comparant les hypothèses de mélange, les schémas numériques ou les schémas chimiques dans des configurations à échelle réelle n'est pas couramment trouvée dans la littérature. Cette thèse étudie les stratégies de LES 3D d'un RDE complet testé à l'Université technique de Berlin et l'influence de divers paramètres de modélisation sur les résultats de la simulation. Pour ce faire, un schéma chimique fiable en une étape est d'abord élaboré pour la prédiction correcte des propriétés de détonation et de déflagration. Ensuite, une procédure d'initialisation fiable est développée et deux indices de post-traitement pour évaluer la qualité du mélange (I_{mix}) et l'efficacité de la détonation (I_{det}) sont introduits pour quantifier davantage les résultats des simulations.

Les résultats confirment que le mélange joue un rôle important dans la performance des RDE et qu'il doit être reproduit avec précision dans les LES afin de capturer les caractéristiques essentielles des RDE. Le manuscrit met également en évidence l'impact que les schémas chimiques et numériques peuvent avoir sur la dynamique de détonation à l'intérieur des RDE. Enfin,

les simulations montrent l'importance de la déflagration dans l'ensemble de la chambre de combustion RDE, ce qui implique que les modèles chimiques doivent tenir compte des propriétés de déflagration ainsi que de la détonation pour capturer l'efficacité des RDE et révèlent que tous les cas perdent une grande quantité de carburant dans la combustion non-détonante.

Sur la base de l'étude de sensibilité, une configuration numérique principale est conçue et des simulations sont effectuées. Les résultats sont validés en comparant la vitesse expérimentale de l'onde de détonation et le gain de pression estimé. La LES surestime la vitesse de l'onde de détonation expérimentale de 21%. La LES confirme également l'absence de gain de pression dans la configuration TUB.

Cette thèse montre que la LES peut être utilisée pour comprendre la dynamique et les mécanismes de stabilisation ainsi que la performance globale des systèmes RDE. Cependant, elle met également en évidence les limites actuelles de la méthode et les nombreux domaines sur lesquels la communauté LES doit se concentrer pour la LES prédictive des RDE.

Contents

Nomenclature

Latin symbols

A	Area	$[m^2]$
A	Pre-exponential factor	$[1/(\sqrt{mol.m^{-3}}s)]$
c	Speed of sound	$[m/s]$
C_p	Specific heat capacity at constant pressure	$[J/(kg/K)]$
C_v	Specific heat capacity at constant volume	$[J/(kg/K)]$
D	Detonation speed	$[m/s]$
E_a	Activation energy	$[cal/mol]$
f	Frequency	$[Hz]$
h	Specific enthalpy	$[m/s]$
I	Index (detonation or mixing)	$[m/s]$
k	Arrhenius rate of progress	$[mol/m^3/s]$
Ma	Mach number	$[-]$
n	Reaction order	$[-]$
P	Pressure	$[Pa]$
$\mathcal{Q}$	Rate of reaction progress	$[mol/(m^3s)]$
Q	Ratio of turbulent and laminar viscosity	$[-]$
q	Released heat by combustion	$[J/kg]$
R	Universal gas constant	$[J/(molK)]$
s	Specific entropy or flame speed	$[J/kg/s]/[m/s]$
T	Temperature	$[K]$
t	Time	$[s]$
V	Volume	$[m^3]$

W	Molecular weight	$[kg/mol]$
X	Species mole fraction	$[-]$
$[X]$	Species X molar concentration	$[mol/m^3]$
Y	Species mass fraction	$[-]$
z	Mixture fraction	$[-]$
Pr	Prandtl number	$[-]$
r	Radius	$[m]$
Sc	Schmidt number	$[-]$

Greek symbols

Δ	Characteristic element size or gap width	$[m]$
δ	thickness	$[m]$
$\dot{\omega}$	Source term of a species	$[kg/m^3s]$
$\dot{\sigma}$	Thermicity	$[1/s]$
γ	Isentropic coefficient	$[-]$
λ_{cell}	Detonation cell width	$[m]$
μ	Dynamic viscosity	kg/ms
ν	Kinematic viscosity	$Pa.s$
ϕ	Equivalence ratio	[-]
Θ	Angle	$[\circ]$

Subscripts

u	Unburnt
b	Burnt
$1/2$	Half
L	Laminar flame
CJ	Chapman-Jouguet state
det	Detonation

mix	Mixing
i	Ideal
t	Total
CC	Combustion chamber
k	Species index
VN	Von-Neumann
F	Fuel
Air	Air
ZND	Zel'dovich-von Neuman-Döring

Chapter 1

Introduction

Contents

1.1 Motivation

1.1.1 Climate change as a global challenge

The modern energy demands as well as aeronautical activities impact the global climate, due to the production of greenhouse gases. Particularly the

increase of emitted CO_2, due to energy production or transportation, into the atmosphere contribute to climate change. On the other hand the demand for energy is increasing because of the technical progress in highly populated countries such as China or India. In fact the world's CO_2 emissions have exceeded 35 billion tons leading to an increase in the concentration of greenhouse gases in the atmosphere (Roser, 2020). Figure 1.1 shows that

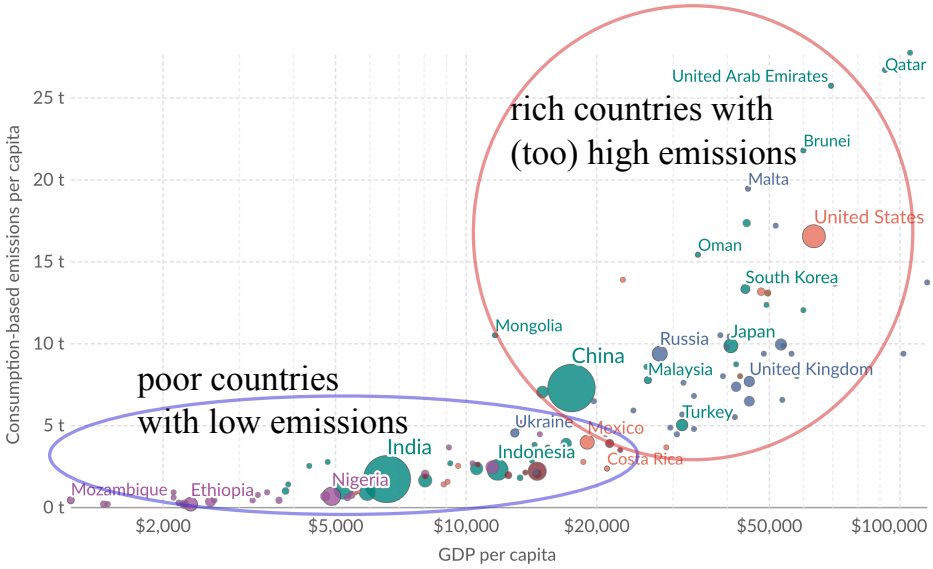

Figure 1.1: Worldwide CO_2 emissions over GDP per capita (*Population based on various sources (2023) – with major processing by Our World in Data* 2023), image from *Our World in Data* (2023). The circles are sized by the respective nations population.

rich and industrialized countries produce a far higher amount of emissions due to consumption of various forms (e.g. electriciy demand). According to Ivanova and Wood (2020), the richest 1 % of EU households have an about 9 times higher contribution to the global emissions than the average and the overall emissions increase approximately linear with an increasing GDP/year for an GDP> \$10.000. The increasing emissions over time are displayed in Fig. 1.2 (a) showing that strategies for more sustainable development in energy production and hence decrease in emissions are of utmost necessity. The international community has increased its effort in pushing for more sustainability with e.g. the in 2015 by 196 nations signed *Paris Agreement* (2015). According to this agreement the participating states commit themselves to

limit the mean world temperature increase to a max of 1.5°C.

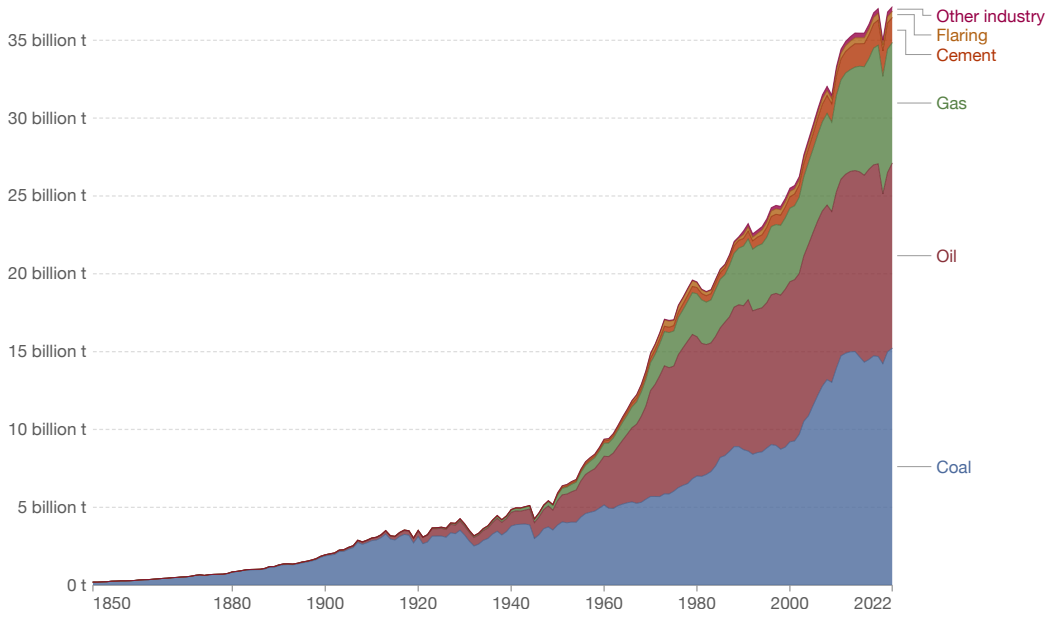

Figure 1.2: Worldwide CO_2 emissions by fuel or industry type. From (*Statistical Review of World Energy (2023); Smil (2017) - with major processing by Our World in Data. "Primary energy from other renewables" [dataset]., "Energy Transitions: Global and National Perspectives" [dataset]. Energy Institute, "Statistical Review of World Energy"; Smil, "Energy Transitions: Global and National Perspectives" [original data]* 2023).

The influence of fossil fuels in this context is immense, as shown in Fig. 1.2. It emphasizes, that in 2022 emissions due to fossil fuels (coal,oil,gas) created up to 35 billion tons of CO_2 emissions, while the global energy demand, as illustrated by Fig. 1.3, keeps increasing since the 19th century and is satisfied predominantly by the consumption of these fossil energy carriers (Ritchie et al., 2020).

Additionally, the European Union (EU) commits itself to become climate neutral by 2050 in the context of the European Green Deal, which is defined as achieving net zero greenhouse gas emissions for EU countries as a whole. This is supposed to be realized mainly by cutting emissions, investing in new green technologies and finally protecting the natural environment.

The measures for achieving these goals are a ban of the usage of fossil fuels, electrification of transport and heating, renewable energies such as solar

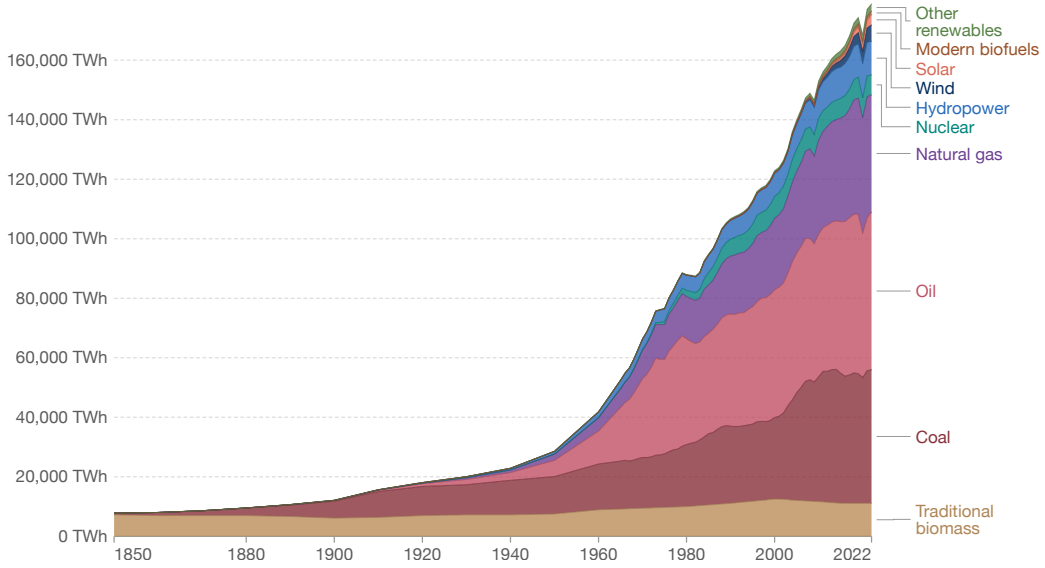

Figure 1.3: Global primary energy demand over time. From *Our World in Data* (2023).

energy or zero-carbon emission technologies. This shows that new energy carriers such as hydrogen are promising candidates to tackle said measures.

1.1.2 Hydrogen as zero-carbon fuel option

Low emission hydrogen is a promising contender as fuel for energy generation or aviation and its global demand is increasing. It can be used as a feedstock, fuel or energy source and storage medium (power-to-gas) for numerous possible applications in industry, transportation, the energy sector and the building sector. Above all, however, it causes no CO_2 emissions and almost no air pollutant emissions during its use. It therefore offers a solution for the decarbonization of industrial processes and economic sectors where a reduction in CO_2 emissions is both urgent and difficult to achieve and the share of hydrogen in the European energy mix is expected to rise from the current level of less than 2% to 13-14% by 2050 (European Commission, 2020).

The European Union launched various research project to support and drive the development of hydrogen based technologies:

1. Clean Hydrogen Joint Undertaking (FCH JU): A public-private part-

nership of industry and research organizations aiming to support and promoting technological developments focusing on hydrogen technologies as well as expediting their market introduction. This focuses particularly on electric power generation, transport and heating related technologies.

2. Testing Hydrogen ad-mixture for Gas Applications (Thyga): This project aims to standards and certification procedures for increasing the volumetric hydrogen content in natural gas applications. This is especially of interest in the context of power-to-gas, where hydrogen as a storage medium is ought to be consumed in e.g. gas turbines.

3. Clean Sky: This study targets feasibility of the development and application of thermal propulsion devices for aviation and includes various international partners.

In the context of these programs, AIRBUS launched its "Zeroe" project, a multi-demonstrator program with the goal of designing the first hydrogen powered zero-emission aircraft by 2035. Additionally, since land-based and aeronautic gas turbine technologies run on similar combustion systems, manufacturers push the development of gas turbine systems which can run on hydrogen or hydrogen/ammonia blends (*Global Hydrogen Review* 2023) or alternatively systems that run on an increasing amount of hydrogen blends with other gases. Investments in these technologies are expected to increase with time (Öberg et al., 2022).

1.1.3 New combustion concepts: Pressure gain combustion

In order to decrease emissions, hydrogen is a popular candidate as an alternative to fossil fuels. Another more fundamental approach which should be combined with such new fuels is the improvement of energy efficiency (Akpan and Olanrewaju, 2023) and hence of thermal efficencies of combustion systems: combustion based energy and propulsion systems have been mainly optimized for deflagration based systems such as combustion in constant pressure in gas turbines or aviation engines. To decrease emissions, the efficiency of these systems has already been widely optimized and just slight increases in efficiency such as 1% require immense effort. These systems, which are based on the Joule(-Brayton) cycle are considered close to their

peak, leading to the necessity of finding new combustion cycles and systems. One approach for improvement is Pressure Gain Combustion (PGC) (Perkins and Paxson, 2018), where combustion leads to additional pressure increase during the reactions and subsequently higher thermal efficiency as shown by e.g. Stathopoulos (2018).

Currently three PGC technologies are heavily investigated to meet the new engine requirements: first Constant Volume Combustion (CVC) (Bellenoue et al., 2016), where in a valved combustion chamber, reactions take place in a confined constant volume and are subsequently discharged as seen in e.g. Michalski et al. (2018a,b). Second, the the pulse detonation engine (PDE) (Heiser and Pratt, 2002), which burns fuel in a detonation regime (supersonic shock with an attached reaction zone, more in Chapt. 4) by cyclic ignition in a tube chamber, leading to pressure gain in the burnt gases and the Rotating Detonation Engine (RDE) (Kailasanath, 2011), which is based on the same principle. Theoretically the CVC and detonation-based concepts correspond to specific thermodynamic cyles: the CVC follows the Humphrey cycle and the PDE/RDE the Fickett-Jacobs cycle, which are explained in the following:

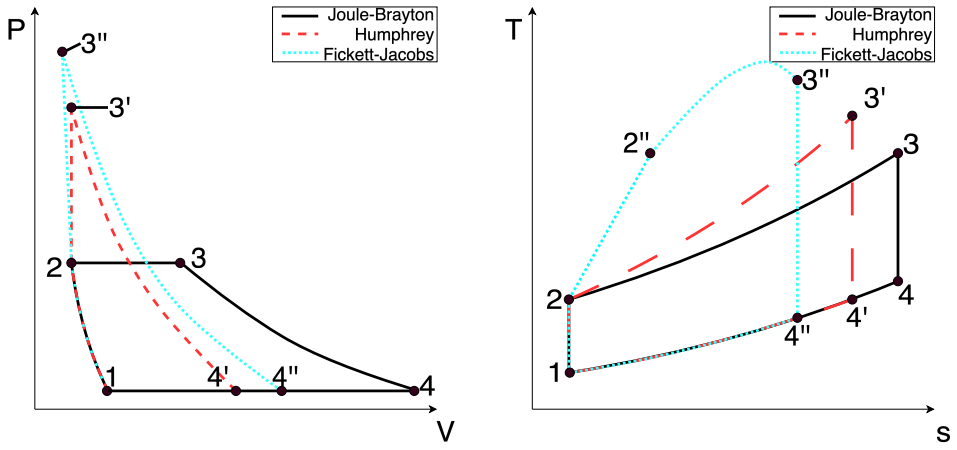

(a) **(b)**

Figure 1.4: Ideal P-V diagram of the Joule-Brayton, Humphrey and Fickett-Jacobs cycles (a) and ideal T-s diagram, comparing the three cycles (b). (a) adapted from Wolański (2013) and (b) adapted from Stathopoulos (2018).

Figure 1.4 compares the different thermodynamic cycles. All cases start at stage 1 and are compressed to stage 2, reaching the same pressure and

temperature. The transition from stage 2 to 3 for the Joule-Brayton cycle denotes combustion of the compressed reactants under constant pressure (Fig. 1.4 (a)). The T-s diagram (Fig. 1.4 (b)) shows that combustion leads to in an increase of temperature of the gas during the transition from 2 to 3, while a considerable amount of entropy is produced, resulting in the gas in 3 having a higher amount of entropy than the gas in 2. In case of the Humphrey cycle combustion occurs in a fully confined volume (state 2 to 3' in Fig. 1.4 (a)), in other words gas burns under constant volume conditions. This is shown by the vertical increase of pressure for an unchanging volume. The transition from 2 to 3' leads to a lower entropy production than 2 to 3 (Fig. 1.4 (b)). The change from 2 to 3" of the Fickett-Jacobs cycle differs from the two other due to the presence of the leading shock of the detonation. This is seen particularly in Fig. 1.4 (b), where an intermediate step 2" exists between the burnt gas state 3" and the compressed gas state 2. The transition from 2 to 2" is a result of the leading shock of the detonation, compressing the gas of state 2 to higher pressures, producing additional entropy, before combustion occurs. This compression is seen in Fig. 1.4 (a) by the lower volume and additional higher pressure of 3". All cycles display an isentropic expansion after their respective burnt gas states (3,3',3") to the final state of the cycle (4,4',4") before being replenished with fresh gases which results in a return to state 1. Note however, that the detonation produces the lowest amount of entropy of all three cycles, while the Joule-Brayton cycle produces the largest entropy. It proves that under idealized conditions, detonations and CVC systems perform more efficiently than classical combustion concepts. This resulted in the emergence of multiple different PGC concepts.

This work has been conducted as part of the INSPIRE (INSpiring Pressure gain combustion Integration, Research and Education) project. INSPIRE is a Marie Skodowska-Curie Innovative Training Network (ITN), dedicated to the research of two PGC solutions, the RDE and the CVC. The project is structured as shown in Fig. 1.5: first there is a work package WP2 (CVC) on CVC and a second WP3 (RDE) which are both dedicated to numerical and experimental research of the PGC concepts. WP4 and WP5 regard the PGC concepts in an entire engine system, where the focus is on the interaction of the combustion chambers with e.g. compressors. This work is part of WP3, focused on the numerical simulation of the TUB RDE test bench.

Figure 1.5: Structure of the INSPIRE ITN.

1.2 Rotating detonation engines for aerospace and energy production

Out of the previously named concepts, the RDE is the most interesting concept, due to its geometrical simplicity, continuous operability and scalability (Kailasanath, 2011). First research on continuously rotating detonations was conducted in the 1960s by, among others, Voitsekhovskii (Voitsekhovskii, 1960; Voitsekhovskii et al., 1963) and Nicholls and Cullen (1964). First analysis on the potential of RDE for rocket engines have been executed by e.g. Adamson (1967), considering it a promising concept for the improvement of the efficiency of the engine.

As mentioned in the previous sections, research on RDEs has increased immensely in the recent years due to the potentially higher efficiency of the combustion. Considering the decarbonization targets set by governments worldwide, it is a very attractive system to combine with hydrogen: one obtains a more efficient engine running on a sustainable fuel.

RDEs operate by one or more detonation waves propagating continuously around the axis of the combustion chamber. Typically RDE chambers are

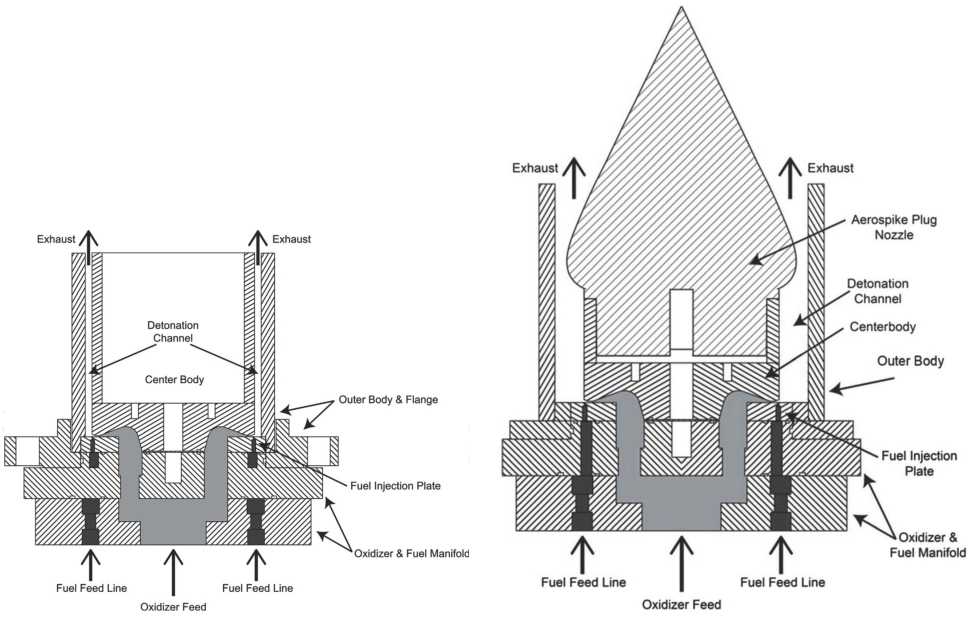

(a) **(b)**

Figure 1.6: Examples of RDEs without (a), from Fotia et al. (2015) and with aerospike nozzle(b), from Rankin et al. (2017a).

designed as annular, cylindrical chambers. Figure 1.6 (a) shows an example of an RDE with axially straight walls, the annular chamber and the fresh gas feeding system. Figure 1.6 (b) shows a modified version of the chamber, where an aerospike nozzle is added at the exhaust of the chamber to directly expand the hot gases from the chamber exit and hence generate thrust. A first test flight of an RDE with an aerospike nozzle in space has been conducted by the Japanese Aerospace Exploration Agency (JAXA), and the results show promising results with an specific impulse (I_{sp}) of $290 \pm 18s$ which corresponds to an almost deal ideal value for constant pressure combustion (Goto et al., 2023), making RDEs canditates for upper stage engines of rockets.

However, different groups have proposed other designs: Nakagami et al. (2017) and Ishii et al. (2023) run a disk shaped RDE, where reactants are injected radially, while others such as Yokoo et al. (2021) or Wang et al. (2018) run tests in a hollow cylindrical chamber. Chacon and Gamba (2018) constructed a chamber in shape of a "racetrack", for easier optical access to the inner chamber. Despite the different chamber designs, the overall flow field structures are qualitatively the same. A sketch of the flow field

developed along the chamber mean perimeter is given in Fig. 1.7:

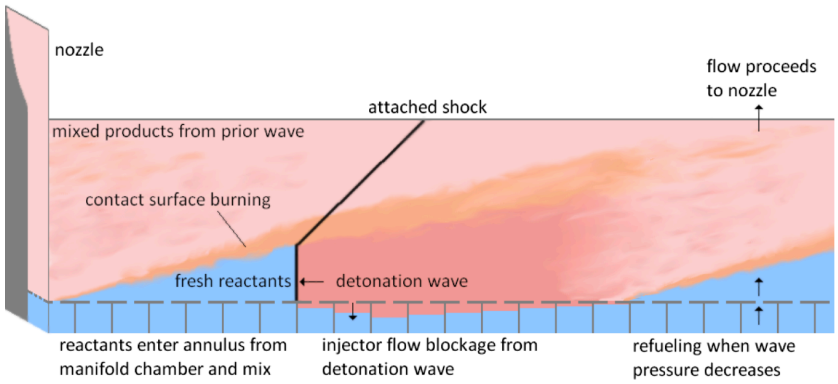

Figure 1.7: Sketch of a typical single wave RDE flow field. From Lu and Braun (2014)

The detonation rotates continuously at the lower chamber, since fresh gases are also continuously provided during the operation. The fresh, mixed reactants are processed by the detonation, resulting in a strong pressure jump, which in turn blocks the refill through injectors. This high pressure can also lead to back flow in the injectors, which is why in a real engine the reactants must be injected separately. The occurring temperature in the detonation region can reach up to $4000K$ and a pressure of 30-40 times the initial pressure in front of the wave. The high pressure area then expands, hereby propelling the detonation front, fresh gases can enter the chamber again and push the products towards the outlet. A contact surface of fresh gases and burnt gases of the previous cycle is formed, leading to local deflagration. Since the flame speed in the deflagration regime is typically lower than the convective bulk flow velocity, the flame front is convected downstream. An attached shock, also known as oblique shock trails from the top of the detonation towards the outlet. The oblique shock rotates along the chamber circumference leading to a rotating shock at the outlet, resulting in a periodically changing flow direction at the exhaust plane. Application wise,

this does not pose a significant problem in propulsion approaches such as a rocket engine, but it is a problem for turbines after the engine exhaust. The shock imposes an additional rotating load on the stator and subsequently on the turbine, which compromises its efficiency.

RDEs have been run with different combinations of fuel and oxidizer. Hydrogen/oxygen mixtures are ideal for modeling purposes due to the relatively simple chemistry, and often used in experimental work (e.g. Bluemner et al. (2020); Bohon et al. (2019); Chacon and Gamba (2018); Ishii et al. (2023); Schwer and Kailasanath (2013); Suchocki et al. (2012)). The high detonation propagation speed and wave front pressures of hydrogen suggest it to be a suitable fuel for real applications. Other setups, such as Sato and Raman (2020); Wang et al. (2018) use ethylene and tests with methane have also been conducted by e.g. Wang and Le (2021) and Nair et al. (2021).

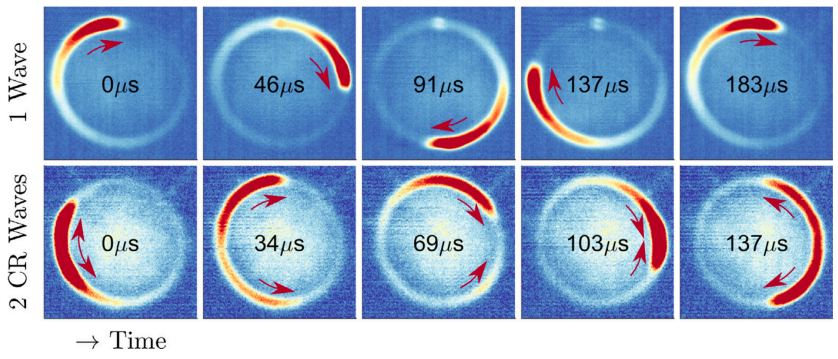

Figure 1.8: Examples of different wave modes in a RDE. Adapted from Bohon et al. (2019).

RDE tests have shown the emergence of various types of instabilies: first, multiple detonation wave modes can occur in an RDE (Fig. 1.8), where wave breakup and coalescence have been observed. During operation, a detonation wave breaks up resulting in multiple waves propagating in the chamber, as shown by Bluemner et al. (2018); Bohon et al. (2019); Chacon and Gamba

(2018); Suchocki et al. (2012). The reason for this break up still has not been found, but is, at least partially attributed to the injector design and overall mixing performance. Rankin et al. (2015, 2017b) use an optically accessible RDE to investigate OH*-chemiluminescence in the detonation front various injection geometries and significant differences in the wave shape, the wave height and the operating mode were found. In tests with insufficient reactant mixing an unsteady operating mode with two counter-rotating waves may occur and variations of the equivalence ratio support multiple detonation waves acc. to Luan et al. (2022). Instabilities leading to quenching have been numerically investigated by e.g. Zhao et al. (2020). They show that under constant pressure condition the rotating detonation is more prone to instability at low pressure, due to the instability from the deflagrative surface. The intrinsic frequency for the unstable cases with different pressures is close, and maybe related to the RDE configuration and/or fuel properties. For the time-varying pressures with various specified frequencies, the RDE shows the different levels of instability characterized by multiple frequencies.

Longitudinal pulsations have also been observed by Bluemner et al. (2020), which occur depending on the axial length of an annual chamber and depend on the amount of outlet restriction of the exhaust plane of the combustors. Instabilities in the reactant plenums have been researched by Anand et al. (2017). The occurrence of such instabilities appears to depend on the fuel injection scheme used and the air flow rates through the RDC.

Another field of research is the integration of RDEs in energy production systems such as gas turbines. First designs for e.g. supersonic turbines with RDEs have been conducted by e.g. Paniagua et al. (2014) and Mushtaq et al. (2022). These studies point to different additional challenges: first, the exhaust flow of an RDE is highly fluctuating which makes the integration with a turbine difficult. In case of a subsonic turbine, the flow is limited by choking due to high subsonic inlet Mach numbers (Liu et al., 2023). In case of a supersonic turbine, other constrains occur such as Kantrowitz unstarting (Kantrowitz et al., 1945) or collective shock unstarting (Mushtaq and Gaetani, 2023). Additionally the untypical incidence (Starken et al., 1984) represents another constraint. Note that the constraints on supersonic turbines become more noticeable for low supersonic inlet Mach numbers. An approach for dealing with the the RDE exhaust flow is the incorporation of an exhaust duct either diffusing (Uhl et al., 2024) or accelerating the flow for a sub-sonic or respectively super-sonic turbine. The process of optimizing the coupling of an RDE to a turbine is clearly a complicated one.

1.3 Review of CFD simulation for RDEs

1.3.1 Common strategies to simulate RDEs

Advanced numerical CFD codes developed over the recent years have become excellent research tools able to play an important role in improving RDE design and analysis, thus limiting the cost and safety issues of experimental testing. Due to their complex features such as compressibility, multiple species, coupled reactions and geometrical design, various levels of simplification have been necessary to decrease the degree of complexity in simulations, while still obtaining basic features of a RDE.

The first approach is the decrease in dimension from a three dimensional configuration to a two dimensional configuration. One assumes for the chamber circumference L_{cc} and annular gap width Δ_{cc} of an annular chamber that $\Delta_{cc} << L_{cc}$, hence the domain is quasi a 2 dimensional cylinder, which is in turn unwrapped. Most simulations using this approach additionally neglect discrete injection systems and instead continuously inject premixed fresh gases into the domain. The downside of this approach is that many influential factors regarding the propagation of a detonation are excluded. The most obvious one is the reactants mixing process, which is detrimental for the operability of a RDE: mixing is either not existent (premixed gases are injected) or over simplified (since 3D effects are neglected). Further three dimensional effects such as detonation cell formation, neglection of shock reflections at the walls and curvature effects compromise the results. Another missing factor is the influence of walls on the detonation propagation, since wall treatment also plays a role for the overall flow structure. Nevertheless, these approaches allow to research basic features, such as droplet detonation wave interaction, which require multiphase computations and thus increase the computational costs immensely for three dimensional cases. While the increasing computational power in the last years allows to compute fully three dimensional configurations, Tab. 1.1 shows that using two dimensional configurations is still commonly used in the community for primary analysis and model development.

Another typical simplification is the general replacement of the injection system, which is of primary interest in real configurations. Instead, they inject a perfectly premixed mixture of reactants into the chamber, via e.g. micro-nozzles. This approach allows to investigate the blockage of the fresh gas injection, but neglects the effect of mixing and stratification in the

chamber. The turbulence generated by the injected gases is consequently also missing and its influence on the detonation propagation not captured. Recent simulations tend to include the full reaction system, due to the previously mentioned increased performance of computers (see Tab. 1.1). The choice of the injection model is mainly based on the spatial dimensions of the numerical studies.

Publication	Injection model	Mixing assumption	Simulation type	Dimension
Vignat et al. (2024)	resolved	non-premixed	LES	3D
Yu et al. (2023)	inlet plane	premixed	URANS	3D
Nassini et al. (2023)	resolved	non-premixed	LES	3D
Ren et al. (2023)	micro-nozzles	premixed	EULER	2D
Wen et al. (2022)	micro-nozzles	premixed	EULER	2D
Tanaka et al. (2022)	micro-nozzles	premixed	EULER	2D
Zhao et al. (2020)	micro-nozzles	premixed	EULER	2D
Batista et al. (2021)	resolved	non-premixed	LES	3D
Sato et al. (2021)	resolved	non-premixed	NS	3D
Prakash et al. (2021)	resolved	non-premixed	NS	3D
Sato and Raman (2020)	resolved	non-premixed	EULER	3D
Katta et al. (2019)	inlet plane	premixed	EULER	3D
Mikoshiba et al. (2019)	micro-nozzles	premixed	EULER	2D
Gaillard et al. (2017)	resolved	non-premixed	LES	3D
Sun et al. (2017)	resolved	premixed	EULER	2D
Tsuboi et al. (2017)	micro-nozzles	premixed	EULER	3D
Cocks et al. (2016)	resolved	non-premixed	hyb.LES	3D
Dubrovskii et al. (2015)	resolved	non-premixed	URANS	3D
Tsuboi et al. (2015)	micro-nozzles	premixed	EULER	3D
Wu et al. (2014)	micro-nozzles	premixed	EULER	3D
Schwer et al. (2014)	micro-nozzles	premixed	EULER	3D
Schwer and Kailasanath (2014)	micro-nozzles	premixed	EULER	3D
Zhou and Wang (2013)	micro-nozzles	premixed	EULER	3D
Naples et al. (2013)	micro-nozzles	premixed	EULER	2D
Frolov et al. (2013)	resolved	non-premixed	URANS	3D

Table 1.1: Selection of numerical studies on RDEs since 2013.

Another issue of importance to build a CFD code for RDEs is to know whether laminar transport must be incorporated or not. If some of the fuel burns in a deflagration, the code must capture it in addition to the detonation. In this case it must incorporate a proper description of molecular transport, which is typically negligible for detonations. Generally the molecular transport is a multitude of orders smaller than with convective

transport. The transport properties viscosity, species diffusion and thermal conduction are deemed negligible in many calculations and the problem is described with the reactive Euler equations. The disadvantage of using Euler equations is their limited applicability only on inviscid, adiabatic flows, whereas the Navier-Stokes equations include the viscous properties. The Euler equations are computationally less costly, since there are no sub-grid stresses to solve, but the potential influence of the sub-grid scale effects can also contribute to phenomena such as viscous mixing. The listed studies in Tab. 1.1 reveal that solving the Euler equations is the predominant approach in the computations of RDEs, while LES are starting to become more common. This reveals that studying the process of reactants mixing increases in importance, since it is the key parameter in evaluating the performance of injection systems and studies on RDE performance and detonation wave propagation based on mixing and sub-grid scale models have not been thoroughly executed yet.

1.3.2 Common strategies in the computations of RDEs: Numerical and physical sub models

Once the choice of the displayed parameters in Tab. 1.1 has been made, the question, which numerical sub models to use, arises. In this section the numerical schemes, chemistry models and (if existant) sub-grid scale (SGS) models of the studies listed in Tab. 1.1 are summarized (see Tab. 1.2) to obtain a proper impression of the current state-of-the-art in simulating RDEs. Note that Tab. 1.2 is limited to 3D cases only, since they are of higher relevance for this thesis.

A variety of numerical schemes hes been applied for computing RDEs. In the most recent publications, one either uses a (Monotonic Upstream-centered Scheme for Conservation Laws) MUSCL-based HLLC scheme of 2nd order accuracy paired with a 2nd order Runge Kutta scheme for time integration. Alternatively authors use a 2nd order MacCormac scheme, which is also coupled to a MUSCL upwinding to alleviate instabilities near detonation wave fronts. None of the most recent studies use schemes of higher order, but use setups with a 2nd order accuracy, with the exception of Wu et al. (2014), who use a 5th order MPWENO scheme.

Different chemical schemes have been adapted for the computation of RDEs. While in the earlier studies 1-step schemes where predominantly

used, more complex reduced and even detailed chemical schemes are adapted. However,Nassini et al. (2023) or Yu et al. (2023) still perform computations with 1-step schemes showing that the community is not in agreement what type of chemical scheme is the best for researching RDEs numerically.

When it comes to LES of RDEs, the performance of different SGS models is not well understood. The SGS models control the sub-grid scale effects, but must also be able to handle shocks, a difficult challenge for many codes. The literature survey shows that the following models have been used: WALE, KIM, Smagorinski and Vreman. Their suitability for the problem, however, is still up to debate.

1.4 Objective of this thesis

The variety of approaches considering numerical schemes, chemistry models, mixing assumption, domain modeling, and the variation of SGS models makes the computational analysis of RDEs very difficult, since a best practice approach isn't established yet. The goal of this study is to evaluate different modeling approaches for the LES of a RDE. For this purpose different computations are performed and based on the impact of the different modeling approaches, a "master" setup is constructed that is finally compared in detail to an experimental configuration placed at the Technical University of Berlin.

1.5 Description of the experimental RDE

This section introduces the test rig of Technical University of Berlin (TUB). It expands on the geometry, operation and instrumentation. The LES is conducted on a test rig installed at TU Berlin by Bluemner et al. (2020). The setup is a down scaled version of the US Air Force Research Lab (AFRL) geometry developed by Shank (2012). The test rig is highly modular, allowing to change fuel, oxidizer and geometrical features such as air inlet slot height, outlet square section, number of fuel injectors or combustor length, for details see (Bluemner et al., 2021). The configuration investigated consists of an annular combustion chamber with a width of $\Delta_{cc} = 7.6mm$ and an inner radius $r_i = 37.4mm$, resulting in an outer diameter $D = 45mm$. The chamber walls are straight, the exhaust flow blows directly into the atmosphere,

Publication	Num. scheme	Chemical model	SGS model
Vignat et al. (2024)	N/A	38R, 12S FFCMy-12 Xu et al. (2018)	Vreman (2004)
Yu et al. (2023)	2nd order upwind	1R species N/A	$k-\epsilon$
Nassini et al. (2023)	LW - 2nd order in space and time	1R, 4S	WALE
Batista et al. (2021)	2nd order MacCormac + 3rd order MUSCL	38R, 12S FFCMy-12 Xu et al. (2018)	KIM WON-WOOK KIM and MONGIA (1999)
Sato et al. (2021)	MUSCL-based HLLC + 2nd order Runge Kutta	19 reactions, 9 species Mueller et al. (1999)	-
Prakash et al. (2021)	MUSCL-based HLLC + 2nd order Runge Kutta	38R, 12S FFCMy-12 Xu et al. (2018)	-
Sato and Raman (2020)	MUSCL-based HLLC + 2nd order Runge Kutta	38R, 21S Varatharajan and Williams (2002)	- -
Katta et al. (2019)	2nd order MacCormac + 4th order diffusion terms and flux corrected transport	2R, 12S -	-
Gaillard et al. (2017)	MUSCL-based HLLC + GMRES method	7R, 6S Davidenko et al. (2010)	Smagorinski
Tsuboi et al. (2017)	2nd order AUSMDV + 3rd order Runge-Kutta	21R, 8S Shimizu et al. (2011)	-
Cocks et al. (2016)	MUSCL 2nd order central + 2nd order Crank-Nicolson	7R, 7S Baurle et al. (1994)	-
Dubrovskii et al. (2015)	SIMPLE + Monte Carlo approach (no further specification)	1R, 4S	$k-\epsilon$
Tsuboi et al. (2015)	2nd order AUSMDV + 3rd order Runge-Kutta (TVD)	21R, 8S Shimizu et al. (2011)	- -
Wu et al. (2014)	5th order MPWENO + 3rd order Runge-Kutta (TVD)	1R, 2S Ma et al. (2006)	- -
Schwer et al. (2014)	FCT	1R, 2S, Induction time equation	- -
Schwer and Kailasanath (2014)	FCT	1R, 2S, Induction time equation	-
Zhou and Wang (2013)	5th order MPWENO + 3rd order Runge-Kutta (TVD)	1R, 2S Ma et al. (2006)	- -
Frolov et al. (2013)	SIMPLE + Monte Carlo method	1R, 2S Ma et al. (2006)	$k-\epsilon$

Table 1.2: Selection of numerical studies on RDEs since 2013.

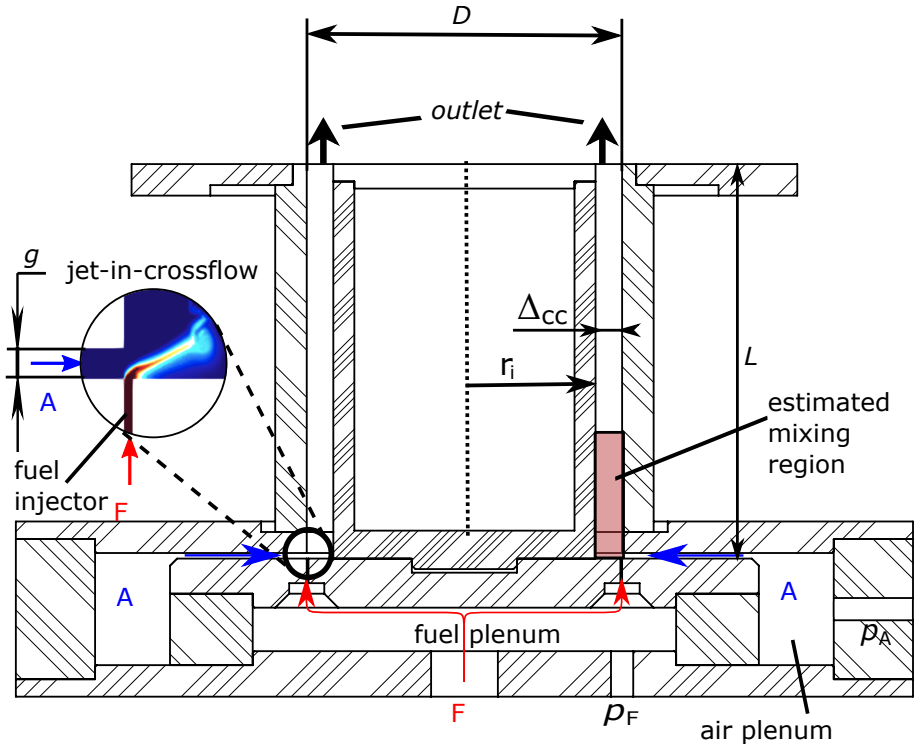

Figure 1.9: Cross section of the combustor with geometrical parameters. A denotes *air* and F denotes fuel in this graph. Adapted from Bluemner et al. (2020).

and the rig has no outer restriction. 100 discrete injectors, are positioned equally, radially and tangentially to the outer radius of the chamber (Fig. 1.10). A radially inwards leading gap blows air into the chamber. This configuration results in the formation of 100 jets-in-crossflow in the chamber. Due to deflection of the upper wall of the air injection slot, the slot height is estimated to increase by 10% to $g = 1.76mm$ (Fig. 1.9). The combustion chamber has a length of $L = 112.5mm$. The discrete fuel injectors have a diameter of $d = 0.5mm$ (Fig. 1.10) and they are positioned so that the outer diameter of the annular chamber tangentially envelops all injectors. The injectors as well as the air slot are undivided from their respective plenums. The operational conditions are given by imposing a mass flow rate of oxidizer and fuel, controlled by a system of sonic nozzles and pressure sensors, here semi-conductor strain gauge relative sensors, which have been specifically de-

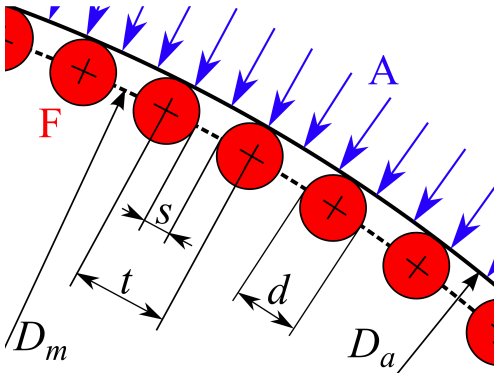

Figure 1.10: Injection principle in the investigated chamber. The red cycles denote the H_2 (F) injectors. A denotes the radially inward injected air. Adapted from Bluemner et al. (2020)

veloped for the combustor (Bluemner (2020)). The detonation is ignited via a predetonator tube mounted to the base of the chamber. The tube contains premixed fuel and oxidizer at stochiometric conditions and is itself ignited by a spark plug, initiating a DDT process. It is also possible to ignite the combustor with a spark plug on the outer, but this has been shown to work only for low mass flow rates (Bluemner (2020)).

1.6 Instrumentation used on the RDE

An image of the test rig including instrumentation is given in Fig. 1.11. The construction of the test rig offers the option of mounting several sensors on the chamber walls as well as sensors at the plenum walls, to obtain pressure and temperature. In Fig 1.9 p_F and p_A denote the static plenum pressures of fuel and oxidizer, respectively. It possible to mount up to 8 pressure sensors along the chamber height, where either relative or absolute dynamic piezo-electric pressure sensors (resonance frequency of 200 kHz) with a variety of adapters to reduce damage due to high thermal loads in the test rig (Bluemner, 2020) are utilized. The Capillary Tube Attenuated Pressure (CTAP) method is another option used in this setup to measure pressure fluctuations. Optionally, a L-shaped Kiel probe positioned 2 mm upstream of the combustor outlet, can be used to measure the time-averaged value of the outlet total pressure, hence allowing to estimate the pressure gain of the test rig. For visualization of the detonation wave Bohon et al. (2019) use a

high speed camera recording at $87.5kHz$ to record the luminosity emitted by hot gas, after the emitted radiation has been reflected by a mirror, since direct exposure to the hot exhaust gases would destroy the camera.

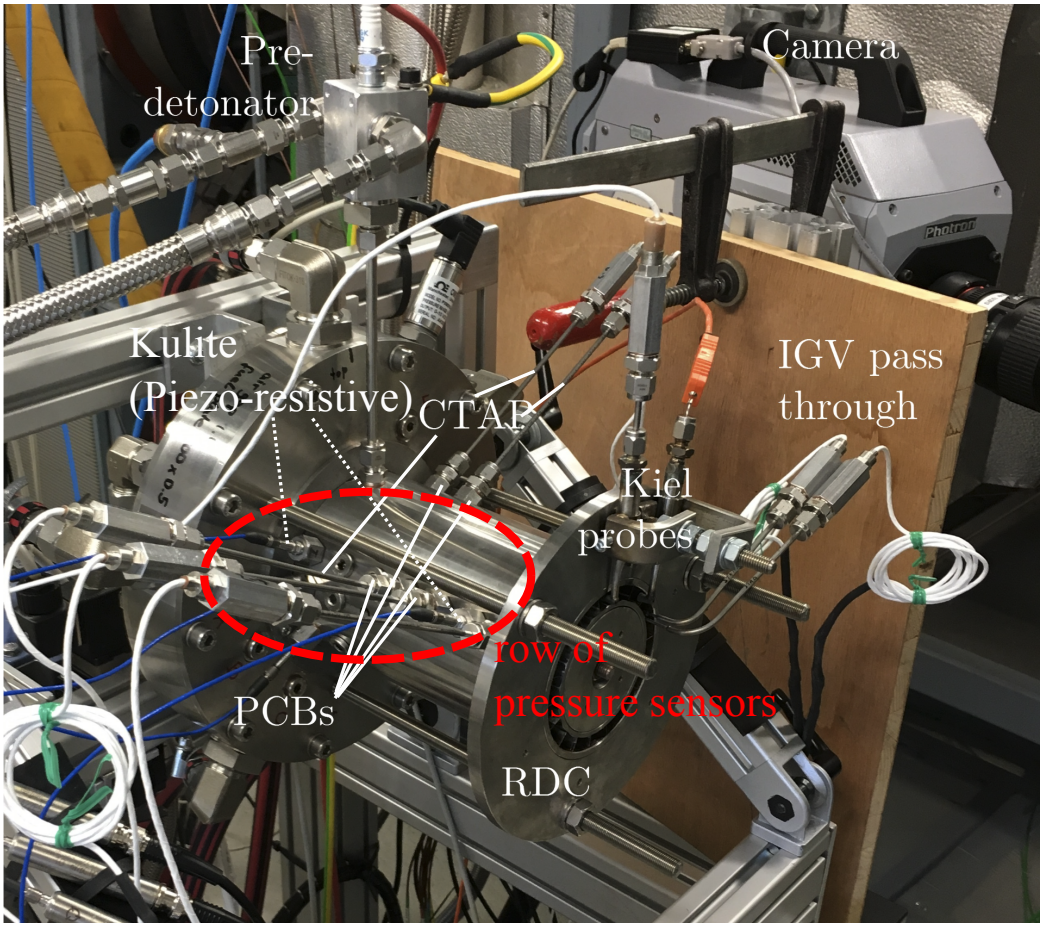

Figure 1.11: Exemplary experimental setup of the TUB RDE. Adapted from Bach et al. (2019)

Chapter 2

Fundamentals of reacting flows

Contents

2.1 Introduction

The description of fluids require a set of equations. Leonhard Euler proposed a set of equations describing inviscid three-dimensional flows, which later have been updated by Louis Navier and George Gabriel Stokes, who included the notion of viscosity into the set of equations. This results in the Navier-Stokes equations, a set of partial differential equations containing highly non-linear terms (Kuo (2005 Second Edition); Poinsot and Veynante (2011)). The non-linear nature of the equations make it close to impossible to derive analytical solutions, except for certain special cases such as a Poisoille current. This chapter recalls the fundamental notions and equations for computational fluid dynamics (CFD) of reacting flows.

2.2 Compressible Navier-Stokes equations

The Navier-Stokes equations (NS-equations) are a set of conservation equations for **mass**, **momentum** and **energy**. In the Einstein notational convention they are:

$$\frac{\partial \rho}{\partial t} + \frac{\partial}{\partial x_i}(\rho u_i) = 0 \tag{2.1}$$

$$\frac{\partial}{\partial t}(\rho u_i) + \frac{\partial}{\partial x_j}(\rho u_i u_j + P\delta_{i,j} - \tau_{i,j}) = 0 \tag{2.2}$$

$$\frac{\partial}{\partial t}\rho E + \frac{\partial}{\partial x_i}(u_i(\rho E + P\delta_{i,j} - \tau_{i,j}) + q_i) = \dot{Q} + \dot{\omega}_T \tag{2.3}$$

$$\frac{\partial}{\partial t}(\rho Y_k) + \frac{\partial}{\partial x_i}(\rho Y_k u_i) = -\frac{\partial}{\partial x_i}(\rho J_{i,k}) + \dot{\omega}_k \tag{2.4}$$

where ρ denotes the density, u (with i, j=1,2,3) denotes velocity and P denotes the **static** pressure. $\dot{Q}$ describes an external source of energy in the system which can be an ignition source, for example a spark. Since this thesis treats the fluid as a perfect gas, the relationship between ρ, P and the **static** Temperature T are given as:

$$\frac{P}{\rho} = RT \tag{2.5}$$

with

$$R = R_{univ}/M_{mean} \tag{2.6}$$

where R_{univ} is the universal gas constant 8.3145 $Jmol^{-1}K^{-1}$ divided by the mean molecular weight of the fluid M_{mean}. E denotes the total (sensible+kinetic) energy.

In reactive flows, multiple species react through chemical reactions. A species k in a mixture of mass m, which contains n moles and N species is characterized by its mass fraction Y_k and its mole fraction X_k:

$$Y_k = \frac{m_k}{m} \tag{2.7}$$

$$X_k = \frac{n_k}{n} \tag{2.8}$$

with the mass (number of moles) m_k (n_k) of species k in a given volume and the total quantity m (n). Note that by definition

$$\sum_{k=1}^{N} Y_k = \sum_{k=1}^{N} X_k = 1 \tag{2.9}$$

The mean molecular weight W_k of a mixture M is:

$$\frac{1}{M} = \sum_{k=1}^{N} \frac{Y_k}{W_k} \tag{2.10}$$

The heat capacities at constant volume/constant pressure C_v/C_p are

$$C_v = \sum_{k=1}^{N} Y_k C_{v,k} \tag{2.11}$$

$$C_p = \sum_{k=1}^{N} Y_k C_{p,k} \tag{2.12}$$

where $C_{v,k}/C_{p,k}$ are the heat capacities at constant volume/constant pressure of the respective species k.

In Eq. (2.2) and (2.3) appears the term $\sigma_{i,j} = \tau_{i,j} - P\sigma_{i,j}$ as sum of the pressure tensor $P\sigma_{i,j}$ and the viscous tensor $\tau_{i,j}$, which is defined as:

$$\tau_{i,j} = -\frac{2}{3}\mu \left(\frac{\partial u_i}{\partial x_j} + \frac{\partial u_j}{\partial x_i} \right) \tag{2.13}$$

with μ denoting the dynamic viscosity and $\delta_{i,j}$ the Kronecker delta where $\delta_{i,j} = 1$ if $i = j$ and otherwise 0.

The diffusive flux of species $J_{i,k}$ appears on the right hand side of Eq. (2.4). Exactly evaluating $J_{i,k}$ is a complex task, since obtaining species diffusion velocities via a linear system of equations of size N^2 in all spacial directions over all time steps for each point is necessary. This is shown to be very difficult and costly. Hence most codes apply an approximation to replace the binary mass diffusion coefficient $D_{k,j}$ of a species k into a species j. There are different approaches to model $D_{k,j}$ to become numerically affordable such as Hirschfelder et al. (1969). It is explained in the following: Hirschfelder et al. (1969) approximate $D_{k,j}$ with a diffusion coefficient D_k,

which describes an equivalent diffusion coefficient of species k into the rest of the mixture. To guarantee mass conservation an additional correction velocity (V_i^c), where $i = 1, 2, 3$, is introduced:

$$J_{k,j} = -\rho \left(D_k \frac{W_k}{M} \frac{\partial X_k}{\partial x_i} - Y_k V_i^c \right) \tag{2.14}$$

where

$$V_i^c = \sum_{k=1}^{N} D_k \frac{W_k}{M} \frac{\partial X_k}{\partial x_i} \tag{2.15}$$

The energy flux q_i in Eq. (2.3) contains two flux mechanisms: heat conduction and the diffusion of species with different enthalpies:

$$q_i = \underbrace{-\lambda \frac{\partial T}{\partial x_i}}_{heat \quad conduction} \underbrace{- \rho \left(D_k \frac{W_k}{M} \frac{\partial X_k}{\partial x_i} - Y_k V_i^c \right) h_{s,k}}_{thermal \quad diffusion}, \tag{2.16}$$

$h_{s,k}$ denotes the sensible enthalpy of species k and λ is the heat diffusion coefficient.

To get the species source term one first considers a chemical reactive system of N species reacting over M reactions:

$$\sum_{k=1}^{N} \nu'_{ki} \mathcal{M}_k \rightleftharpoons \sum_{k=1}^{N} \nu''_{ki} \mathcal{M}_m \quad i = 1, M \tag{2.17}$$

$\mathcal{M}_k$ symbolizes a species k. ν'_{kj} and ν''_{kj} denote the molar stochiometric coefficients of a species k in a specific reaction i. The sum of the rates $\dot{\omega}_{k,i}$, which are produced by each reaction, results in the total mass reaction rate $\dot{\omega}_k$:

$$\dot{\omega}_k = \sum_{i=1}^{M} \dot{\omega}_{k,i} = W_k \sum_{k=1}^{M} \nu_{k,i} \mathcal{Q}_i \tag{2.18}$$

with $\nu_{k,i} = \nu''_{k,i} - \nu'_{k,i}$ and the progress rate $\mathcal{Q}_i$ of reaction i, defined as:

$$\mathcal{Q}_i = K_{f,i} \prod_{k=1}^{N} \left(\frac{\rho Y_k}{W_k} \right)^{\nu'_{ki}} - K_{r,i} \prod_{k=1}^{N} \left(\frac{\rho Y_k}{W_k} \right)^{\nu''_{ki}} \tag{2.19}$$

The $K_{f,i}$ and $K_{r,i}$ coefficients denote the forward and reverse rates of reaction i and are typically modeled via the empirical Arrhenius law:

$$K_{f,i} = A_{fi} T^{\beta} e^{-E_{a,i}/(RT)}, \tag{2.20}$$

while the reverse rate is obtained by the forward rate divided by the equilibrium constants:

$$K_{r,i} = \frac{K_{f,i}}{\left(\frac{P_a}{RT}\right)^{\sum_{k=1}^{N} \nu_{k,i}} e^{\left(\frac{\Delta S_i^0}{R} - \frac{\Delta H_i^0}{RT}\right)}} \tag{2.21}$$

where $P_a = 103125Pa$. ΔH_i^0 is the change of sensible and chemical enthalpy in a reaction i, and ΔS_i^0 is the respective change in entropy. With the enthalpy of formation $\Delta h_{s,k}$ at $T_0 = 0K$ of a species k, the combustion heat release $\dot{\omega}_T$ can be defined as:

$$\dot{\omega}_T = -\sum_{k=1}^{N} \dot{\omega}_k \Delta h_{f,k}^0 \tag{2.22}$$

The sensible enthalpy $h_{s,k} = \int_{T_0}^{T} C_{p,k} dT$ is defined so that the condition $h_{s,k}(T = T_0) = 0$ is met. As a result the sensible energy is defined as:

$$e_{s,k} = \int_{T_0}^{T} C_{v,k} dT \tag{2.23}$$

so that it complies to $e_{s,k} = h_{s,k} - RT/W_k$.

Calculating the transport properties requires approximations to keep the computational costs reasonable. This done by first assuming the Prandtl number Pr constant. Pr is defined as:

$$Pr = \frac{\mu C_p}{\lambda} \tag{2.24}$$

and compares momentum to heat transfer. The second assumption is to set the Schmidt number Sc_k also to constant. The Schmidt number

$$Sc_k = \frac{\mu}{\rho D_k} \tag{2.25}$$

compares momentum and species diffusion in a mixture. Via the viscosity μ a simplified relation to the species diffusion coefficient is obtained. For

including the temperature dependency of μ AVBP offers different options such as the law of Sutherland (1893) or, used in this thesis, a power law:

$$\mu = \mu_{ref} \left(\frac{T}{T_{ref}} \right)^b \tag{2.26}$$

where the subscript ref denotes a reference state, while b is a model-constant in range [0.5,1]. In this thesis $b = 0.686$.

2.3 Chemical kinetics

Since during the combustion process new species form while others are consumed the question arises how to describe the process properly in the frame of the problem at hand. They are included in the source terms $\dot{\omega}_k$ in Eq. (2.3) and (2.4). To compute these sources one needs the chemical reaction rate k_r, typically obtained via an Arrhenius law, which is a simplified assumption for molecular collision phenomena:

$$k_r \approx A \exp(-E_a/RT) \tag{2.27}$$

Eq. 2.27 states that to initiate chemical reactions the energy due to colliding molecules must be higher than the so called activation energy E_a, which serves as a threshold for molecular bonds to open. Additionally there is an influence of the orientation of the colliding molecules to favor the initiation of a reaction. This is introduced in Eq. 2.27 via the preexponential factor A. It is to note, that the orientation of the molecules in also dependent on the temperature T, hence A is usually written as $A \equiv AT^\beta$, with a temperature exponent β.

2.4 Numerical Methods for computing reactive NS-equations

Analytically computing the (reactive) NS-equations is in general impossible, due to their non-linear nature. Hence computing them via numerical methods is the main approach of dealing with them (Hirsch (2007); Poinsot and Veynante (2011)). This normally requires the discretization of a domain of interest into computational grids begging the highly important question of

accurate grid resolution, which is governed by the range of relevant time- and length-scales of a certain configuration. Especially in terms of reacting flows, these scales can vary massively from very small domains to very large domains (e.g. explosions), they are governed by the coupling of turbulence and the combustion processes themselves. Note that turbulence itself is one of the most complex phenomena in fluid mechanics and its modeling is one of the key topics in the scientific community.

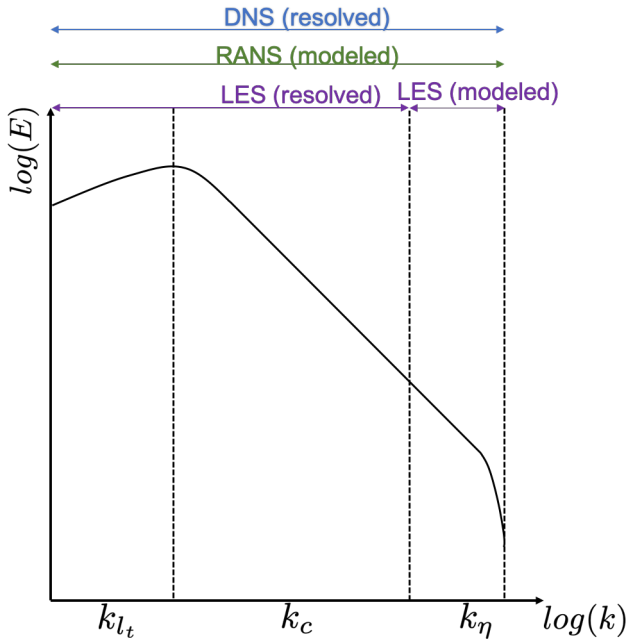

Figure 2.1: Turbulent energy spectrum as a function of the wave number k.

Turbulence is characterized as a fluctuation f' of a certain quantity f, which is split into a mean $\overline{f}$ and the fluctuation, so that $f = \overline{f} + f'$. f' are affiliated with varying length scales, the smallest one being the Kolmogorov length scale η_k to the largest one, the integral length scale l_t. η_k is typically of the order of the free mean length between molecules, whereas l_t is close to the characteristic length scale of a geometry, e.g. the edge length of a cube. With decreasing size of the structures viscous forces increase in dominance. Once at η_k viscous forces balance at inertia. This is often illustrated with the turbulent energy spectrum. Consequently there are 3 typical approaches for numerical simulations of reactive flows systems: 1. Direct Numerical Simu-

lation (DNS), 2. Large Eddy Simulation (LES) and 3. Reynolds-Averaged-Navier-Stokes Simulation (RANS) (Poinsot and Veynante (2011)).

1. DNS is characterized by a sufficient grid resolution to capture all length scales in a flow field, so that no additional modeling is necessary. However this usually requires a very high number of points for capturing the flow flow field and flame structures, so that DNS is normally restricted to academic and canonical configurations and although high performance computing (HPC) has advanced considerably the general costs of a DNS still exceed in term of computational cost. Never the less DNS is a highly useful approach to gain knowledge on the interdependencies between different complex mechanisms.

2. LES is a method which filters the instantaneous balance equations using a cut-off length scale l_c associated to the wave number k_c as seen in Fig. 2.1. This means that large scales of turbulence larger that the characteristic turbulent length scale l_c are directly calculated, while scales smaller than l_c are modeled using subgrid closure models. This results in reasonable costs compared to DNS while delivering excellent results on a variety of configuration. Also by decreasing the cut-off length scale l_c to zero LES tends towards DNS. LES has the become the standard research tool in the field of turbulent reactive flows and is increasingly used in the industry.

3. RANS solves the averaged Navier-Stokes balance equations. This method computes the mean quantities of a flow field and requires two main closure rules: First a turbulence model to capture the effects of turbulence without directly solving it and a (turbulent) combustion model to adequately model the reactive source terms for heat release and chemical species conversion. Historically speaking, RANS approaches are the first since it was impossible for a long time to solve the instantaneous turbulent flow. Due to their low computational cost RANS are still a standard method in commercial codes today.

2.5 Fundamentals of Large Eddy Simulations (LES)

As mentioned in the previous section, LES methods perform a filtering operation on the Navier-Stokes balance equations by a filter size Δ (Poinsot and Veynante (2011)). The filtering operation on a quantity f is:

$$\overline{f} = \int f(x') G_{\Delta}(x - x') dx' \tag{2.28}$$

with a low pass filter G_{Δ}. The effects of the subscale structures (structures smaller than Δ) is defined as

$$f' = f - \overline{f} \tag{2.29}$$

In case of compressible flows, usually a mass-weighted Favre Filtering is applied:

$$\overline{\rho} = \tilde{f} \int \rho f(x') G_{\Delta}(x - x') dx' \tag{2.30}$$

It is important to note that:

- The filtered quantity of a LES fluctuation $\overline{f'}$ is not zero and filtering a filtered quantity $\overline{\overline{f}}$ is NOT equal to $\overline{f}$.
- Filtering of the Navier-Stokes equations demands to commute integral and partial differential operators. This is not valid under most conditions, but the error related to this exchange of operators is generally neglected.

Applying a filter operation on the Navier-Stokes equations leads to a new set of equations:

$$\frac{\partial \overline{\rho}}{\partial t} + \frac{\partial}{\partial x_i}(\overline{\rho}\widetilde{u_i}) \tag{2.31}$$

$$\frac{\partial}{\partial t}(\overline{\rho}\widetilde{u_i}) + \frac{\partial}{\partial x_i}(\overline{\rho}\widetilde{u_i}\widetilde{u_j}) = \frac{\partial}{\partial x_i}(\overline{\tau_{i,j}} - \rho(\widetilde{u_i u_j} - \widetilde{u_i}\widetilde{u_j})) - \frac{\overline{P}}{\partial x_i} \tag{2.32}$$

$$\begin{aligned}
&\frac{\partial}{\partial t}\left(\overline{\rho}\widetilde{E}\right)+\frac{\partial}{\partial x_i}\left(\overline{\rho}\widetilde{u_i}\widetilde{E}\right)= \\
&-\frac{\partial}{\partial x_i}\left(\overline{\rho}\left(\widetilde{u_iE}-\widetilde{u_i}\widetilde{E}\right)\right)- \\
&\frac{\partial}{\partial x_i}\left(\lambda\widetilde{\frac{\partial T}{\partial x_i}}\right)-\frac{\partial}{\partial x_i}\left(\overline{\sum_k h_{s,k}J_{i,k}}\right)- \\
&\frac{\partial}{\partial x_i}\left(\overline{u_i\left(P\delta_{i,j}-\tau_{i,j}\right)}\right)+\overline{\dot{Q}}+\overline{\dot{\omega}_k}
\end{aligned} \tag{2.33}$$

$$\frac{\partial}{\partial t}\left(\overline{\rho}\widetilde{Y_k}\right)+\frac{\overline{\rho}\widetilde{Y_k}\widetilde{u_i}}{\partial x_i}=-\frac{\partial}{\partial x_i}\left(\overline{\rho}\left(\widetilde{u_iY_k}-\widetilde{u_i}\widetilde{Y_k}\right)\right)-\frac{\partial\overline{J_{i,k}}}{\partial x_i}+\overline{\dot{\omega}_k} \tag{2.34}$$

Compared to the species and enthalpy turbulent fluxes, the laminar fluxes are generally negligible. In this work, they modeled by using a gradient assumption:

$$\overline{J_{i,k}}=-\overline{\rho}\left(\overline{D_k}\frac{W_k}{\overline{W}}\frac{\partial\widetilde{X_k}}{\partial x_i}-\widetilde{Y_k}\widetilde{V_i^c}\right) \tag{2.35}$$

$$\overline{\lambda\frac{\partial T}{\partial x_i}}=\overline{\lambda}\frac{\partial\tilde{T}}{\partial x_i} \tag{2.36}$$

$$\overline{\sum_k h_{s,k}J_{i,k}}\sum_k\widetilde{h_{s,k}}\overline{J_{i,k}} \tag{2.37}$$

with a correction velocity $\widetilde{V_i^c}$ (Poinsot and Veynante (2011))

$$\widetilde{V_i^c}=\sum_k N\left(\overline{D_k}\frac{W_k}{\overline{W}}\frac{\partial\widetilde{X_k}}{\partial x_i}\right) \tag{2.38}$$

The transport properties of the turbulent (reacting) flow are also estimated, via resolved quantities, resulting in:

$$\tilde{\mu}=\mu\left(\widetilde{T}\right) \tag{2.39}$$

$$\overline{D_k}=\frac{\overline{\mu}}{\overline{\rho}Sc_k} \tag{2.40}$$

$$\overline{\lambda}=\frac{\overline{\mu}\overline{C_p}\left(\widetilde{T}\right)}{Pr} \tag{2.41}$$

If checked again, one can see that there are other terms in Eq. 2.31-2.34, which cannot be computed directly, hence must be modeled. These terms

are the Reynolds stress tensor $\tau_{i,j}$ (see Sec. 5.4), the species and enthalpy turbulent fluxes and the species chemical source term $\overline{\dot{\omega}_k}$ (see Sec. 5.5).
The **species and enthalpy turbulent fluxes** are typically evaluated via resolved gradients:

$$\overline{\rho}\left(\widetilde{u_i Y_k} - \widetilde{u}_i \widetilde{Y}_k\right) = -\overline{\rho}\left(\overline{D_k^t}\frac{W_k}{\overline{W}}\frac{\partial \widetilde{X_k}}{\partial x_i} - \widetilde{Y}_k \widetilde{V_i^{c,t}}\right) \tag{2.42}$$

$$V_i^{c,t} = \sum_k D_k^t \frac{W_k}{W}\frac{\partial \widetilde{X_k}}{\partial x_i} \tag{2.43}$$

with a turbulent mass diffusion

$$D_k^t = \frac{\mu_t}{\rho Sc_k^t} \tag{2.44}$$

where Sc_k^t denotes the turbulent Schmidt number. On the same basis the turbulent enthalpy flux is modeled:

$$\overline{\rho}\left(\widetilde{u_i E} - \widetilde{u}_i \widetilde{E}\right) = -D_{th}^t \frac{\partial \widetilde{T}}{\partial x_i} + \sum_k \widetilde{h_{s,k}}\,\overline{J_{i,k}^t}. \tag{2.45}$$

The turbulent heat diffusion coefficient is defined as

$$D_{th}^t = \nu_t \frac{\overline{C_p}}{Pr^t} \tag{2.46}$$

where Pr^t is the turbulent Prandtl number.

Chapter 3

Fundamentals of Deflagration

Contents

3.1 Introduction

This chapter gives an overview over the basics of laminar flames, since deflagration can be also observed in RDE systems and must hence be explained. The structure of a laminar premixed flame is first examined and basic properties are introduced. This is followed by an overview of different regimes of turbulent premixed flames.

3.2 Laminar premixed flames

3.2.1 Flame structure

An unstretched premixed flame is a classic case for understanding basic combustion processes. This represents a situation where fuel and oxidizer are mixed before combustion. Temperature, pressure, and gas composition of the mixture determine the initial conditions such a flame (Poinsot and Veynante (2011); Turns et al. (1996)). The composition is characterized by the equivalence ratio ϕ:

$$\phi = s\frac{Y_F}{Y_{Ox}}. \tag{3.1}$$

Y_F and Y_{Ox} are the fuel and oxidizer mass fractions in the mixture. s denotes the mass stoichiometric ratio:

$$s = \left(\frac{Y_F}{Y_{Ox}}\right)_{st} = \frac{\nu'_O W_O}{\nu'_F W_F} \tag{3.2}$$

where ν'_F and ν'_O are the fuel and oxidizer stoichiometric molar coefficients of the respective global reaction.

In a first step, the characterization of a flame and particularly its structure is described via a control volume in the reference of a one-dimensional flame. This simplifies the NS-equations and one can add 3 basic assumptions. The first assumption is that combustion can be characterized by a single, irreversible exothermic reaction following an Arrhenius formulation, containing a high activation energy. The second one assumes that one of the species is excessively present so that its consumption doesn't overall impact the reaction rate, allowing to describe the reaction basically as $R \rightarrow P+Q$, R denoting the reactants, P the products and Q released chemical energy. The last simplification yields to R and P being of the same molecular weight, uniform molecular diffusion coefficient D, a Lewis number $Le = 1$ and a constant heat capacity C_p. The resulting equations are:

$$\frac{\partial \rho u}{\partial x} = 0 \tag{3.3}$$

$$\rho_u C_p s_L \frac{\partial T}{\partial x} = \frac{\partial}{\partial x}\left(\lambda \frac{\partial T}{\partial x}\right) - Q\dot{\omega}_R \tag{3.4}$$

$$\rho_u s_L \frac{\partial Y_R}{\partial x} = \frac{\partial}{\partial x}\left(\rho D \frac{\partial Y_R}{\partial x}\right) + \dot{\omega}_R \tag{3.5}$$

In spite of the presumably strong assumptions made, the set of equations conserves the global flame features such as changes in density and temperature and highly non-linear heat release. The flame structure one obtains contains a preheat zone, where thermal fluxes heat up the fresh gases, followed by the reaction zone with an increasingly strong reaction $R \rightarrow P$, where reactants turn into products. Once the reactions are completed, the temperature arrives at the adiabatic equilibrium state in a post-flame zone (Fig. 3.1 (a)).

Equation 3.3 is equivalent to the expression $\rho u = \rho_u s_L$, where s_L denotes the laminar flame speed, which is the velocity at which the flame propagates with respect to the unburnt gases. An analytic expression for s_L can be obtained by asymptotic analysis (Williams (1985), Echekki and Ferziger (1993)). An asymptotic analysis of the governing equations reveals a scaling law for s_L:

$$s_L \propto (AD_{th})^{0.5} \tag{3.6}$$

which allows to conduct a first estimation of the flame thickness, namely the diffusive thickness δ_{th}, via a dimensional analysis:

$$\delta_{th} \equiv D_{th}/s_L \propto (D_{th}/A)^{0.5} \tag{3.7}$$

Besides other possibilities, a common definition for the flame thickness is the thermal thickness δ_L which can be determined by the temperature profile:

$$\delta_L = \frac{T_b - T_u}{max(|\partial T/\partial x|)} \tag{3.8}$$

T_b denotes the burnt gas temperature after all chemical energy has been released. T_u is the unburnt gas temperature of the fresh gases. Assuming constant pressure conditions one can derive T_b as a function of the released heat and the fresh gas' fuel mass fraction Y_F^u:

$$T_b = T_u + QY_F^u/C_P \tag{3.9}$$

Although the simple model for the flame structure is a good approximation for the real case, other phenomena require more detailed modeling (Fig. 3.1 (b). A typical example is ignition, which requires a proper detailed scheme, since real flames do not convert their reactants directly into product, but form intermediate species Y_{int}. These species are not present in the fresh gas composition and are formed by endothermic initiation reactions and subsequently react in exothermic chain branching reactions into stable products.

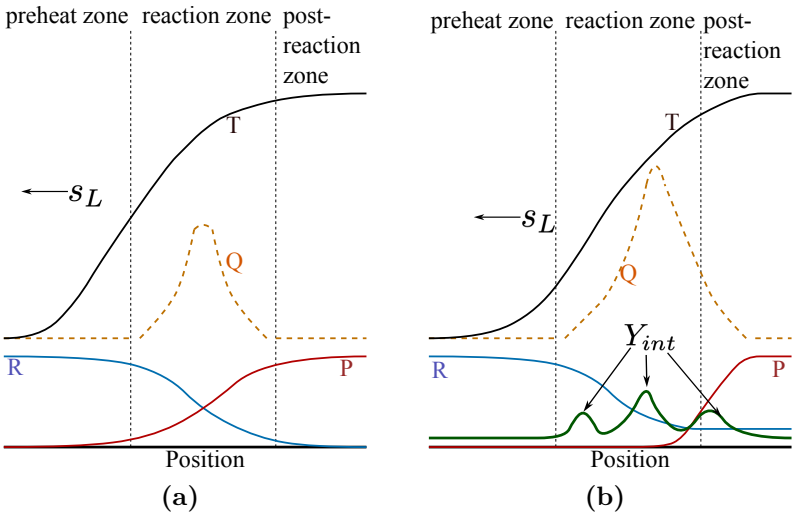

Figure 3.1: Sketch of a 1D flame with the simplified chemical approach (a) and with a detailed chemical model (b).

3.2.2 Definitions of the flame speed

In addition to the previously introduced laminar flame speed s_L, other definitions of the flame speed exist, which can be derived from kinematic conditions. The flame absolute speed $s_a = \mathbf{w.n}$ is the normal velocity component of the flame front speed $\mathbf{w} = (w_i)_{i=1,3}$ in an absolute reference frame speed. Alternatively one can determine the flame displacement speed $s_d = s_a$-$\mathbf{w.n}$, which is the relative speed of the flame front with respect to the local flow velocity (Fig. 3.2)

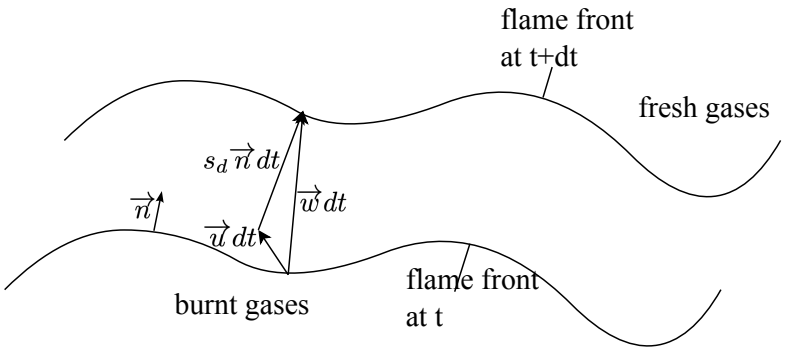

Figure 3.2: Sketch of a moving flame front, from Poinsot and Veynante (2011).

Based on the rate of the consumption of reactants normal to the flame front one can also define the consumption speed s_c:

$$s_c = \frac{1}{\rho_u(Y_F^u - Y_F^b)} \int_{-\infty}^{\infty} \dot{\omega}_F dn \tag{3.10}$$

where Y_F^b denotes the fuel mass fraction of the burnt gases. Contrary to s_d, varying from fresh to burnt gases as a result of flow dilatation, s_c is a global quantity normal to the full flame front. For a laminar unstretched premixed flame $s_a = 0$ and $s_L = s_c$ in the reference frame of the flame.

The flame speed can be altered by effects such as stretch, the temporal variation of a flame surface element (Matalon and Matkowsky (1982), Candel and Poinsot (1990)). Since stretch is not subject of research in this thesis, it is briefly mentioned but not discussed in detail. The effects of stretch have been thoroughly studied theoretically by usage of the ZFK model and it has been e.g. shown that low stretch linearly alters s_c and s_d (Clavin, 1985). It has also been shown that the burnt gas temperature deviated from T_{ad} when $Le_F \neq 1$ and stretch is present (Clavin and Williams, 1982).

3.3 Turbulent premixed flames

In this section the concept of turbulence is briefly introduced and its influence on flames will be roughly explained.

3.3.1 Turbulence

A flow becomes turbulent when the Reynolds number is large enough. Re is defines as:

$$Re = \frac{\rho u L}{\mu} \tag{3.11}$$

where L denotes a characteristic length scale of the problem at hand, μ is the dynamic viscosity of the fluid and u the local flow speed of the fluid. Re is a measure of the ratio of the inertia and the viscous forces in a flow. If Re exceeds a certain threshold value (which is also problem specific) the flow becomes turbulent. In aeronautic applications, turbulence is an important phenomenon that drives mixing of non-premixed reactants and its numerical treatment is, as mentioned before, not easy to model.

3.3.2 Turbulence - flame interaction

So far the flows were assumed to be laminar. However if a flame encounters a turbulent flow field, turbulence and the flames interact leading to so called turbulent flames: the flame is impacted by the eddies in the flow and hence different "types" of turbulent flame regimes can occur.

To distinguish between different regimes, different length and time scales are introduced (Poinsot and Veynante, 2011): the integral length scale l_t, the Kolmogorov length scale η_k. Based on the length scales one can derive the integral time scale $\tau = L_t/u'(l_t)$ and $\tau_K = \eta_k/u'_{\xi_k}$, where $u'(l_t)$ denotes the flow velocity fluctuations at the scale l_t and u'_{η_k} the flow velocity fluctuations at η_k. A combustion time scale $\tau_c = \delta_L/s_L$. This leads to the formulation of the Damköhler number

$$Da = \frac{\tau_t}{\tau_c} = \frac{l_t}{\delta_L}\frac{s_L}{u'(l_t)} \tag{3.12}$$

To compare the smallest turbulent length scales and the reactive scales the Karlovitz number Ka is introduced:

$$Ka = \frac{\tau_c}{\tau_K} = \frac{\delta_L}{\eta_k}\frac{u_{\eta_k}}{s_L} \tag{3.13}$$

The Da and Ka are linked via:

$$Re_t = Da^2 Ka^2 \tag{3.14}$$

In addition to Ka a Ka_r based on the thickness of the reaction zone δ_r can be defined. Since δ_r is orders of magnitude smaller than δ_L, Ka_r is smaller than Ka:

$$Ka_r = \frac{\delta_r}{\eta_k}\frac{u_{\eta_k}}{s_L} < Ka \tag{3.15}$$

Based on a number of assumptions such as homogenous isentropic turbulence, steady state treatment, simplified chemical schemes, etc., non-dimensional numbers allow to classify the different combustion regimes (Fig. 3.3):
Laminar flames ($Re_t < 1$): the flame can be wrinkled by hydrodynamic and thermodiffusive instabilities but the flame structure is not a result of the turbulence in the flow. Hence the flame is considered laminar.
Turbulent flames ($Re_t > 1$): these flames can be divided into subcategories

based on Ka and Ka_r. If $Ka < 1$ one obtains a so called thin flame, which is characterized by a flame thickness smaller than the smallest turbulent structures, which in turn means they do not interact with the internal structure of the flame. In case of moderate turbulent fluctuations ($u'/s_L < 1$) the flame surface wrinkles and stretches only slightly leading to so-called **wrinkled flamelets**. In the opposite case ($u'/s_L > 1$) the turbulent fluctuations are higher than the flame speed, hence the flame surface is object to high stretch and wrinkling, leading to so-called **corrugated flamelets**.
Reaction sheets ($Ka > 1$, $Ka_r < 1$): the smallest eddies are able to modify the properties in the preheat zone, but the reaction zone itself keeps a laminar structure.
Well-stirred reactors ($Ka > 1$, $Ka_r > 1$): the whole internal structure of the flame is modified by the turbulent structures.

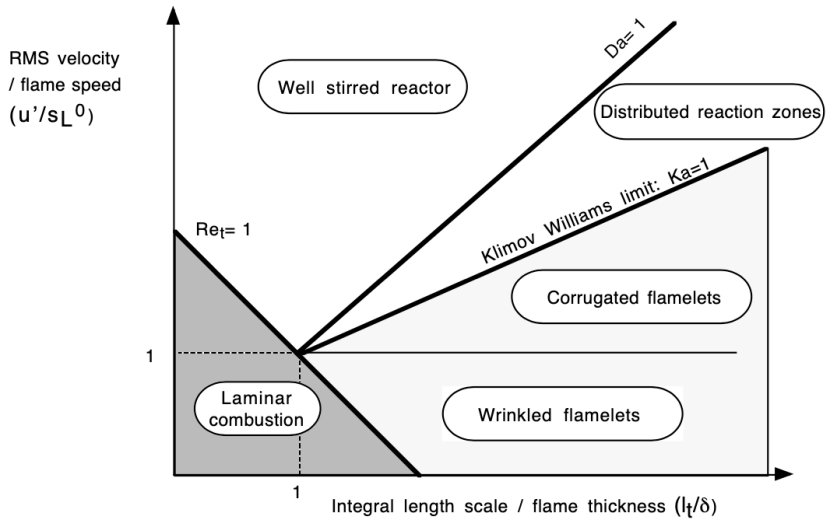

Figure 3.3: Combustion regimes identified by length (l_t/δ) and velocity (u'/s_L^0) ratios using a log-log scale, from Poinsot and Veynante (2011).

Chapter 4

Fundamentals of Detonations

Contents

4.1 Introduction

While the propagation of (partially) premixed flames is mainly controlled by thermal conduction, detonation properties are governed by shock dynamics. This chapter will introduce the basic theory of detonations, starting at the detonation structure and subsequently explaining the multidimensional effects influencing the detonation propagation.

4.2 One-dimensional detonations

Detonations is a combustion regime, which is not controlled by heat conduction like deflagration, but by shock dynamics. A combustion wave moves at high velocity relative to the corresponding fresh gases at supersonic speed.

A shock wave denotes an instantaneous (in a continuum sense) increase in pressure and temperature of the mixture along the propagation direction in a gas. In case of reactive gases the increased temperature can suffice for exothermic reactions to occur, leading to a reacting zone attached to the shock. A sketch of the structure of a 1D detonation propagating at constant velocity D with respect to fresh gases is shown in Fig. 4.1. The structure of the detonation wave involves three gas states (Clavin and Searby, 2016; Fickett and Davis, 2000; Lee, 2008):

1. the fresh gas state upstream the incident shock wave
2. the VN state: the state of the gas just downstream the incident shock wave.
3. the burnt gas state, which denotes the state of gas after complete heat release. (b)

Chemical reactions are initiated by the favorable thermodynamic conditions at the VN state after and characteristic induction time τ_i. This induction zone has a characteristic length scale of

$$\delta_i = u_N \tau_i, \tag{4.1}$$

being the product of the induction time and the downstream velocity of the gas u_N. Just after the induction zone, reactions are initiated and proceed while burning the reactive mixture. Another characteristic quantity is the half reaction thickness $\delta_{1/2}$, which denotes the length from the VN state towards the position where 50% fuel is has been consumed.
In the following the internal detonation structure is described by:

1. analyzing of the thermodynamic conditions at the VN state by evaluating the jump conditions across the leading shock,
2. obtaining the thermodynamic conditions of the burnt gas state, by assuming the detonation to be a reactive shock (bypassing the intermediate stated between burnt and fresh)

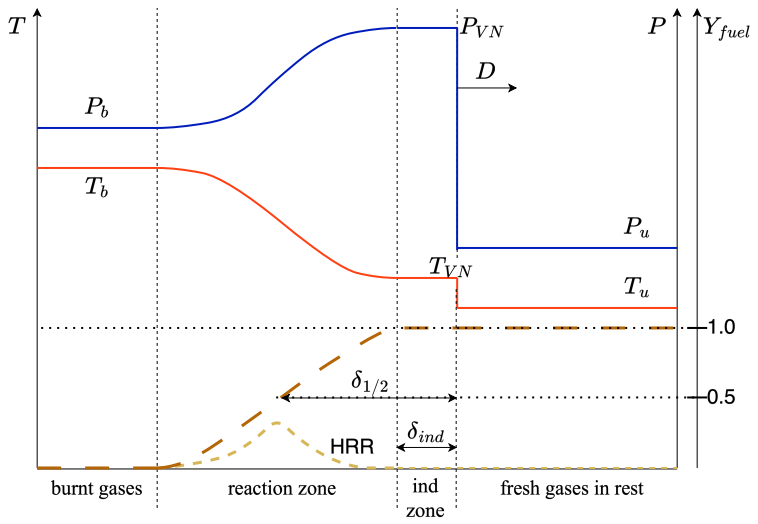

Figure 4.1: Detonation front propagating at constant speed D. Downstream of the leading shock the so called Von-Neumann state (VN) is found. After the VN-state, exothermic reactions are initiated after an induction time τ_i in the induction (ind) zone. The burnt gas state, denoted by the subscript b, is reached after the combustion products are formed. Adapted from Lee (2008).

3. and incorporating the intermediate states by including the influence of the reaction rate.

4.2.1 The Von-Neumann state and Rankine-Hugoniot relations

In the reference frame of the detonation the mass conservation with the mass flow rate $\dot{m}$ is defined as (Lee, 2008):

$$\rho_u D = \rho_N u_N = \dot{m} \tag{4.2}$$

The momentum equation reads as:

$$\rho_u D^2 + P_u = \rho_u u_n^2 + P_N \tag{4.3}$$

which is obtained by imposing a homogeneous velocity u except inside the shock itself. In the $p - v$ ($v = 1/\rho$) diagram the states satisfying Eq.4.2 and

4.3 form the Rayleigh line:

$$\frac{P_u - P_N}{(1/\rho_N) - (1/\rho_N)} = \frac{P_u - P_N}{v_N - v_u} = -\dot{m}^2 \tag{4.4}$$

One can see that the slope of the Rayleigh line is $-\dot{m}^2$. Equation 4.4 gives a family of solutions, thus the energy equation is necessary to retrieve the VN state. Across the shock, no chemical energy is released resulting in the energy equation of the form:

$$h_u + \frac{D^2}{2} = h_{VN} + \frac{u_{VN}^2}{2} \tag{4.5}$$

and combined with Eq. 4.4 the energy equation reads as:

$$h_{VN} - h_u = \frac{1}{2}(v_{VN} + v_u)(P_{VN} - P_u) \tag{4.6}$$

For an ideal gas with constant heat capacities per unit mass C_P and C_v, Eq 4.6 becomes:

$$\frac{\gamma}{\gamma - 1}\left(\frac{P_{VN}}{\rho_{VN}} - \frac{P_u}{\rho_u}\right) = \frac{1}{2}(v_{VN} + v_u)(P_{VN} - P_u) \tag{4.7}$$

$$(\gamma + 1)\left(\frac{P_{VN}}{P_u} - 1\right)\left(\frac{v_{VN}}{v_u} - 1\right) = -2\left(\frac{P_{VN}}{P_u} - 1\right) - 2\gamma\left(\frac{v_{VN}}{v_u} - 1\right) \tag{4.8}$$

The non-dimensional quantities $\mathcal{P}$ and $\mathcal{V}$

$$\mathcal{P} \equiv \frac{\gamma + 1}{2\gamma}\left(\frac{P_{VN}}{P_u} - 1\right) \tag{4.9}$$

$$\mathcal{V} \equiv \frac{\gamma + 1}{2}\left(\frac{v_{VN}}{v_u} - 1\right) \tag{4.10}$$

reduce the obtained Eq.4.5 and Eq.4.8 to a linear and equilateral hyperbola in the $\mathcal{P} - \mathcal{V}$ space:

$$\mathcal{P} = -\mathcal{M}_u^2 \mathcal{V} \tag{4.11}$$

$$(\mathcal{P} + 1)(\mathcal{V} + 1) = 1 \tag{4.12}$$

$\mathcal{M} = D/a_u$ is the Mach number of the detonation with respect to the fresh gases and a_u is the sound speed in the unburned mixture. These relations together describe the VN-state with the two asymptotes $\mathcal{P} = -1$ and $\mathcal{V} = -1$

4.2.2 The burned gas state

Similar as in Section 4.2.1 the jumping conditions across a detonation can be obtained by skipping all intermediate states between fresh and burnt gases. The difference is the exothermic reaction zone with which Eq.4.8 becomes:

$$\frac{\gamma}{\gamma-1}\left(\frac{P_b}{\rho_u}-\frac{P_u}{\rho_u}\right)-\frac{1}{2}(v_b+v_u)(P_b-P_u)=q_m, \tag{4.13}$$

where q_m denotes the released chemical energy, per unit mass once all of this energy is released:

$$q_m = C_p(T_b - T_u) + (u_b^2 - D^2)/2 \tag{4.14}$$

This introduces the non-dimensional quantities

$$\mathcal{P} \equiv \frac{\gamma+1}{2\gamma}\left(\frac{P_b}{P_u}-1\right) \tag{4.15}$$

$$\mathcal{V} \equiv \frac{\gamma+1}{2}\left(\frac{v_b}{v_u}-1\right) \tag{4.16}$$

$$\mathcal{Q} \equiv \frac{\gamma+1}{2}\left(\frac{q_m}{C_p T_u}\right) \tag{4.17}$$

which subsequently lead to the relations:

$$\mathcal{P} = -\mathcal{M}_u^2 \mathcal{V} \tag{4.18}$$

$$(\mathcal{P}+1)(\mathcal{V}+1) = 1 + \mathcal{Q} \tag{4.19}$$

Due to $\mathcal{Q} > 0$, the equilateral hyperbola is shifted above in the $p-v$ Diagram compared to the frozen hyperbola expressed in Eq.4.12. Still, both curves have the same asymptotes.

Figure 4.2 shows the Rayleigh line and two examples of Hugoniot curves (previously derived hyperbolae). The intersection of the Rayleigh line with the non-reactive Hugoniot curve denotes the VN-state. Respectively the intersection of the Rayleigh line and the Hugoniot curve after heat release denotes the burnt gas state. Subsequently the states VN and b depend on the slope of the Rayleigh line, which in turn is given via the detonation propagation speed D.

For a given D, if $(\mathcal{M}_u^2 - 1)^2 - 4\mathcal{Q}\mathcal{M}_u^2 \geq 0$ is satisfied, the Rayleigh line and the Hugoniot curve after heat release intersect. Hence only if the

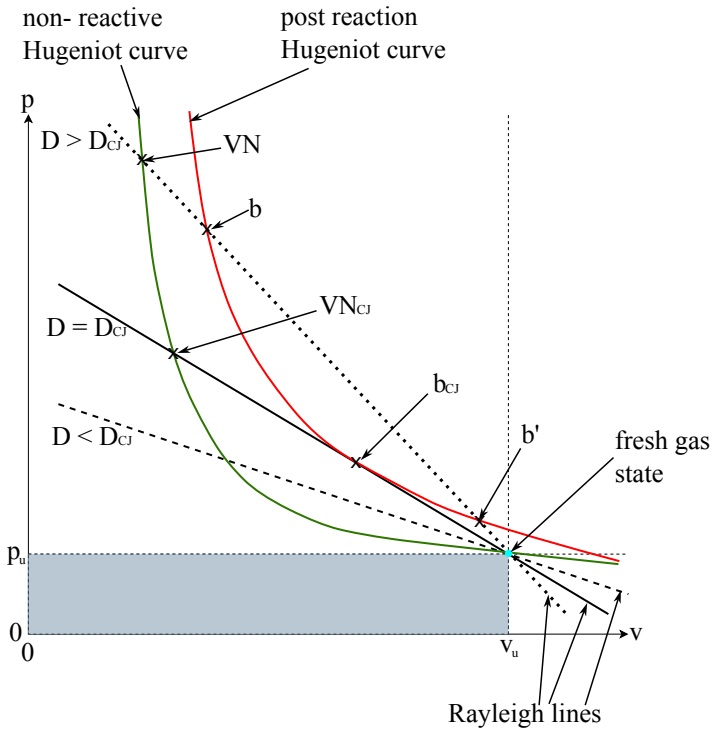

Figure 4.2: Qualitative plot of a detonation in the $p-v$ plane, where the initial state corresponds to (p_u,v_u). VN is the Von-Neumann state and b is the burnt gas state. Adapted from Lee (2008).

detonation speed D is bigger than a threshold value D_{CJ}, the Chapman-Jouguet detonation speed, a detonation can be present. This condition is equivalent to $\mathcal{M}_u \geq \mathcal{M}_{u,CJ}$, meaning that a steady planar detonation cannot propagate at a constant speed $D < D_{CJ}$. Additionally, for $D > D_{CJ}$ the Rayleigh line and Hugoniot curve after heat release intersect twice in the regime points b and b'. The former is known as a strong detonation, while the latter is known as weak detonation. The state when the Rayleigh line is tangent to the Hugoniot curve after heat release is unique and called CJ state.

The existence of weak detonations has been a a topic of research and many researchers such as Lee (2008) or Clavin and Searby (2016) and many of them discard the existence of weak detonations. Typically this is based on assuming the pathway of a weak detonation solution in the $p-v$ diagram:

1. The solution reaches from an initial state u the equilibrium state b'

via the Rayleigh line. However, acc. to Clavin and Searby (2016) the thickness of a supersonic wave attached to a flame is too high and thus unrealistic at room temperature.

2. It is assumed that the solution is first adiabatically compressed to VN before it transitions to state b'. An argument against this is the violation of the second law of thermodynamic or instability of the structure since the flow behind a weak detonation is shown to be supersonic, resulting in disturbances being unable to escape the detonation front. The later argument has been opposed by Zeldovich (1992), who argues that an instability requires that the disturbances grow in amplitude with time and concludes that the presence of disturbances at the detonation tail does not automatically insinuate instability.

The possibility of weak detonations is provided by von Neumann (1942) via the nowadays so called pathological detonations, whose existence were confirmed for $H_2 - Cl_2$ mixtures by Dionne et al. (2000). Based on that, the weak detonation solution cannot be simply excluded.

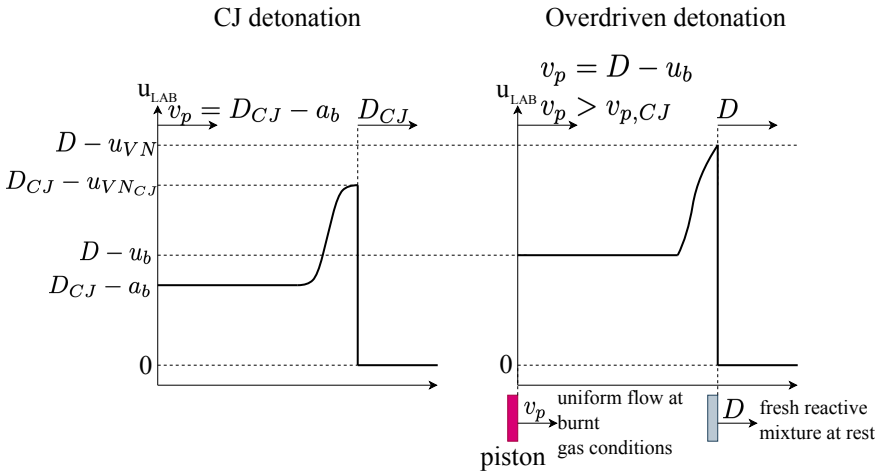

Figure 4.3: Velocity profile in the laboratory frame u_{lab}, in case of a steady planar detonation (left) and an overdriven detonation (right). The overdriven detonation occurs when a piston downstream of the detonation moves at the velocity $v_p > v_{p,CJ}$. Adapted from Clavin and Searby (2016).

4.2.3 The ZND structure

To describe the internal structure of a detonation, a generalized version of Eq. (4.19) is introduced, containing a progress variable c, where c =0 denotes the fresh mixture state and c =1 denotes the burnt mixture.

$$(\mathcal{P}+1)(\mathcal{V}+1) = 1 + \mathcal{Q}c \tag{4.20}$$

Equation (4.20) describes the hyperbolae between the non reacted (c =0) and fully reacted (c =1) Hugoniot curve. The structure of the detonation can then be expressed by the flow velocity and the thermodynamic variables as functions of the progress variable $c(x)$.
In the reference frame of the detonation, the velocity of the flow behind the shock is subsonic. For an increasing c the velocity increases as well. In case of $D > D_{CJ}$, the flow remains subsonic through the whole detonation front. On the other hand, when $D = D_{CJ}$ the flow reaches a sonic state when the mixture arrives at the burnt gas state b_{CJ}.

4.3 Obtaining CJ Detonations

It has been shown in experiments that after ignition/initiation (e.g. via a DDT) detonation propagate at first at velocities $D > D_{CJ}$ and subsequently decay towards a quasi-steady state D_{CJ} after a sufficient amount of time. Generally detonation speeds close to the theoretical D_{CJ} have been obtained in experimental studies, which in turn implies the existence of a mechanism leading to a convergence towards near CJ conditions after ignition/initiation. This can be related to the fact that the downstream conditions of a strong detonation are subsonic, allowing an expansion wave to reach the detonation front and thus attenuate the detonation until CJ conditions are reached. In other words strong detonations cannot sustain themselves, and the the detonation becomes stable at D_{CJ} since $Ma = 1$ at CJ plane, blocking waves moving upstream. The existence of strong detonations can be explained by regarding the detonation in its reference frame: due to mass conservation the burnt gas velocity is $u_b = \rho_u D/\rho_b$. Hence the boundary condition downstream of the detonation can be considered as a piston which pushes the burnt gases at a speed $v_p = D - u_b > 0$. The subsequent question: which one is the minimum v_p for a strong (and planar) detonation? The lowest possible detonation speed for a self-sustained detonation is $D = D_{CJ}$, resulting,

based on the previously mentioned definition for v_p and mass conservation, in $v_{p,CJ} = D_{CJ}(1 - \rho_u/\rho_{b,CJ})$. In other words the condition $v_p > v_{p,CJ}$ has to be fulfilled to obtain a strong detonation, giving it also the name "overdriven" detonation.

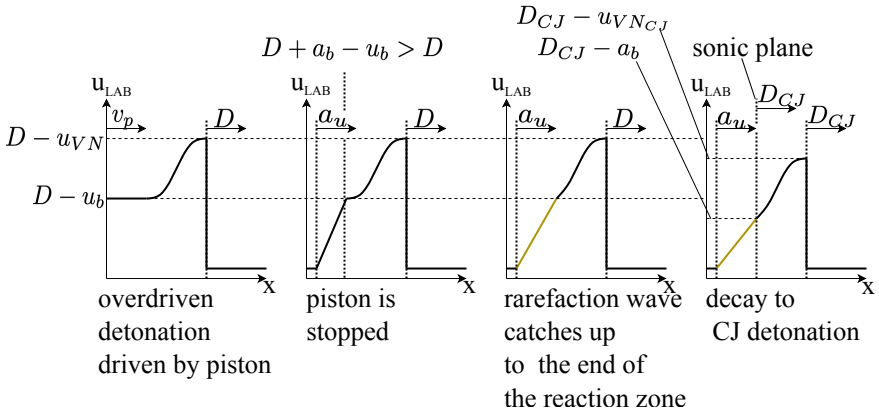

Figure 4.4: Sketch explaining the transition from overdrive to a CJ detonation. Adapted from Dounia (2018).

How does an overdriven detonation progress into a CJ detonation? Assuming one immediately stops the supporting piston, v_p becomes 0 leading to a rarefaction wave traveling upstream. This wave propagates at sonic speed with respect to the burnt gases and the velocity can be expressed as $D - u_b + a_b$. With the burnt gas conditions after the detonationn being subsonic, the rarefaction wave can consequently catch up to the detonation front decelerating the current D to D_{CJ}. Since under CJ conditions the burnt gases propagate at sonic conditions, the rarefaction wave cannot reach the detonation front anymore, which in turn fixes the detonation speed to D_{CJ}. Details are illustrated in Fig. 4.4.

4.4 Detonation instabilities

On average, self sustained detonations have a constant propagation speed. However experiments show that detonation fronts behave unstably, hence it is necessary to discuss these instabilities in the following.

The first experiments, which revealed the structure of instabilities were conducted in the 1960s by different researchers such as Duff (1961), White

(1961), Schott (1965) or Strehlow (1968). The experimental technique to obtain an idea of these instabilities is the application of soot coated foils on walls. The different shocks of the unstable detonation front leave imprints of their trajectories on the soot-foil allowing to get a "footprint" of the past detonation. The result of such an experiment can be seen in the Fig. 4.5.

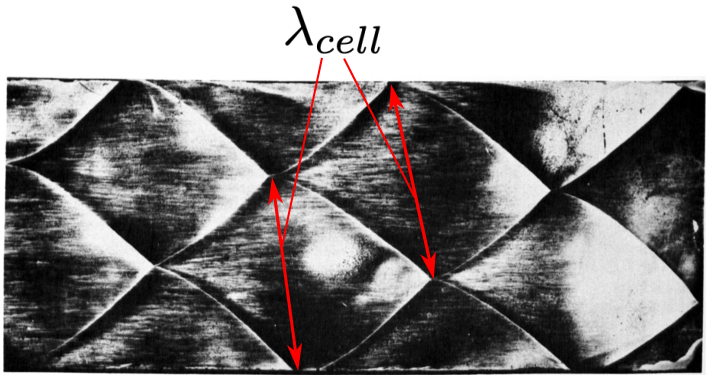

Figure 4.5: Soot-foil of a $2H_2+O_2+70\%Ar$ dilution detonation. The experiment shows a very well captured detonation cell structure with a highly regular pattern. λ_{cell} is the detonation cell size. Adapted from Strehlow (1968).

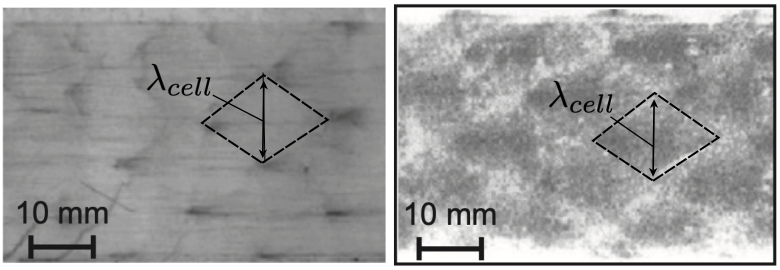

Figure 4.6: Captured pattern for heat-sensitive (left) and pressure-sensitive (right) papers for $2H_2 + O_2 + 7Ar$, $p_0 = 39$ kPa. λ_{cell} is the detonation cell size. Adapted from Ishii et al. (2013).

In a bit more recent studies other approaches such as the application of different particle types, e.g. $CaCO_3$ or pressure/temperature sensitive papers (see Fig. 4.6) are used to capture the diamond like structure of detonations. Details can be looked up in Ishii et al. (2013).

In modern day a huge database for the characteristics of these cellular pattern can be accessed online, exemplary the Detonation Database, spanning

a huge variety of mixtures and conditions. These databases are continuously updated due to the efforts of numerous groups worldwide. The mechanism behind the unstable detonation front is a combination of one-dimensional instabilities in the ZND stucture of a detonation and transverse running pressure waves that create singularities in the leading shock front.

4.4.1 One-dimensional instabilities

Assuming one-dimensional detonation, the instabilities express themselves as longitudinal pulsations in propagation direction. This is a result of the sensitivity of the induction zone to changes in the thermodynamic conditions at the shock front. If, for example, a disturbance amplifies the shock strength (see Fig. 4.7), which in turn results in a reduction of the ignition delay, the reaction area will move upstream.

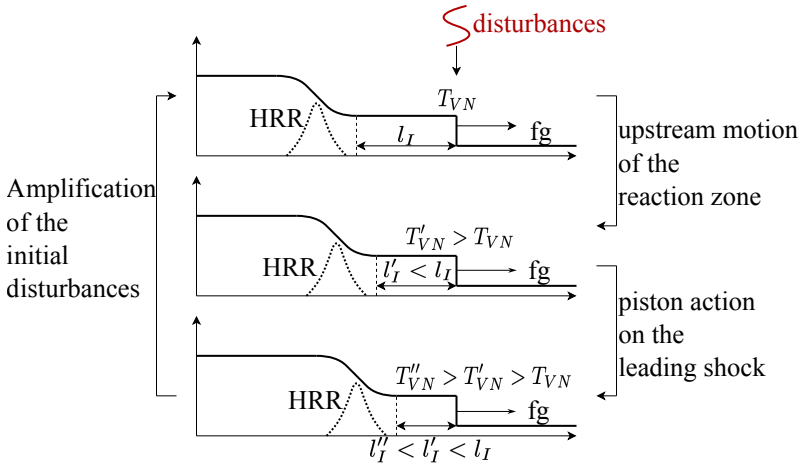

Figure 4.7: Sketch of a one-dimensional instability of the ZND structure, with the induction zone length l_I. HRR denotes the local heat release rate and fg fresh premixed reactants at rest. Adapted from Dounia (2018).

The disturbances between reaction zone and the leading shock are to be differentiated. The upstream moving ones are caused by acoustic waves, propagating at the speed of sound. The downstream moving disturbances are a combination of acoustic and entropy waves, therefore a phase shift occurs creating an oscillatory behavior of the instability. Note that the entropy waves cause the longest delay, due to the subsonic flow after the leading shock. Detonations who propagate under these conditions are usually referred to as

"galloping detonations". Two parameters are the main contributors to the unstable behavior (Lee, 2008): first, the sensitivity of the induction kinetics which can be linked to the activation energy E_a and second the so-called degree of overdrive $f = (Ma_0/Ma_{CJ})^2 \geq 1$. Clavin and He (1996) have demonstrated theoretically that for strongly overdriven detonations the delay due to entropy waves in a quasi isobaric mass conservation is the origin of the oscillations. In case of slighty overdriven detonations where $f \sim 1$, in other words close to CJ-conditions Clavin and Williams (2002) show that in fact upstream running acoustic waves are the origin of the instability. To investigate the influence of instabilities caused by chain-branching kinetics Ng et al. (2005) introduce the stability parameter χ:

$$\chi \equiv \epsilon_I \frac{\Delta_I}{\Delta_R} = \epsilon_I \Delta_I \frac{\dot{\sigma}_{max}}{u_{CJ}}. \tag{4.21}$$

ϵ_I denotes the activation energy, which governs the sensitivity of the induction period. Δ_I and Δ_R are the characteristic induction length and the reaction length. The reaction length in this case is defined as the the particle velocity at the CJ plane in the frame of the detonation and $\dot{\sigma}_{max}$ is the maximum thermicity which is a time scale for the heat release. χ allows to obtain a stability threshold value under which a detonation propagates stabilizes. If the limiting χ is sufficiently exceeded initial pertubations in the reaction zone become augmented and the detonation becomes unstable and can even quench.

4.4.2 Multi-dimensional instabilities: detonation cell structure

The structures shown in Fig. 4.5 and 4.6 result from the one-dimensional instabilities in a ZND detonation and the transverse pressure waves that move perpendicular to the the main propagation direction. The superposition of the transverse waves and the leading shock lead to the formation of so called triple points on the leading shock front (Fig. 4.8). Different authors have observed these triple points on different perturbed shock fronts. In case of Larsson et al. (2013) it was on shock fronts interacting with vortices and turbulence, whereas Briscoe and Kovitz (1968) observed triple points on shock fronts perturbed by undulated walls. These instabilities are highly dependent on the mixture composition and the respective thermodynamic

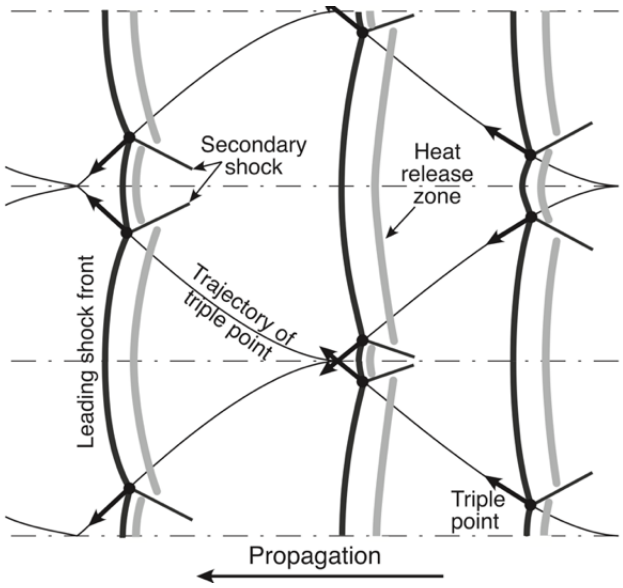

Figure 4.8: Time evolution of a cellular detonation. Transverse propagation of triple points coupled to the longitudinal pulsation of the internal and quasi-planar structure creates the diamond pattern. From Clavin and Searby (2016).

conditions. Also triple points typically appear after transitioning from a stable condition to an unstable one when interacting with perturbations. During this transition triple points start to form and subsequently a steady condition is reached. This has been thoroughly investigated by e.g. Clavin and Denet (2002).

The result of these instabilities is displayed in Fig. 4.5 and 4.6, where very regular patterns are shown, which makes the measurement of the detonation cell size λ_{cell} relatively straightforward. On the other hand the soot foils can show patterns with cells of varying size making it difficult to determine which λ_{cell} is the "correct" one. Smaller cells can occur within a dominant cell depending on the setup such as in tests by Moen et al. (1982) (Fig. 4.9).

Obtaining the detonation cell size mathematically is a difficult task and different approaches to determine it have been proposed. The assumption is that the detonation cell size λ_{cell} is a function of a characteristic length of the 1D ZND detonation such as δ_i or $\delta_{1/2}$. Other lengths such as $\delta_{0.75}$ (distance from VN to where $Ma = 0.75$, Tieszen et al. (1987)) and δ_T (distance from VN to the $max(dT/dx)$, Ciccarelli et al. (1997)) have been used as well. Depending on the research group, λ_{cell} is then computed as $\lambda_{cell} = A_{prop}\delta_X$,

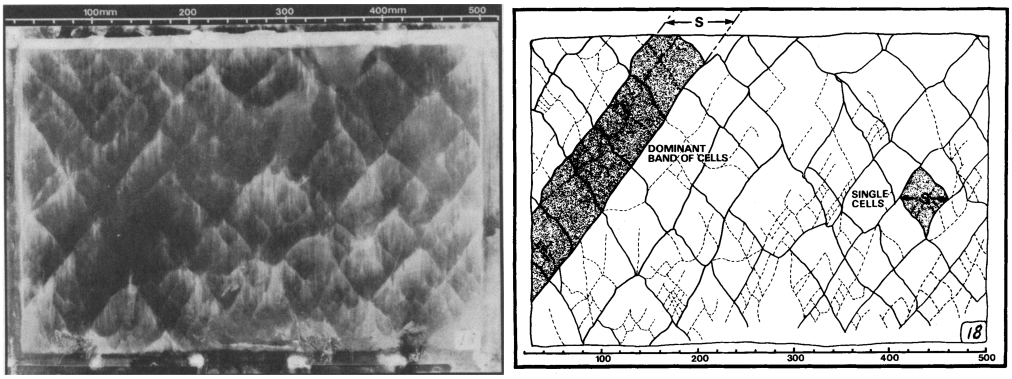

Figure 4.9: Smoked foil (4.6% C_2H_4 in a tube with a diameter of 0.89m) on the left with an interpretation sketch pointing out both a single cell and a dominant diagonal band of cells on the right. The dashed lines denote smaller cells formed withing the bigger ones. From Moen et al. (1982)

where the subscript X is a placeholder for the different characteristic lengths. The obtained values for A_{prop} range from 10-50. Different authors point out that A_{prop} is additionally dependent on the equivalence ratio, since the deviations of the predicted λ_{cell} to the measured ones increases when approaching the limits in terms of the equivalence ratio. Gavrikov et al. (2000) have developed a simple, yet more sophisticated model to compute the λ_{cell}, which is a function of two parameters: the dimensionless effective activation energy and a parameter describing the connection between chemical energy and initial thermal energy of the fresh gases. Monnier (2023) derived algebraic relations, which allow to estimate the average detonation cell size from the respective ZND structure of the fresh gases. Although different strategies exist, none of them appear to deliver reliable values for the λ_{cell}, or at best for a fixed initial gas state. This is aggravated by the complicated measuring process. Due to potential irregularities in λ_{cell}, e.g. in Fig. 4.9, the measurements are prone to observer bias.

The fact that the detonation cell size can be estimated from $\delta_{1/2}$, which can be numerically obtained with 1D chemistry solvers (details in Chapter 6), shows that the design of a chemical scheme, which incorporates $\delta_{1/2}$, results in an indirectly prescribed λ_{cell}, which needs to be kept in mind.

4.4.3 Detonations in curved channels

Since this thesis is on rotating detonation engines, influences of wall curvature is expected. The turns in a channel influence the the transverse waves on the detonation front and hence alter the detonation cell formation. Thomas and Williams (2002) show in a bend pipe experiment that the detonation structure between the inner and outer wall differs considerably in a curved channel and that the detonation appears to realign itself with the local channel axis (Fig. 4.10).

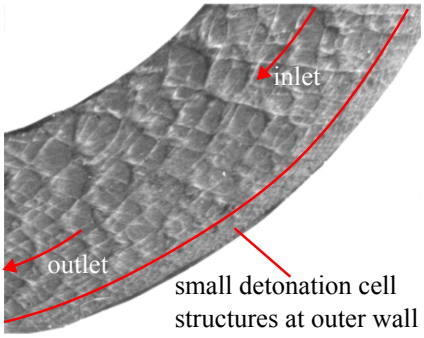

Figure 4.10: Experimental smoked foil for a curved channel with $C_2H_2 + 2.5O_2$ at $P_{init} = 13kPa$. Adapted from Thomas and Williams (2002).

According to Kudo et al. (2011) three different propagation modes occur for detonations in curved channels: stable, critical and unstable. They defined a critical detonation for detonation speeds of $0.6 - 0.8D_{CJ}$ and below this threshold as unstable. The detonation transitioned to a stable condition, once the inner radius $r_i > 14 - 40\lambda_{cell}$. Nakayama et al. (2012) show, for an ethylene-oxygen mixture gas, that a detonation propagates stably, if the condition $r_i/\lambda_{cell} \geq 32$ is upheld. The detonation speed normal to the channel cross section D_n increases with the distance from the inner wall. Additionally, they show that the curvature κ of the detonation decreases with increasing distance from the inner wall. In a later publication Nakayama et al. (2013) show that κ increases when r_a/r_i increases (r_a is the outer channel wall) and the relation of D_n and D_{CJ} and the detonation front curvature normalized by λ_{cell} can be described by a cubic relation $D_n/D_{CJ} = a_j(\lambda\kappa)^j$, where $j = 0 - 3$, $a_0 = 1$, $a_1 = 1.3017$, $a_2 = 16.089$, and $a_3 = 169.67$. This relation is independent of the test gas and not strongly influenced by differences in the tested channel geometries.

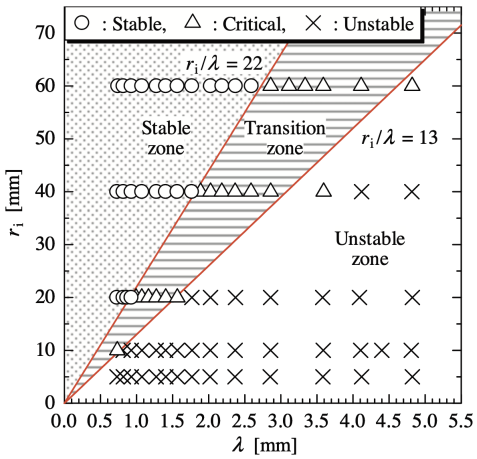

Figure 4.11: Relations between r_i and λ_{cell} in terms of propagation stability. From Nakayama et al. (2012).

Based on experiments, Olson et al. (2020) point out that for the stability of a rotating detonation, it is important do decrease λ_{cell} and increase the ratio r_a/r_i. They propose a criterion for the stability of a detonation in a curved channel $r_i \geq 0.01\lambda_{cell} + 12.7mm$. A numerical study by Short et al. (2019) illustrates the effect of the channel width: for thin channels the detonation is significantly less curved than for thicker ones and displays instabilities such as detonation cell formation. Also the detonation propagates faster in thin channels indicating acceleration due to the boundary layers at the channel walls. For increasing channel widths the instabilities and transverse pressure waves weaken and the detonation becomes slower. They also point out that the detonation is mainly driven by a small subsonic flow zone (in the detonations frame of motion) attached to the inner wall, since it is the place where the main heat release occurs.

Chapter 5

Solver and numerical methods

Contents

5.1 Introduction

This chapter will give an overview about the LES solver AVBP and the different numerical models utilized in this thesis for the computation of an RDE flow. The LES solver AVBP of CERFACS (Gourdain et al., 2009) is a high performance code to perform DNS and LES of compressible, reacting and non-reacting, turbulent, multispecies flows, running on big parallel CPU and GPU architectures. The code solves equations via the explicit method on unstructured and hybrid grids and on a cell-vertex discretization method. Boundary conditions are treated according to the Navier Stokes Characteristic Boundary Conditions (NSCBC) formalism of Poinsot and Lele (1992). The solver is explicit and the time-step is controlled by the acoustic CFL number, chosen so that the time step is always sufficiently low.

5.2 Numerical Schemes

AVBP offers a variety of numerical schemes e.g. Lax-Wendroff (LW) (Lax and Wendroff (1960)), Two-step Taylor Galerkin (TTGC or TTG4A (Colin and Rudgyard, 2000)). The different schemes have different dispersion and dissipation properties, which are of fundamental importance for the accurate reproduction of flow and flame structures. In this thesis LW and TTG4A are applied:

1. The Lax-Wendroff (LW) scheme is a finite volume scheme with an explicit single step time integration with a second order accuracy in time and space. Its main advantage is a low computational cost, due to the single step time integration, while delivering acceptable results. A downside is that it is prone to develop overshoots and wiggles in areas of strong gradients (high dispersivity), while it is also very diffusive.

2. Two-step Taylor Galerkin (TTG4A) scheme is a finite element scheme, which were introduced by Donea et al. (1987). It has an explicit two-step integration in time and is fourth order accurate in time and third order accurate in space. Compared to LW it has a better dispersion and dissipation behavior, but is about 2.5 times more computationally expensive.

AVBP discretizes the diffusion operator via a finite element diffusion scheme, called 2Δ, developed by Colin (2000).

5.3 Artificial viscosity and shock treatment

Due to the centered numerical schemes in AVBP, the simulations are at risk to develop point-to-point oscillations (or wiggles) close to regions of steep gradients. This is an obvious issue for RDE flows, where flames and also shocks must be captured. As a result, different artificial viscosity treatments are introduced to attenuate these oscillations. There is e.g. a variety of sensors which introduce two parameters:

1. The amplitudes of the oscillations are attenuated by a 4^{th} order hyper-viscosity. This works as a background dissipation term.

2. To smooth local gradients, artificial dispersion is added with a 2^{nd} order viscosity term. To avoid the dissipation of the whole solution a sensor,

which detects strong deviations of variables from linear behavior, is used to limit the application of additional viscosity to regions on strong gradient.

However, since detonations always include a strong shock(front), which results in very steep gradients, an additional adequate shock treatment is necessary. In this thesis, the LAD (Localiced Artificial Diffusivity) method, acc. to Kawai and Lele (2008), is utilized. This method helps to deal with strong gradients and can at the same time be used as an artificial viscosity treatment to deal with the previously mentioned numerical oscillations introduced by the numerical schemes.

LAD is a method based on the approach of Cook (2007), where the author introduces a high wave-number biased artificial diffusivity, which smears a discontinuity over a numerical resolvable scale. This is done by the addition of grid-dependent artificial fluid transport coefficients:

$$\mu = \mu_f + \mu^a \tag{5.1}$$

$$\lambda = \lambda_f + \lambda^a \tag{5.2}$$

$$D_k = D_{k,f} + D_k^a, \tag{5.3}$$

where the subscript f denotes the fluid, and a the artificial transport properties. The artificial properties are then modeled on a generalized grid for and then transformed into the physical space, to account for multi-dimensional curvilinear and anisotropic meshes. The detailes of the modeling can be found in Kawai and Lele (2008).

5.4 Closure of the Reynolds-Stress-Tensor

The **Reynolds stress tensor** $\tau_{i,j}$ is closed via a turbulence model. Based on the Bousinesq assumption, the unresolved momentum fluxes can be written as (Pope, 2000):

$$\tau_{i,j} = -\mu_t \left(\frac{\partial \widetilde{u_i}}{\partial x_j} + \frac{\partial \widetilde{u_j}}{\partial x_i} - \frac{2}{3}\delta_{i,j} \frac{\partial \widetilde{u_k}}{\partial x_k} \right) \tag{5.4}$$

where μ_t denotes the sub-grid scale (SGS) viscosity or turbulent viscosity. Different models are available to obtain μ_t. In this thesis the WALE model of Nicoud and Ducros (1999) and the SIGMA model of Nicoud et al. (2011) are applied. Both models are chosen due to their specific advantages:

1. a correct asymptotic behaviour in near wall regions and

2. in case of pure shear, no subgrid viscosity is applied.

The SGS models provide an evaluation of the dynamic turbulent viscosity ν_t: the approach is to model the sub-grid stresses by introducing ν_t:

$$\nu_t = (C_m \Delta)^2 D_m(\overrightarrow{u}), \tag{5.5}$$

where C_m is a model constant, Δ is the characteristic length scale of the grid, which is in practice the mesh size and D_m is a model dependent differential operator, applied on the resolved velocity field $\overrightarrow{u}$.
For **WALE** the differential operator is a function of the traceless symmetric part of the square of the velocity tensor $\mathscr{S}_{ij}^d$ and the strain rate S_{ij}

$$D_{m,WALE} = \frac{(\mathscr{S}_{ij}^d \mathscr{S}_{ij}^d)^{3/2}}{(S_{ij}S_{ij})^{5/2} + (\mathscr{S}_{ij}^d \mathscr{S}_{ij}^d)^{5/2}}, \tag{5.6}$$

where C_m becomes the constant $C_{m,WALE}$, obtained via canonical tests and comparisons with experiments, typically about $C_{m,WALE} = 0.5$.
For **SIGMA** the differential operator $D_{m,SIGMA}$ is computed as

$$D_{m,SIGMA} = \frac{\sigma_3(\sigma_1 - \sigma_2)(\sigma_2 - \sigma_3)}{\sigma_1^2}, \tag{5.7}$$

where σ_{1-3} denote the velocity tensor invariances obtained from the resolved velocity field. Here $C_{m,SIGMA}$ is typically around 1.35.

WALE and SIGMA usually lead to different fields of ν_t and comparing the two models allows to check their influence of the SGS model.

5.5 Closure of the species source term $\dot{\omega}_k$

The species chemical source term $\dot{\omega}_k$ is a crucial quantity in the computations of reactive turbulent flows and there are different approaches to close the source term. Since in general terms, combustion models are developed for flames and not detonations, most numerical work on detonations do not apply combustion models in their setups. The main reason is that detonation research is performed in canonical configurations with very high resolutions, so that combustion models are not necessary.

In the context of LES of RDEs, flamelet approaches which are based on tabulated reaction rates of unstretched premixed laminar flames, which get scaled to describe detonation conditions in RDEs, have recently emerged (Shunn et al. (2023)). Other famous models such as the thickened flame model (TF, Colin et al. (2000)) and its derivations (e.g. Wang et al. (2011)) modify the structure of a flame by thickening the reaction zone so that the flames are resolved on a multitude of typically 5-10 points (Gicquel and Roux (2011)). While this has resulted in impressive results for flames, the TF model is not applicable in cases of detonations, since a modification of the half reaction thickness $\delta_{1,2}$ leads to considerable changes in the multidimensional structures of a detonation.

In the RDE simulations presented in this work, flame/turbulence interaction can be assumed to play a limited role, because the detonation speeds are much larger than any turbulent speed. In other words, the detonation waves do not "see" turbulent fluctuations. Although some authors numerically show, e.g. Massa et al. (2011) or Iwata et al. (2023), that pre-shock turbulence can have an influence on the detonation front, capturing these effects requires very a high mesh resolution, which is out of scope for this work, hence it will not be captured. It points to the potential necessity of developing a detonation-turbulence interaction model to account for potential turbulence-detonation interaction in an RDE. However, in zones, where deflagration may occur, handling flame/turbulence interaction is still an open problem. Conclusively the reactions are solved by species transport equations, while possible numerical issues regarding deflagration will be stabilized by artificial viscosity.

5.6 Wall treatment

The treatment of walls in LES is another issue one needs to account for in RDEs. Since realistic applications typically contain complex geometry as well as high Reynolds number flows, the near-wall region requires a high resolution to correctly model the viscous sub-layers. This, however, would increase the number of grid elements to extensively high values and can also potentially decrease the numerical time-step due to locally very small cells.

In this work two wall treatments will be compared:

- Adiabatic slip walls: a wall normal velocity of zero is imposed and no

species diffusion flux nor tangential stresses are considered. Additionally the heat fluxes at the walls are zero, due to the adiabatic condition.

- Adiabatic law-of-the-wall: wall shear stresses are applied via a velocity/temperature wall-model which takes significant density/temperature variations into account as well as molecular Prandtl number effects. This model is derived from the Van Driest transformation (Van Driest, 1951). The velocity profile is scaled as $u^+ = 1/kln(y^+) + 5.5$ with the model constant $k = 0.41$.

Chapter 6

Development of a 1-Step Chemical Scheme: 1S-Deto

Contents

6.1 Introduction

This chapter focuses on the role of chemical schemes for RDE flows, the challenges of their development and subsequently the design process and derivation of a global 1 step chemical scheme. The first part will explore different detailed chemical schemes and introduce a new 1 step scheme. The new scheme is then validated in 1D and 2D configurations and an analysis of the grid size Δx is additionally performed to investigate the schemes predictive abilities for 2D instabilities.

6.2 Background on the development of chemical schemes for detonations

Chapter 4 has established that the physics of detonations requires special care regarding the development of a chemical scheme. The question of the chemistry model to compute detonation is still debated in the community. Historically speaking, the community relied on simple reduced order schemes to study detonations numerically and some of the first computations back in the 1990s, such as Khokhlov and Oran (1999); Tonello et al. (1996); Williams et al. (1996) until more recent studies, such as Dounia et al. (2019); Kessler et al. (2010); Wang et al. (2012), develop new reduced order schemes, for a variety of problems. The application of detailed chemical schemes is still not that common and it is argued that they are less useful than reduced order schemes. This is attributed to their unreliable prediction of detonation cells. Taylor et al. (2013) argue that detailed mechanisms are usually developed for thermodynamic equilibrium conditions, excluding important non-equilibrium effects behind the detonation shock. Shi et al. (2017) demonstrate that the mechanism needs to account for vibrational non-equilibrium effects on the detonation cell formation.

Reduced chemical schemes are only able to reproduce a reduced set of parameters at the same time. This is a limit for many applications, e.g. DDT where a chemical scheme must be able to reproduce flame properties, detonation properties as well as ignition times. Many authors (Dounia et al., 2019; Ivanov et al., 2011; Liberman et al., 2010) have shown that the choice of the chemical scheme (reduced or detailed) has a direct influence on the DDT mechanism itself, with strong evidence that reduced schemes, when not fitted in terms of ignition times, tend to ignite more easily and favor the Zeldovich mechanism (Zel'dovich et al., 1970) compared to detailed schemes.

Another downside of detailed chemical schemes are the costs to be considered in the most realistic configurations for most hydrocarbon fuels. The problem lies in the large number of involved reactions and species, which significantly increases the computational cost of the simulation. The number of species and reactions in these chemical schemes can be significantly reduced by eliminating species and reactions that are not relevant to the problem at hand. An example for this is the skeletal mechanism of Boivin et al. (2011), which is derived from the San Diego mechanism (UCSD, Saxena and Williams (2006)). The validity of the resulting skeletal mechanism

is limited to a certain range of operating conditions. It is also possible to replace the transport equation for certain species with negligible production rates by an algebraic expression of their mass fraction. Because calculating an analytical expression is much cheaper than solving the transport equation, this procedure significantly reduces the total cost of such mechanisms, known as ARC (Analytical Reduction Chemistry) schemes. The application of ARC schemes can considerably, as shown in Franzelli et al. (2013); Jaravel et al. (2017); Jones and Prasad (2010); Schulz et al. (2017).

In this work a 1-step Arrhenius based chemical scheme is developed for modeling correct detonation and deflagration quantities. For the development of chemical schemes for detonations it is typical to calibrate key quantities, the classic ones being $\delta_{1/2}$ and D_{CJ} based on detailed mechanisms. Another approach would be fitting the detonation cell size, respective $\delta_{1/2}$, on experimental data. Nevertheless, if the deflagrative mode is negligible in a specific application, targeting experimental values is a valid alternative in the design of reduced order chemical schemes. The calibration in this thesis has been executed via the computation tool CANTERA by Goodwin et al. (2023).

6.3 Derivation of a 1-Step-Chemical Scheme

For the derivation of the 1-step chemical scheme in this work, it is first necessary to pick a proper detailed reference scheme. The choice for this is not straightforward and different authors have chosen different references. For example, Nassini et al. (2023) develop a mechanism based on Boivin et al. (2011), while others such as Gallier et al. (2017) derive a mechanism based on the detailed mechanism of Mevel (Mével et al. (2011, 2009)). The computations of the 1D ZND solution are performed in CANTERA (Goodwin et al. (2023)) using the Shepherd ToolBox (Browne et al. (2008)).

Figure 6.1 compares four detailed mechanisms to each other: Mevel's mechanism, the San Diego mechanism (UCSD), the Alekseev mechanism (Alekseev et al. (2015)) and the Polimi mechanism (RANZI et al. (2014)). The results of the different mechanisms for D_{CJ}, displayed in Fig. 6.1 (a), are in overall very good agreement, with Mevel's chemical scheme delivering slightly higher D_{CJ} for richer conditions. The main difference is visible in the prediction of $\delta_{1/2}$. Mevel's mechanism results in the lowest $\delta_{1/2}$. UCSD and Alekseev are in best agreement of the four and the Polimi mechanism

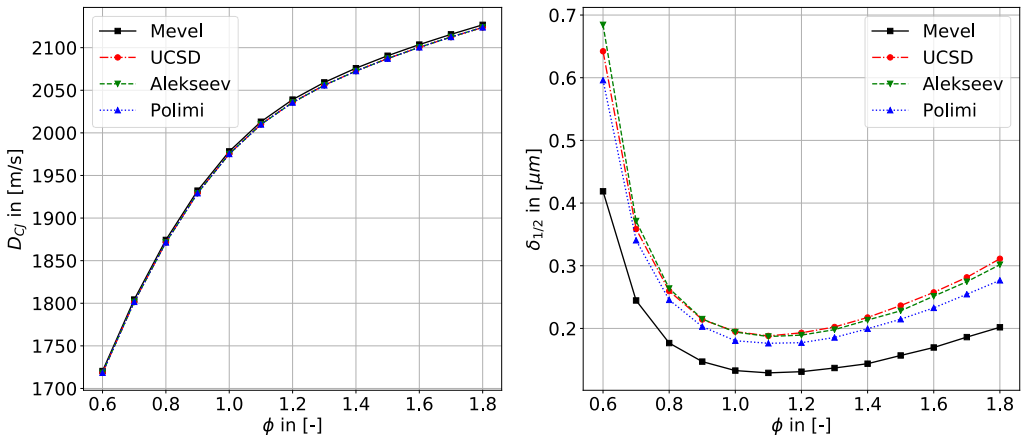

(a) **(b)**

Figure 6.1: D_{CJ} (a) and $\delta_{1/2}$ (b) for a range of $\phi \epsilon$ [0.6,1.8] under initial conditions of $T_0 = 300K$ and $P_0 = 101325Pa$.

predicts a slightly lower $\delta_{1/2}$ compared to UCSD and Alekseev. This is an emphasis on the difference of the numerical schemes. While the thermodynamic properties are in very good agreement, as can be seen in the computation of D_{CJ} (Fig. 6.1), the difference in the modeled reactions results in different $\delta_{1/2}$, which in this case show that Mevel computes the fastest reactions in comparison to the other three.

Further the VN- and CJ states in form of pressure and temperature are examined for the detailed chemical schemes in Fig. 6.2. As expected, all detailed mechanisms are in very good agreement for the VN-and CJ state variables, showing that in fact the decisive factor for the design of the 1-step chemistry is $\delta_{1/2}$. The reference chemistry chosen for the development of the 1-step scheme is the one of Mevel. The procedure for obtaining the 1-step chemical model is adapted from Kessler et al. (2010).

The new scheme, called 1S-Deto, contains 4 species: H_2, O_2, N_2 and H_2O and is modeled as a reversible reaction

$$H_2 + 0.5O_2 \rightleftharpoons H_2O. \tag{6.1}$$

Targeting $\delta_{1/2,Mevel}$ for a 1D-ZND detonation, the parameters listed in Tab. 6.1 have been chosen for the 1S-Deto. The detonation specific targeted parameters are listed in Tab. 6.2.

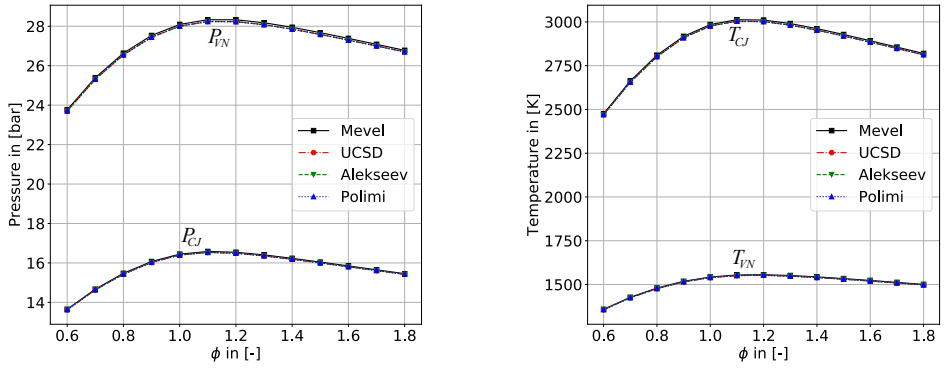

(a) **(b)**

Figure 6.2: P_{VN} and P_{CJ} (a) and T_{VN} and T_{CJ} (b) for a range of $\phi \epsilon$ [0.6,1.8] under initial conditions of $T_0 = 300K$ and $P_0 = 101325Pa$.

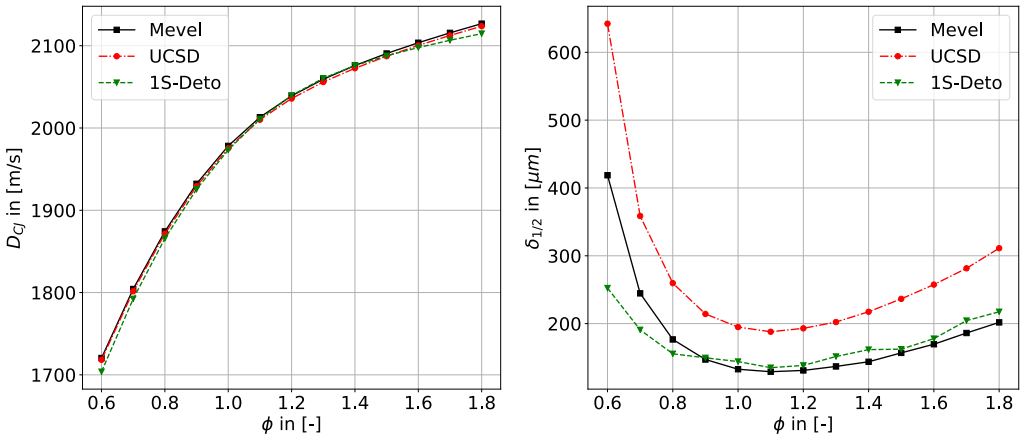

(a) **(b)**

Figure 6.3: D_{CJ} (a) and $\delta_{1/2}$ (b) for a range of $\phi \epsilon$ [0.6,1.8] under initial conditions of $T_0 = 300K$ and $P_0 = 101325Pa$.

An increase of the enthalpy of formation $\Delta H_f^{0K}(H_2O)$ from $-238.9[kJ/mol]$ to $-226.8[kJ/mol]$ for the changed dissociation and reaction rates during the combustion with respect to a detailed scheme is necessary for obtaining the correct D_{CJ} (Fig. 6.3(a)). After said correction, 1S-Deto delivers a well

matched D_{CJ} with slight under predictions for lean and rich mixtures.

To check the performance of the scheme for different ϕ in terms $\delta_{1/2}$, 1S-Deto is compared to Mevel and UCSD. In terms of $\delta_{1/2}$ thickness, 1S-Deto matches best around its design point of $\phi = 0.9$. For leaner mixtures $\delta_{1/2}$ is underestimated, while for richer mixtures the scheme overestimates the parameter. Nevertheless the slope of $\delta_{1/2}$ for richer mixtures is in good agreement with the slope predicted by Mevel, hence one can consider that 1S-Deto delivers the detonation relevant parameters to a satisfying degree. However, the scheme needs to be validated for the previously listed laminar flame parameters.

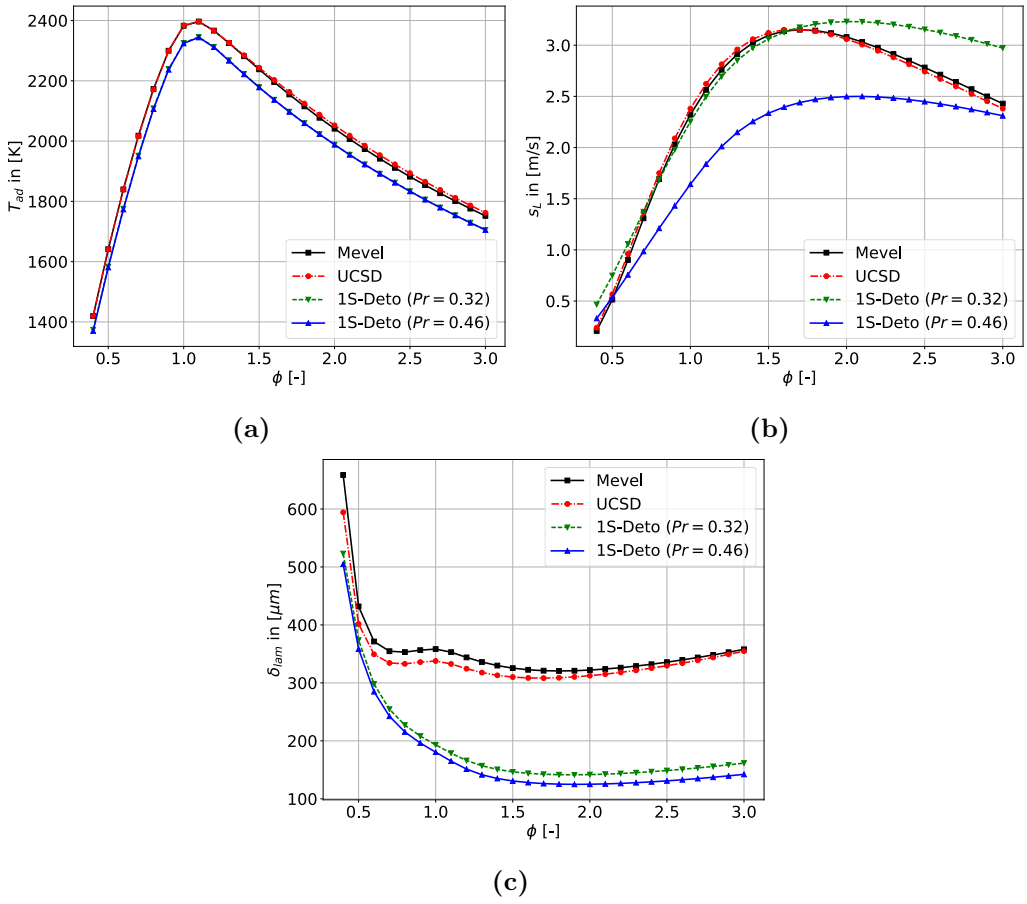

Figure 6.4: T_{ad} (a), s_L (b) and δ_L (c) for a range of ϕ ϵ [0.4,3.0] under initial conditions of $T_0 = 300K$ and $P_0 = 101325Pa$.

Equation 3.7 has established dimensional scaling laws for laminar flame properties, namely $s_L \propto (AD_{th})^{0.5}$ and $\delta_{th} \propto (D_{th}/A)^{0.5}$. This means that one cannot simply tune the pre-exponential factor to match both flame properties and detonation chemical properties. However, one can make use of the insensitivity of detonation profiles to transport properties, and use them to match the flame speed while the pre-exponential factor is tuned to match $\delta_{1/2}$. Therefore, fixing A to be the value at which the 1S-Deto scheme matches the half-reaction thckness predicted by the detailed chemistry, one can introduce a modification of the Prandlt number to match the flame speed, knowing that: $s_L \propto \left(A\frac{\mu}{\rho Pr}\right)^{0.5}$. Note that AVBP uses simplified transport and with a constant Pr for the whole mixture and constant Sc for the different species, so that the modification of the Prandtl number is easier compared to other codes with complex transport models.

The laminar flame parameters computed via 1S-Deto deviate considerably from their counterparts obtained via detailed mechanisms. The increase of $\Delta H_f^{0K}(H_2O)$ decreases the adiabatic flame temperature T_{ad} (Fig. 6.4 (a)) and for a sufficient prediction of s_L the Prandtl Pr number is decreased from $Pr = 0.46$ to $Pr = 0.32$. The influence of Pr is exemplified by comparing 1S-Deto with $Pr = 0.46$ and 1S-Deto with $Pr = 0.32$ in Fig. 6.4 (a), (b) and (c).

The biggest and most critical difference left between the detailed scheme and 1S-Deto is the large under prediction of the laminar flame thickness δ_L by 1S-Deto ((Fig. 6.4 (c)). In the context of LES, this decrease in δ_L of about 50% increases the resolution demand for the mesh to properly resolve flame fronts. Overall however, 1S-Deto computes acceptable values of all relevant quantities (except δ_L) and can be further tested in canonical configurations in AVBP.

Figure 6.5 displays the difference on the 1D ZND structure predicted by Mevel and 1S-Deto. Mevel predicts in Fig. 6.5 (a)-(c) an initial plateau of pressure, temperature and mass fraction after the detonation front. These plateaus occur due to the initial formation of radicals, computed by the detailed chemistry to actually start the detonation reaction. On the other hand no induction zone is visible with 1D-Deto, due to the absence of a cut-off temperature in the formulation of the arrhenius law in 1S-Deto. Figure 6.5 a) and (b) also show that the distant necessary to reach the CJ state is considerably lower with the 1S-Deto scheme. The same observation applies for the temperature in Fig. 6.5 (b), where T_{CJ} is reached after 1mm.

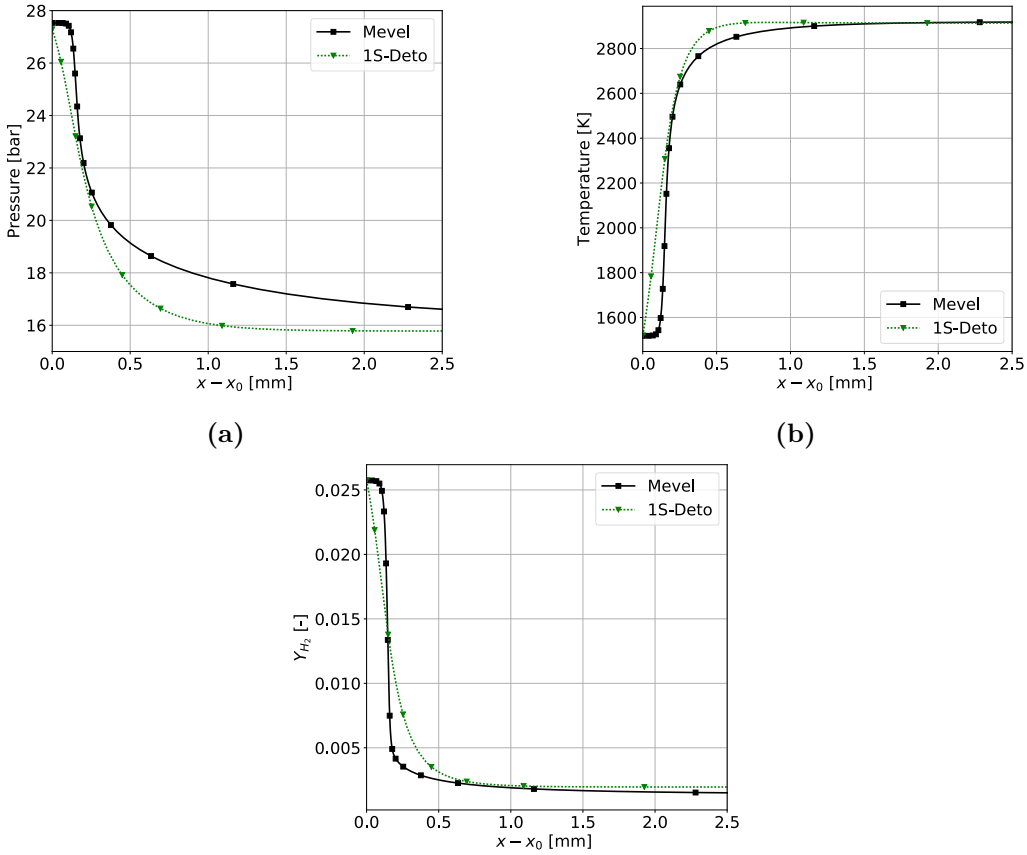

Figure 6.5: Pressure (a), temperature (b) and Y_{H_2} (c) in the frame of the detonation under initial conditions of $T_0 = 300K$ and $P_0 = 101325Pa$. $x = 0$ denotes the position of the detonation front.

n_{H_2}	1
n_{O_2}	0.5
E_a	18000.0 $[cal/mol]$
A	5.3 x 10^{10} $1/(\sqrt{mol.m^{-3}}s)$
$\Delta H_f^{0K}(H_2O)$	-226.8 $[kJ/mol]$

Table 6.1: Parameters of 1S-Deto

Name	Parameters at $\phi = 0.9$
1S-Deto	$D_{CJ} = 1925\ m/s$
	$\delta_{\frac{1}{2}} = 149.7\mu m$
Mevel	$D_{CJ} = 1932\ m/s$
	$\delta_{\frac{1}{2}} = 147.0\mu m$
San Diego	$D_{CJ} = 1929\ m/s$
	$\delta_{\frac{1}{2}} = 215\mu m$

Table 6.2: Comparison of chemical schemes for the investigated properties at $P_{init} = 1bar$ and $T_{init} = 300K$.

6.4 Sensitivity to initial conditions of 1S-Deto

1S-Deto is designed for a specific operational condition. Nevertheless, one has to expect deviations of the initial conditions during the computational runs in an RDE, especially in terms of equivalence ratio ϕ. Hence, the behavior of 1S-Deto for varying initial conditions is investigated in the following. 1S-Deto and Mevel are compared with respect to the same initial conditions, to illustrate the differences between a detailed and a 1-step scheme. The compared quantities for the detonation are D_{CJ} and $\delta_{1/2}$. For deflagration an investigation of s_L is deemed sufficient. The deviation plots show the deviation of 1S-Deto from Mevel via the expression: Deviation= $Var(\text{1S-Deto})/Var(\text{Mevel}) - 1$, where VAR represents the quantity of interest, e.g. D_{CJ}

The initial temperature T_{init} ranges from $300K$ to $500K$ and the initial equivalence ratio ϕ_{init} ranges from $0.6 - 1.8$. The schemes will be compared for an initial pressure $P_{init} = 1\ bar$.

Figure 6.6 reports the performances of 1S-Deto and Mevel for varying ϕ and T_{init}. In terms of D_{CJ} (Figure 6.6 (a) and (c)) the schemes are in high agreement and the range of predicted values is overall the same. This is based on the fact that D_{CJ} is governed by the thermodynamical properties of the fresh gases. Figure 6.6 (e) shows, that the occurring slight deviations in D_{CJ} are in the order of per mills, which are a negligible deviation. The positive deviation (1S-Deto faster than Mevel) starts at $T_{init} = 300K$ and $1.2 \leq \phi \leq 1.4$, and "spreads" for in increasing T_{init} to a wider range of ϕ. The relevant area, where this occurs is enveloped by the contour lines at 0%.

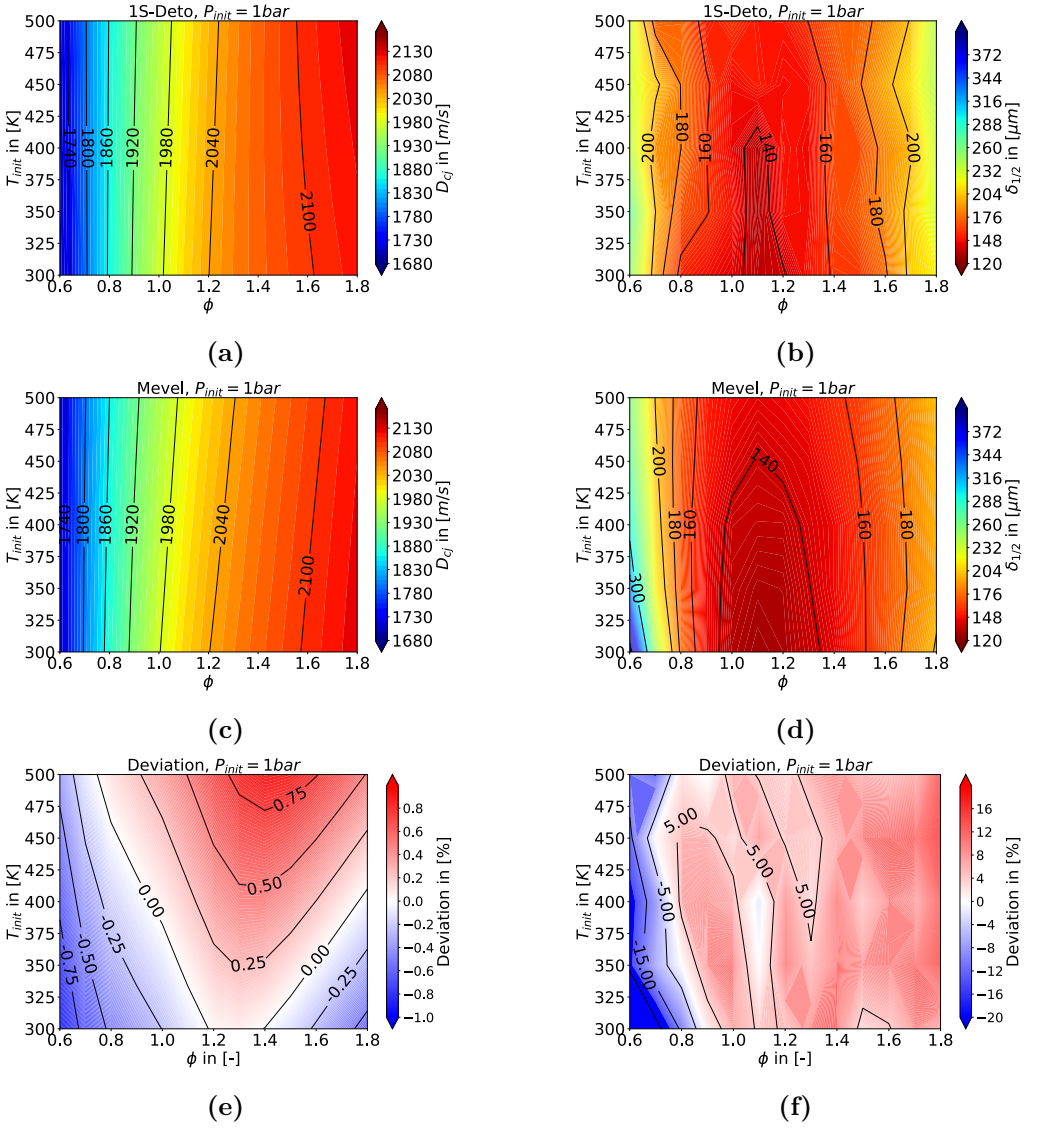

Figure 6.6: D_{CJ} (a) and $\delta_{1/2}$ (b) predicted by 1S-Deto for an initial pressure of $P_{init} = 1bar$ and different initial temperatures and equivalence ratios. For the same initial conditions, (c) and (d) display the predicted D_{CJ} and $\delta_{1/2}$ predicted by Mevel. The last rows depict the deviations of the predicted D_{CJ} of 1S-Deto from Mevel (e) and (f) depicts the deviation of the predicted $\delta_{1/2}$.

On the other hand, one sees a slight under-prediction of D_{CJ} by 1S-Deto for

lean conditions. The trend of an increasing D_{CJ} in comparison to Mevel for an increasing T_{init} prevails for lean as well as rich conditions.

In terms of predicted $\delta_{1/2}$ 1S-Deto (Fig. 6.6 (b)) predicts overall similar values for $\delta_{1/2}$ as Mevel (Fig. 6.6 (d)), except for $300K \leq T_{init} \leq 350K$ and $\phi \leq O.8$, where a local deviation of up to -25% with respect to Mevel for $\delta_{1/2}$ ((Fig. 6.6 (f))). Else the deviation from Mevel tends to diminish for increasing T_{init}. In case of $\phi = 0.6$ and $T_{init} = 500$ the deviation is about -10%. For a richer mixture ($\phi > 1.0$) the error decreases to the order of 5% and stays overall constant with minor deviation for the full range of T_{init}. This shows that 1S-Deto performs satisfactorily in the overall prediction of $\delta_{1/2}$.

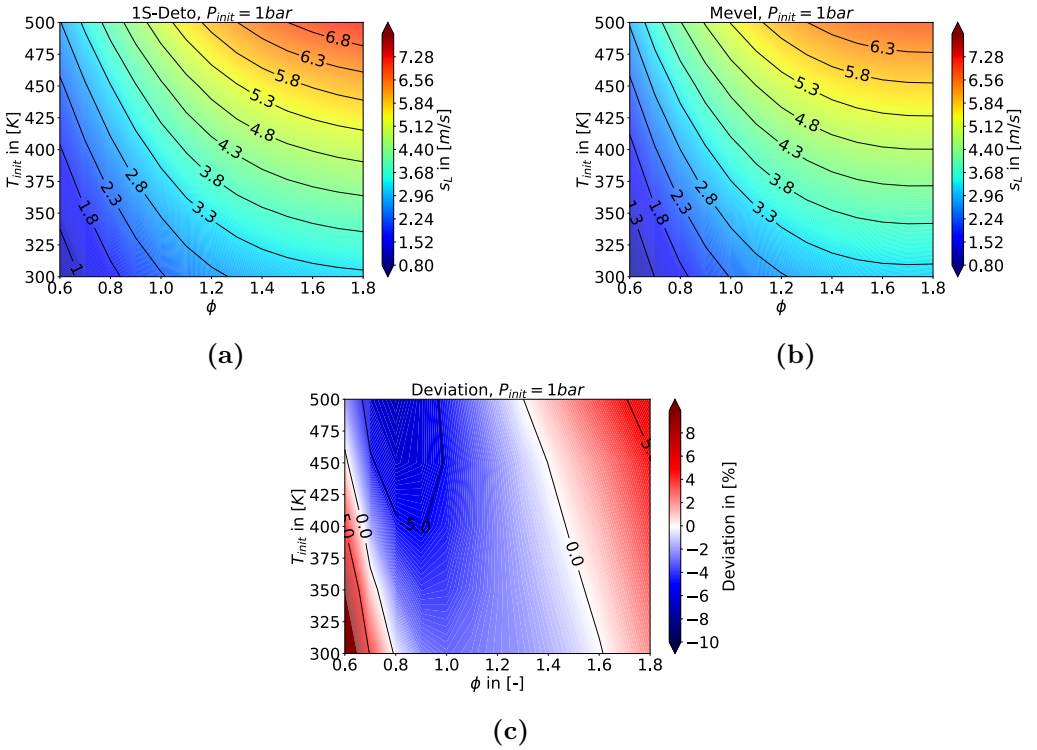

Figure 6.7: s_L predicted by 1S-Deto (a) and Mevel (b) for an initial pressure of $P_{init} = 1bar$ and different initial temperatures and equivalence ratios. The derivation of the predicted s_L is given in (c).

The contour plots of s_L resulting from 1S-Deto (Fig. 6.7 (a)) and Mevel (Fig. 6.7 (b)) are displayed for a range of $0.6 \leq \phi \leq 1.8$. The resulting

deviation in Fig. 6.7 (c) shows that, for initial atmospheric conditions and $0.8 \leq \phi \leq 1.6$, s_L is underpredicted by 1S-Deto with respect to Mevel. This under prediction amplifies for an increasing T_{init}.

Conclusively, 1S-Deto predicts acceptable values of $\delta_{1/2}$ for $\phi > 0.9$ and $300K \leq T_{init} \leq 500K$, while only having deviations from the $\delta_{1/2}$ predicted by Mevel for lean conditions, which has to be kept in mind. 1S-Deto also performs satisfactorily in the prediction of s_L where only minor deviations occor compared to Mevel.

A final step for the applicability of the scheme is to test its performance in a 1D configuration in the code AVBP. This is to make sure, that the performance of the scheme in AVBP leads to the same results as in CANTERA.

6.5 Validation of 1S-Deto: 1D

In the following 1S-Deto's performance in AVBP is investigated. For this purpose a simple 1D detonation tube is computed and the results are compared to the ZND solution obtained via CANTERA. The simulation is conducted with the LAD treatment for the shock and artificial viscosity treatment. The numerical scheme utilized is TTG4A. To validate the result, the prediction of D, P, T and Y_{H_2} of 1S-Deto is quantified and compared with the results obtained in CANTERA. This run is called TEST1.

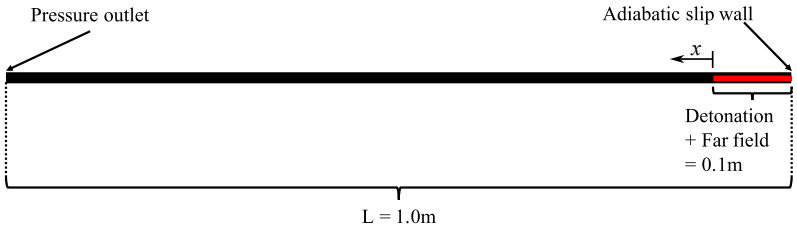

Figure 6.8: Initialisation of TEST1. A ZND detonation is inserted to directly force a detonation.

A domain of length $L = 1m$ is discretized with a grid size of $\Delta x = \delta_{1/2}/10 = 15\mu m$. The top and bottom boundaries are treated as symmetrical and the left boundary is treated as a pressure outlet at atmospheric conditions. The right boundary is treated as an adiabatic slip-wall, mimicking a piston that stops moving at $t = 0s$. The cases are initialized by

inserting the 1D ZND solution, obtained in CANTERA, into the respective position. Since CANTERA gives the solution in the frame of the detonation, it is first transformed into the laboratory frame via the transformation $u_{lab-frame} = D_{CJ} - u_{det-frame}$. It is then inserted into the domain of TEST1 (Fig 6.8). The insertion of a ZND detonation allows to decrease the length of the typically occurring transition from an overdriven detonation to a self sustained CJ detonation, which else happens when the domain is initialized at the VN point only.

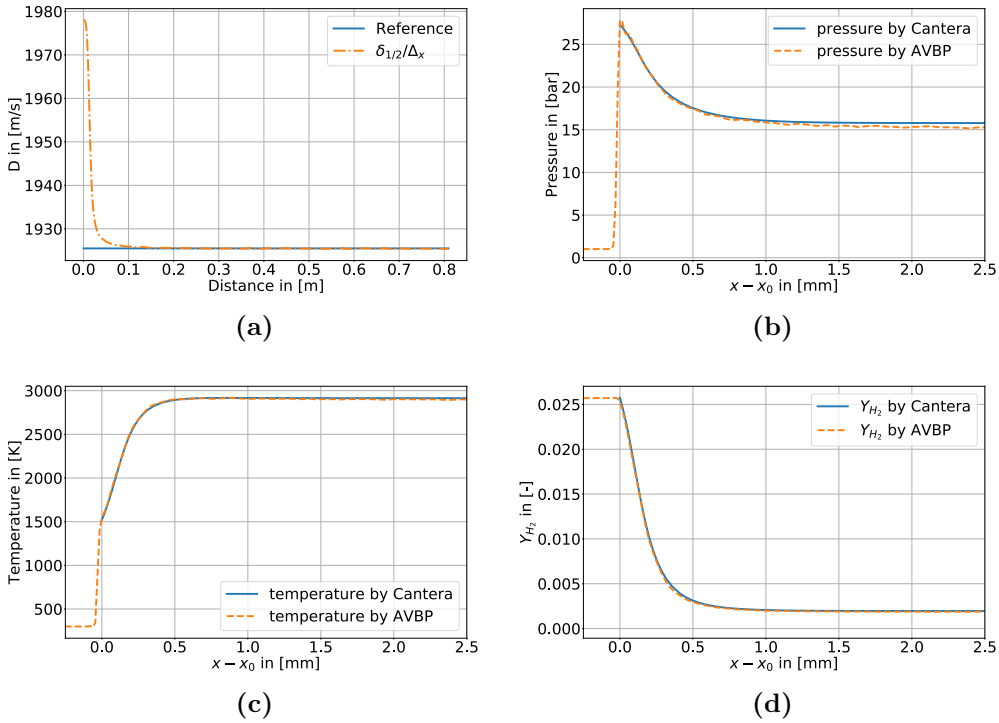

Figure 6.9: Comparison of the computed D in AVBP and CANTERA (a) and an instantaneous solution obtained in AVBP and the 1-D ZND solution from CANTERA: pressure (b) temperature (c) and Y_{H_2} (d) in the frame of the detonation under initial conditions of $T_{init} = 300K$, $P_{init} = 101325Pa$ and $\phi = 0.9$. For (b)-(d), $x = 0$ denotes the position of the detonation front. The curves displayed in (b-d) are taken from a randomly chosen instantaneous solution. The reference denotes $D_{CJ} = 1925m/s$.

Figure 6.9 (a) shows the evolution of D along the 1D domain. D is

measured by tracking the detonation front during its propagation in the domain. The initialization leads to an initially overdriven detonation at the beginning of the run. After a slight initial overdrive, the detonation wave converges directly towards $D_{CJ}(= 1925m/s)$ conditions, so that at $(x \geq 0.1m)$ a converged D is achieved.

The comparison between the results of TEST1 and the ZND solution from CANTERA, reveals slight pressure overestimations at the VN state (Fig. 6.9 (b)). These overestimations are about 2% of the nominal P_{VN} and hence negligible. Overall however, the pressure curves are in good agreement in the transition from VN to CJ. A slight underestimation occurs, beginning $1mm$ downstream of the detonation, which can also be considered negligible. The temperature curves in Fig. 6.9 (c) are also in good agreement and have a slight underestimation in temperature for $x \geq 1mm$. An almost perfect agreement is to be found in Fig. 6.9 (d), where the Y_{H_2} curves display an identical behaviour downstream of the detonation front. These tests show that AVBP is able to predict 1D detonations in a satisfying manner and can be reliably used for further tests.

6.6 Validation of 1S-Deto: 2D

The 1S-Deto scheme has proven its predictive capabilities in computing 1D detonations. These tests however, do not allow any research on 1S-Deto's behavior once e.g. multidimensional effect begin to form. This is investigated in the current section.

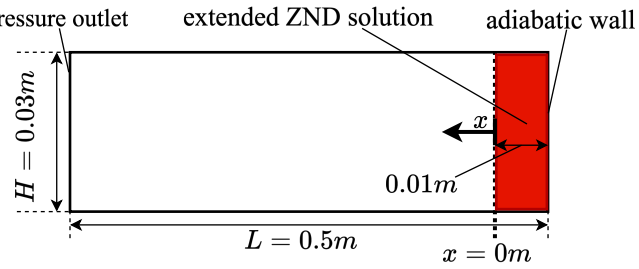

Figure 6.10: Sketch of the 2D domain investigated for detonations.

The simplest configuration to investigate is a 2D detonation front. This setup allows to investigate the detonation cell prediction of 1S-Deto. An additionally interesting question is the mesh dependence achieved by AVBP with regards to the detonation cell size. It is obvious that having a larger grid size leads to lower computational costs, but it needs to be investigated how the detonation and its key parameters are influenced by it. The simulations are conducted on a 2D rectangular domain of a length of $0.5m$ and a height of $0.03m$. To investigate the influence of the grid size Δx, 3 different uniform grid sizes are applied for the domain: $\Delta x_1 = \delta_{1/2}/10$ (2D-Nx10), $\Delta x_2 = \delta_{1/2}/5$ (2D-Nx5) and $\Delta x_3 = \delta_{1/2}/1$ (2D-Nx1).

CASE	Δx	Convection scheme
2D-Nx10	$\delta_{1/2}/10$	TTG4A
2D-Nx5	$\delta_{1/2}/5$	TTG4A
2D-Nx1	$\delta_{1/2}/1$	TTG4A

Table 6.3: Grid size Δx and convection scheme of the 2D detonation cases.

The left and right boundary conditions are set to an outlet at 1bar and an adiabatic slip wall respectively. The top/bottom boundary conditions are set to symmetry. The detonation is initialized in a similar manner as case TEST1

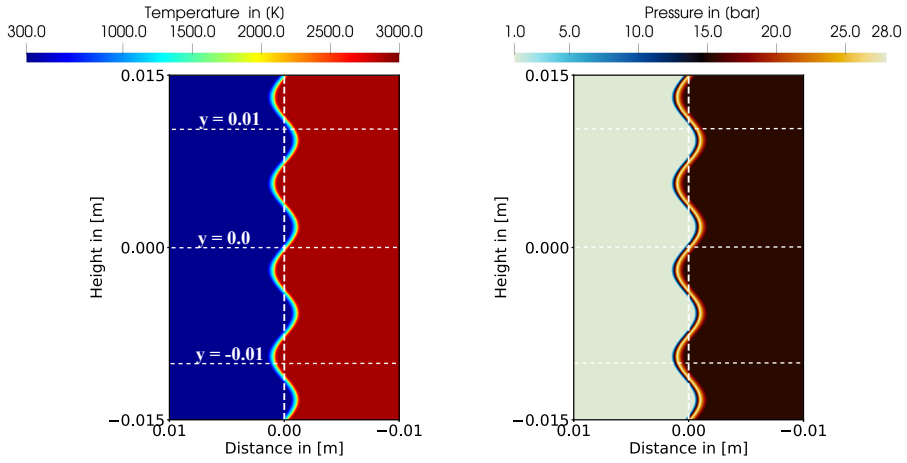

(a) **(b)**

Figure 6.11: Section of the initial solution of case 2D-Nx10 around the detonation front. The white dashed line denotes the initial mean $x-$position. This initial distribution has been chosen for all cases in the current section. Along each of the dotted horizontal lines 30 probes are equidistantly positioned for $x \geq 0.0m$ to obtain D.

(Fig. 6.8). A ZND detonation is set into the domain at $x = 0.0$ and the CJ state is extended to the right wall. Since the aim is to initialize detonation cell formation, the detonation front is not planar but inserted as a sine wave with a wavelength corresponding to 1/4 of the domain height (Fig. 6.11). This initial distribution leads to an immediate creation of transverse instabilities, so that detonation cells get formed at once, skipping the transition from a planar wave to an unstable detonation front. In the following, after analyzing the detonation speed for a simulated time frame from $t_0 = 0\mu s$ to $t_1 = 240\mu s$ for all three cases, the numerical soot foils in Fig. 6.14. are compared

The recorded D in Fig. 6.12, in all cases, shows an overdrive of the detonations in the beginning of the runs with 2D-Nx1 displaying the highest overdrive, due to the initially high gradients on the coarse mesh. Once a distance of $0.1m$ is passed, all cases display a relatively stable detonation propagation with fluctuations of the D along the regarded heights. The measured D is overall close to the theoretical D_{CJ} and the fluctuation can be attributed to variations in the local detonation structure based on detonation cell formation.

The detonation fronts displayed in Fig. 6.13 exhibit a clear cellular pattern

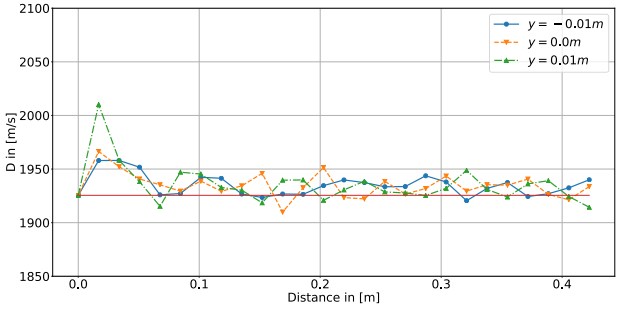

(a)

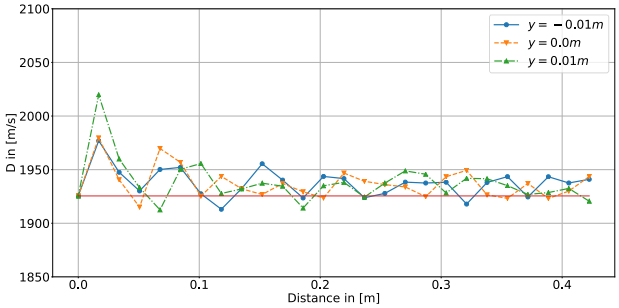

(b)

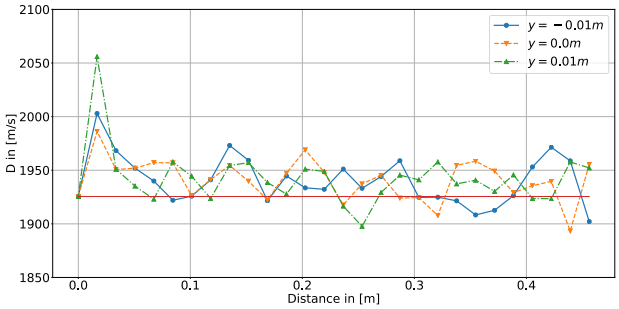

(c)

Figure 6.12: Detonation speed D along three different heights in the domain. 2D-Nx10 corresponds to a), 2D-Nx5 corresponds to b) and 2D-Nx1 corresponds to c). The measurement begins at $x = 0m$. The red solid line denotes D_{CJ}.

formed by the interaction of an incident shock and multiple transvers shocks. In Fig. 6.13 (a) and (b) triple points are clearly visible and correspond to

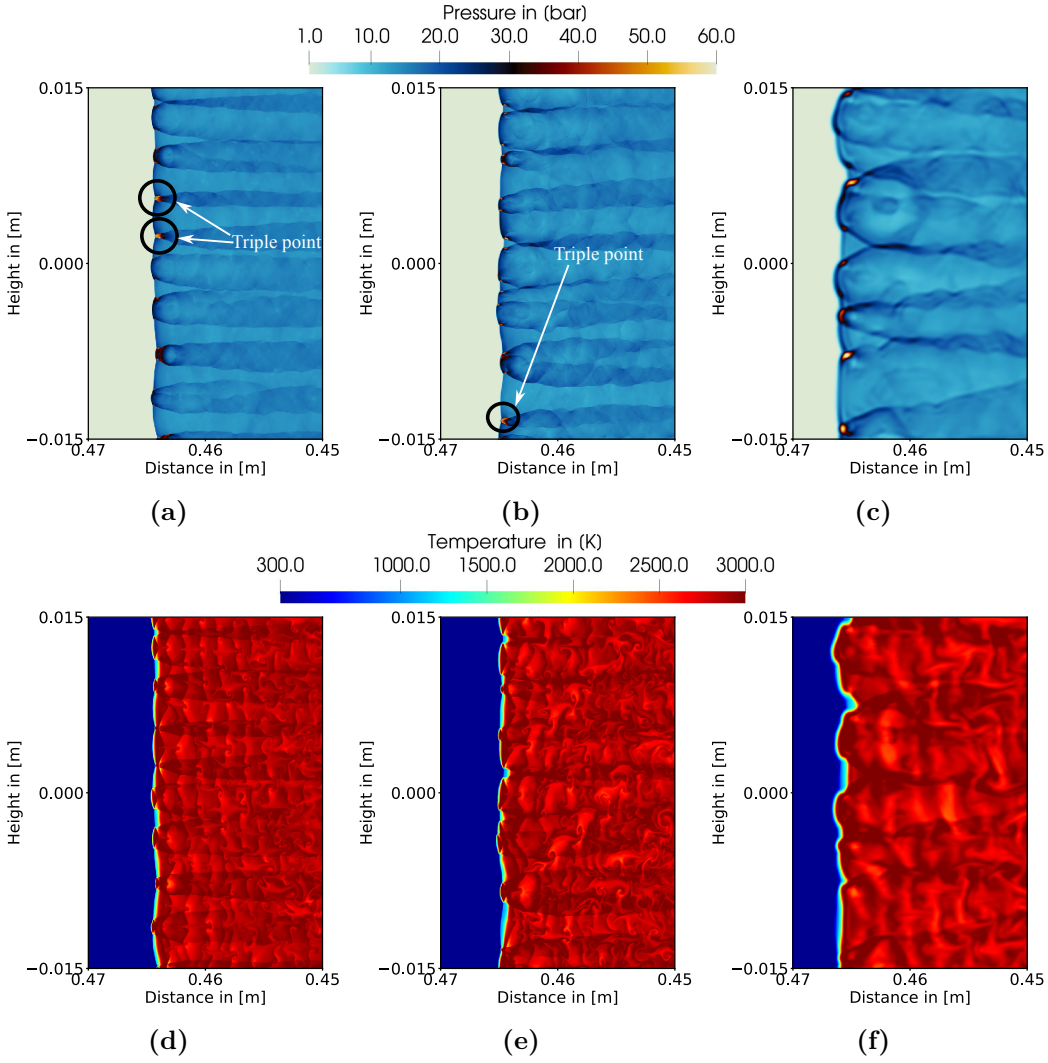

Figure 6.13: Detonation fronts at $t \sim 240\mu s$. The top row shows the pressure fields and the lower row shows the temperature fields. Images (a) and (d) belong to 2D-Nx10, (b) and (e) belong to 2D-Nx5 and (c) and (f) belong to 2D-Nx1. Examples of triple points are shown in (a), and (b)

the locus of relatively higher overpressures. One can guess by Fig. 6.13 (c) that the detonation cells predicted for 2D-Nx1 are larger than for 2D-Nx10 and 2D-Nx5. To investigate the detonation cell formation of the three runs the numerical soot foil is computed. This allows a qualitative analysis of the

cell development and its connection to the Δx values.

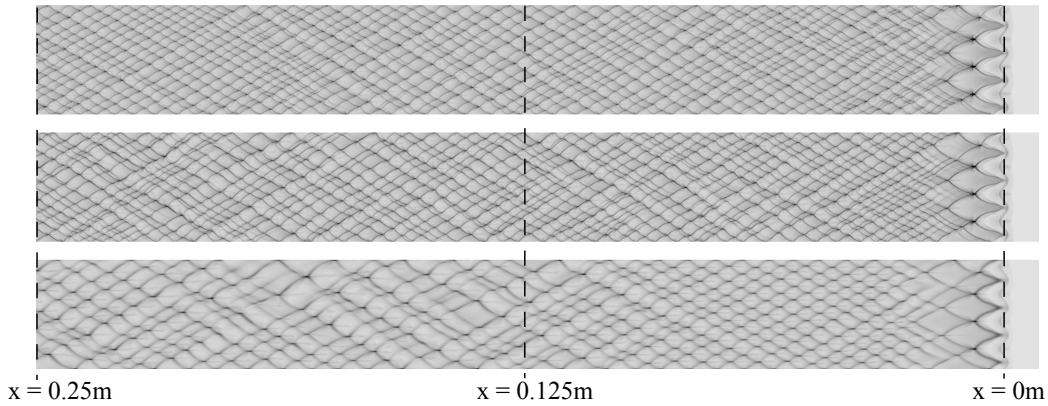

Figure 6.14: First half of the domain: numerical soot foils of 2D-Nx10 (top), 2D-Nx5 (middle) and 2D-Nx1 (bottom).

The transition from the initial solution field to a quasi-CJ detonation can be traced with the numerical soot foil presented in Fig. 6.14. The figure shows the first half of the domain, which captures the initial transition to a quasi CJ-state at $x = 0.01m$ (see Fig. 6.12) and the first part of the "converged" detonation front ($x \geq 0.01m$).

Initially one finds the formation of large detonation cells (Fig. 6.14) due to the initial detonation front: the "minima" with respect to the x-axis become the sources of local blasts and pressure waves start to propagate normal to the detonation front. These initially large cells break down into smaller cells, followed by the formation of an increasingly more regular cell size pattern. One can see that the soot foils of the finer grids in 2D-Nx10 and 2D-Nx5 predict additional shocks withing the initial large cells (Fig. 6.15) and contribute to the detonation cell formation. On the other hand 2D-Nx1 does not show such shocks, which results from the finer meshes resolving more instabilities, hence allowing the existence of these additional shocks, while the mesh of 2D-Nx1 is too coarse to resolve these secondary shocks withing cells. For $x \geq 0.125m$ 2D-Nx10 and 2D-Nx5 display an overall regular, evenly distributed detonation cell pattern, while 2D-Nx10 shows larger cells with more varying cell sizes. Overall the soot foil shows that for an increasing grid size the detonation cell size also increases.

Figure 6.16 (a) displays the PDFs of the triple point (TP) pressure for the three respective cases. The TP pressures are assumed to be above $120bar$.

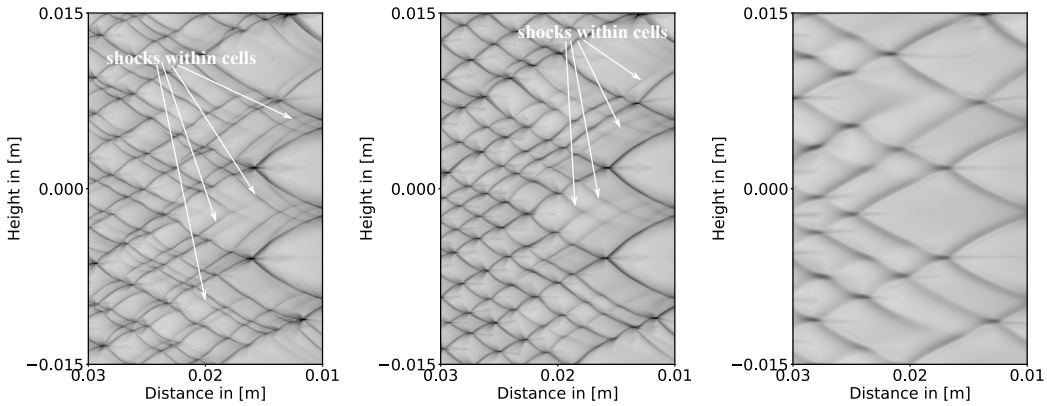

Figure 6.15: Numerical soot foil at $0.01 \leq x \leq 0.03$, where a) shows 2D-Nx10, b) 2D-Nx5 and c) 2D-Nx1. The detonation cell formation starts in this area.

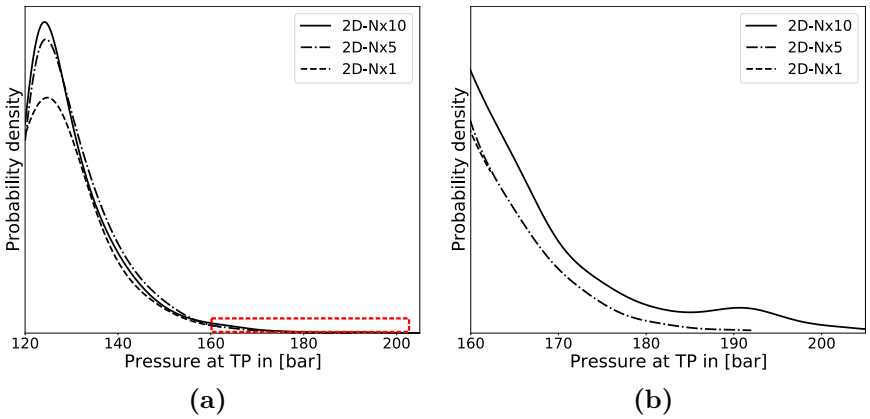

Figure 6.16: PDF of the pressure ranges of all cases for $P \geq 120bar$ (a), where (b) is a zoom on the marked dashed rectangle in (a), for better visibility of the curves.

The conclusions of this chapter do not depend on the exact value for the threshold pressure. While all three runs have a peak close to the minimum cut-off pressure, the PDF of 2D-Nx1 is the most narrow with a maximum pressure around $160bar$, the one of 2D-Nx5 is broader with a maximum pressure around $192bar$ and the one of 2D-Nx1 is the broadest with a maximum pressure around $205bar$. The maximum pressures are taken from Fig. 6.16 (b). This shows that an increasing mesh resolution results in higher peak

pressures for a 2D configuration such as here. On the other hand, a finer grid results introduces more numerical instabilities which in turn promote the formation of detonation cells.

The performed exercise emphasizes two things: detonation cells are formed even for a very coarse mesh, while the strength of the triple points decreases. This means that detonation waves on a coarse mesh tend to easier quench, once strong deviations in the fresh gas state occurs. The detonation speed (globally speaking) is not significantly modified by the coarse grid resolution of 2D-Nx1. For the performance of RDEs it shows that detonation instabilities will be present even for a relatively coarse grid size in the computational 3D domain (see Sec. 7.3), and their effects need to be taken into account.

PART I : Influence of the numerical and physical models on LES of Rotating Detonation Engines

Chapter 7

Setup and diagnostics for the LES of RDEs

Contents

7.1 Introduction

This chapter first summarizes the challenges of performing simulations on RDEs. The objective in not to perform a direct comparison between the a LES and the experimental data. Before reaching this point, the different factors (numerical and physical) controlling the results of an LES of an RDE are investigated. This sensitivity step is important: instead of tuning one or another model, it is mandatory to determine, which part of the LES modeling is important or not.

The meshing is introduced with detailed information of the different parts of the numerical domain and the boundary conditions are given. Then the investigated cases and their differences in numerical as well as physical setups are explained and the initialization procedure for the computation is illustrated. Finally the diagnostic tools and post processing procedures are introduced.

7.2 Challenges of performing LES of RDEs

The numerical computation of RDEs is a huge challenge and the difficulties in computing RDEs are summarized and discussed in this section.

Due to their complexity, authors often simplify their RDE configuration by assuming it to be an unwrapped, planar, periodic chamber 2D, neglecting the injection system or decreasing the geometric complexity by assuming e.g. a 3D periodic slot chamber. However, RDEs are fully 3 dimensional and in general contain a complex mixing system which requires a careful treatment. Due to increasing and improving computational resources, computations of 3D configurations including the full injection system have been performed.

Another point is that the 3D simulation of detonations is still a basic unsolved problem in the community: detonations have very thin reaction fronts and require a high mesh resolution, typically around 30 cells per half reaction thickness (Reynaud et al., 2020; Taileb et al., 2020), to capture the correct detonation cell formation process, which is important for the prediction of the detonation dynamics. These shock interactions and the extreme pressures and temperatures created by a detonation makes their numerical treatment additionally difficult. Very few groups are able to handle three-dimensional meshes, which would be required to simulate detonations, so that

many fundamental studies of detonations are performed in two dimensions. Since RDEs are three dimensional and generally involve multiple small jets, additional heavy meshing constraints are imposed. These points are elaborated on in Chapter 1.

The numerical treatment of shocks becomes an issue since RDEs gather shocks a mixing zones, requiring proper shock treatments, which require numerical limiters e.g. (Cook and Cabot, 2004; Kawai and Lele, 2008). This ensures monotonicity along shocks. In the current setup there is additional challenge of modeling a jet-in-crossflow, where a fuel jet is injected into an oxidizer cross flow. Numerous groups have shown, that a proper investigation of a jet-in-cross flow poses a complex challenge in itself (Chai et al., 2015; Hassan et al., 2013; Karagozian, 2014; Smith and Mungal, 1998; Yuan et al., 1999). This represents an additional degree of complexity on top of the shock and mixing structures and comes at the cost of additional numerical viscosity and artificial dissipation, being clearly detrimental in the mixing zones. For an RDE the mixing zones are critical, because it is here, where fuel and oxidizer have to mix between each passage of the detonation waves.

RDEs may involve simultaneously zones of detonation and zones of deflagration, also often named parasitic combustion (Chacon and Gamba, 2019; Prakash et al., 2021; Sato et al., 2021). While the precision of molecular transport models is not of critical importance for the global propagation of a detonation, it is still critical for deflagration, so that the codes performing LES of RDE must be able to compute deflagration and detonation on the same mesh and with the same sub models for chemistry as well as numerical parameters.

This list of restrictions and challenges emphasizes that performing a LES of a RDE is clearly a difficult task.

7.3 Meshing approach

7.3.1 Mesh resolution

Obtaining a adequate mesh is a difficult task and the local grid size Δ in an RDE is governed by numerous constraints:

1) Geometrical constraints: assuming d is the size of the smallest geometry

detail to be captured (here the diameter of the fuel jets), the ratio d/Δ has to be adequate. This is obviously an issue for the TUB test rig in the 100 H_2 injector tubes, which have a diameter $d_{H_2} = 0.5mm$. In this work $d/\Delta \simeq 10$.

2) Detonation constraints: for the half reaction thickness $\delta_{1/2}$, $\delta_{1/2}/\Delta$ is a second critical ratio controlling the number of points used to resolve the detonation internal structure. While it is common practice to require at least 7-10 points per thermal flame thickness to resolve stable deflagration waves, recent numerical studies on 3D RDE configurations have shown stable detonation propagation without "properly" resolving the detonation front (Batista et al. (2021); Cocks et al. (2016); Nassini et al. (2023); Prakash et al. (2021)), due to thicker detonations resulting from non-ideal conditions. This thesis works with a $\delta_{1/2}/\Delta \simeq 1$

3) Deflagration constraints: the requirement of having at least 7-10 points per thermal flame thickness to properly resolve deflagration fronts can hardly be met in LES type meshes. To circumvent this problem, a solution is to use the thickened flame approach (Colin et al., 2000) to artificially thicken the deflagration fronts and allow their resolution in LES meshes. While this solution is common practice for premixed flames, the deflagrative combustion in RDEs occurs in the form of a strongly stratified mixture of fresh gases meeting burnt gases from the previous cycle. The application of the thickened flame approach to this type of reaction front is not straighforward and no particular treatment will be applied to treat them in this thesis, similarly to what is done in the literature so far (Cocks et al., 2016; Nassini et al., 2023; Vignat et al., 2024). This is a strong limitation in current LES of RDEs.

4) Turbulent eddies constraints: estimating the size of the largest structures created inside the RDE chamber is difficult. Since this work performs LES, there is no need to try to resolve the smallest scales. However, resolving the largest ones is clearly needed. Resolving the larger scales of turbulent eddies is additionally critical for adequately modeling the turbulent reactant mixing in the domain. Since the resolution in the RDE is mainly governed by the previous constraints we assume the large eddies are reasonably captured.

7.3.2 Computational domain

The next question is how much of the domain should be modeled? While Weiss et al. (2020) only include parts of the injectors for their study, others include the fresh gas plena into the computational domain (Cocks et al., 2016; Nassini et al., 2023). This is useful, since a rotating detonation will lead to upstream moving shocks and thus interact with the mass flow rate by e.g. blockage or even back flow. Since this must be taken into account for numerical stability of the boundary conditions, the plenums are included in this work. The resulting fluid vein is displayed in Fig. 7.1.

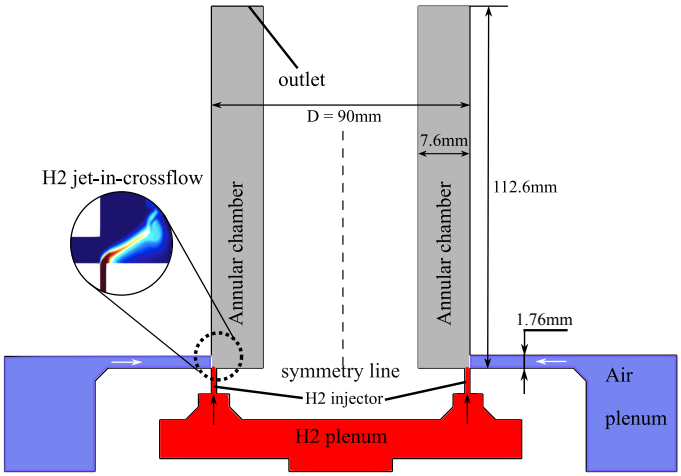

Figure 7.1: Fluid vein of the investigated experimental configuration.

Figure 7.2 illustrates the topology of the mesh used in this study: It is a purely tetrahedral mesh with local mesh size Δ. The $H2$ injectors have a cell size of $50\mu m$, corresponding to $d_{H_2}/\Delta_{H_2} = 10$, which ensures a proper resolution in the H_2-injectors. The cells in the air gap are $160\mu m$, corresponding $d_{Air}/\Delta_{Airslot} = 11$, thereby ensuring a sufficient resolution of the flow in the air slot. The cross flow is discretized by elements of $100\mu m$ (dot-dashed box in Fig. 7.2) to resolve the mixing in the crossflow. In the lower chamber (without the dashed box) a resolution of $140\mu m$, which corresponds to the expected $\delta_{1/2}$, is chosen to further resolve the mixing process, the turbulent eddies and the detonation. For the LES of deflagrations, the number of points should be typically around 5-10 points across the flame front (Gicquel and Roux (2011)). As previously mentioned, recent numerical studies show that 3D detonation fronts in non-ideal conditions representative of RDEs are

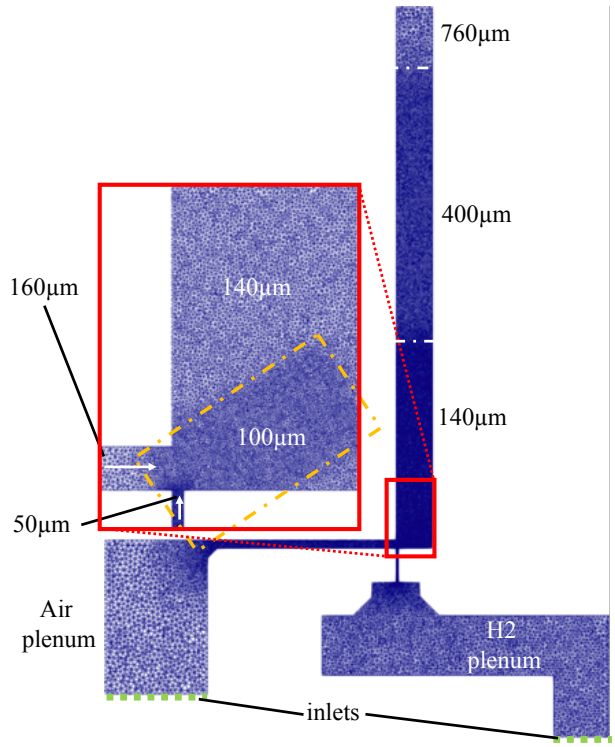

Figure 7.2: Cut of the mesh for the present study.

much thicker than their 1D counterpart, hence mesh sizes of the order of $\delta_{1/2}$ are often used. The meshes are of course too coarse to properly capture the detailed dynamics of detonation fronts and their cellular structure, but they allow to propagate a detonation front in a 3D RDE with reasonable computational cost. However, Sec. 6.6 has shown that a resolution of the front with mesh sizes of the order of $\delta_{1/2}$ in combination with 1S-Deto predict a good approximation of the cellular structure of a detonation, which further justifies the coarse resolution of the detonation front. Further downstream, the lower chamber is followed by a coarser area of $400\mu m$ and a coarse area of $760\mu m$ to attenuate minor oscillations at the outlet. This results in a mesh with overall 260Mio tetrahedrals grid cells.

7.4 Boundary conditions

The inlet and outlet boundary conditions are imposed via the NSCBC formalism of Poinsot and Lele (1992). At the inlets the mass flow is imposed, since the initial plenum conditions are a result of the imposed mass flow in the experiments. The outlet is treated as a pressure outlet at 1 atm, since the combustor blows into the atmosphere. It is to note that no further tests of the outlet boundary condition has been performed. Under the assumption of a very low Mach number at the inlets, the static temperature at the inlets is assumed equal to the measured static plenum temperature. Initially, all walls are treated as adiabatic slip walls. The modeled operational condition is listed in Tab. 7.1.

H_2 mass flow	g/s	13.7
O_2 mass flow	g/s	517.7
H_2 temperature	K	287
Air temperature	K	287
H_2 plenum pressure	bar	11.2
Air plenum pressure	bar	5.2
ϕ	-	0.9

Table 7.1: Boundary condition of the of the LES.

7.5 Cases

In terms of computing RDEs, the best strategy to perform LES of RDEs is not yet known: over predictions of D may occur, because different types of chemical models are applied and meshes are generally not resolving all the characteristic reaction length scales. In this thesis the following modeling approaches are tested to check for their influence on the results. The runs are evaluated by comparing D and the flow field structures. Table 7.2 lists the performed LES, presented in this chapter:

Comparing the mixing configuration (2 cases), the SGS model (2 cases), wall treatment (2 cases), numerical scheme (2 cases) and $\delta_{1/2,target}$ (3 cases) would, in total, result in $2^4 * 3 = 48$ cases. This is obviously out of scope and in fact not necessary to determine different modeling effects. The study is

RUN NAME	MIXING CONFIGURATION	NUMERICAL SCHEME	SGS MODEL	WALL TREATMENT	$\delta_{1/2,target}$ in μm	$z_{nom} = \frac{\dot{m}_{H_2}}{\dot{m}_{H_2}+\dot{m}_{O_2}}$ in [-]
CASE1	**PREMIXED**	LW	WALE	ADIAB. SLIP-WALL	149.6	0.0258
CASE2	NON-PREMIXED	LW	WALE	ADIAB. SLIP-WALL	149.6	0.0258
CASE3	NON-PREMIXED	LW	**SIGMA**	ADIAB. SLIP-WALL	149.6	0.0258
CASE4	NON-PREMIXED	LW	WALE	**ADIAB. LAW-OF-THE-WALL**	149.6	0.0258
CASE5	NON-PREMIXED	LW	WALE	ADIAB. SLIP-WALL	**180.0**	0.0258
CASE6	NON-PREMIXED	LW	WALE	ADIAB. SLIP-WALL	**206.0**	0.0258
CASE7	NON-PREMIXED	**TTG4A**	WALE	ADIAB. SLIP-WALL	149.6	0.0258

Table 7.2: Summary of LES runs

limited to six critical comparisons, which are sufficient to bring conclusion. The 7 cases are compared as follows:

1) **CASE1 vs CASE2**: allows to compare the effect of (pre-) mixing in LES of the current operational conditions. The idea is to premix air and H_2 (CASE1) before they enter the simulation domain to decrease the complexity of the problem by one degree, since all issues relating to H_2/Air mixing are excluded from the model. It allows to evaluate the importance of mixing, especially because no other mixing option works better than directly premixing the reactants. The mass flow rates at the inlet boundary conditions the same amount of gases is injected at each patch (H_2 and Air inlets) with premixed cases at $\phi = 0.9$. In CASE2 the reactants are injected seperately, exposing them to the influence of mesh resolution, LES mixing and injection system design. This "realistic" setup allows to evaluate the losses introduced by the injection configuration.

2) **CASE2 vs CASE3**: is an extension of the previous comparison. The SGS models impose the turbulent viscosity ν_t, which in turn influences the sub-grid scale mixing and can alter the result of the LES. Hence the WALE and SIGMA models, two well proven models, will be compared to check if and how the computation of ν_t influences the results of the LES.

3) **CASE2 vs CASE4**: CASE1-CASE3 are performed with adiabatic slip walls. It is to expect however, that the influence of the walls (e.g. friction losses or changes of the mixing field) needs to be better integrated. Since resolving the wall is not feasible for this configuration at least one case with an applied wall law needs to be incorporated. This comparison will allow to to evaluate the influence of wall treatment on the result of the LES.

4) **CASE2 vs CASE5 vs CASE6**: it is not clear if the choice of target value for the half-reaction thickeness significantly impacts the results such as the detonation speed $D.\delta_{1/2}$ influences the multidimensional structures of the detonation front, thereby impacting the detonation dynamics during its propagation in the RDE. Hence 3 different cases with different $\delta_{1/2,target}$ are performed and the influence of the $\delta_{1/2}$ on D is investigated.

5) **CASE2 vs CASE7**: since most numerical RDE configurations use 2nd order schemes, LW is also used in this thesis. However, it is important to compare the LW scheme to a higher order scheme, here TTG4A, to be sure that the numerical scheme does not impact the results in a significant way. This is especially important, since strong shocks are included which pose a general challenge for numerical schemes.

The listed comparisons allow to develop a further understanding of the modeling influences on the LES and to develop a strategy to perform more reliable LES simulations. Further the gained insight will be used to define a numerical master setup, targeted to obtain the closest D to the experiments.

7.6 Initialization

7.6.1 Importance of the ignition process

To start the calculations, a proper initialization process has to be executed. This leads to one of the main issues in performing LES of RDEs with respect to the initial flow field: if the detonation is too fast, it comes back before mixing has progressed sufficiently to detonate again, else if the detonation is too slow, combustion is not completed before the end of the chamber. Experiments show (Bai et al., 2024; Bluemner, 2020), that ignition is critical and can lead to different regimes depending on the procedure. LES is similar and in many cases igniting the first stable RDE cycles is actually the main issue.

For this work, the effects of various initialization strategies on the capacity of the RDE wave to become self-sustained have been tested and the best working approach is presented in the following. The initialization is conducted in three steps (Fig. 7.3):

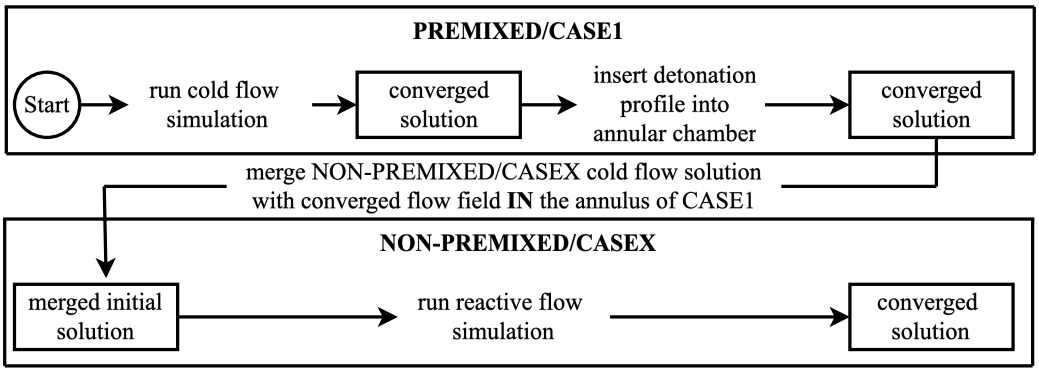

Figure 7.3: Fluid vein of the investigated experimental configuration.

1. A cold flow simulation is conducted until a stabilized cold flow is reached, so that steady plenum conditions and boundaries are obtained.

2. The obtained premixed cold flow solution of CASE1 is then modified by changing the initial flow field in the annular combustion chamber. For this purpose a 1D ZND detonation based solution is inserted into the domain and the rest of the flow field such as refill area, axial velocity, species distribution and temperature of burnt gases have to be adequately estimated (see Sec. 7.6.2), e.g. from flow fields obtained from 2D RDE simulations. This procedure allows to skip the transient ignition behavior seen in experiments, which in itself is numerically challenging to model and costly in terms of time. It also imposes the detonation in one fixed direction and subsequently forces a one-detonation regime.

3. With the converged solution of CASE1, obtained after the procedure described in 2., one can repeat the procedure for the other cases. However, now, one can use the solution field of CASE1 for the modification of the flow field in the annular chamber, since it provides a far better guess for an initial solution.

7.6.2 Numerical ignition procedure

In the following, the procedure described under point 2 is described in detail. The main issue is to insert the structure of a 1D ZND detonation into the RDE, by making it periodic and compatible with the expected RDE wave.

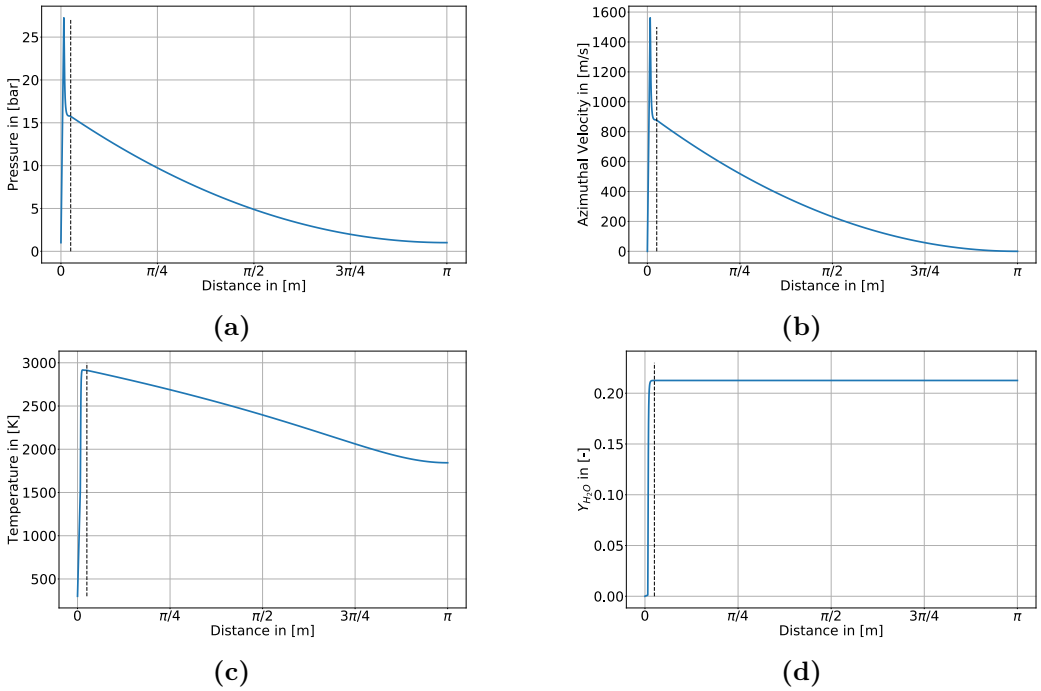

Figure 7.4: Extended initial profile for the initialization of CASE1. The vertical dashed line denotes the beginning of the extended solution. Before the dotted line the ZND solution is unchanged. After the dotted line, the solution is modified to reach periodicity. Image (a) shows the pressure, (b) the azimuthal velocity, (c) the temperature and (d) the mass fraction of H_2O.

To do this, the ZND structure is conserved at the detonation front, but its far field values are adjusted to make them periodic (Fig. 7.4). The adjustments are done for pressure, velocity, temperature and species. The distribution and azimuthal velocity V_{CJ} after the CJ point are guessed to decrease in a quadratic manner to achieve periodicity. The pressure decreases from P_{CJ} to $1bar$ and the velocity V_{CJ} decreases to $0m/s$. The temperature is then obtained via the isentropic relation

$$T_{exp} = T_{CJ} \left(\frac{P_{exp}}{P_{CJ}} \right)^{\frac{\gamma_{CJ}-1}{\gamma_{CJ}}} \tag{7.1}$$

resulting in the expansion region temperature T_{exp}. P_{exp} denotes the pressure in the expansion region. The resulting profiles are displayed in Fig. 7.4. A second choice is the height of the initial detonation along the chamber:

an initial refill area is guessed for 50% of the circumference of the annular combustion chamber and the maximum height is chosen at $50mm$ above the bottom plate. This means that the refill area is filled with premixed fresh gases, while the composition of the hot gas is the same as at the CJ state. The hot gas temperature above the refill height is set to $min(T_{exp})$ resulting in the initial field shown in Fig. 7.5.

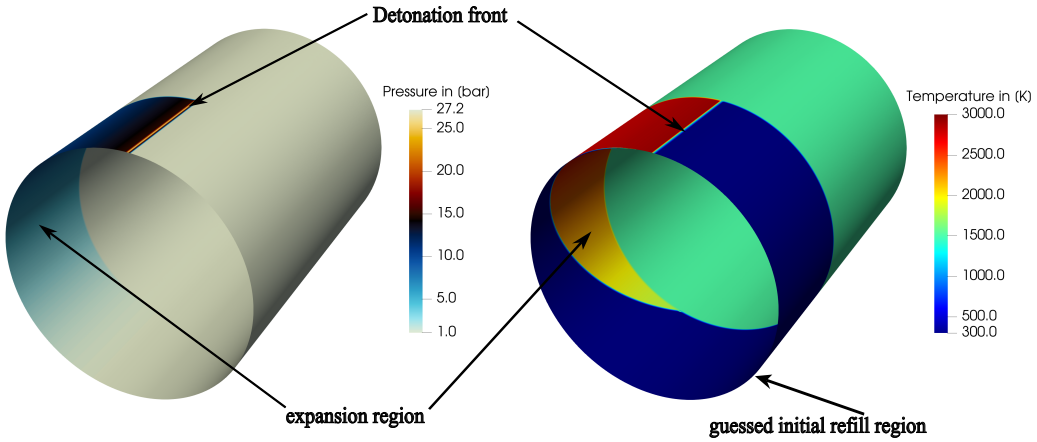

Figure 7.5: Schematic illustration of the initial solution of CASE1.

7.7 Diagnostics

Once the LES listed in Tab. 7.2 are performed, the question of post processing them to get coparisons arises. In this section the different ways of quantifying the conducted simulations are introduced. Gathering reliable experimental data of RDEs is difficult. The first value obtained is the detonation speed D via pressure measurements and stagnation pressure measurements at the outlet plane. Additionally, it is possible to measure the axial pressure distribution with different measurements along the chamber. However, to understand effects such as mixing, overall detonation structure and combustion/detonation efficiencies, new parameters have to be included. The different global post processing procedures are explained in the following. In many cases, LES analysis is performed, which can not be directly obtained/compared in experiments.

7.7.1 Mixing Index: I_{mix}

Since mixing is crucial in all non-premixed combustion systems, we include a new index I_{mix}, to quantify the mixing in the fresh gases. I_{mix} is constructed based on the mixture fraction z (Poinsot and Veynante, 2011).

Knowing local the mixture fraction z fields, the mixing lines allow to construct the local H_2 and O_2 mass fraction, which would occur without combustion. The mixing lines correspond to $Y^m_{H_2} = Y^0_{H_2} z$ and $Y^m_{O_2} = Y^0_{O_2}(1 - z)$, if one constructs

$$I_{mix} = \frac{Y_{H_2} Y_{O_2}}{Y^m_{H_2} Y^m_{O_2}} = \frac{Y_{H_2} Y_{O_2}}{z_{nom} Y^0_{H_2} Y^0_{O_2}(1 - z_{nom})}, \tag{7.2}$$

where the nominal $z_{nom} = \frac{\dot{m}_{H_2}}{\dot{m}_{H_2} + \dot{m}_{O_2}}$ is given in Tab. 7.2. I_{mix} can be used to measure how H_2 and O_2 have mixed and if the mixture has been burnt or not. For a perfectly mixed case (CASE1), I_{mix} is constant, because the mixing process is completed and the fuel/oxidizer ratio fixed. For a non-premixed case, the index varies and gives information on the degree of mixing. I_{mix} is built to reach 1 when all gases are mixed for CASE1 to 3. It can reach values larger than unity during the mixing process. Its maximum value can also be obtained: it is reached when z goes to 0.5, for which $I^{max}_{mix} = \frac{0.5 * 0.5}{0.0258 * (1 - 0.0258)} = 10$ for this thesis.

7.7.2 Detonation Index: I_{det}

It is established that deflagration as well as detonation combustion can occur in a RDE. Intuitively one would presume, that D increases with more detonated fuel, hence it is necessary to determine the amount of detonated fuel in the different cases. For this purpose a detonation index I_{det} is introduced. I_{det} indicates if local combustion occurs in a detonation by checking for zones with high values of the fuel source term $\dot{\omega}_k$ and for high pressure values 'around' the respective local point. A proper RDE should work with a very high I_{det} because deflagration decreases the overall efficiency. Elasrag et al. (2022) propose a criterion, which is based on Chemical Explosive Mode Analysis (CEMA) (Liu et al., 2010; Lu et al., 2010), comparing the characteristic Damköhler number of the H radical. This approach is heavy and instead a simple form for I_{det} had to be found. A semi-empirical definition, combining zones of high heat release and by extension high fuel consumption rates with zones of high pressure (, a signature of detonations) is proposed:

$$I_{det} = S_\omega S_{\overline{P}} \tag{7.3}$$

with S_ω defined as

$$S_\omega = \frac{1}{2}\left[1 + tanh\left(\left(\frac{1}{\Gamma}\frac{|\dot{\omega}_{fuel}|}{|\dot{\omega}_{fuel,1D}^{max,Deflag}|} - 1\right) * \alpha\right)\right] \tag{7.4}$$

and $S_{\overline{P}}$ is defined as

$$S_{\overline{P}} = \frac{1}{2}\left[1 + tanh\left(\left(\frac{P}{P_{CJ,input}} - 1\right) * \alpha\right)\right] \tag{7.5}$$

I_{det} is constructed by the sensor S_ω (Eq. 7.4), which flags the reactions in a detonation regime and $S_{\overline{P}}$ (Eq. 7.5), which captures the presence of high pressures. To obtaining S_ω, the relation between the deflagration based and detonation based $\dot{\omega}_k$ is investigated. For this purpose the maximum fuel species source term value $\dot{\omega}_{fuel,max}$ resulting from a deflagration, and the maximum fuel species source term value $\dot{\omega}_{fuel,1D}^{max,Deflag}$ resulting from a detonation are computed via 1D detonations/deflagrations in CANTERA. In the next step, the resulting ratio $\dot{\omega}_{fuel,max}/\dot{\omega}_{fuel,1D}^{max,Deflag}$ is investigated.

The images in Fig. 7.6 (a) display the maximum $\dot{\omega}_{fuel}$ along a ZND detonation profile, and (b) displays the maximum $\dot{\omega}_{fuel}$ along a 1D flame. The maximum values for a detonation occur in the area of equiv. ratios of $1.2 \leq \phi \leq 1.6$ for $T_{init} = 300K$. In case of a 1D flame the maximum value occurs for the maximum displayed ϕ and $T_{init} = 500K$. The ratio of the fuel source terms of the different combustion regimes (Fig. 7.6 (c)) shows decreasing dominance of the detonation based source terms for an increasing ϕ and an increasing initial temperature. However, the first major result is that $\dot{\omega}_F$ is much larger in a detonation than in a deflagration and the ratio of these two quantities (Fig. 7.6 (c)) is always larger than 100, which shows that a detonation produces source terms, which are at least two orders of magnitude higher than the ones of a deflagration. This justifies the usage of $\dot{\omega}_{fuel}$ and $\dot{\omega}_{fuel,1D}^{max,Deflag}$ in Eq. 7.4 for the first part of I_{det}. The parameter Γ amplifies $\dot{\omega}_{fuel,1D}^{max,Deflag}$, to account for local deflagration conditions of for $1bar \leq P \leq P_{CJ,input}$, so that e.g. potential reactions in the wake of a detonation are excluded.

The minimum P_{cj} predicted by 1S-Deto occurs for $\phi = 0.6$ and $T_{init} = 500K$ (Fig. 7.6 (d)). The pressure treatment of I_{det} contains a input parameter $P_{cj,input}$ to guarantee the application of I_{det} in a high pressure region

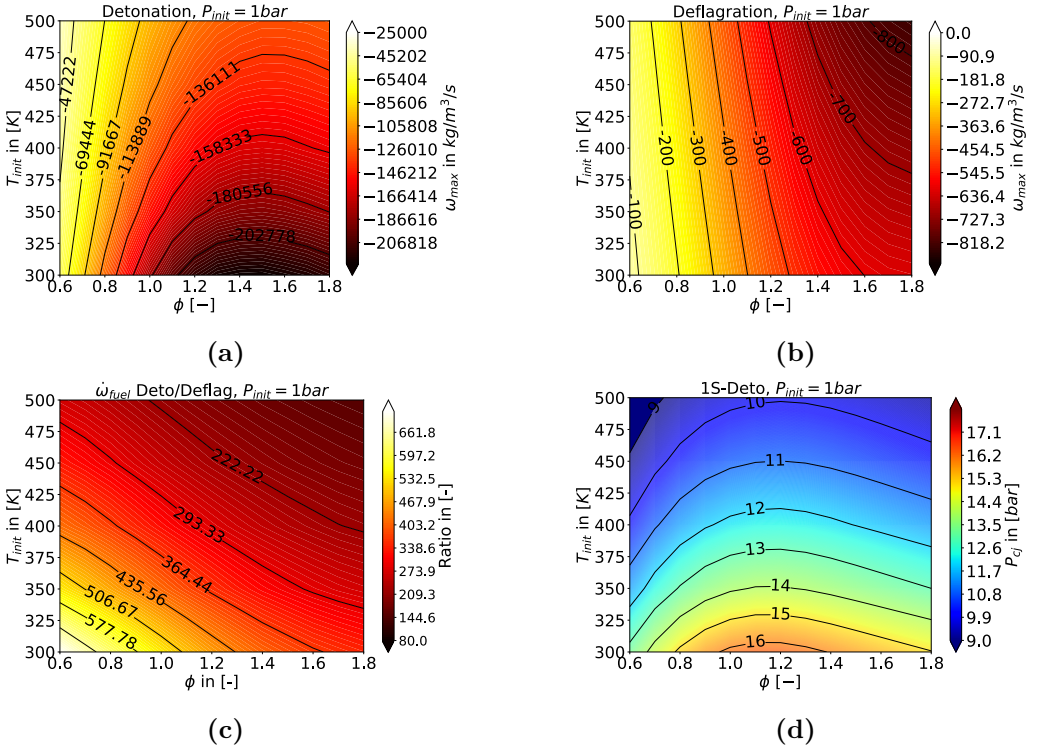

Figure 7.6: Maximum $\dot{\omega}_{fuel}$ for a 1D ZND detonation for various initial conditions (a), maximum $\dot{\omega}_{fuel}$ for a 1D flame (deflagration) for various initial conditions (b), ratio of the displayed $\dot{\omega}_{fuel}$ between detonation and deflagration (c) and P_{CJ} for a 1D ZND detonation for various initial conditions (d).

representative of a detonation. The choice for $P_{cj,input}$ is dependent on the expected range of initial conditions a detonation encounters, which in this work is the range of parameters displayed in Fig. 7.6. The factor $\alpha \gg 1$ in Eq. 7.4 and 7.5 is an amplification factor narrowing the transition between deflagration and detonation regions, leading to a quasi step-function so that S_ω and $S_{\overline{P}}$ are either 0 or 1. Γ is calibrated on a 1D and 2D detonation configuration resulting in $\Gamma = 50$ for the rest of this thesis.

Figure 7.7 displays the performance of I_{det} (Eq. 7.3) with respect to $\dot{\omega}_{fuel}$ and the cut-off value $\Gamma\dot{\omega}_{fuel,1D}^{max,Deflag}$. I_{det} is 1 as long as the source term values are higher than the cut-off value and decrease directly to 0 once the fuel source terms of the detonation fall below the threshold. In this case it happens for $x - x_0 \geq 0.5mm$. This introduces a slight, but overall negligible, error in the

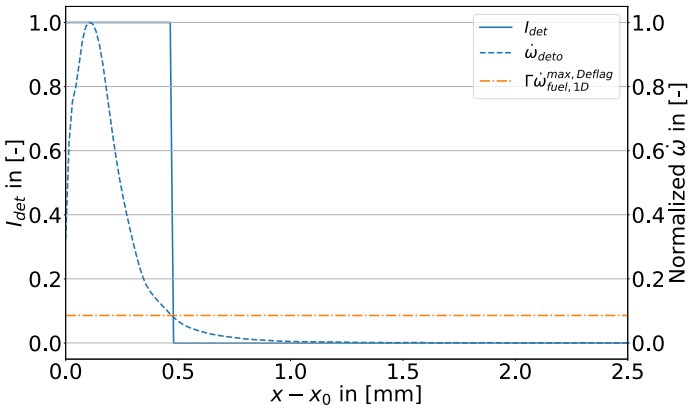

Figure 7.7: I_{det}, $\dot{\omega}_k$ and the cut-off source term including its amplification $\Gamma\dot{\omega}^{max,Deflag}_{fuel,1D}$ for a 1D detonation. Source terms are normalized by the maximum value of $\dot{\omega}_{deto}$.

determination of the detonated fuel.

The sensor I_{det} could be broadened by decreasing the value of Γ, however this would compromise the sensor's performance in 2D. To emphasize this point, the I_{det} fields of two instantaneous solutions of case 2D-Nx10 (see Sec. 6.6) with $\Gamma = 20$ and $\Gamma = 50$ are compared (Fig. 7.8) and shows the different results for I_{det} depending on the choice for Γ.

The first main difference are the iso contours of $I_{det,\Gamma=20}$ in the wake of the detonation (Figure 7.8 (a)). These result from elevated source terms due to non-detonated reactants left behind the detonation front coupled with elevated pressure from the transverse pressure waves originating at the detonation front. It proves that $\Gamma = 20$ is too low of a threshold properly single-out the detonation front. The second difference is the inclusion of pockets with low amounts of fuel (see circles in Fig. 7.8 (a)) by $I_{det,\Gamma=20}$, which does not occur for $I_{det,\Gamma=50}$. This leads to an overprediction of detonated fuel in the computed configuration. In general one can see that $I_{det,\Gamma=20}$ is visibly thicker than the detonation front of $I_{det,\Gamma=50}$ due to lower threshold on S_ω and tends to include areas of reactions which cannot be attributed to the detonation regime.

The choice for $P_{CJ,input}$ depends on the problem at hand such as the expected pressure P_{init} in front of the detonation, equivalence ratio ϕ and initial temperature T_{init}. In this work it can be assumed that P_{init} is around

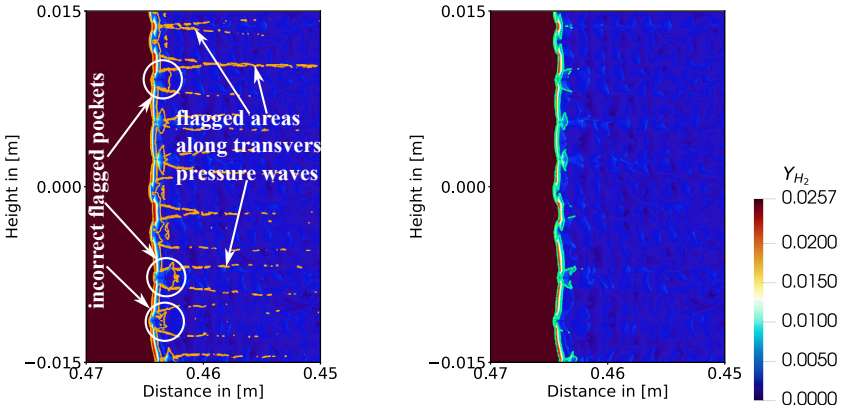

(a) $\Gamma = 20$ **(b)** $\Gamma = 50$

Figure 7.8: Section of the end area of case 2D-Nx10 (Sec. 6.6) around the detonation front, displaying the fuel mass fraction Y_{H_2}. $I_{det,\Gamma=20}$ is displayed as an orange iso contour in (a) and $I_{det,\Gamma=50}$ is plotted as a green isocontour in (b). The displayed solutions are exactly the same except the applied Γ for I_{det}.

$1bar$, hence the minimum $P_{CJ,input}$ expected in an RDE is, based on Fig. 7.6 (d), conservatively chosen as $P_{CJ,input} = 9bar$.

In AVBP, the values for $\dot{\omega}_{fuel,1D}^{max,Deflag}$ are tabulated as functions of P_{init}, T_{init} and ϕ. The user gives the estimate for P_{init} and T_{init} as input variables to the routines (in this work assumed to be $1bar$ and $300K$). $\dot{\omega}_{fuel,1D}^{max,Deflag}$ is then taken from the table based on the local equivalence ratio, so that variations due to changes in the mixture of the fresh gases are accounted for and then used to compute the sensor values.

7.7.3 Combustion and Detonation efficiency

Once a detonation local criterion I_{det} is computed, it can be used to build a global deflagration based fuel source term:

$$\dot{\Omega}_{defl} = \int_V \dot{\omega}_k (1 - I_{det}) dV \tag{7.6}$$

as well as a detonation global reaction rate:

$$\dot{\Omega}_{det} = \int_V \dot{\omega}_k I_{det} dV \tag{7.7}$$

A detonation efficiency E_{det} is then obtained with

$$E_{det} = \dot{\Omega}_{det}/\dot{\Omega}_{tot} \tag{7.8}$$

The efficiency E_{det} allows to see which parameters affect the way detonation proceeds in the RDE.

Additionally one can compute the combustion efficiency E of the overall system by balancing the in flowing and out flowing fuel mass:

$$E = \left(1 - \frac{\dot{m}_{H_2,out}}{\dot{m}_{H_2,in}}\right) * 100 \tag{7.9}$$

E does not distinguish between detonation and deflagration so that both E and E_{det} are necessary to quantify the efficiency of the detonation process.

7.7.4 Additional post-processing procedures

Finally the instantaneous fields of temperature and Y_{H_2} will be plotted and compared, including the mixing index I_{mix} to track mixing between the H_2 jets and air. Additionally, the phase-averaged structure of the same fields will be produced by averaging results in a reference frame moving at the speed of the detonation wave, based on 150 snapshots taken during one revolution, once the simulation is in steady operating mode.

Chapter 8

Primary investigation: Non-reactive case

Contents

8.1 Introduction

A first investigation of a non reactive, non-premixed case is performed in this chapter to obtain a first estimation of the mixture field as well as potential re-circulation zones which might impact the detonation wave in a reactive case.

Various studies point at the importance of the injection system for mixing (Driscoll et al., 2016; Weiss et al., 2020; Zhao and Zhang, 2020) and wave stability (Luan et al., 2022; Rankin et al., 2015, 2017b) as it obviously

controls the flushing of hot gases after detonation passage and the mixing of newly introduced reactants to sustain the detonation. Due to its importance for the sustainability of the detonation wave, the non-reactive case must be explored to single out the injection process in the present RDE and the quality of the mixing it produces. First the chapter investigates the flow field in the annular chamber, the plenum conditions and the discharge coefficient of the injectors with the main focus on mixing performance.

8.2 Numerical setup of the non-reacting case

The numerical parameters are chosen in accordance to CASE2 (see. Sec. 7.5, Tab. 7.2), which is the reference case in this thesis: the mass flow rate and the temperature are imposed at the inlet boundary conditions and at the outlet, pressure ($P_{outlet} = 1bar$) is imposed. All walls are treated as adiabatic slip walls. The numerical scheme chosen for this setup is LW and WALE is used for modeling the sub-grid stresses. Since the non-reactive case does not contain a detonation wave, the simulation is performed on a sector part of the chamber consisting only of 10% of the annular circumference, which includes 10 H_2 injectors. This reduces the computational cost associated to the non-reactive simulations while capturing potential interactions between the injectors.

8.3 Results of the non-reactive simulations

8.3.1 Setting up inlet conditions

The cold flow simulation is run until a steady state for the plenum pressure and mass flow rates is achieved. The pressure signals are taken from local probes in each of the plenums. The resulting plenum pressures for the converged solution is shown in Tab. 8.1.

To match the flow rates entering the chamber, the H_2 and air plenum pressures are adjusted until the LES flow rates match the experimental target values, explaining why the deviation in Tab. 8.1 is zero for flow rates. On the other hand Tab. 8.1 shows that significant differences occur between the experimentally measured plenum pressures and the numerical one: for both plenums the pressure is overestimated, especially for H_2. Difficulties in capturing the correct plenum pressures and correct mass flow have been

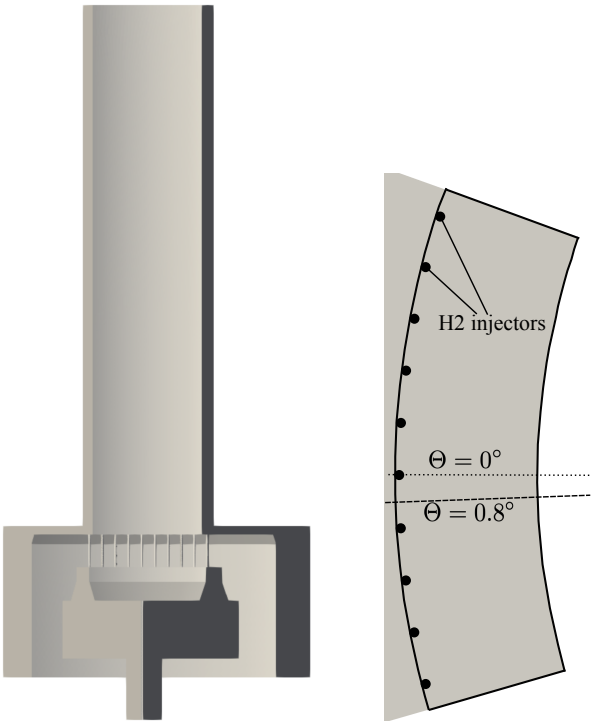

Figure 8.1: Computational domain of the 3D cold flow simulation with 10 H_2 injectors (left) and a cut through the air injection plane with black circles denoting the $H2$ injectors (right), colored by Ma.

	Simulation	Experiment	Deviation from experiment in [%]
Mass flow rate H_2 in $[g/s]$	13.7	13.7	0
Mass flow rate Air in $[g/s]$	517.7	517.7	0
Plenum pressure H_2 in $[bar]$	15.5	11.2	+38%
Plenum pressure Air in $[bar]$	5.1	4.2	+20%

Table 8.1: Comparison of mass flow rate and plenum pressures between the current LES and experimental data.

reported in other work: Nassini (2022), for example, imposes the plenum pressure and temperature but obtains deviation from the experimental Air mass flow rate of -11% and -14% in the H_2 mass flow in a non-reacting flow. This shows that the discharge coefficient C_D of the system is not captured as in experiments. This point is further investigated in the following section.

Cocks et al. (2016) have shown a similar behavior in their work, which they attribute to the mesh resolution of the injectors and the plenums.

Since the obtained results report the correct mass flow rates and hence the imposed equivalence ratio through the combustor, the obtained values for the plenum can be considered acceptable and this setup is further used as a basis of this work.

8.3.2 The question of the discharge coefficient C_D

In the following the C_D of the experiment as well as the computed ones are compared. The discharge coefficient is a parameter typically used for nozzles and holes (Gritsch et al., 1998; Guo et al., 2011) to account for the fact that the smallest section A controlling the flow rate may not be the geometrical smallest one [1]:

$$C_D = \frac{\dot{m}}{A_{crit} \frac{P_t}{\sqrt{RT_t}} \sqrt{\gamma} \left(\frac{2}{\gamma+1}\right)^{\frac{\gamma+1}{2(\gamma-1)}}} \tag{8.1}$$

Equation 8.1 represents the ratio of the actual (measured) mass flow over the theoretical critical mass flow thorough the holes under the assumption of no pressure and thermal losses. A_{crit} denotes the total cross section of the H_2 injector holes or the geometrical inlet area of the air slot at the entrance to the annular chamber. P_t denotes the total pressure, T_t the total temperature and $\dot{m}$ the actual mass flow rate, which are both assumed to be equal to the measured static values in the plenum under the assumption of a low Mach number $Ma \ll 1.0$ The resulting C_D for the presented case is displayed in Tab. 8.2. The estimated C_D obtained from experiments is close to 0.99 for

	Simulation	Experiment
H_2 discharge	0.70	0.99
Air discharge	0.89	1.0

Table 8.2: Comparison of C_D between the current LES and the experimental data.

the hydrogen injectors, which would correspond to an ideal flow through

[1] For all cases here, both the H_2 and the air flows are choked since pressures in the plenums are larger than the critical choking pressure.

a nozzle. This appears to be too high and might point to inconsistencies in the measurements of the test rig. The numerically obtained C_D in this work is smaller especially with $C_D = 0.70$ for the H_2 flow. While such a value appears to be more realistic, one cannot say for sure if it represents the correct flow characteristics, since the C_D is highly dependent on the jet geometry as well as the bulk cross flow, inclination between main flow direction, jet flow direction and geometrical dimensions of the problem (Gritsch et al., 2001; Guo et al., 2011). Another additional point might be the resolution in the injectors/cross flow region or the numerical scheme. Hassan et al. (2013) for example point out, that supersonic cross flow configurations require a high wall resolution to properly capture the flow physics. For of a subsonic cross flow with low Ma, Ruiz et al. (2015) use a resolution of 15 elements in the jet. In a subsonic configuration ($Ma \leq 0.3$) Liu et al. (2020) resolve the injectors with 67 elements along the diameter of the jet tube. Chai et al. (2015) investigate an underexpanded sonic jet into a supersonic cross flow with a structured mesh, where they resolve the injector with 100 points in radial direction, 100 points in tangential direction and 100 points in axial direction. This amount of resolution exceeds the resolution of injectors typically found in RDE simulations and can explain the deviations from numerical plenum pressure or mass flows to their respective experimental counterparts.

At this point it is concluded that matching the exact flow rates of H_2 and air was the first target (Tab. 8.1) and understanding why such high pressure losses occur in H_2 and in the air stream are left to further studies.

8.3.3 Flow field and shock structures

The current injector configuration is a jet-in cross flow setup, hence certain structures can be expected, which are shown in Fig. 8.2:

The flow structure is composed of a complex shock and vorticity structure. The cross flow causes a bow shock around the jet, and the jet itself is enveloped by a barrel shock, followed by a Mach disc. Behind the Mach disc the flow curls up into two counter rotating vortices. At the bottom after the jet injection a secondary shock is formed. Further horse shoe vortices are formed and convect around the jet.

Figure 8.3 (a, left) shows an iso contour of $Y_{H_2} = 0.0258$ which allows a good visualization of the vortex structures in the chamber. At the bottom of the chamber, H_2 rolls up and starts forming two counter rotating vortices, which become increasingly unstable in downstream direction. Figure 8.3 (a,

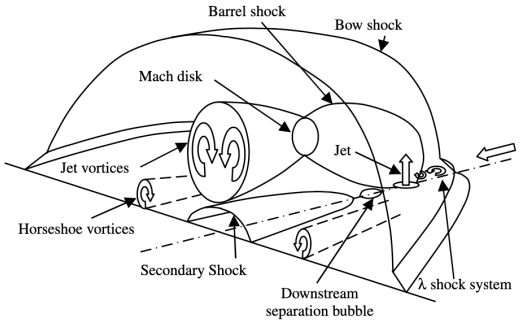

Figure 8.2: Schematic of a jet-in cross flow flow structure. From Dickmann and Lu (2009)

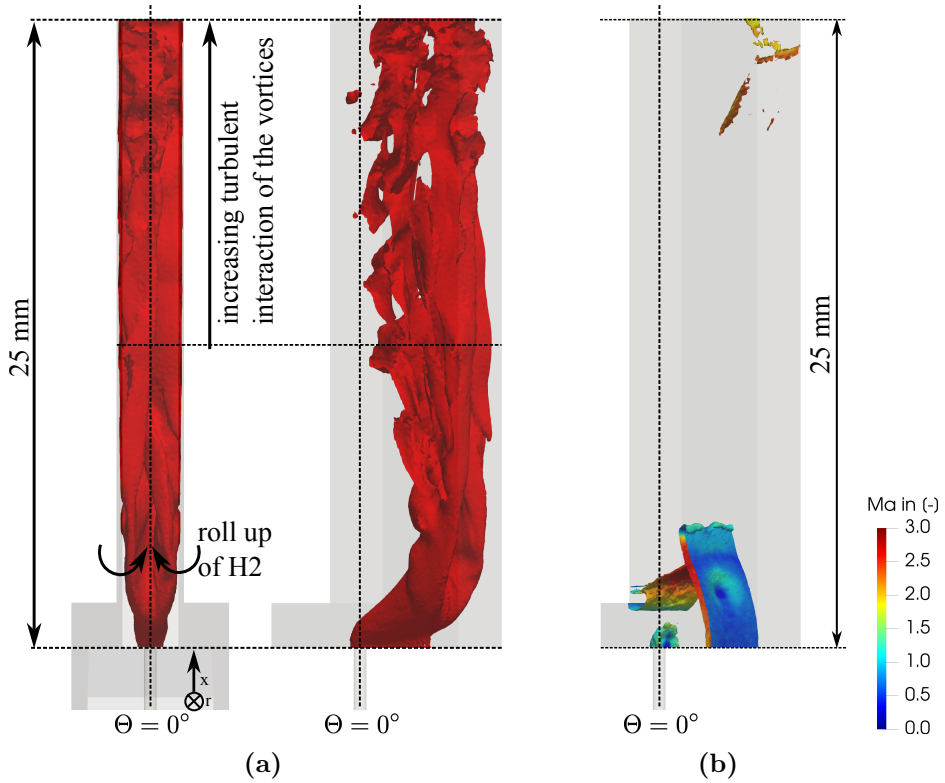

Figure 8.3: Instantaneous frontal view of an iso contour at $Y_{H2} = 0.0258$ with one injector (a, left) and rotated by 40° (a, right). Shock structures are visualized in (b) via an iso contour of $\Delta P/P = 2000/\text{m}$.

right) displays the same iso contour as (a) rotated by 40°, thereby highlighting the strong deflection of the H_2 jet towards the inner wall by the air flow. It shows an increasing interaction of vortices in downstream direction leading to vortex break-up into highly irregular structures. Additionally complicated shock structures occur in the cross flow area (Fig. 8.3 (b)).

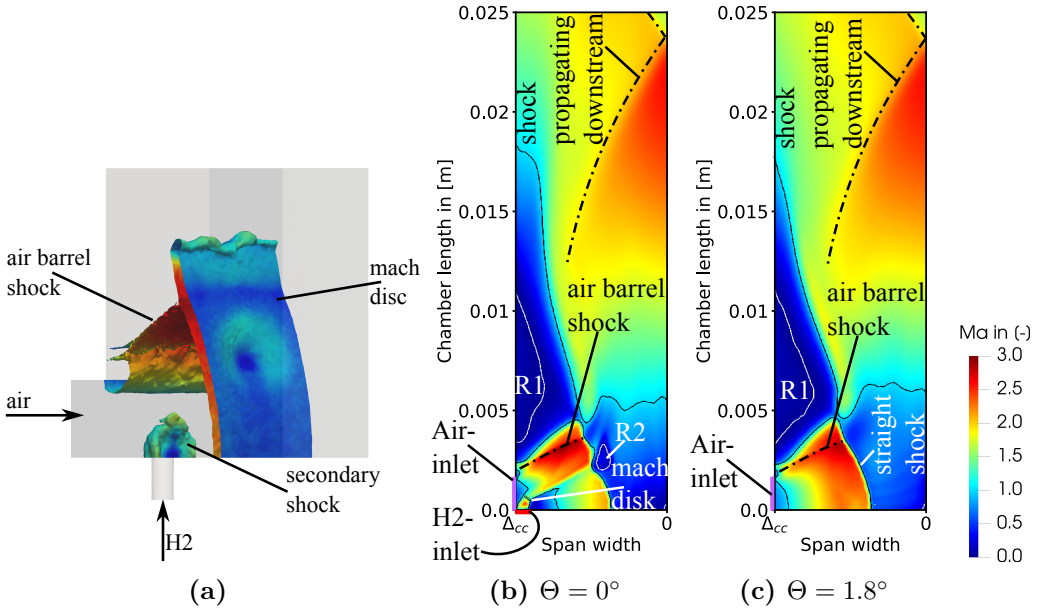

(a) **(b)** $\Theta = 0°$ **(c)** $\Theta = 1.8°$

Figure 8.4: 3D shock structure at the chamber inlet for one segment colored by Ma (a). The shown iso contour depicts $\Delta P/P = 2000/m$ at position $\Theta = 0°$. (b) time averaged Mach number field for $\Theta = 0°$, (c) time averaged Mach number field for $\Theta = 1.8°$. The black iso contours in (b) and (c) denote $Ma = 1$. The white iso contour denotes an axial velocity $u = 0m/s$, so that re-circulation zones are revealed.

Figure 8.4 illustrates the shock structures found close to the air and H_2 injection. The air enters the combustion chamber and expands, reaching $Ma = 3$. At a height of 0.005m, the flow expands again into supersonic conditions. The air flow is enveloped by a barrel shock in both cases (Fig. 8.4 (b) and (c)) and is deflected by the inner wall to align with the symmetry axis of the combustor. Figure 8.4 (b) also shows that H_2 is deflected towards the inner wall by the air flow. Due to the deflection a slight barrel shock occurs, followed by a Mach disk, highlighted in Fig 8.4 (b) close to the H_2 injection. Two re-circulation zones R1 and R2 occur in Fig. 8.4 (a) and (b): (R1) traps

air in the corner close to the outer wall and just above the injectors and will play a major role in the reactive cases.

8.3.4 Mixing field

To further investigate the mixing performance of the system, the time averaged Y_{H_2} and I_{mix} fields are plotted as 2D cuts in Fig. 8.5. The Y_{H_2} fields of planes through an injector and between two injectors (Fig. 8.5 (a) and (b)) show that the air cross flow prevents the transport of H_2 into the outer chamber, but instead deflects it towards the inner wall. In the plane through the injectors, I_{mix} (Fig. 8.5 (c)) reveals a strong mixing process in the shear layers of the H_2 jet and air flow at the bottom of the chamber. The plane between the injectors shows that, upstream of the occurrence of the vortex structures, no relevant mixing occurs between the injectors, emphasizing that the mixture at the bottom of the chamber is highly stratified. H_2 is transported into the $\Theta = 1.8°$ plane, once the H_2 vortices expand in downstream direction, which is the case for a height $> 0.005m$ above the bottom plate. The white iso contour in Fig. 8.5 (c) illustrates the deflected H_2 jet propagating towards the inner wall. The region at the corner of the bottom plate and inner wall does not contain significant amounts of fuel.

For a better visualization of the interaction between the H_2 injectors, I_{mix} is investigated through various axial planes shown in Fig. 8.6. The result is displayed in Fig. 8.7. At the bottom plate (Fig. 8.7 (a)), mixing is very localized and occurs at the shear layers of the hydrogen jets and the air cross flow, first around the H_2 injection itself (jets are seen as white circles) and towards the inner wall (follows the deflection of the H2 jets). At the plane located at the middle of the air gap height (Fig. 8.7 (b)), the deflection of the H2 jet is clearly highlighted with mixing predominantly pushed towards the inner wall. At a height of $2.6mm$ (Fig. 8.7 (c)), i.e. well above the air gap slot, the counter rotating vortices start to form. Further downstream, at a height of $5mm$ (Fig. 8.7 (d)), the vortices are fully developed and mixing only takes place in their vicinity, while the outer chamber stays without H_2. Once at a height of $10.0mm$ (Fig. 8.7 (e)) the vortices are shown to be considerably unstable, creating stronger fluctuations in the I_{mix} field, which in turn augments the mixing process. The last displayed cut (Fig. 8.7 (f)) illustrates, that the vortices have broken up completely and the mixing field is highly irregular. In summary, the bottom plate is dominated by fuel stratification and an overall poor mixing quality and only improves further

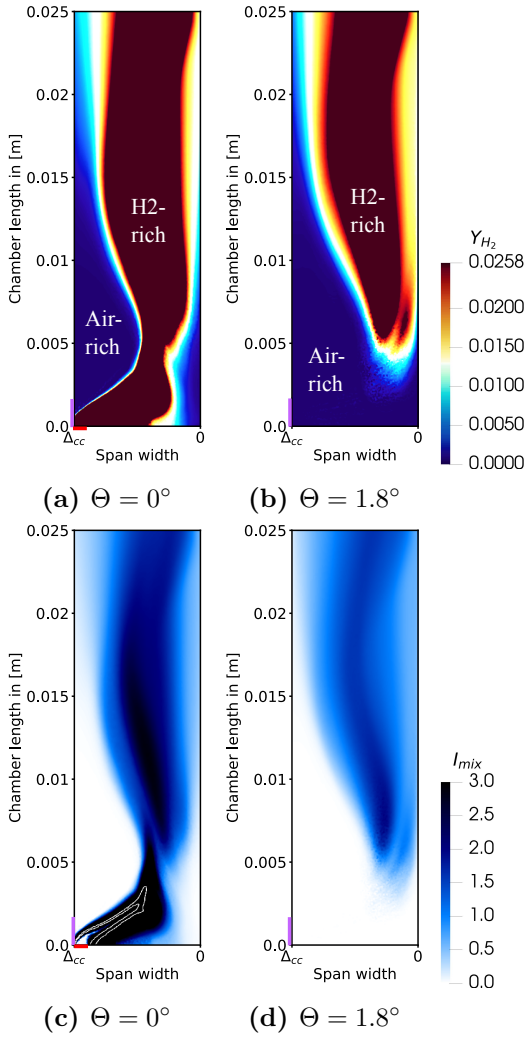

(a) $\Theta = 0°$ **(b)** $\Theta = 1.8°$

(c) $\Theta = 0°$ **(d)** $\Theta = 1.8°$

Figure 8.5: (a) and (b) show the Y_{H_2} field and (c) and (d) the field of the mixing index I_{mix} of a time averaged solution of the non reactive flow. A white iso contour in (c) displays $I_{mix} = 9$ to highlight the H_2 jet.

downstream. This will have strong implications with the reactive cases.

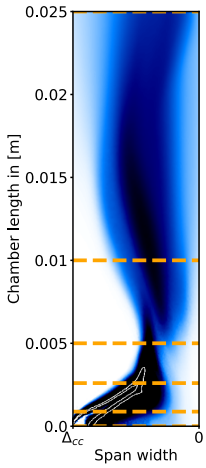

Figure 8.6: Positions of cuts presented in Fig. 8.7 as dashed lines. The position of the lines from bottom to top: bottom wall, $0.00088m$, $0.0026m$, $0.005m$, $0.01m$ and $0.025m$.

8.4 Conclusion

This chapter performs a pre-study on the TUB RDE for a non-reactive cold flow. The goal was to investigate the general flow field in the injection region and, by extension, to obtain an estimate for the refill process in the chamber. The shock structures in this study are a result of under-expanded fuel jets and oxidizer flow, which interact with the local geometry of the injection system. Due to the development of vortices and super sonic flow, the mixing process shows a deficient behavior in the lower chamber, with high fuel stratification. Additionally fuel is concentrated at the inner span of the annulus, while the outer span contains purely air, which is expected to limit the detonation propagation to the inner span of the RDE chamber.

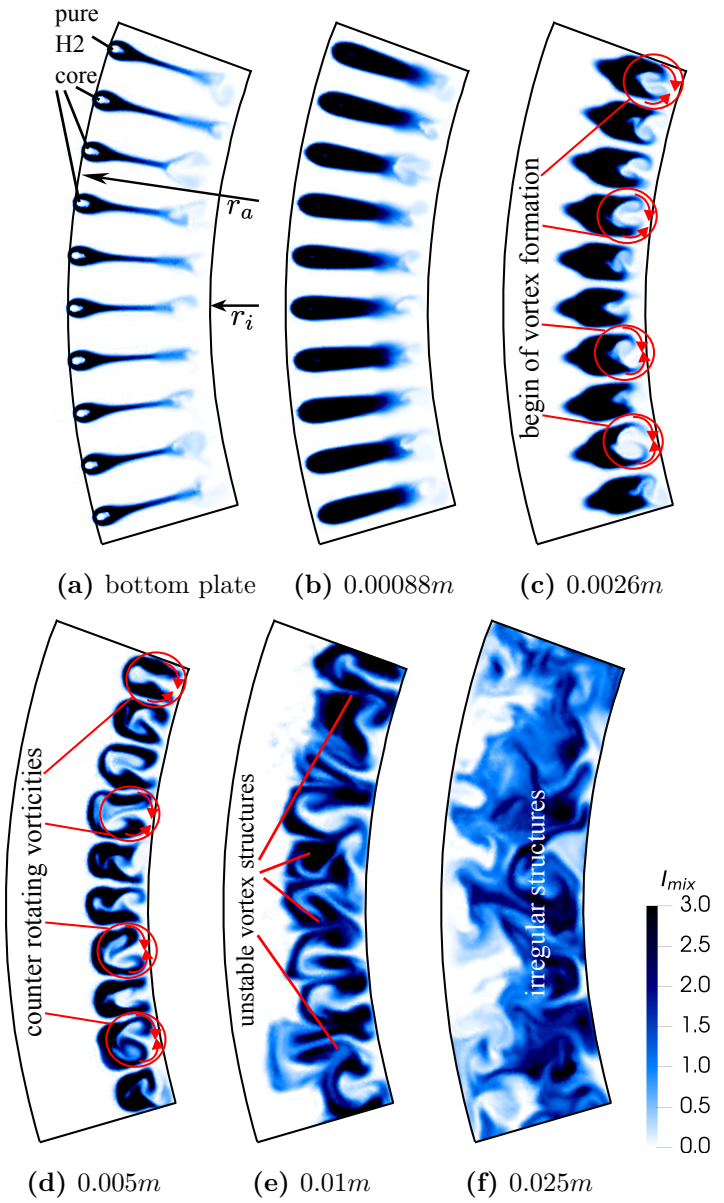

(a) bottom plate **(b)** $0.00088m$ **(c)** $0.0026m$

(d) $0.005m$ **(e)** $0.01m$ **(f)** $0.025m$

Figure 8.7: Axial cuts (a) at the bottom plate, (b) $0.00088m$ (air slot height/2), (c) $0.0026m$, (d) $0.005m$, (e) $0.01m$ and (f) $0.025m$ above the bottom plate.

Chapter 9

Effects of mixing assumptions on the LES of Rotating Detonation Engines

Contents

9.1 Introduction

The current chapter investigates the effects of mixing assumptions and subgrid scale (SGS) models. For this purpose CASE1-3 (see Tab. 7.2) are simulated and their results compared. This allows to qualify the effects of the injection and mixing system as well as the additional influence of SGS models on the mixture quality. A general view of the flow structures inside the RDE is shown in Fig. 9.1 (a) for CASE1. All the simulations performed in this thesis show the same structure consisting of a sustained single detonation wave mode. The impact of the different LES models and numerical methods on this structure will be discussed progressively in this and following chapters. Figure 9.1 (b) also displays the detonation index I_{det}, introduced in Chapter 7, which is shown to correctly detect the detonation wave inside the RDE and will therefore serve as a reliable tool to quantify the detonation efficiency inside the RDE. Due to the passing detonation wave and the resulting increasing pressure in the chamber, the plenum pressures of the reactive cases increase with respect to the cold case. Once converged, CASE1 displays an air plenum pressure of $6.6bar$ and an H_2-plenum pressure of $7bar$. CASE2 and CASE3 display an air plenum pressure of $6.4bar$ and an H_2-plenum pressure of $15.9bar$. The low pressure of $7bar$ in CASE1 corresponds to the premixed gases where the properties of air dominate the resulting pressure in the H_2 plenum.

Note that for CASE1 the species source terms are fixed to 0 outside of the combustion chamber, so that any type of flashback into the plenums is prevented and this model case can be run without problems relating to backflash.

RUN NAME	MIXING CONFIGURATION	NUMERICAL SCHEME	SGS MODEL	WALL TREATMENT	$\delta_{1/2,target}$ in μm	$z_{nom} = \frac{\dot{m}_{H_2}}{\dot{m}_{H_2}+\dot{m}_{O_2}}$ in [-]
CASE1	**PREMIXED**	LW	WALE	ADIAB. SLIP-WALL	149.6	0.0258
CASE2	NON-PREMIXED	LW	WALE	ADIAB. SLIP-WALL	149.6	0.0258
CASE3	NON-PREMIXED	LW	**SIGMA**	ADIAB. SLIP-WALL	149.6	0.0258
CASE4	NON-PREMIXED	LW	WALE	**ADIAB. LAW-OF-THE-WALL**	149.6	0.0258
CASE5	NON-PREMIXED	LW	WALE	ADIAB. SLIP-WALL	**180.0**	0.0258
CASE6	NON-PREMIXED	LW	WALE	ADIAB. SLIP-WALL	**206.0**	0.0258
CASE7	NON-PREMIXED	**TTG4A**	WALE	ADIAB. SLIP-WALL	149.6	0.0258

Table 9.1: Summary of LES runs

9.2 Wave speed

In this work the pressure signal of one probe, positioned 25mm above the bottom plate, is used to obtain the wave speed D. The pressure signals are shown in Fig. 9.2. The detonation speed and wave modes of CASE1, CASE2 and CASE3 are displayed in Tab. 9.2, D is computed as $2\pi r_{max} * f_{deto}$, since the experimental measurements are taken from the outer wall.

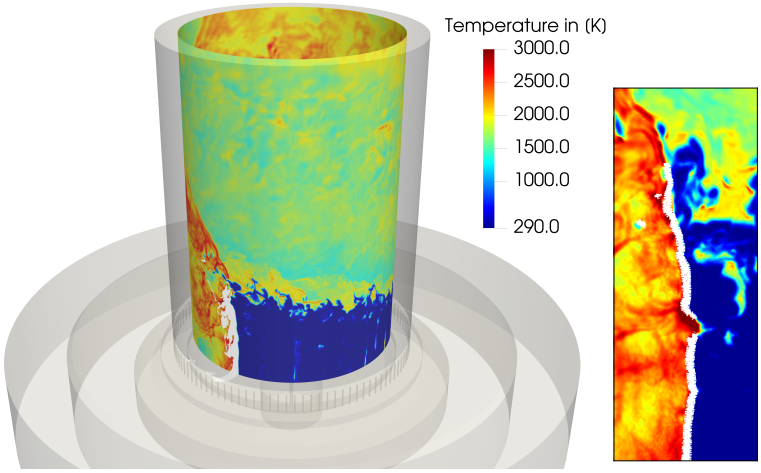

(a) **(b)**

Figure 9.1: a) Instantaneous solution of CASE1. The temperature field along the inner wall is displayed, to visualize the domain. Additionally the detonation front is displayed via the iso contour of $I_{det} = 1$ in white. b) an instantaneous cut of CASE1 at 33% span width displaying $I_{det} = 1$ as a white iso contour on the detonation front.

The detonation speed in simulations is often over-predicted in one wave mode setups (Cocks et al., 2016; Nassini et al., 2023; Sato and Raman, 2020), showing that the deviation from the experimentally measured wave speed can increase with the nominal mass flow rate. The over-prediction can be seen in the present LES, too, with CASE1 (which is fully premixed) displaying the fastest wave speed. The reason for this phenomenon is not trivial to determine and still the topic of ongoing work. Potential sources of discrepancies have been identified in the recent years: the strong resolution requirement to accurately predict the dynamics of detonation waves in curved channels (Melguizo-Gavilanes et al., 2021; Sugiyama et al., 2014), the absence

of consensus on the real impact of deflagrative combustion on detonation propagation and how to accurately take it into account in CFD simulations (Nassini et al., 2023; Sato et al., 2021), the strong resolution requirements to accurately simulate the complex mixing close to the injectors and its strong coupling with the passing detonation wave (Chen et al., 2023; Zhou and Wang, 2012), ...

CASE1 is especially interesting in this regard, since the detonation is not exposed to a stratified mixture (due to mixing), which has been shown to decrease the detonation speed as well as changing the detonation structure (Metrow et al., 2021).

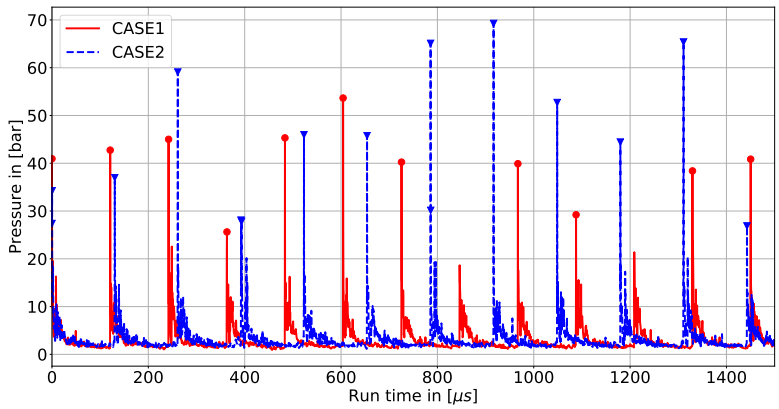

Figure 9.2: Mid-span pressure signals at $y = 25\ mm$. The signals are recorded after a steady detonation propagation has been achieved and are sampled at a frequency of $3.8 MHz$.

Figure 9.2 shows that the detonation speed D of CASE1 is about 10% faster than the one in CASE2. Since the difference of the cases lies in the mixing assumption, it can be concluded that the improved quality of the mixing process in the refill zone of CASE1 is responsible for the increase in detonation speed. This is in agreement with recently conducted experiments of a variably premixed RDE (Ayers et al., 2023). In fact, Burke et al. (2021) have shown that by additional injection of premixed bypass gases, the detonation speed increases, emphasizing that a slight improvement in the mixture quality can significantly increase the detonation speed. The variation in maximum pressure of the signals highlights the flucuations in the detonation front

during the wave propagation, even in CASE1 (Fig. 9.12). Table 9.2 lists the different LES wave speeds versus the experimental one and compares them to the nominal Chapman-Jouguet detonation speed D_{CJ}. The measured detonation speed in LES is always significantly higher than the experimental value, which already shows that considering mixing, the LES is not sufficient to capture the correct detonation dynamics. Possible reasons for this gap between LES and experiments will be discussed in details while considering the other modeling bricks of the LES all along the next chapters.

	CASE1	CASE2	CASE3	EXPERIMENT
Wave mode [-]	single	single	single	single
Rotation Frequency f_{rot} $[Hz]$	8280	7630	7630	5800
Detonation wave speed $[m/s]$	2341	2157	2157	1640
D/D_{cj} [-]	1.216	1.12	1.12	0.85

Table 9.2: Comparison of the different predicted detonation frequencies of CASE1 and CASE2 with respect to the experimentally obtained wave speed. D_{cj} (=1925 m/s) is based on the nominal $\phi = 0.9$, T_{init} and P_{init}.

9.3 Effects of mixing assumptions

9.3.1 Perfectly premixed vs non-premixed injection

For the flow fields a general analysis of the instantaneous field is conducted and subsequently a detailed analysis of the phase averaged solution executed. The detonation wave passage results in the slight blockage of mass flow, which is seen in Fig. 9.3 (a)-(f) for $-\pi/2 \leq \Theta \leq 0$. A look at the instantaneous temperature and H_2 fields (Fig. 9.3 (a)-(d)) shows for all cases the typical flow field structure of a RDE. In front of the detonation wave a triangular refill zone is filled with fresh reactants (blue zone in Fig. 9.3 (a) and (b)). Downstream of the detonation an oblique shock propagates towards the outlet. Between products of the current and previous cycle a slip line is formed.

Compared to CASE1 (Fig. 9.3 (a)) the temperature distribution in CASE2 (Fig. 9.3 (b)) shows more local hot spots after the detonation wave, especially in the wake of the foot of the detonation. Although both cases have leftover fuel along the slip line after the detonation (Fig. 9.3 (c) and (d)),

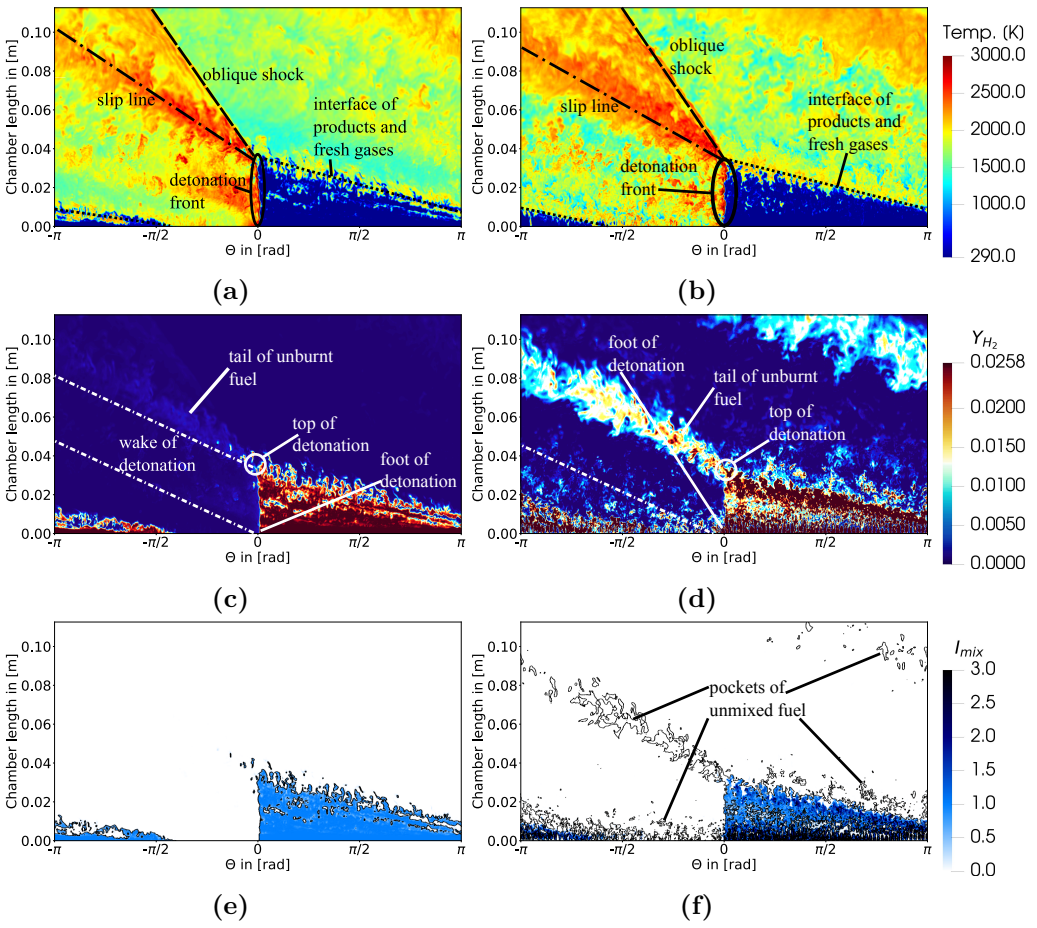

Figure 9.3: Instantaneous temperature field of CASE1 (a) /CASE2 (b) and instantaneous Y_{H_2} distribution of CASE1 (c) /CASE2 (d) and fields of I_{mix} for CASE1 (e) and CASE2 (f) along 33% span width of the annulus. The black iso contours denote an iso contour of $Y_{H_2} = Y_{H_2,sto}/2$, which delivers a good threshold for the visibility of H_2 pockets.

only CASE2 contains multiple fuel pockets in the wake of the detonation and leaves much more fuel to exit the chamber, having a similar refill height as CASE1. The large amount of unburnt H_2 in CASE2 is a first indicator of the importance of mixing in this configuration.

Figure 9.3 (e) and (f) show the I_{mix} fields of CASE1 and CASE2. The black iso contour identifies pockets of H_2. Since CASE1 is fully premixed from the beginning, mixing of H_2 and O_2 is almost uniformly constant in

the whole refill area with $I_{mix} = 1$ with a few local areas of a dropping I_{mix}, due to the presence of residual combustion products (Fig. 9.3 (a)). This is not the same for CASE2 where higher values of I_{mix} occur due to the influence of the hydrogen jets at the bottom plate of the chamber. An important distinguishing feature between CASE1 and CASE2 is the absence of mixed reactants after the detonation front in CASE1, whereas CASE2 contains leftover H_2 after the detonation wave, although $I_{mix} = 0$. This demonstrates the existence of losses due to non mixed H_2. Interestingly not even the perfectly premixed CASE1 is able to process 100% of the premixed reactants close to the interface of fresh gases and product gases of the previous detonation cycle.

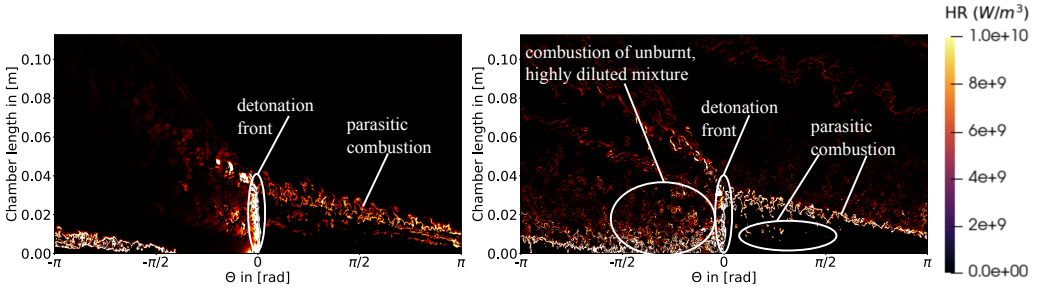

Figure 9.4: Instantaneous heat release field of CASE1 (a) /CASE2 (b)

The high temperature spots in front of the detonation as well as the contact surface between hot gases and fresh reactants are potential sources of parasitic combustion. This is shown in Fig. 9.4 (a) for CASE1 and (b) for CASE2. Both images display a visible heat release in the fresh gases in front of the detonation. Both cases also show a significant heat release where hot gases and fresh, mixed reactants meet. Figure 9.4 (a) and (b) differ behind the detonation: CASE2 shows significant amounts of combustion of unburnt, diluted mixed fuels. This emphasizes that leftover, unmixed reactants are not consumed by the detonation, and instead burnt after an additional mixing in the wake of the detonation.

By analyzing the phase locked averages of the fields, a better understanding of the global flow features can be achieved. The field of Y_{H_2} of CASE1 (Fig. 9.5 (c)) shows that the maximum amount of fuel is at the bottom of the chamber (see Fig. 9.5 (c) 2) and then decreases downstream due to the intermittent presence of pockets of combustion products from the previous cycle

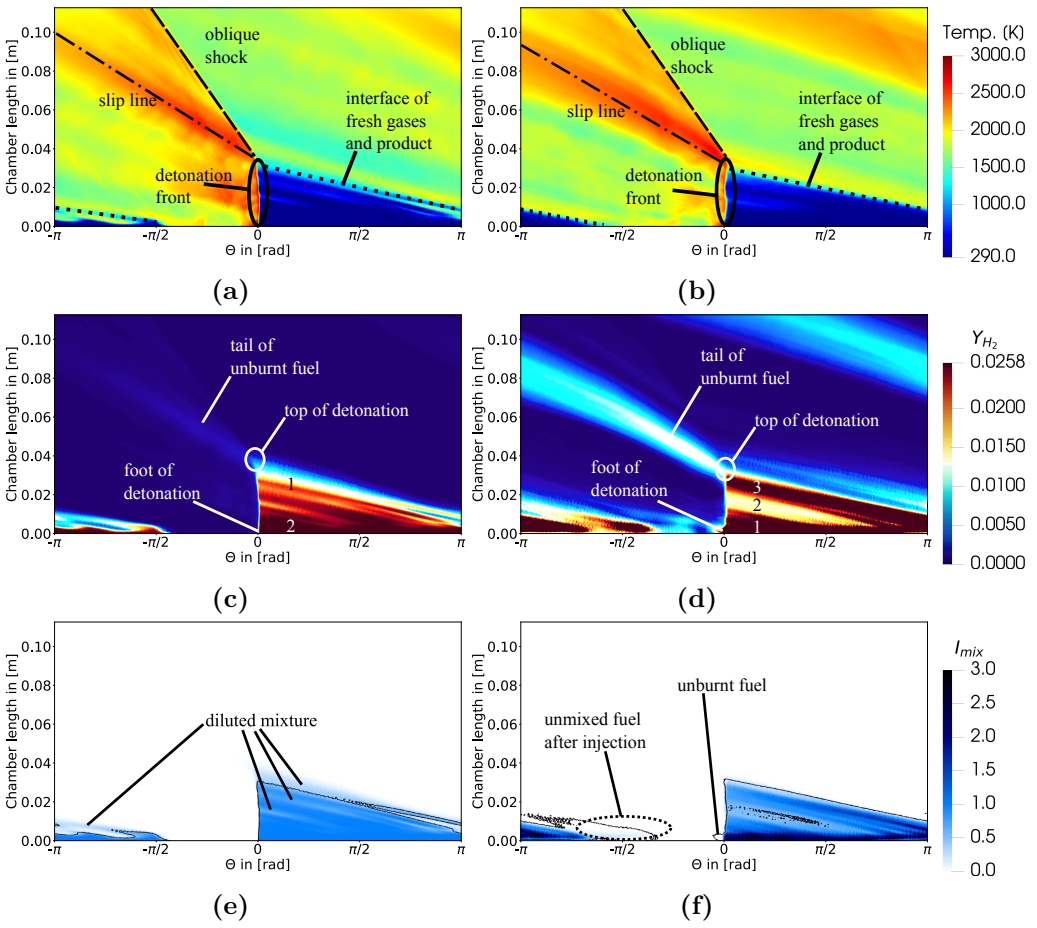

Figure 9.5: Phase averaged temperature field of CASE1 (a) /CASE2 (b), phase averaged Y_{H_2} distribution of CASE1 (c) /CASE2 (d) and fields of I_{mix} for CASE1 (e) and CASE2 (f) along 33% span width of the annulus. The black iso contours denote an iso contour of $Y_{H_2} = Y_{H_2,sto}/2$, which delivers a good threshold for the visibility of H_2 pockets.

(see Fig. 9.5 (c) 1). The field of Y_{H_2} in CASE 2 shows three distinct regions (Fig. 9.5 (d)) in front of the detonation wave: 1) a rich area at the bottom of the chamber as a result of the injection of H_2 at the bottom, where the fuel does not have time to mix properly. After this first region, mixing then proceeds downstream leading to a decrease in Y_{H_2}. 2) a triangular area where Y_{H_2} decreases considerably. The low amont of Y_{H_2} in this region (Fig. 9.5 (d)), suggests that this region is filled with air coming from the air injection

gaps. Finally, 3) a rich band of fuel close to the product of the previous cycle.

Taking into account I_{mix} in Fig. 9.5 (e), CASE1 displays an overall homogeneous mixing field of $I_{mix} = 1.0$. However bands with a low $I_{mix} < 1$ occur and they denote the presence of a diluted band of mixture, since the value of I_{mix} is fixed due to the premixing condition, allowing only the presence of combustion products to lower it. Fig. 9.5 (e) contains an additional band of a diluted reactant mixture above the black H_2 iso contour in the contact area of products of the previous detonation cycle and the fresh gases of the current cycle. The presence of combustion products will naturally influence the propagation of the detonation, compromising the overall detonation efficiency. These bands can be sources of deflagration burning resulting in another loss in fuel, hence a lower efficiency in the detonation.

CASE2 differs considerably from the premixed CASE1 in terms of fuel distribution. Indeed, the phase locked averaging shows that the mixture in front of the detonation wave in CASE2 is markedly rich close to the interface with the burnt gases in zone (3), which explains the trail of unburnt H2 left behing the detonation wave (see e.g. Fig. 9.5 (d))

The quality of mixing can be further investigated by plotting the probability density function of the mixing index I_{mix}. To do this we assume that a gas mixture at temperature $T \leq 500K$ corresponds to unburnt gases. We then plot the distribution of I_{mix} in this region.

The averaged and instantaneous curves of these PDFs in Fig. 9.6 show that the distribution of I_{mix} is qualitatively time independent for CASE1 and CASE2. The PDFs of CASE1 have a peak at $I_{mix} = 1$ due to the premixing. The minimum value is at $I_{mix} = 0.67$ showing that there is a small zone, where the premixed reactants are diluted by combustion products. Hence, during the refill process, combustion products are entrained and mixed with fresh premixed gases. CASE2 on the other hand displays a different distribution, due to the required mixing process. The peak occurs for a $I_{mix} = 0$. This reveals the presence of unmixed regions where at least one of the reactants is missing. Here I_{mix} spans over a range from 0 to 10, displaying the maximum possible range for I_{mix} in CASE2.

The range of I_{mix} and the peaks for $I_{mix} < 1$ of CASE2 in comparison with the PDF of CASE1 emphasize, that the mixing quality of CASE2 is not optimal and explains its lower detonation speed. The PDF of CASE2 has a second peak around $I_{mix} = 0.65$. This means that in the chamber the effective global equivalence ratio is lower that the nominal one, hence the mixture predominantly burns in lean conditions. This confirms that mixing

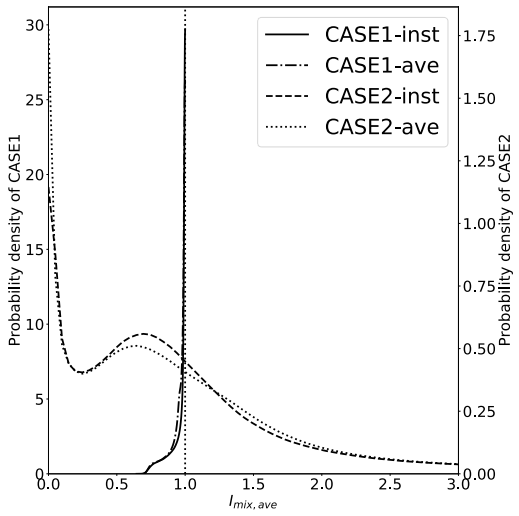

Figure 9.6: Instantaneous and averaged qualitative PDFs of mixing index I_{mix} for CASE1 and CASE2 for the fresh gases, (declared at $T \leq 500K$). A vertical dotted line is positioned at $I_{mix} = 1$.

plays a major role in the efficiency of the combustor and that LES should always include the full injection and mixing system.

The cylindrical cuts of Fig. 9.5 do not show the radial distribution of the investigated cases. To understand the actual mixing and fuel consumption, two planes normal to the detonation propagation direction and shifted by ± 7.2 degrees with respect to the detontion plane are investigated for CASE 1 (Fig. 9.8) and CASE 2 (Fig. 9.9). These planes show the flow ahead (+7.2) and downstream (-7.2) the detonation front. Their position is shown in Fig. 9.7. This angle is sufficiently small to allow for a qualitative analysis of the mixture state that the detonation burns.

Figure 9.8 focuses on CASE 1. Fig. 9.8 (a) shows that in front of the detonation a refill of the inner span of the chamber extends to 35mm in height. Pre-detonation, as observed in Nassini et al. (2023), the chamber is not effectively flushed by the new reactants: only the inner span is fed with new reactants and a re-circulation zone above the air inlet slot is formed, while the outer span width stays filled with combustion products of the previous cycle. Hence, no detonation can be achieved along the whole span width. The contact surface between fresh gases and combustion products of the previous cycle constitutes a source for parasitic combustion. The I_{mix} field (Fig. 9.8

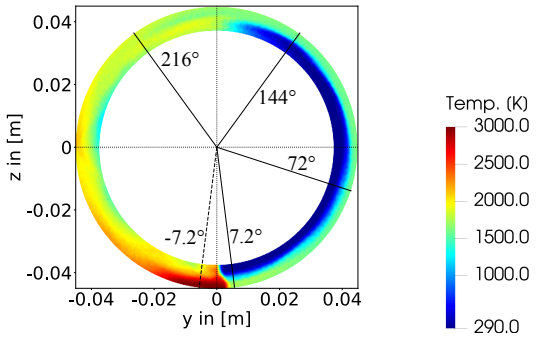

Figure 9.7: Cut at $x = 10.6mm$ above the faceplate of the phase average of the field of temperature for CASE2 with the position of the cuts: the angle of the cuts with respect to the detonation front at -7.2 (dashed line) and 7.2 degrees in counterclockwise direction are represented by Fig. 9.8 and 9.9. The cuts with respect to the detonation front of 7.2, 72, 144 and 216 degrees are shown in Fig. 9.10. In this graph, y and z denote spatial coordinates. The detonation rotates in counterclockwise direction.

(b)) pre-detonation has a homogeneous distribution in the fresh gas region with a decrease of I_{mix} in span wise direction for a span width of $> 50\%$. This is due to the increasing dilution of fresh gases by combustion products in span-wise direction.

After detonation passage, the temperature distribution shows a higher temperature for a span width of $> 50\%$ than for the inner span of the chamber (Fig. 9.8 (a)). This cannot be a result of a detonation, since the amount of mixed reactants pre-detonation passing is too low for a span width of $> 50\%$. Instead, the shock wave attached to the detonation compresses the hot products of the previous cycle to these temperatures. Looking at the I_{mix} field post-detonation, one can also observe that across the refill height, reactants have been effectively consumed however, pockets of lean premixed unburnt gases are left unconsumed by the detonation, which is consistent with the tail of unburnt gases observed in Fig. 9.5 (c).

Figure 9.9 focuses on CASE2. The cuts in front of the detonation in e.g. Fig. 9.9 (a) reveal the same non-ideal flushing of the annulus as CASE1. The inner half of the annulus is supplied with fresh gases, whereas the outer span (span width $> 50\%$) contains combustion products of the previous cycle. Fig. 9.9 (a) also shows a re-circulation zone formed above the air inlet. Contrary to CASE1 (Fig. 9.8 (b)) the distribution of I_{mix} in CASE2 (Fig. 9.9 (b))

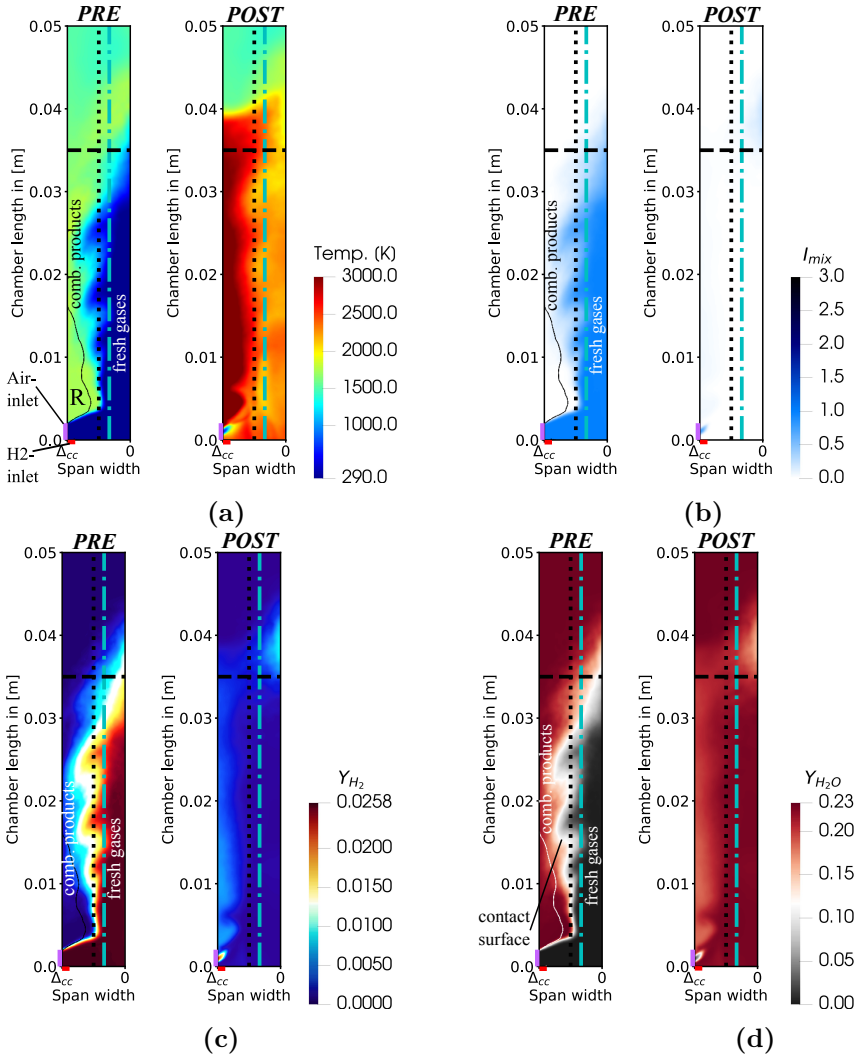

Figure 9.8: CASE1 - Phase locked averaged cuts in front and after the detonation front pre-and post-detonation: the first pair shows the temperature fields (a), the second I_{mix} (b), the third H_2 (c) and the last the H_2O fields (d). The dot-dashed line denotes the radial position of the previously displayed unwrapped cuts and the dotted line denotes 50% span width. A black (white in (d)) iso contour at $u = 0$ (axial downstream velocity) reveals a re-circulation zone R in front of the detonation. The colormaps are saturated as established, additionally the H_2O colormap is saturated at the maximum value for a stochiometric reaction. The x-axis goes from Δ_{cc}, the outer wall to 0, the inner wall.

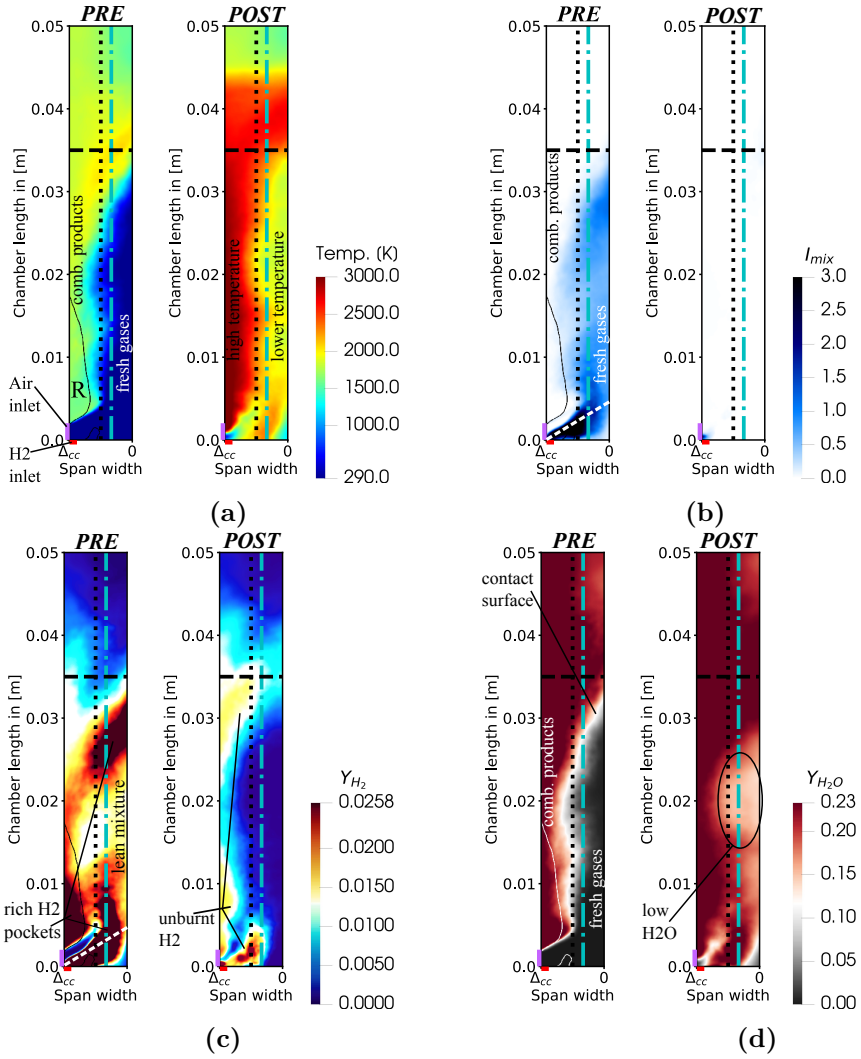

Figure 9.9: CASE2 - Phase locked averaged cuts in front and after the detonation front in pairings pre-and post-detonation: the first pair shows the temperature fields (a), the second I_{mix} (b), the third H_2 (c) and the last the H_2O (d) fields. The dot-dashed line denotes the radial position of the previously displayed unwrapped cuts and the dotted line denotes 50% span width. A black (white in (d)) iso contour at $u = 0$ (axial downstream velocity) reveals a re-circulation zone R in front of the detonation. The colormaps are saturated as established. The x-axis goes from Δ_{cc}, the outer wall to 0, the inner wall.

is highly non uniform and reaches values $I_{mix} > 1$. In Fig. 9.9 (b) and Fig. 9.9 (c) a white dashed line marks the redirection of the axially injected fuel jets towards the inner wall, at an angle of ~ 30 degrees with respect to the face plate.

Figure 9.9 (c) complements the distribution of H_2 already displayed in Fig. 9.5 (d), where 3 distinct bands (1-3) have been highlighted in front of the detonation wave. Figure 9.9 (c) shows that the redirection of the fuel jets is responsible for the H_2-rich region (1) found close to the bottom wall in Fig. 9.5 (d) and is shown to only take place close to the inner wall (1) in Fig. 9.9 (c). A H_2-lean region (2) takes place just above the previous region as a sign of stronger interaction between H_2 and air jets. A third region (3), rich in H2, sits on top of region (2) and corresponds to the H_2 injected just after the blockage region and propagates downsteam in contact with burnt gases. A fourth pocket of H_2 appears in Fig. 9.9 (b) and coincides with the recirculation region above the injectors where unburnt H_2 from the previous cycle is trapped and mixes with burnt gases.

The temperatures after detonation in the previously mixed area are below the high temperatures observed in Fig. 9.8(b), emphasizing a non ideal detonation of fuel and oxidizer in the region, or an already advanced expansion after the detonation. The post-detonation plane of Fig. 9.9 (d) shows areas with low amounts of H_2O. This emphasizes that the detonation processes mainly lean mixtures and a significant amount of air preserves.

Note that the temperature fields in Fig. 9.8 and Fig. 9.9 show instabilities in the shear layer of fresh and burnt gases. Due to the high temperature gradients (hence density gradients as well) between the two regions and fluctuations in the downstream velocity, one can attribute this to a combination of Kelvin-Helmholtz (velocity gradient based) and Rayleigh-Taylor (density gradient based) instabilities. Another reason could be the interaction of the fresh gases with an acoustic mode, created by the detonation in the respective setup.

The comparison of CASE1 and CASE2 shows that the design of the injection system is a major contributor to losses and an optimization of the injection system is detrimental for improving the operability of the RDE. First, a better flushing of combustion products is necessary to profit from the full span of the annular chamber and to minimize non-detonative combustion in the contact area of fresh gases and hot combustion products. Second, it is important to maximize the mixing performance for a higher detonation efficiency.

9.3.2 Effects of SGS mixing models

One has seen in the previous subsection, that the mixing assumptions (perfectly premixed vs. non premixed) play a major role. The next criterion for real injection (CASE2) is to know whether the SGS model also plays a role, since it also controls mixing.

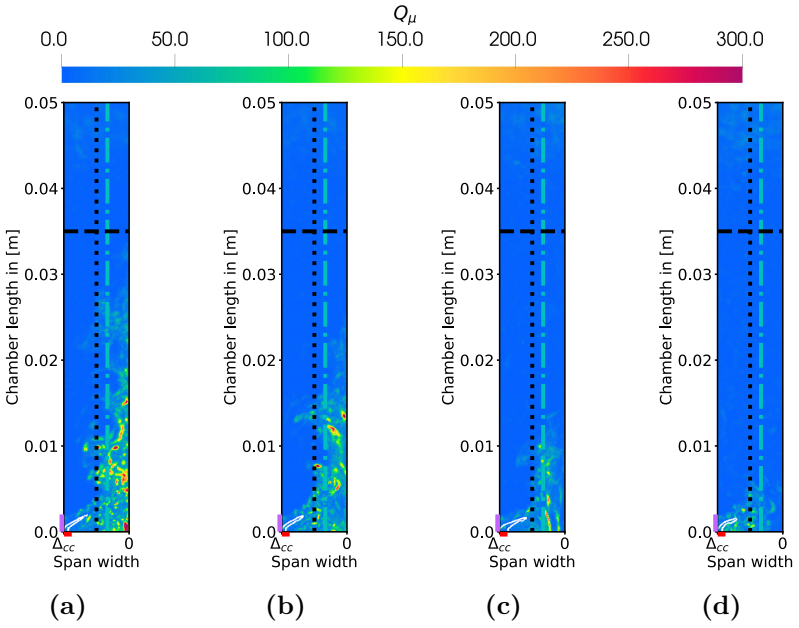

Figure 9.10: $Q_\mu = \frac{\mu_t}{\mu_{lam}}$ on cuts performed on an representative instantaneous solution of CASE2 in front the detonation in increasing phase: (a)-(d) display the cuts at an offset of 7.2, 72, 144, 216 degrees in front of the detonation. The black dashed lines denote the respective maximum fill height and the vertical dashed line denotes the position of the unwrapped cuts previously shown. An additional white iso contour at $z = 0.5$ outlines the H_2 jets at the bottom of the chamber.

Mixing in the LES approach is dependent on the turbulent viscosity ν_t (Eq. 5.5), imposed via the sub-grid scale turbulence model for LES. To confirm its influence we first compute the corresponding dynamic turbulent viscosity $\mu_t = \nu_t \rho$ and investigate the ratio of μ_t divided by μ_{lam} (Eq. 2.26), here called $Q_\mu = \frac{\mu_t}{\mu_{lam}}$, on a representative instantaneous snapshot, covering the refill area. For high values of Q_μ the simulation of the mixing process is dominated by μ_t introduced via the SGS, whereas low values indicate a minor contribution of μ_t. The fields of Q_μ are provided in Fig. 9.10. The

planes for CASE2 in Fig. 9.10, show that Q_μ has its highest values (up to 300) in the refill zone directly, due the occuring high amount of turbulence, resulting from the high velocity of the incoming fresh gases. The drop of Q_μ downstream is a consequence of the high temperatures in the burnt gases: μ_{lam} scales like $\sim (T/T_{ref})^{0.686}$, meaning that μ_{lam} increases by 4 to 5 times going from cold gases to hot gases. Particularly for CASE2, it emphasizes that the mixing of H_2 and air is the strongest at the bottom of the chamber and is dominantly governed by μ_t, showing that the influence of the SGS model on the mixing performance is very influential in the fresh gases.

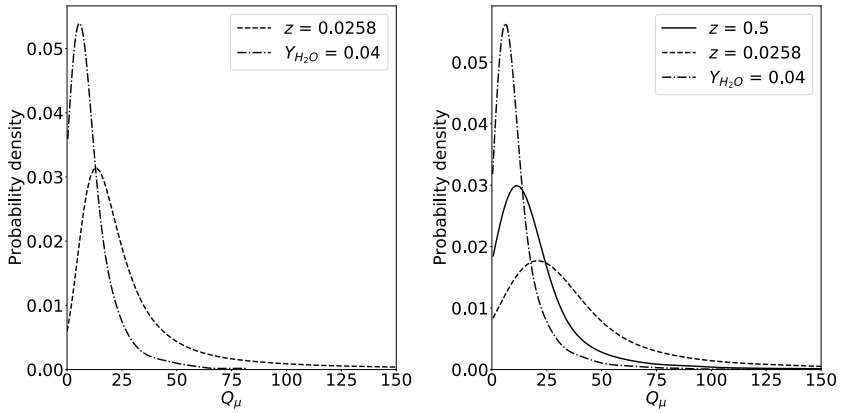

(a) **(b)**

Figure 9.11: PDF of Q_μ along different iso surfaces in the fresh gases at $T \leq 500K$ for a representative instantaneous solution. The left image (a) shows the PDF of Q_μ for $z = 0.0258$ and $Y_{H_2O} = 0.04$ of CASE1. The right image (b) represents CASE2 and adds $z = 0.5$ to include the mixing in the H_2 cross flow.

The influence of μ_t on the reactants in CASE1 and CASE2 is shown via PDFs of Q_μ along different iso surfaces in Fig. 9.11: $z = 0.0258$ (for $T \leq 500K$) as a representative for the ideally premixed fresh gas condition in CASE1 and CASE2. The magnitude of μ_t in the dilution process with H_2O is represented by the distribution of Q_μ along the iso surface of $Y_{H_2O} = 0.04$, which corresponds to 17% of the maximum Y_{H_2O} for a premixed case, making it a good value to check mixing with H_2O. Additionally the PDF of Q_μ along $z = 0.5$ ($T \leq 500K$) is plotted for CASE2 to include the mixing process in the cross flow at the injection. Along the common iso surfaces in Fig. 9.11 (a) and (b) one finds the same behavior: Q_μ along $z = 0.0258$ has in both cases a similar peak around $Q_{\mu,CASE1,z=0.0258} = 12$ and $Q_{\mu,CASE2,z=0.0258} = 18$, hence

mixing in the refill area is dominated by μ_t. The dilution process is also dominated by μ_t, with $Q_{\mu,Y_{H_2O}=0.04} = 6$ in CASE1 and $Q_{\mu,Y_{H_2O}=0.04} = 7$ in CASE2, is about a factor 2 smaller than seen for $z = 0.0258$.

Overall, Fig. 9.10 and Fig. 9.11 highlight the strong role played by the turbulent SGS model in the LES, but also the good quality of the LES with relatively moderate values of Q_ν.

A direct check of the effects of the SGS model is to change it. For this purpose we conduct an additional run CASE3, where CASE3 is run with the SIGMA model instead of the WALE model. The result on the pressure signals is displayed in Fig. 9.12.

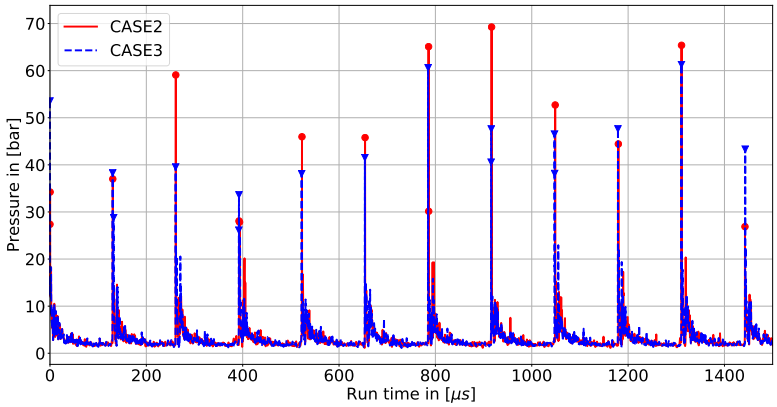

Figure 9.12: Mid-span pressure signals of CASE2 and CASE3 at $y = 25\ mm$. The signals are recorded after a steady detonation propagation has been achieved and are sampled at a frequency of $3.8 MHz$.

The pressure jumps corresponding to the passing detonation are superimposing each other, while the peak values differ from each other. This shows that the SGS model does not impact the detonation speed, which implies that the influence of μ_t on the fresh gas mixing is not significantly altered by the SGS model. A comparison of the PDFs of CASE2 and CASE3 (Fig. 9.13), gives further insight on the influence of the SGS model. The respective curves all show peaks at similar values of Q_μ, where the relevant range is $5 \leq Q_\mu \leq 50$, which is present for both SGS. The position of the peaks of the curves for $z = 0.5$ are in agreement, as well as the peaks of $z = 0.0258$. This emphasizes that the SGS models apply μ_t in a very similar

manner, making the sub-grid mixing highly similar. Overall, μ_t is one order of magnitude larger than μ_{lam}, which is generally accepted as an indicator of a reasonable impact of the SGS model on the results.

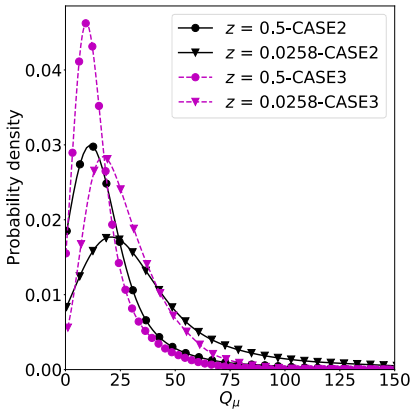

Figure 9.13: PDF of Q_μ along the iso contours of $z = 0.0258$ and $z = 0.5$ in the fresh gases at $T \leq 500K$ of CASE2 and CASE3.

The comparison of WALE and SIGMA shows that the SGS model does not impact the results in a significant way, at least regarding the two SGS models considered. Instead the focus must be shifted to optimizing the modeling of detonations and deflagrations in RDEs.

9.4 Influence on the blockage behavior

The previous analysis have shown that a considerable amount of fuel is not completely detonated in CASE2. Figures 9.5 f) has shown that blocking occurs, which could be the reason for delayed injection of air and hence no mixing between the H_2 and air. Since it is not evident whether the blockage for fuel and air is identical, polar plots of the mass flow rates at the H_2-injectors and the air inlet slot for an instantaneous solution of CASE1 and CASE2 are shown. Figure 9.14 shows that the passing detonation wave leads to a strong blockage in both cases (block1), which leads to short time frame where even back flow into the air injection slot occurs for CASE2. This is in fact not observed for CASE1 where the minimum value of $\dot{m}_{air} \approx 0$. Instead the main blockage in block1 of CASE1 occurs in the H_2 injectors due to the premixed gases having a significantly lower flow velocity in the

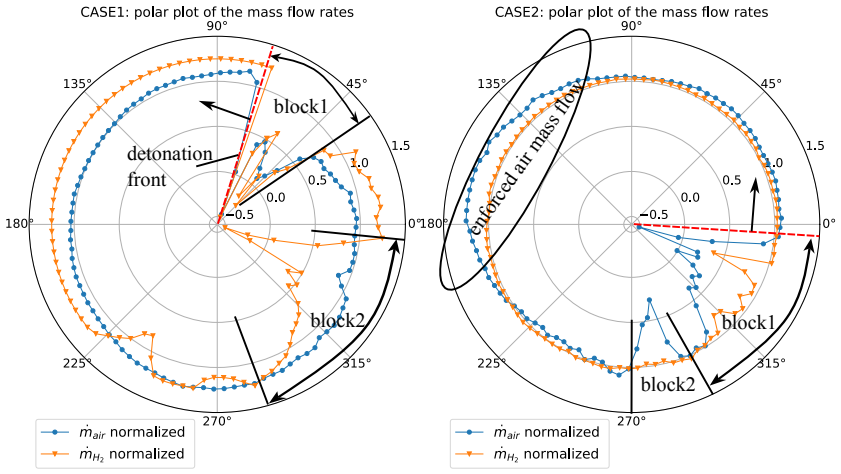

(a) **(b)**

Figure 9.14: Polar plot of CASE1 (a) and CASE2 (b). The curves show the mass flow rates through the air gap and the H_2 injectors normalized by the nominal mass flow through the injectors. The detonation propagates counter clock-wise direction and is denoted by a red dashed line in each graph.

choked H_2 injectors due to a low speed of sound. This behaviour reoccurs in block2 for CASE1, due to a reflected shock, however the mass flow through the air slot stays quasi unchanged. In terms of fresh gas mixing, one can see that the blockage of air mass flow is significantly higher than for H_2. It shows that during recovery of the air mass flow a significant amount of fuel is already injected into the chamber and hence does not mix with air, leading to the previously shown unmixed air pockets in Figures 9.5 f). A secondary air blockage in block2 results from a reflected shock, which again compromises the mixing of fresh gases due to a lack of air, especially since the H_2 injection stays unphased by the secondary shock. Figure 9.14 b) also highlights the reason for the stratification seen in Fig. 9.5 d): region 3) is in fact a consequence of block1 and block2 in CASE2, since fuel does not mix with air. 2) is a result of the temporarily reinforced air mass flow after blockage and finally 1) results from the restabilized injection of fresh gases into the chamber.

9.5 Efficiencies

The analysis of the overall efficiencies of the RDE chamber is conducted in 2 steps:

- Overall combustion: the efficiency E (Eq. (7.9)) is examined to see how much fuel burnt in the chamber.
- Detonation: the detonation index I_{det} (Eq. (7.3)) is introduced to distinguish the occurring reaction regimes and to obtain the detonation efficiency E_{det} (Eq. 7.8). This parameter identifies which percentage of the fuel source terms occurs in a detonation.

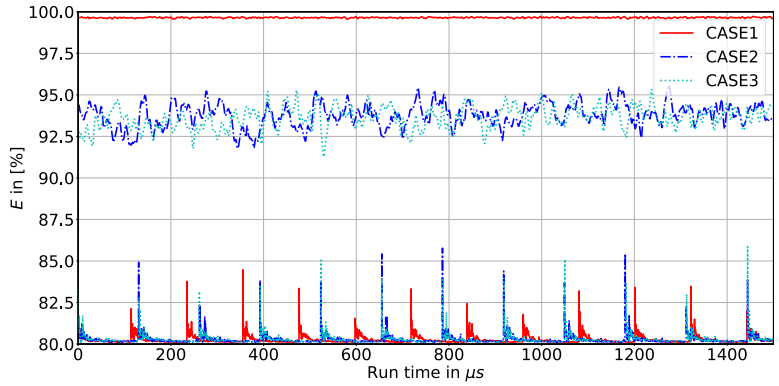

Figure 9.15: Top: Combustion efficiency of CASE1, CASE2 and CASE3 for 11 consecutive cycles. Bottom: probe pressure signals of the runs.

Combustion efficiencies are presented in Fig. 9.15. The combustion efficiency of CASE1 is the highest with over 99%. Due to premixing, the fresh gases can burn almost ideally, only being influenced by local dilution via H_2O. The combustion efficiency is also quite constant over time, which indicates a steady detonation propagation and fuel consumption. CASE2 and CASE3 display lower efficiencies at 93%, showing that the combustion efficiency is heavily influenced by the mixing regime, as expected from the previous section. This deficit in combustion efficiency for CASE2 and CASE3 is coherent with the tail of leftover fuel observed in Fig. 9.5 (d).

The detonation efficiency measured by E_{det} (Fig. 9.16) allows a similar conclusion: premixing in CASE1 results in more fuel effectively detonating.

80% of the consumed fuel is burnt in a detonation. On the other hand a considerable loss in detonation efficiency is observed with the non-premixed cases CASE2 and CASE3 (65% of the consumed fuel in average), due to mixing losses.

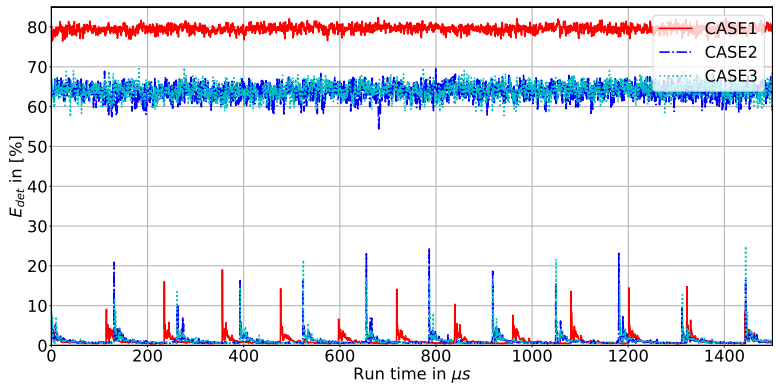

Figure 9.16: Top: Detonation efficiency of the three investigated runs for 11 consecutive cycles. Bottom: probe pressure signals.

9.6 Conclusion on mixing assumptions and SGS influence

This chapter identifies two main mechanisms for the efficiency of the combustor: first, imperfect mixing results in worse conditions for detonating the mixture and a consequential decrease in D. Secondly, dilution with product gases of the previous cycles compromises an optimal operation of the RDE. In the LES, mixing is dominated by the imposed by the SGS model, since it is at least an order of magnitude higher than the corresponding μ_{lam}. A change of the SGS from WALE to SIGMA has results in the same D, which makes the choice of the SGS less important as long as the SGS model is chosen accurately. Premixing increases the amount of fuel consumed in a detonation regime and combustion efficiency E increases significantly increases, as well as D. The chapter shows that the detonation speed is linked to the mixing performance of the injection configuration and E_{det} is directly linked to D.

9.7 Excursus: Influence of the numerical scheme on mixing

The previous studies have elaborated on physical sub models and their influence on the detonation speed D, the flow field, mixing and efficiency. For all cases the scheme of Lax and Wendroff (1960) (LW) has been used so far. On the other hand AVBP offers higher order Taylor-Galerkin based schemes such as the TTG4A and TTGC, which perform better when dealing with high gradients and are considerably less diffusive than LW. To understand the influence of the numerical scheme, the differences of LW and the TTG4A scheme are investigated in the following. Note that the switch to TTG4A results in a reduction of the discharge of the H_2 injectors resulting in an increase of the H_2 plenums to $16.4bar$.

RUN NAME	MIXING CONFIGURATION	NUMERICAL SCHEME	SGS MODEL	WALL TREATMENT	$\delta_{1/2,target}$ in μm	$z_{nom} = \frac{\dot{m}_{H_2}}{\dot{m}_{H_2}+\dot{m}_{O_2}}$ in [-]
CASE1	**PREMIXED**	LW	WALE	ADIAB. SLIP-WALL	149.6	0.0258
CASE2	NON-PREMIXED	LW	WALE	ADIAB. SLIP-WALL	149.6	0.0258
CASE3	NON-PREMIXED	LW	**SIGMA**	ADIAB. SLIP-WALL	149.6	0.0258
CASE4	NON-PREMIXED	LW	WALE	**ADIAB. LAW-OF-THE-WALL**	149.6	0.0258
CASE5	NON-PREMIXED	LW	WALE	ADIAB. SLIP-WALL	**180.0**	0.0258
CASE6	NON-PREMIXED	LW	WALE	ADIAB. SLIP-WALL	**206.0**	0.0258
CASE7	NON-PREMIXED	**TTG4A**	WALE	ADIAB. SLIP-WALL	149.6	0.0258

Table 9.3: Summary of LES runs

9.7.1 Wave speed

The recorded pressure signals in Fig. 9.17 reveal the detonation wave speed decreases considerably when applying TTG4A instead of LW. The resulting rotation frequencies and D are tabulated in Tab. 9.4. This is a first hint to the influence of the numerical scheme: a low order numerical scheme, such as LW results in s faster detonation speed while the higher order scheme TTG4A leads to a decrease of the wave speed. This can have different reasons: first, the numerical scheme can potentially modify the mixing process. The higher diffusivity of LW could augment the mixing quality in a significant manner, whereas TTG4A performs worse in terms of mixing. Second, the prediction of triple point pressures could be altered, potentially due to LW's over-prediction of triple point pressures, which could lead to higher local overdrives than predicted by TTG4A. In the following the effects of the numerical scheme on the mixing field is investigated.

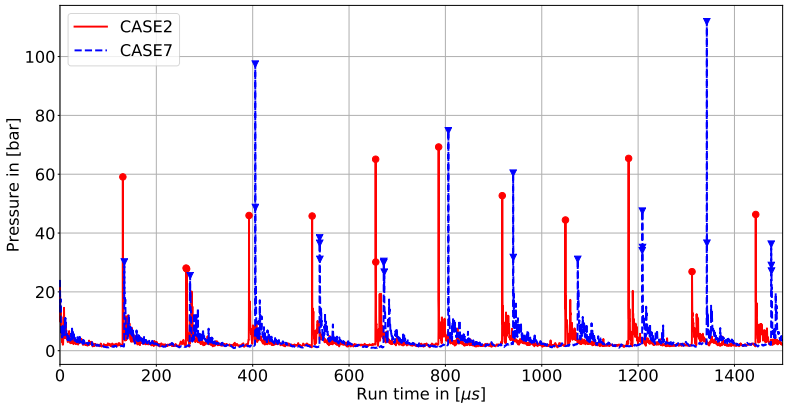

Figure 9.17: Mid-span pressure signals at $y = 25\ mm$. The signals are recorded after a steady detonation propagation has been achieved and are sampled at a frequency of $3.8 MHz$.

	CASE2	CASE7	EXPERIMENT
Wave mode [-]	single	single	single
Rotation Frequency $[Hz]$	7630	7440	5800
Detonation wave speed $[m/s]$	2157	2103	1640
D/D_{cj} [-]	1.12	1.09	0.85

Table 9.4: Comparison of the different predicted detonation frequencies with respect to the experimentally obtained wave speed. D_{cj}, based on the nominal $\phi = 0.9$, T_{init}, P_{init}, is 1925 m/s.

9.7.2 Effect of the numerical scheme on the flow field

This section compares the flow topology predicted by CASE2 and CASE7. The flow fields of the cases are investigated via the phase averages only, since the instantaneous fields do not contribute significantly to the analysis:

The main differences between CASE2 and CASE7 are shown by the field of Y_{H_2} (Fig. 9.18 d)), where the previously found pattern marked by numbers 1-3 reveals some differences between CASE2 and CASE7: 2), is a lean area resulting from the air injection after it has recovered from blockage, which is slightly richer in CASE7 than in CASE2. On the other hand, 3) a band of fuel close to the hot cases of the previous cycle is leaner in CASE7 than in CASE2. Another significant difference between CASE2 and CASE7 is the

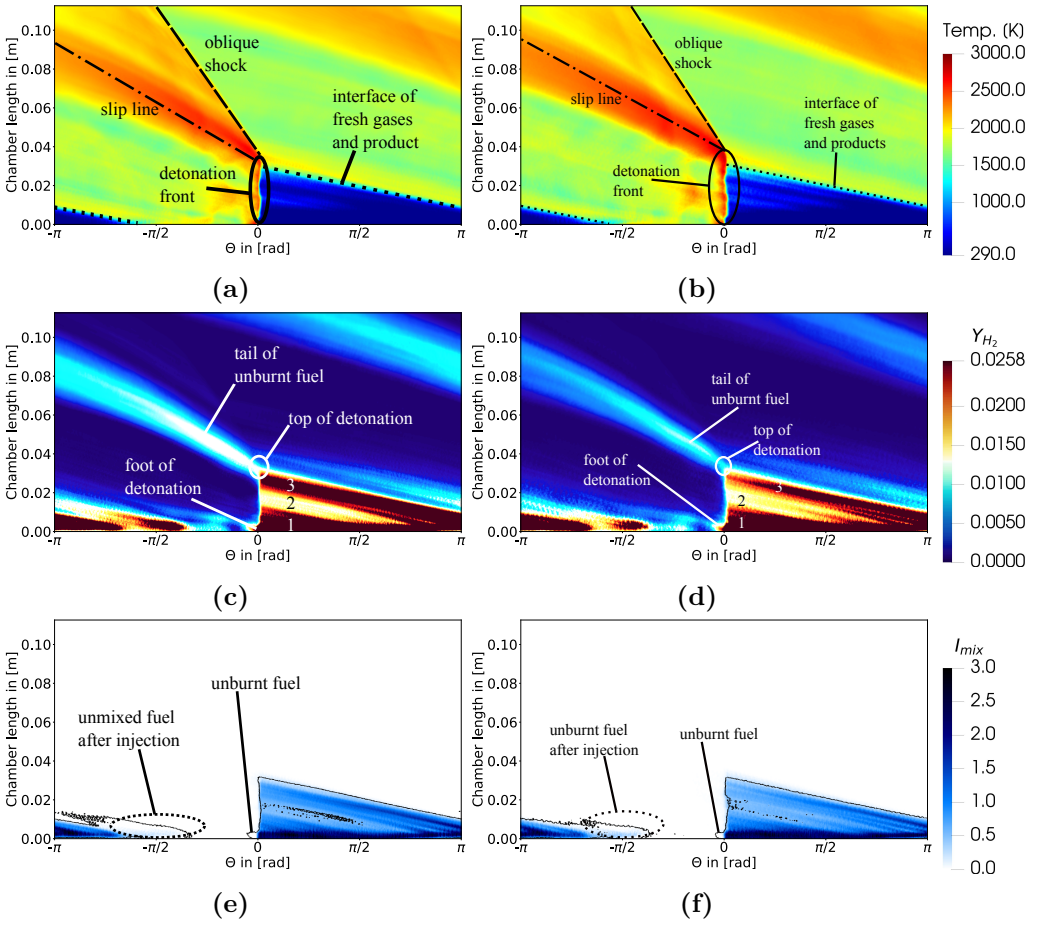

Figure 9.18: Instantaneous temperature field of CASE2 (a) /CASE7 (b) and instantaneous Y_{H_2} distribution of CASE1 (c) /CASE7 (d) and fields of I_{mix} for CASE1 (e) and CASE2 (f) along 33% span width of the annulus. The black iso contours denote an iso contour of $Y_{H_2} = Y_{H_2,sto}/2$, which delivers a good threshold for the visibility of H_2 pockets.

amount of fuel in the tail of unburnt fuel, where the latter contains a visibly lower amount of H_2, which results from the leaner region 3) in CASE7, pointing two potential impacts of the numerical scheme: first, an increase of the combustion efficiency in CASE7 compared to CASE2; and second, a higher degree of preburning in the contact surface of fresh gases and hot gases of the previous cycle with the consequent reduction in detonation efficiency. These two effects are confirmed in Fig. 9.22 and Fig. 9.23 respectively.

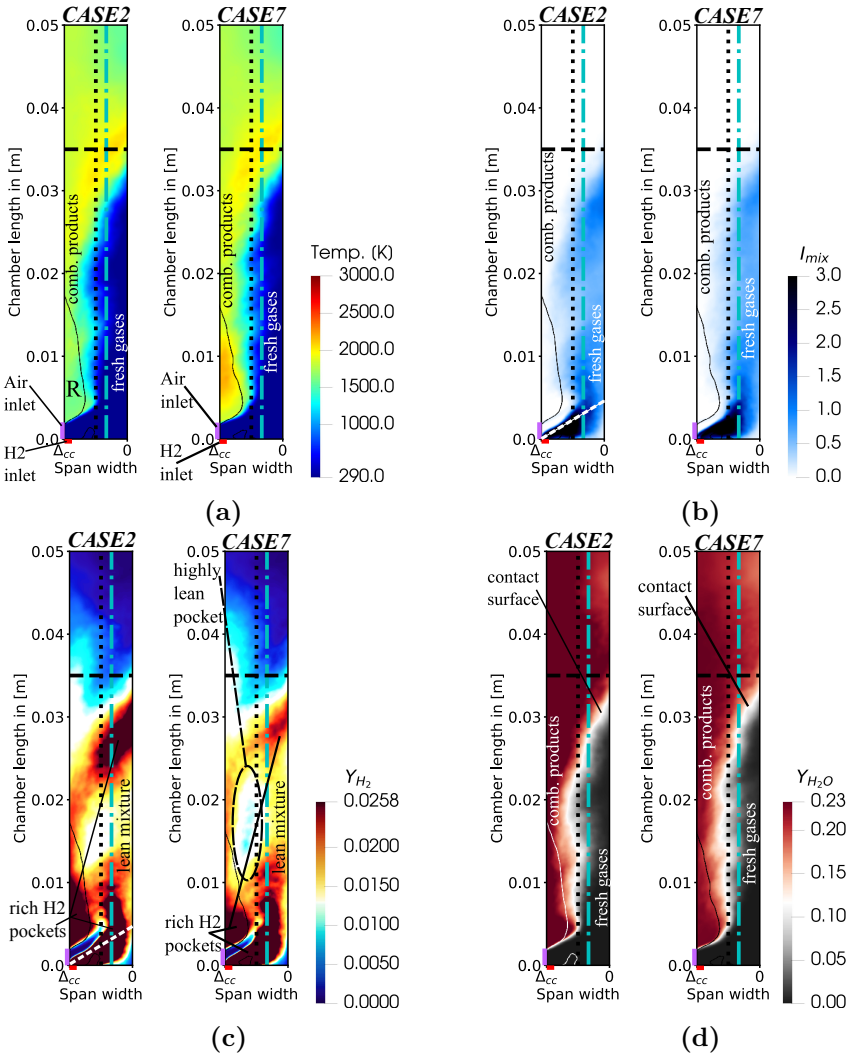

Figure 9.19: CASE7 - Phase locked averaged cuts in front of the detonation front comparing CASE2 and CASE7: the first pair shows the temperature fields (a), the second I_{mix} (b), the third H_2 (c) and the last the H_2O (d) fields. The dot-dashed line denotes the radial position of the previously displayed unwrapped cuts and the dotted line denotes 50% span width. A black (white in (d)) iso contour at $u = 0$ (axial downstream velocity) reveals a re-circulation zone R in front of the detonation. The colormaps are saturated as established. The x-axis goes from Δ_{cc}, the **outer wall** to 0, the **inner wall**.

The fields in Fig. 9.18 show that the change of the numerical scheme has slightly altered the mixing performance of the simulation. This is also confirmed in Fig. 9.19 and Fig. 9.20 where the averaged solution pre- and post- detonation passage show no significant impact of the numerical scheme on the flow structures. Finally, Fig. 9.21 shows that the PDF of the mixing index is also only mildly impact by the numerical scheme.

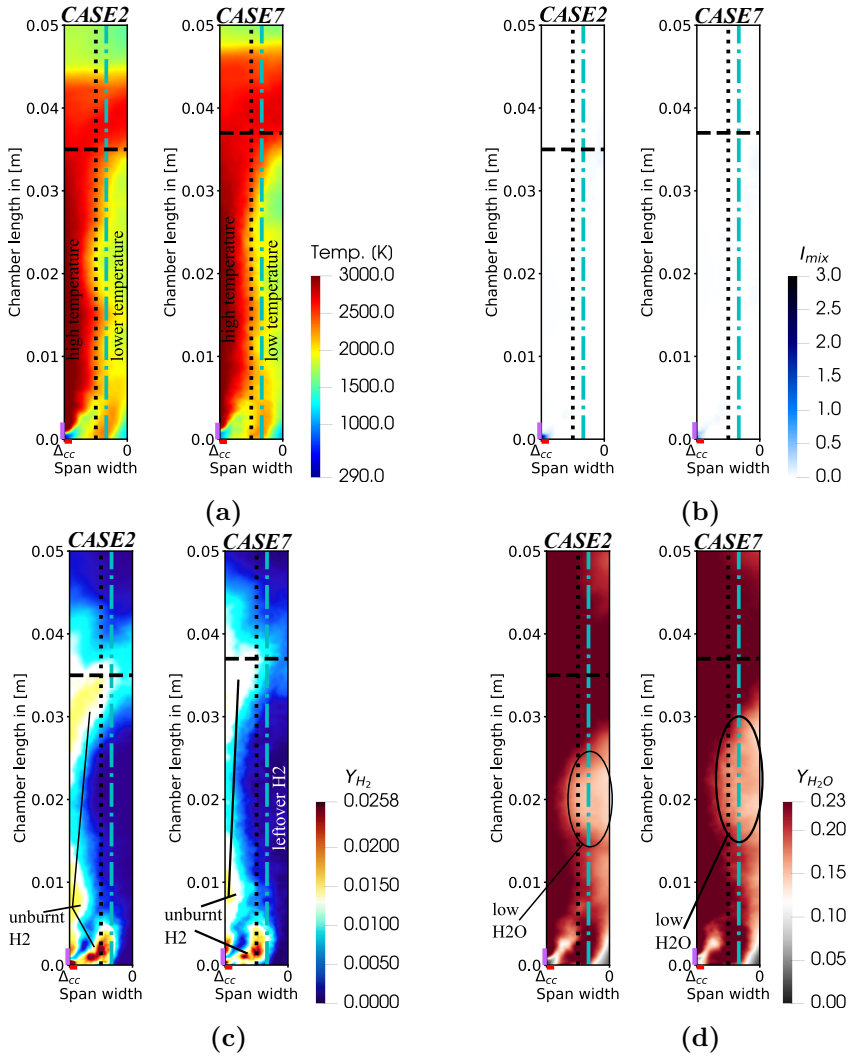

Figure 9.20: CASE7 - Phase locked averaged cuts after the detonation front comparing CASE2 and CASE7: the first pair shows the temperature fields (a), the second I_{mix} (b), the third H_2 (c) and the last the H_2O (d) fields.

After detonation passage the temperature field of CASE7 Fig. 9.20 (a) shows, just as all other cases before, a high temperature area in the outer half of the annulus, while the temperature in the inner half, previously filled with fresh gas mixture is significantly lower. In terms of consumed mixture one can see that the field of I_{mix} post detonation is plain white, showing that the fresh mixture has been consumed Fig. 9.20 (b). The same conclusion can be drawn by regarding the Y_{H_2} distribution of CASE7 in Fig. 9.20 (c).

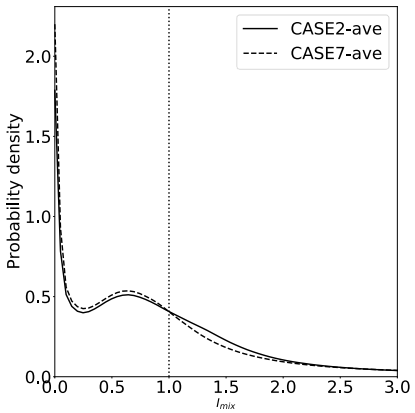

Figure 9.21: Instantaneous qualitative PDF of CASE2 and CASE7 for the fresh gases, declared at $T \leq 500K$. A vertical dotted line is positioned at $I_{mix} = 1$.

The probability density functions of CASE2 and CASE7, displayed in Fig. 9.21 only show slight deviations from each other.

The efficiencies represent the results seen in the previous sections: the efficiency E of CASE7 is slightly higher than the one of CASE2, while E_{det} is significantly lower, which is reflected in D. E_{det} of CASE7 is in average 8% lower than the one of CASE2. The application of the TTG4A scheme results in a direct decrease of fuel burnt in a detonation regime.

The reason for the lower E_{det} can be connected to the mixing performance of the system, since Fig. 9.21 shows that the mixture in front of the detonation is leaner on average, thereby reducing the detonation speed and enhancing the contribution of parasitic combustion.

9.7.3 Conclusion on the influence of the numerical scheme

This chapter investigated the effect of the numerical scheme on the detonation propagation speed and the mixing process. For this purpose the LW

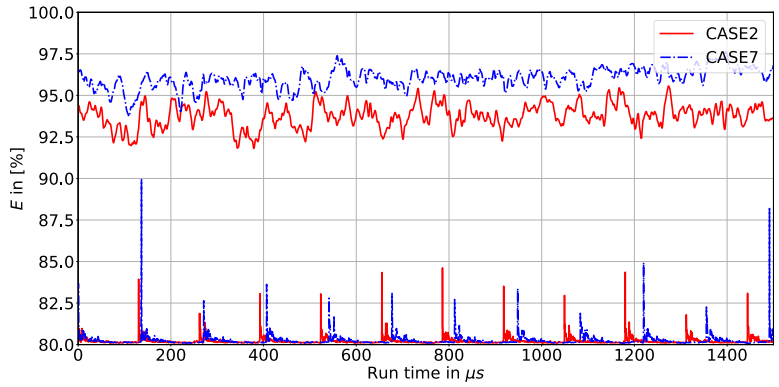

Figure 9.22: Top: Combustion efficiency of CASE2 and CASE7 for 11 consecutive cycles. Bottom: the figure, probe pressure signals of the runs.

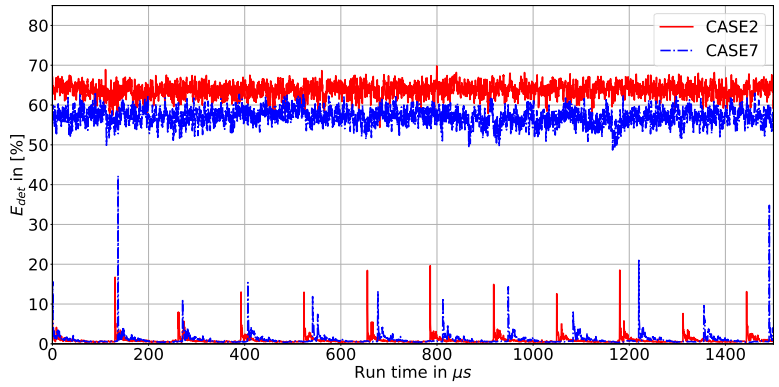

Figure 9.23: Top: Detonation efficiency of CASE2 and CASE7 for 11 consecutive cycles. Bottom: the figure, probe pressure signals of the runs.

and TTG4A schemes were compared. The resulting detonation frequency of CASE7 is $7440Hz$ which is lower than the reference of CASE2 with $7640Hz$. The comparison shows that TTG4A leads to a lower detonation speed due to a lower detonation efficiency and higher amount of pre-burning. Nevertheless Fig. 9.23 shows that the detonation wave propagates stably over the computed run time.

Chapter 10

Effects of wall models on LES of Rotating Detonation Engines

Contents

10.1 Introduction

The wall treatment in RDE simulations is another difficult task. Many simulations apply adiabatic no-slip walls, although the necessary resolution is not provided (see e.g. Batista et al. (2021); Prakash et al. (2021); Tsuboi et al. (2017); Vignat et al. (2024)) and cases actually trying to resolve the boundary layers are rare (e.g. Athmanathan et al. (2022)). Another option is so-called hybrid LES, where the wall near region is modeled by unsteady RANS modeling and the core flow of the annulus is modeled via LES modeling (Cocks et al. (2016)). The last applicable option are law of the wall models to approximate the effect of the viscous boundary layers at the wall (Nassini et al., 2023). Since the resolution at the walls is not highly refined in this work, the application of no-slip walls is neglected and a law-of-the-wall

approach is tested and its potential influences on the detonation speed and mixing field are investigated. The compared cases are CASE2 (slip-walls) and CASE4 (law of the wall).

RUN NAME	MIXING CONFIGURATION	NUMERICAL SCHEME	SGS MODEL	WALL TREATMENT	$\delta_{1/2,target}$ in μm	$z_{nom} = \frac{\dot{m}_{H_2}}{\dot{m}_{H_2}+\dot{m}_{O_2}}$ in [-]
CASE1	**PREMIXED**	LW	WALE	ADIAB. SLIP-WALL	149.6	0.0258
CASE2	NON-PREMIXED	LW	WALE	ADIAB. SLIP-WALL	149.6	0.0258
CASE3	NON-PREMIXED	LW	**SIGMA**	ADIAB. SLIP-WALL	149.6	0.0258
CASE4	NON-PREMIXED	LW	WALE	**ADIAB. LAW-OF-THE-WALL**	149.6	0.0258
CASE5	NON-PREMIXED	LW	WALE	ADIAB. SLIP-WALL	**180.0**	0.0258
CASE6	NON-PREMIXED	LW	WALE	ADIAB. SLIP-WALL	**206.0**	0.0258
CASE7	NON-PREMIXED	**TTG4A**	WALE	ADIAB. SLIP-WALL	149.6	0.0258

Table 10.1: Summary of LES runs

10.2 Wave speed

The pressure signals of CASE2 and CASE4 (see nomenclature of runs in Tab. 7.2) reveal in Fig. 10.1 that the application of a law of the wall results in a slight decrease in the detonation speed D. Here, D decreases from $2157 m/s$ (CASE2) to $2118 m/s$ (CASE4), corresponding to a 2% reduction in D (see Tab. 10.1). The slow decrease in detonation speed can have different

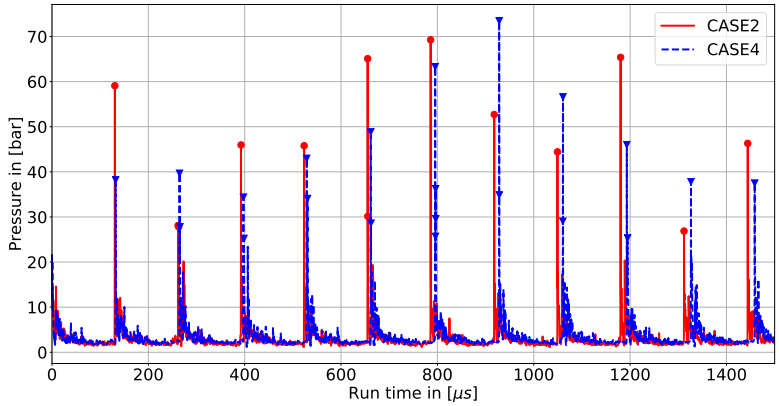

Figure 10.1: Mid-span pressure signals at $y = 25\ mm$. The signals are recorded after a steady detonation propagation has been achieved and are sampled at a frequency of $3.8 MHz$.

reasons: the analysis of the mixing approaches have shown that D is highly dependent on the mixture state in front of the detonation. The introduction of the law of the wall leads to changes in the flow field and potentially alters the mixing state in front of the detonation. These alterations could lead to a deterioration of the fresh gas mixing resulting in a decrease of D.

	CASE2	CASE4	EXPERIMENT
Wave mode [-]	single	single	single
Rotation Frequency $[Hz]$	7630	7490	5800
Detonation wave speed $[m/s]$	2157	2118	1640
D/D_{cj} [-]	1.12	1.1	0.85

Table 10.2: Comparison of the different predicted detonation frequencies of CASE2 and CASE4 with respect to the experimentally obtained wave speed. D_{cj} (=1925 m/s) is based on the nominal $\phi = 0.9$, T_{init} and P_{init}.

10.3 Effect of the law of the wall on the mixing field

First the flow fields of CASE2 and CASE4 are only investigated for phase averaged solutions, since the instantaneous fields do not deliver additional information. The focus is on CASE4, since the fields of CASE2 have been thoroughly studied in Chapter 9.

The evaluation of the phase-averaged fields reveals that the application of law of the wall leads to a deformation of the detonation at the bottom plate with a significantly curved detonation front close to the bottom wall. Note however, that the tail of unburnt fuel left behind the top of the detonation is significantly reduced compared to CASE2.

The comparison of Fig. 10.2 (c) and (d) reveals that the application of the law of the law does not drastically change the global features of the flow except for the additional band of unburnt fuel in CASE4, which originates from the bottom part of the detonation front and propagates upstream, a behavior which was not observed with the slip walls (CASE2). Also, the tail of unburnt fuel originating from the top of the detonation contains significantly less fuel compared to CASE2, which could suggest a higher combustion efficiency in CASE4 as will be highlighted in Sec. 10.4. The refill zone is structured as for CASE4 with a rich mixture at the bottom of the chamber

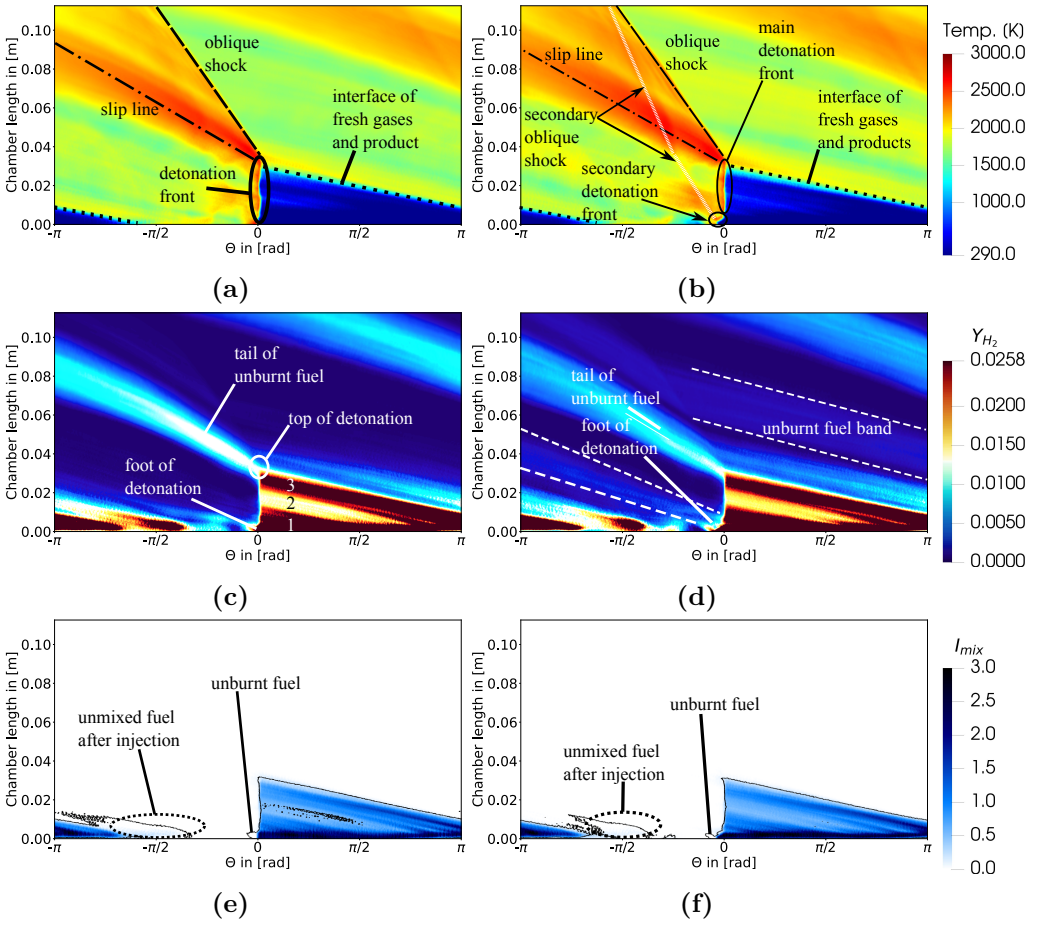

Figure 10.2: Phase averaged temperature field of CASE2 (a) /CASE4 (b) and phase averaged Y_{H_2} distribution of CASE2 (c) /CASE4 (d) and fields of I_{mix} for CASE2 (e) and CASE4 (f) along 33% span width of the annulus. The black iso contours denote an iso contour of $Y_{H_2} = Y_{H_2,sto}/2$, which delivers a good threshold for the visibility of H_2 pockets.

due to the presence of the fuel jets, then a lean area and a rich area again, which results in the unburnt fuel tail.

Figure 10.3 compares the phase-locked average flow fields obtained pre-detonation for CASE2 and CASE4. Two significant differences are worth mentionning: (1) the refill height with the law of the wall (CASE4) is lower than with the slip walls (CASE2); (2) Although the same features are found in the H2 distribution fields (Fig. 10.3 (c)), the H_2 stratification is more

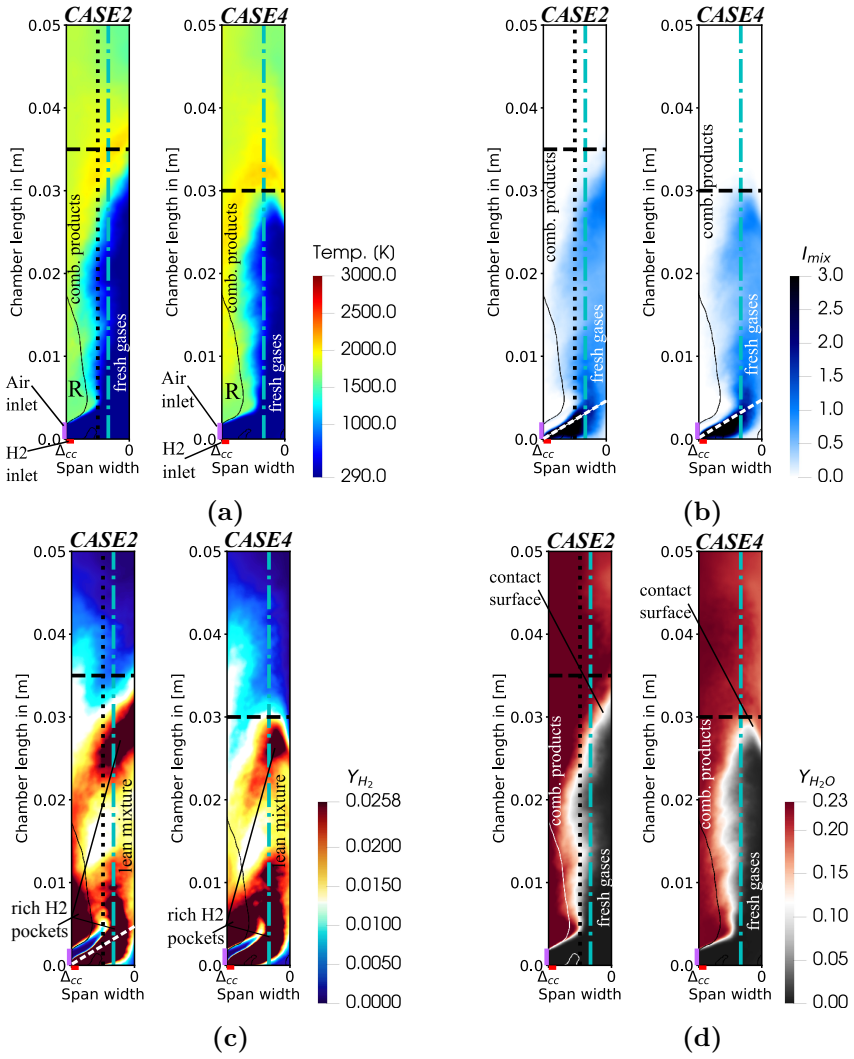

Figure 10.3: CASE4 - Phase locked averaged cuts **before the detonation front** comparing CASE2 and CASE4: the first pair shows the temperature fields (a), the second I_{mix} (b), the third H_2 (c) and the last the H_2O (d) fields. The dot-dashed line denotes the radial position of the previously displayed unwrapped cuts and the dotted line denotes 50% span width. A black (white in (d)) iso contour at $u = 0$ (axial downstream velocity) reveals a re-circulation zone R in front of the detonation. The colormaps are saturated as established. The x-axis goes from Δ_{cc}, the **outer wall** to 0, the **inner wall**.

pronounced in CASE4 with the H_2 rich pockets are visibly larger than their CASE2 counterpart.

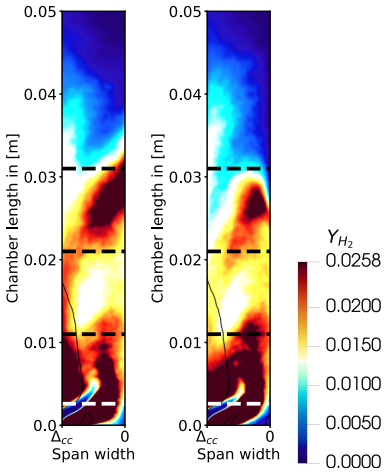

(a) CASE2 **(b)** CASE4

Figure 10.4: Phase locked averaged cuts in front of the detonation front H_2 marking the locus of the cuts presented in Fig. 10.5: From bottom to top: $2.6mm$, $11.0mm$, $21.0mm$ and $31.0mm$.

A more quantitative comparaison between CASE2 and CASE4 in terms of pre-detonation phase locked average fields is offered in Fig. 10.5 where the axial velocity u, mixing index I_{mix} and Y_{H_2} distribution are plotted for different heights. This allows to follow the development of the temporal averaged velocity, mixing and dilution behavior. The comparison of CASE1 and CASE2 has already shown that the detonation speed is linked to the mixture quality, hence it is mandatory to check if the mixing quality is deprecated by the application of the new boundary condition of CASE4. The main takeaway of Fig. 10.5 is that the application of a law of the wall does impact the flow close to the walls but this impact is quite minor and does not lead to significant changes in the bulk of the flow inside the RDE, with a slight increase in the axial velocity in the bulk flow and a higher dilution compared to CASE2. This explains the negligible impact of the law of the wall on the detonation speed.

Once the detonation has passed, Fig. 10.6 shows that the main differences between CASE4 and CASE2 is regarding the unburnt H_2 left behind the detonation front. More unburnt H_2 can be found close to the bottom wall

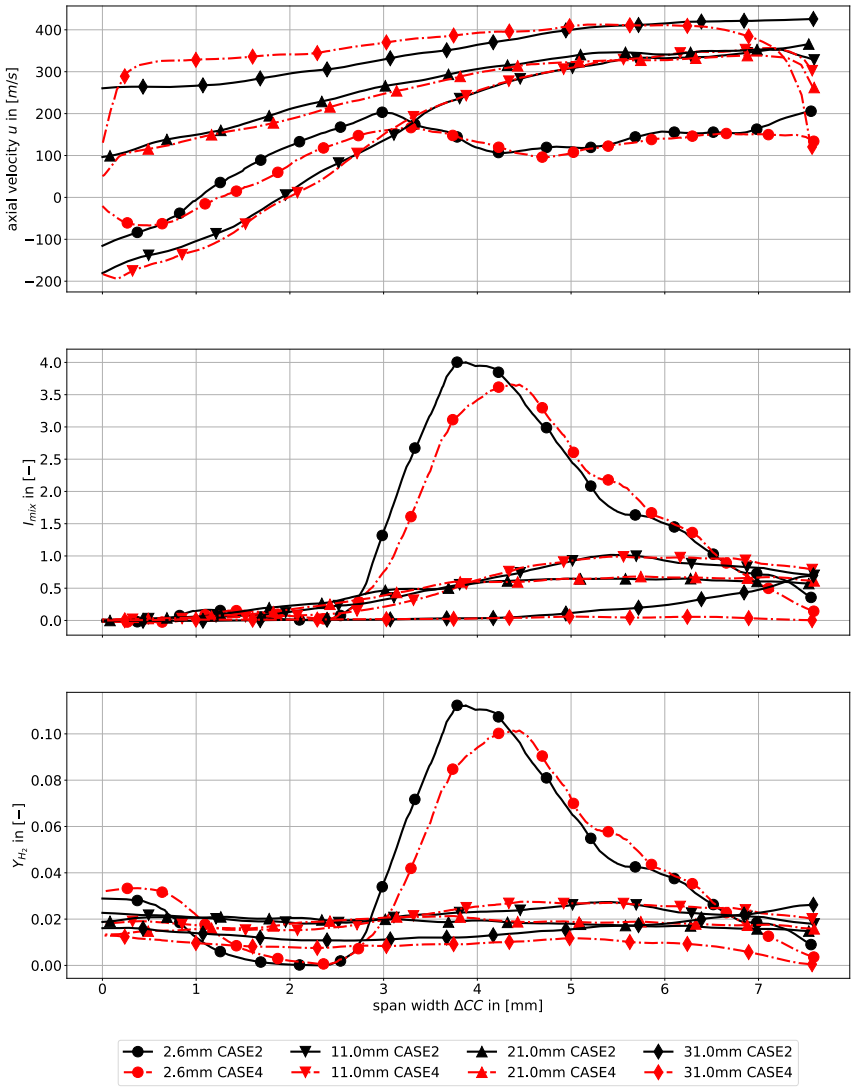

Figure 10.5: Radial distribution of u (top), I_{mix} (middle) and Y_{H_2O} (bottom) for different heights on the phase averaged pre detonation plane.

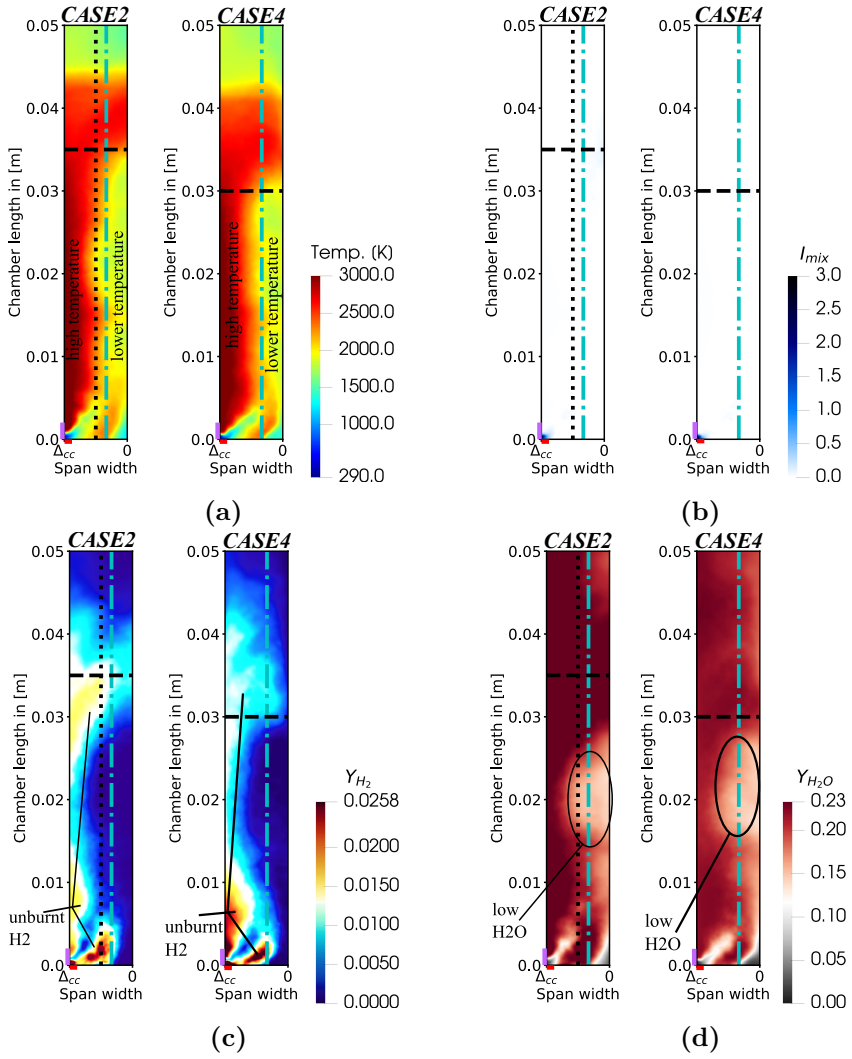

Figure 10.6: CASE4 - Phase locked averaged cuts **after the detonation front** comparing CASE2 and CASE4: the first pair shows the temperature fields (a), the second I_{mix} (b), the third H_2 (c) and the last the H_2O (d) fields. The dot-dashed line denotes the radial position of the previously displayed unwrapped cuts and the dotted line denotes 50% span width. A black (white in (d)) iso contour at $u = 0$ (axial downstream velocity) reveals a re-circulation zone R in front of the detonation. The colormaps are saturated as established. The x-axis goes from Δ_{cc}, the **outer wall** to 0, the **inner wall**.

for CASE4 but the tail of unburnt fuel at the top of the detonation is more pronounced in CASE2. This observation is in accordance with Fig. 11.2 (c-d). As seen before for CASE2, a significant amount of H_2 is not consumed by the detonation, located in the previously rich areas (Fig. 10.6 (c)). The H_2 fields reveal that the detonation processes mainly a lean mixture, emphasized by the lower Y_{H_2O} areas in Fig. 10.3 (d).

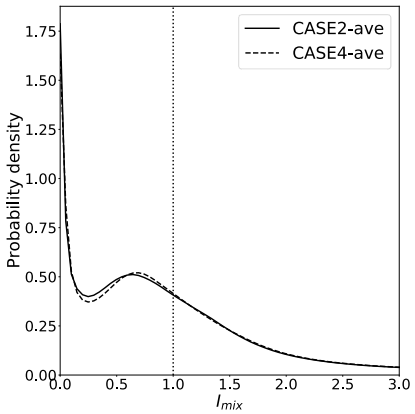

Figure 10.7: Averaged qualitative PDF of CASE2 and CASE4 for the fresh gases, declared at $T \leq 500K$. A vertical dotted line is positioned at $I_{mix} = 1$.

The final comparison between two cases is displayed in Fig. 10.7 in terms of average PDF of I_{mix} in the fresh gases. Again, the application of the law of the wall does not impact mixing in a significant manner.

10.4 Efficiencies

The combustion efficiency E is displayed in Fig. 10.8, where both curves show a relative constant behavior. CASE4 has an overall slightly higher combustion efficiency than CASE2, with a mean value of around $E \sim 96\%$ compared to $E \sim 93\%$ for CASE2. This is in agreement with Fig. 10.2 (c) and (d) where the tail of unburnt fuel left behind the detonation is evidently less pronounced in CASE4. Fig. 10.9 shows that the detonation efficiency is slighly lower for CASE4, again confirming the result of Fig. 10.2 where leftover fuel can be found close to the bottom of the chamber, unburnt by the detonation and lost to deflagrative combustion. All in all, the application of the law of the wall, does not lead to a drastic change in the flow structures

but impact the detonation propagation close to the bottom wall, leading to reduced detonation efficiency but increases combustion efficiency with the leftover fuel, unprocessed by the detonation, hence lost to deflagrative combustion. This is in accordance with the reduced detonation speed observed for CASE4.

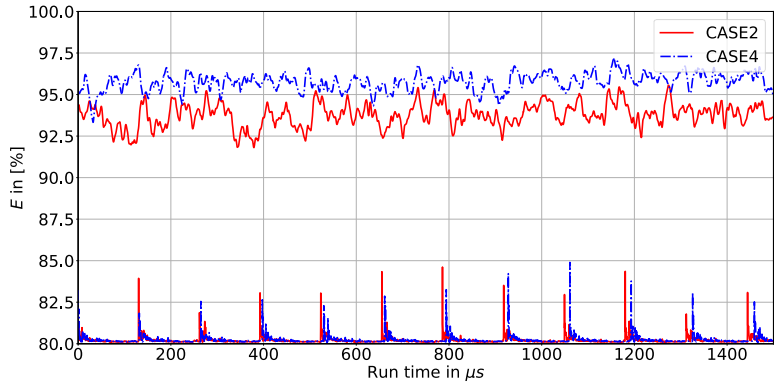

Figure 10.8: Top: Combustion efficiency of CASE2 and CASE4 for 11 consecutive cycles. Bottom: probe pressure signals of the runs.

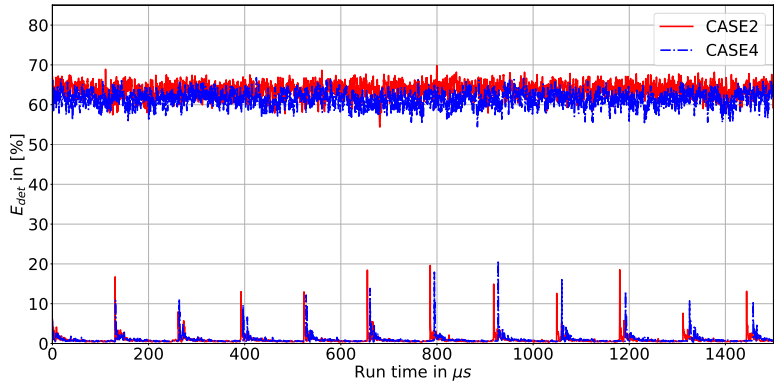

Figure 10.9: Top: Detonation efficiency of CASE2 and CASE4 for 11 consecutive cycles. Bottom: probe pressure signals of the runs.

10.5 Conclusion

In this chapter the effect of wall treatments in the LES in the annular combustor has been investigated. Two cases are compared: the reference CASE2 using slip walls and CASE4 where a law of the wall was applied. Both cases exhibit one detonation wave at slightly different detonation speed D, where $D_{CASE4} \sim 0.98 D_{CASE2}$. The application of the wall laws in CASE4 has slightly changed the flow field leading to higher axial velocity in the bulk flow and a higher dilution compared to CASE2. The impact on the overall performance of the RDE and its flow structures is however marginal.

Chapter 11

Effect of target $\delta_{1/2}$ on LES of Rotating Detonation Engines

Contents

11.1 Introduction

In fundamental detonation research chemical kinetics play an important role, since it typically dictates the mesh resolution and the scales of multidimensional detonation instabilities. In terms of 3D simulations of RDEs various chemical schemes are mentioned and typically the $CJ-$speed D_{CJ} is taken as a validation variable for their performance. This is however a bad practice, since D_{CJ} is dominated by the thermodynamic conditions of the fresh gases and not the chemical kinetics. The influence of a characteristic length scale such as $\delta_{1/2}$ is not explicitly mentioned and some authors actively discard

the role of the intrinsic detonation structure (Cocks et al., 2016). On the other hand very few simulations mention $\delta_{1/2}$ in their work e.g. Nassini et al. (2023).

Given the simple chemical scheme used in this thesis and its dependence on a target value for $\delta_{1/2,target}$, it is crucial to quantify the effect that the choice for this target chemical parameter has on the performance of RDEs. For this purpose, a second and third chemical scheme called 1S-Deto-II and 1S-Deto-III are introduced. The new schemes are derived from 1S-Deto with a new target $\delta_{1/2,target,II} = 180\mu m$ and $\delta_{1/2,target,III} = 206\mu m$, which are between the UCSD and Mevel respective output for $\delta_{1/2,target}$. 1S-Deto-II and 1S-Deto-III are obtained by re-scaling the pre-exponential factor A for $\delta_{1/2}$ and a re-scaling of Pr, so that s_L is conserved. Here two new cases, CASE5 and CASE6, are run under the same setup as CASE2 except the chemical schemes. A comparison of the changed parameters of the chemical schemes is displayed in Tab. 11.1. In the following CASE2 and CASE5 are compared in terms of D, mixing, efficiencies and potential multidimensional structures.

	1S-Deto	1S-Deto-II	1S-Deto-III
Preexp. factor A $\times 10^{10}$ $[1/(\sqrt{mol.m^{-3}}s)]$	0.53	0.47	0.392
Pr	0.32	0.28	0.26

Table 11.1: Comparison of the changes between 1S-Deto, 1S-Deto-II and 1S-Deto-III

RUN NAME	MIXING CONFIGURATION	NUMERICAL SCHEME	SGS MODEL	WALL TREATMENT	$\delta_{1/2,target}$ in μm	$z_{nom} = \frac{\dot{m}_{H_2}}{\dot{m}_{H_2}+\dot{m}_{O_2}}$ in [-]
CASE1	**PREMIXED**	LW	WALE	ADIAB. SLIP-WALL	149.6	0.0258
CASE2	NON-PREMIXED	LW	WALE	ADIAB. SLIP-WALL	149.6	0.0258
CASE3	NON-PREMIXED	LW	**SIGMA**	ADIAB. SLIP-WALL	149.6	0.0258
CASE4	NON-PREMIXED	LW	WALE	**ADIAB. LAW-OF-THE-WALL**	149.6	0.0258
CASE5	NON-PREMIXED	LW	WALE	ADIAB. SLIP-WALL	**180.0**	0.0258
CASE6	NON-PREMIXED	LW	WALE	ADIAB. SLIP-WALL	**206.0**	0.0258
CASE7	NON-PREMIXED	**TTG4A**	WALE	ADIAB. SLIP-WALL	149.6	0.0258

Table 11.2: Summary of LES runs

11.2 Wave speed

The pressure signals for CASE2, CASE5 and CASE6 are compared in Fig. 11.1. While the recorded pressure peaks occur at a lower frequency for

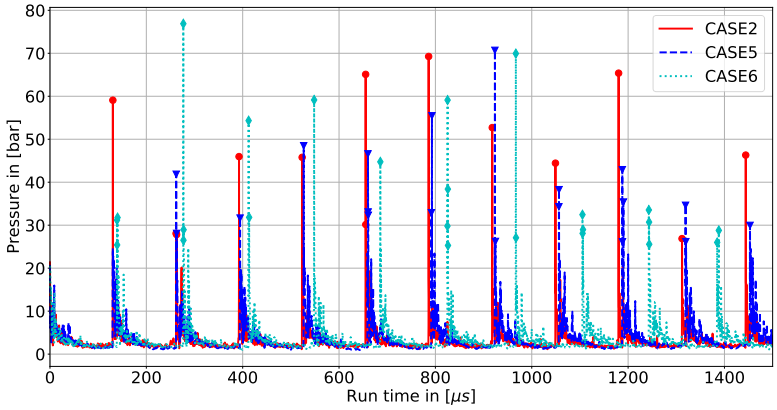

Figure 11.1: Mid-span pressure signals at $y = 25\ mm$. The signals are recorded after a steady detonation propagation has been achieved and are sampled at a frequency of $3.8 MHz$.

higher $\delta_{1/2,target}$, the Fig. 11.1 reveals a significantly slower detonation wave in CASE6 than CASE2 or CASE5. So far CASE6 displays the highest decrease of the detonation speed of the investigated cases. Note that attempt of further increasing $\delta_{1/2,target}$ ($= 250\mu m$ and $= 300\mu m$) lead to detonation quenching.

	CASE2	CASE5	CASE6	EXPERIMENT
Wave mode [-]	single	single	single	single
$\delta_{1/2,target}$ $[\mu m]$	150	180	206	?
Rotation Frequency $[Hz]$	7630	7575	7200	5800
Detonation wave speed $[m/s]$	2157	2141	2036	1640
D/D_{cj} [-]	1.12	1.11	1.06	0.85

Table 11.3: Comparison of the different predicted detonation frequencies with respect to the experimentally obtained wave speed. $D_{CJ} = 1925 m/s$ is based on the nominal $\phi = 0.9$, $T_{init} = 300K$ and $P_{init} = 1 bar$.

Figure 11.2 illustrates the behavior of the detonation speed (respective frequency) for increasing $\delta_{1/2,target}$. The slope indicates a non linear decrease of the detonation speed with $\delta_{1/2,target}$. Additionally, one can conclude from Fig. 11.1 and Fig. 11.2 that the chemical kinetics are a major factor in the performance of the simulations, and one cannot simply neglect it for the course of a numerical investigation of a real RDE configuration. This is

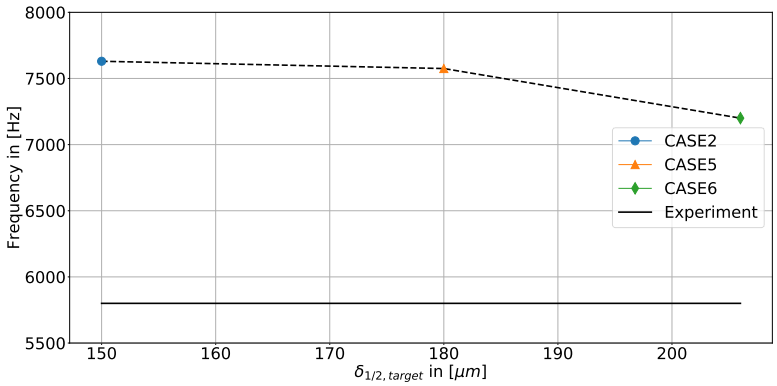

Figure 11.2: Detonation rotation frequency over $\delta_{1/2,target}$.

emphasized by the fact that no other additional (loss inducing) model is introduced in CASE5 and CASE6 with respect to CASE2. The next step is to find out how different $\delta_{1/2,target}$ alter the flow field features. This is investigated in the following section.

11.3 Effect of $\delta_{1/2}$ on the flow field

In this section the flow field structure of CASE2 and CASE6 are compared for an instantaneous and averaged field. Comparing only CASE2 and CASE6 is deemed sufficient for this part, since the mechanisms for the decrease in D can be assumed to be the same for CASE5 and CASE6.

Figure 11.3 compares the flow fields of CASE2 and CASE6. Overall, both cases show similar features except for two main differences worth highlighting: (1) in Fig. 11.3 (b), the detonation front of CASE6 exhibits signs of high instability with a markedly distorted front; (2) in Fig. 11.3 (f) pockets of unburnt mixed reactive material can be found, which also points to a possible unstable detonation front unable to process the reactive mixture efficiently.

The phase averaged fields in Fig. 11.4 emphasize the behavior observed in the instantaneous field: first, the detonation front exhibits a markedly weaker reactivity towards the bottom wall (Fig. 11.4 (b)) and seems more curved close to the bottom of the chamber (Fig. 11.4 (b,d,f)); second, Fig. 11.4 (d) reveals that although the refill triangle has the same three bands (1-3) observed so-far, the third band is leaner in H_2, a sign that fuel and air have more time to mix because of the reduced detonation speed in CASE6, which is

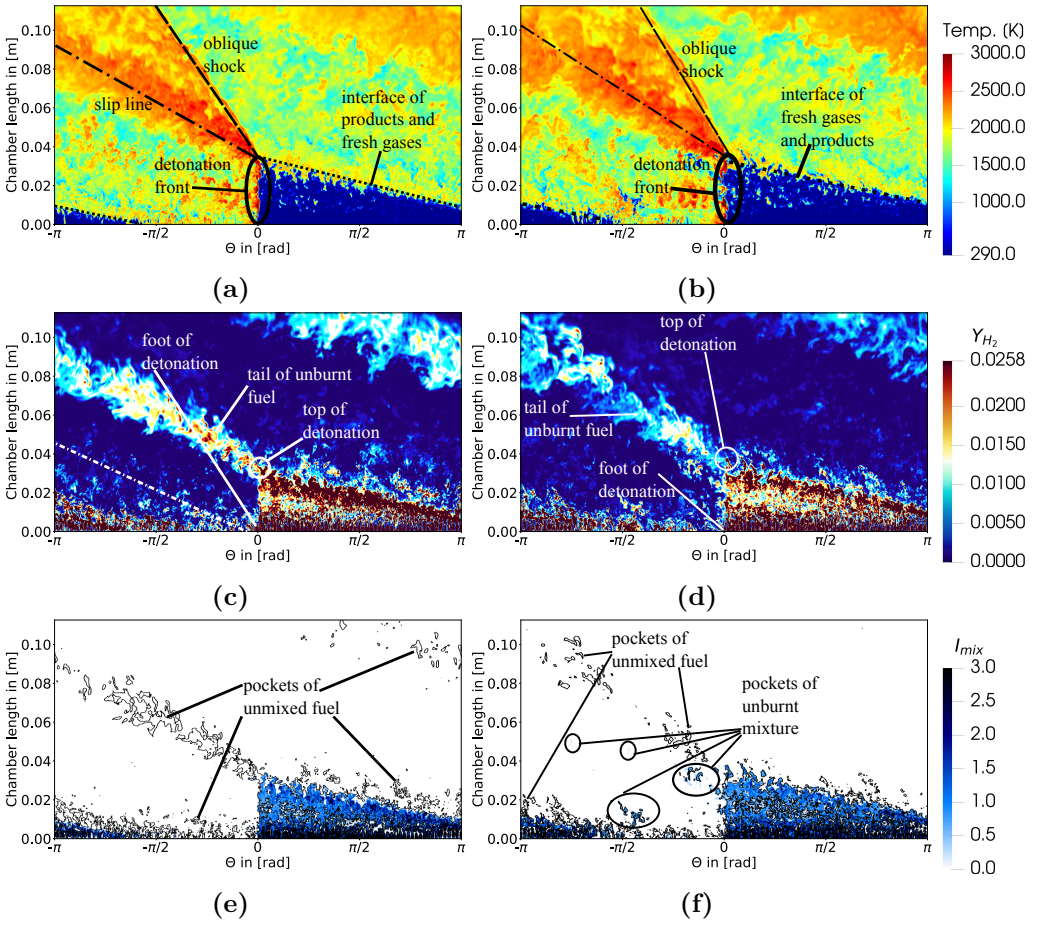

Figure 11.3: Instantaneous temperature field of CASE2 (a) /CASE2 (b) and instantaneous Y_{H_2} distribution of CASE1 (c) /CASE2 (d) and fields of I_{mix} for CASE1 (e) and CASE2 (f) along 33% span width of the annulus. The black iso contours denote an iso contour of $Y_{H_2} = Y_{H_2,sto}/2$, which delivers a good threshold for the visibility of H_2 pockets.

also confirmed by the I_{mix} fields in Fig. 11.4 (f), consequently the detonation can more efficiently burn the mixture at the top of the refill height (less fuel in the tail of unburnt fuel left behind the detonation) and third the I_{mix} field in Fig. 11.4 (f) also shows that a considerable amount of mixed reactive material is not processed by the bottom part of the detonation front and is lost to deflagrative combustion, which also confirms the unstable nature of the detonation front in CASE6.

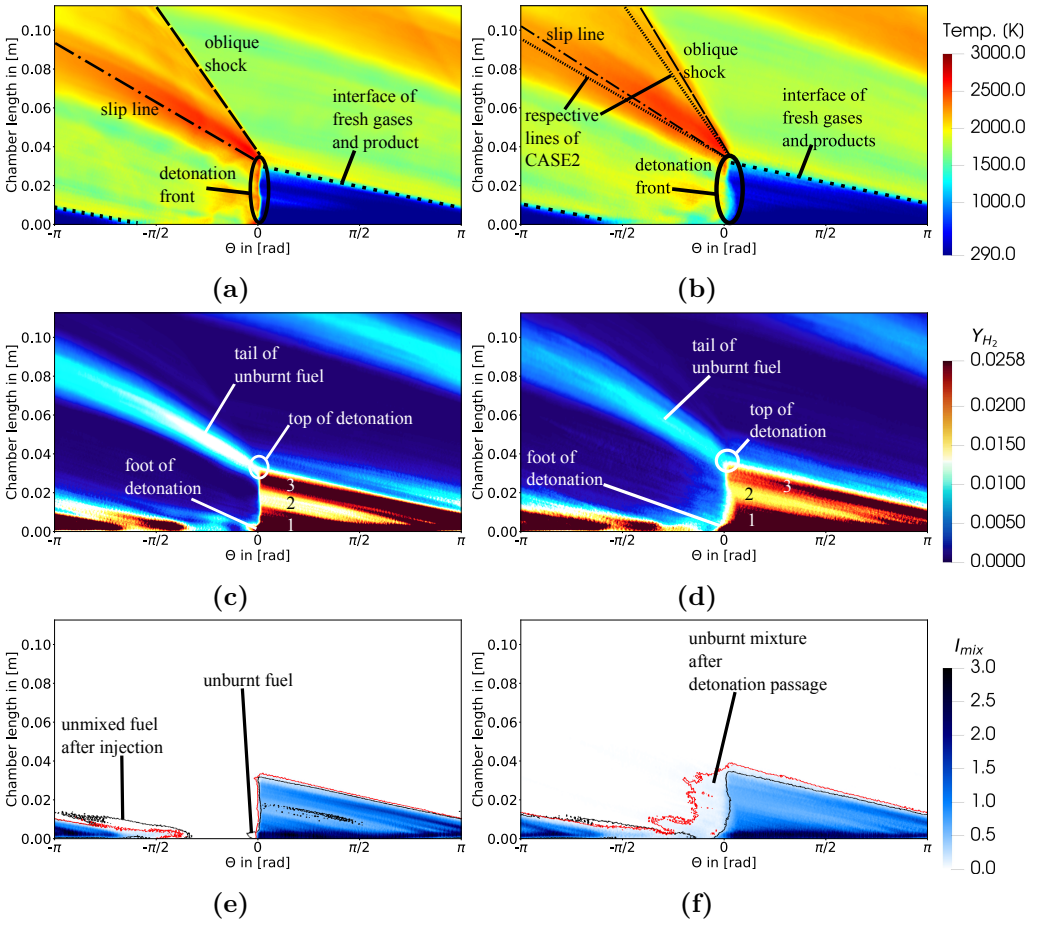

Figure 11.4: Instantaneous temperature field of CASE2 (a) /CASE2 (b) and instantaneous Y_{H_2} distribution of CASE1 (c) /CASE2 (d) and fields of I_{mix} for CASE1 (e) and CASE2 (f) along 33% span width of the annulus. The black iso contours denote an iso contour of $Y_{H_2} = Y_{H_2,sto}/2$, which delivers a good threshold for the visibility of H_2 pockets. An additional red iso contour denotes $I_{mix} = 0.1$ for highlighting the presence of unburnt mixed reactants.

The significantly lower detonation speed might impact the mixing performance of the injection system, hence the phase averaged cuts pre and post detonation for CASE6 are shown in Fig. 11.5 and Fig. 11.6 respectively. As in CASE2, the effective refill area in CASE6 is the inner span of the annular chamber, seen in Fig. 11.5 (a) and the highest point with fresh gases is at the inner wall of the chamber. The effective refill area however, is higher

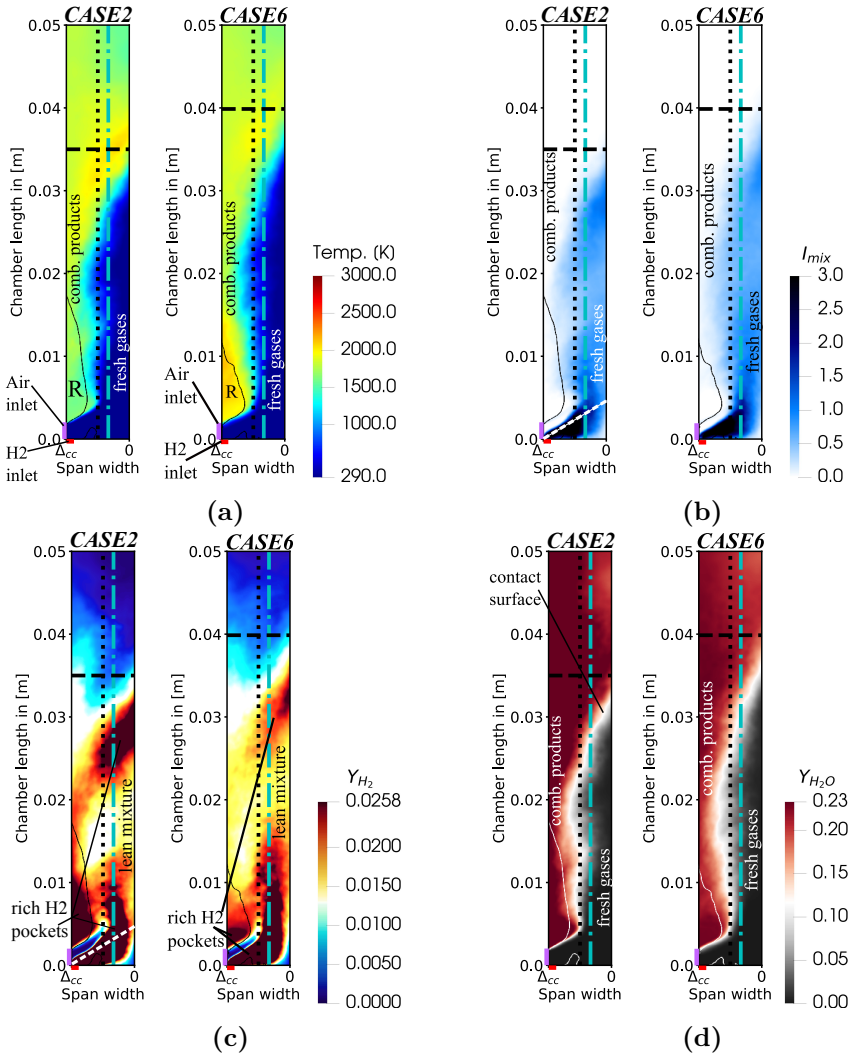

Figure 11.5: CASE6 - Phase locked averaged cuts **before the detonation front** comparing CASE2 and CASE6: the first pair shows the temperature fields (a), the second I_{mix} (b), the third H_2 (c) and the last the H_2O (d) fields. The dot-dashed line denotes the radial position of the previously displayed unwrapped cuts and the dotted line denotes 50% span width. A black (white in (d)) iso contour at $u = 0$ (axial downstream velocity) reveals a re-circulation zone R in front of the detonation. The colormaps are saturated as established. The x-axis goes from Δ_{cc}, the **outer wall** to 0, the **inner wall**.

than the one in CASE2 (Fig 11.5 (a)). This shows, that the lower detonation speed leads to an increase in the refill time frame, so that the fresh gases can penetrate the chamber further in axial direction in comparison to CASE2.

The I_{mix} field of CASE6 in Fig. 11.5 (b) shows minor differences compared to the one of CASE2. Regarding the Y_{H_2} field before detonation passage (Fig. 11.5 (c)), similar rich regions are still found at the top of the refill, in the recirculation zone and directly in the injection area (chamber length $< 10mm$). Due to the shorter recirculation zone in CASE6, less fuel is entrained in the region above the air injection gap and can therefore mix with air further downstream. Figure 11.5 c) also shows that the fuel rich region at the top of the refill height is still present in CASE 6 but is much smaller than in CASE2 and pushed towards the inner wall, explaining its disappearance in Fig. 11.4. The higher refill length of CASE6 also increases the contact surface of fresh and hot gases compared to CASE2 leading to an increase of parasitic combustion.

While the pre detonation planes show overall no exorbitant differences, the post detonation planes of CASE2 and CASE6 deviate strongly. The first big difference is the temperature deviation in Fig. 11.6 (a). The temperature in the inner half of the annulus after detonation passage is dominantly $\sim 1500K$. This is a significanly lower value than in CASE2, where the temperature in the inner half of the chamber is $\sim 2000K$. The lower temperature points to less consumed reactant mixture so that less heat is produced. This is curious since the the I_{mix} field of both cases pre detonation in Fig. 11.5 (b) show a relatively homogeneous mixture field. In CASE2, after detonation passage, the reactant mixture in the annulus is consumed without leaving significant leftovers. This is not true for CASE6. Here, one can find leftover $H_2 - Air$ mixture beginning at the bottom of the chamber and continuing downstream, roughly until the refill height is reached. This proves that the application of 1S-Deto-III results in a detonation front, that is incapable of processing all the reactants, even if they are properly mixed. This is further emphasized in Fig. 11.5 (c), where a significant amount of H_2 is found in the whole refill area of CASE6, including the inner wall. The fact that not all the reactants are burnt in CASE6 is additionally seen in Fig. 11.5 (d), where in the inner half of the chamber, for the whole refill height, low values of Y_{H_2O} occur. This means that other species, besides N_2 are in this area, which can only be H_2 and Air.

Theoretically speaking, a lower D results in a higher mixing time frame. For investigating the changes in the mixing quality between CASE2 and

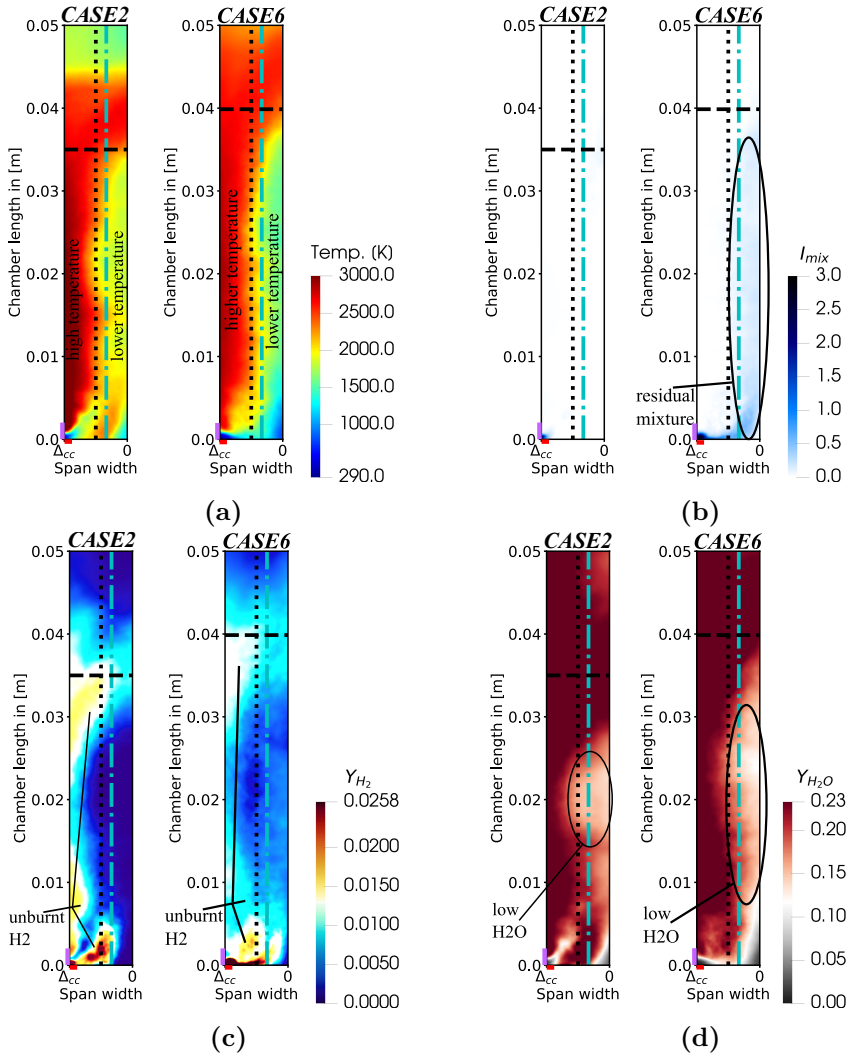

Figure 11.6: CASE6 - Phase locked averaged cuts **after the detonation front** comparing CASE2 and CASE6: the first pair shows the temperature fields (a), the second I_{mix} (b), the third H_2 (c) and the last the H_2O (d) fields. The dot-dashed line denotes the radial position of the previously displayed unwrapped cuts and the dotted line denotes 50% span width. A black (white in (d)) iso contour at $u = 0$ (axial downstream velocity) reveals a re-circulation zone R in front of the detonation. The colormaps are saturated as established. The x-axis goes from Δ_{cc}, the **outer wall** to 0, the **inner wall**.

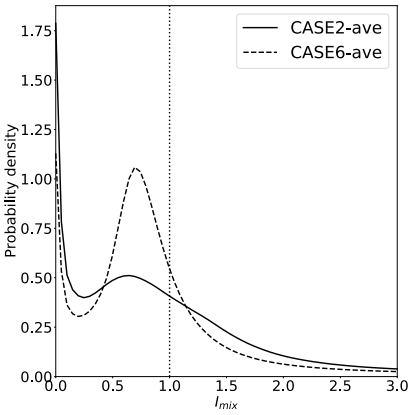

Figure 11.7: Instantaneous qualitative PDF of CASE2 and CASE6 for the fresh gases, declared at $T \leq 500K$. A vertical dotted line is positioned at $I_{mix} = 1$.

CASE6, the PDFs of their respective I_{mix} in the fresh gases ($T \leq 500K$) are investigated. They are shown in Fig. 11.7. Both curves share qualitatively the same behaviour: the PDF of CASE2 and CASE6 have a maximum for $I_{mix} = 0$ pointing to a significant amount of unmixed reactants. The second peak of both curves occurs at $I_{mix} \sim 0.65$, where the probability density of the CASE6 is considerably higher than for CASE2. It shows that the mixture state is in fact the best in CASE6 for all of the displayed cases. This is in apparent contradiction with the reduced detonation speed in CASE6. This supposedly contradiction is resolved by the results from Fig. 11.5(a)-(d) and Fig. 11.7. They prove, that a change in the chemical kinetics such as from 1S-Deto to 1S-Deto-III leads to a detonation wave partially incapable of processing mixed H_2 and Air, which could be processed by 1S-Deto and since 1S-Deto-III cannot convert all the reactants into products, the resulting detonation is slower than its counterpart computed with 1S-Deto. In other words the mixture quality can improve with a lower detonation wave, but the improved mixture is not properly consumed due to the chemical scheme.

11.4 Efficiencies

The combustion efficiencies of CASE2, CASE5 and CASE6 are compared in Fig. 11.8. The efficiencies display an overall similar course over time, and the mean all three cases show a similar E_{mean} of about 94%.

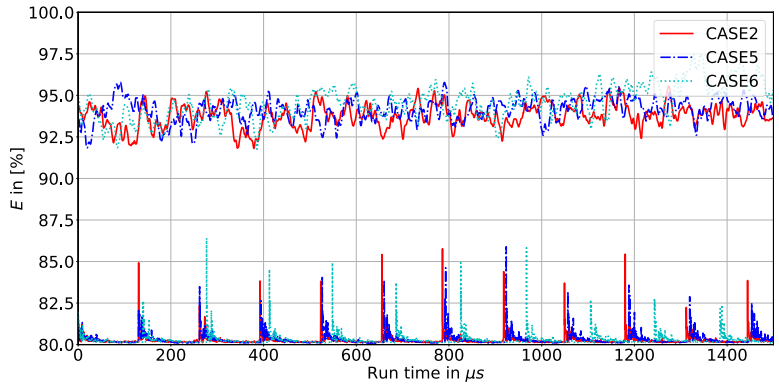

Figure 11.8: Top: Combustion efficiency of CASE2, CASE5 and CASE6 for 11 consecutive cycles. Bottom: probe pressure signals of the runs.

The detonation efficiencies E_{det} of CASE2, CASE5 and CASE6 (Fig. 11.9) shows high discrepancies over the measured run time. While CASE2 and CASE5 show only minimal differences and are qualitatively constant over the measured run time, CASE6 displays a highly irregular E_{det} ranging from $40\% - 65\%$. The variations of E_{det} in CASE6 allows to assume, that the detonation wave in CASE6 is propagating in an unstable manner, compared to CASE2 and CASE5.

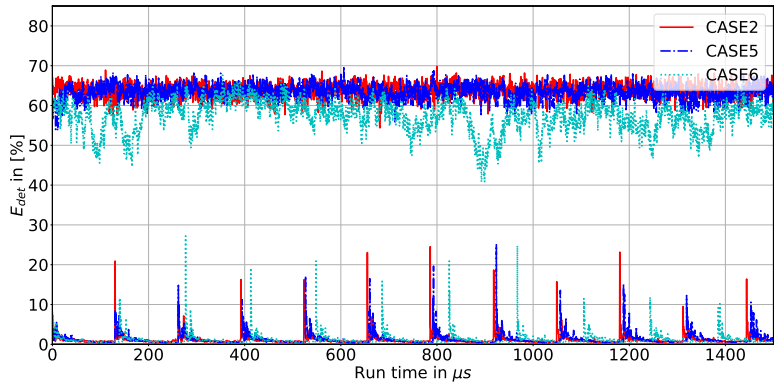

Figure 11.9: Top: Detonation efficiency of CASE2 and CASE5 for 11 consecutive cycles. Bottom: probe pressure signals of the runs.

Figure 11.9 shows that a stable detonation propagation and fuel consumption is linked to the chosen $\delta_{1/2,target}$, resulting in two major takeaways: the

first takeaway is that the detonation speed is marginally modified as long as $\delta_{1/2,target}$ is chosen in a way that allows a stable detonation propagation. The second takeaway is the dependence of the quenching behavior on $\delta_{1/2,target}$, since runs with a higher $\delta_{1/2,target}$, e.g. $\delta_{1/2,target} = 250\mu m$, did not sustain the detonation wave. In other words the performance of RDEs simulations is significantly impacted by the chemical scheme.

11.5 Investigation of the stability of the propagating waves due to $\delta_{1/2,target}$

The results of Fig. 11.9 imply that $\delta_{1/2,target}$ is essential for obtaining a stable detonation in an RDE, hence an analysis on the stability of the detonation wave is mandatory. A direct way to investigate the detonation propagation is to obtain a numerical soot foil at the inner wall and then increasing span widths. This approach allows to track the triple points which are the main mechanism in sustaining a detonation in the RDE. The investigated cases are CASE2 and CASE6, since Fig. 11.9 allows the assumption that CASE5 qualitatively behaves as CASE2. Figure 11.10 displays the numerical soot foil of CASE2 and CASE6. The soot foils show the end of the recorded pressure history at $\pi = 0$, the detonation proceeds to the right.

The soot foil of CASE2 displays a mean height of the detonation at $x = 0.035m$ from the bottom plate, which is in agreement with the refill height shown in Fig. 11.10. The soot foil can be divided into three sections: (a2), at the vicinity of the bottom wall, which shows the smallest cells and highest pressure in the soot foil. This section suffers from a deprivation of reactive material as the bottom wall is approached (see I_{mix} and Y_{H_2} curves) and the high pressure peaks can be attributed to reflected pressure waves leading to strong compression of the gases; (b2) is characterized by the presence of sufficient amount of reactive material to sustain a detonation (see I_{mix} and Y_{H_2} curves), however the detonation cell size is highly irregular as a result of the highly stratified mixture in front of the detonation; (c2) finally, after the second peak of I_{mix}, a contact surface between the reactive mixture and the burnt gases from the previous cycle rapidly marks the end of the cellular structure, since that the transverse waves dynamics can no longer be sustained by the inert layer on top of the refill height.

Compared to CASE2, two main differences in soot foil post processing

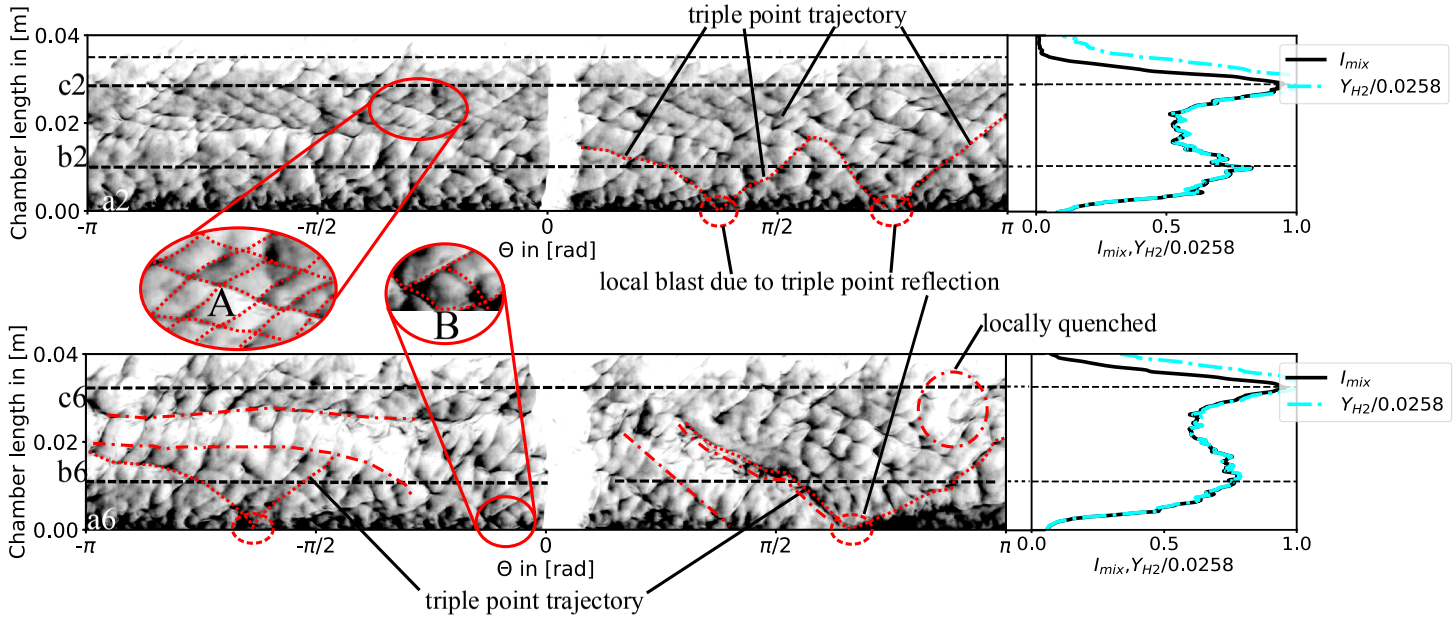

Figure 11.10: Numerically obtained soot foil of the inner wall and axial distribution of I_{mix} at the inner wall, top: CASE2, bottom: CASE6

can be highlighted : (1) the triple point trajectories reach a higher axial position for CASE6, in accordance with the higher fill height observed in CASE6 (see I_{mix} curves); (2) clear traces of local extinction are visible in section (b6) where the reactive mixture is sensibly of the similar quality as CASE6, again pointing towards the unstable mode of propagation exhibited by the detonation in CASE6.

Both soot foils display triple points propagating up- and downstream. The dotted red lines in both images point to examples, where triple points propagate upstream and are reflected at the bottom wall. This results in a local blast wave, which creates new triple points, that propagate downstream igniting the mixed reactants which are then consumed by a detonation. Additionally triple points originate at the top of the detonation. once reflected shock waves penetrate the reactive mixture and starts interacting with the detonation front.

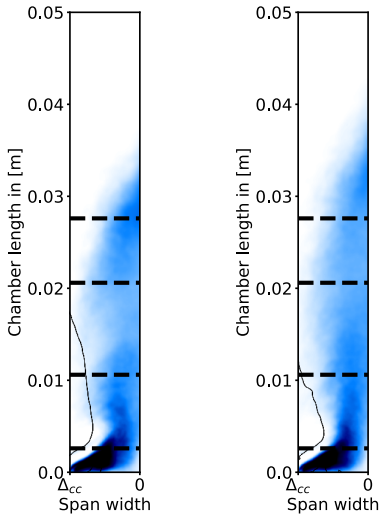

(a) CASE2 **(b)** CASE6

Figure 11.11: Axial position of the following displayed axial cuts from bottom to top: $0.0026m$, $0.0106m$, $0.0206m$, $0.0276m$ above the bottom plate.

With Fig. 11.10 the axial/azimuthal propagation behavior of the propagating detonations in CASE2 and CASE6 have been investigated. The second question is if, and how the detonation propagation occurs in radial direction. It has been established that the refill occurs effectively in the inner half of the annular chamber, which imposes an additional constraint on

the stability of the detonation. For this purpose 4 numerical soot foils at $x \epsilon 0.0026m$, $0.0106m$, $0.0206m$, $0.0276m$ (see Fig. 11.11) are investigated. This approach allows to obtain a characterization of the radial structure of the detonations.

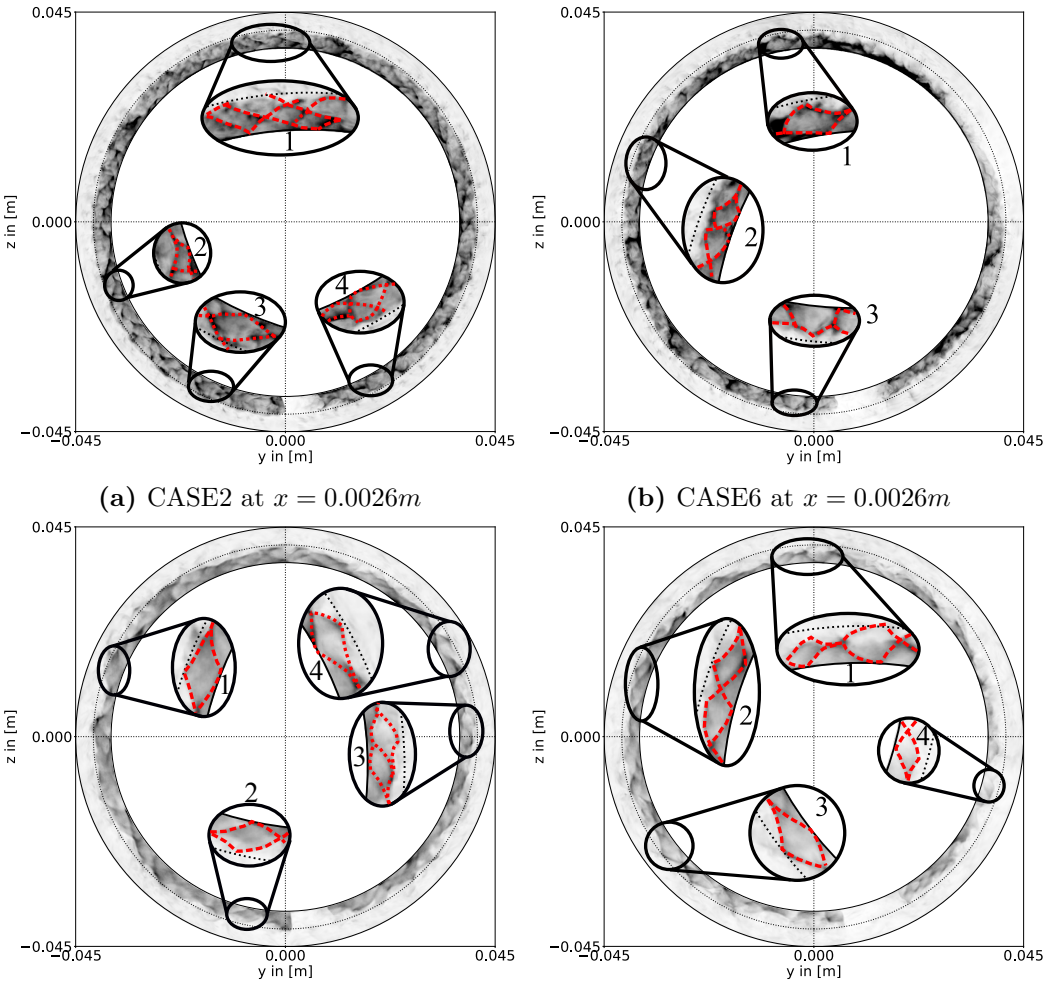

(a) CASE2 at $x = 0.0026m$

(b) CASE6 at $x = 0.0026m$

(c) CASE2 at $x = 0.0106m$

(d) CASE6 at $x = 0.0106m$

Figure 11.12: Numerical soot foils of CASE2 and CASE6 at $x = 0.0026m$ and $x = 0.0106m$. The solid lines denote the inner and outer wall of the annulus. The dashed line denotes the mean perimeter.

The first set of axial numerical soot foils are displayed in Fig. 11.12. Both cases show high pressures at $x = 0.0026m$, which can be attributed to the

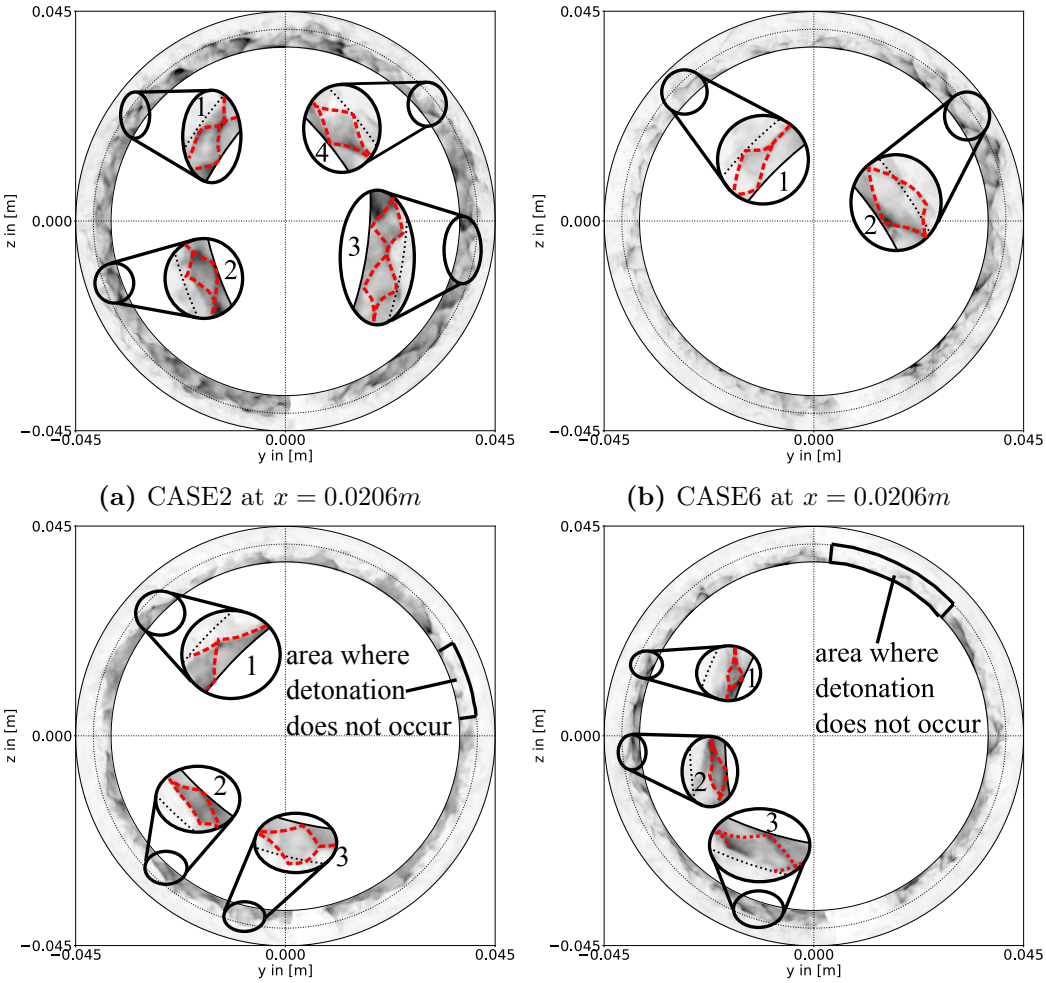

(a) CASE2 at $x = 0.0206m$

(b) CASE6 at $x = 0.0206m$

(c) CASE2 at $x = 0.0276m$

(d) CASE6 at $x = 0.0276m$

Figure 11.13: Numerical soot foils of CASE2 and CASE6 at $x = 0.0206m$ and $x = 0.0276m$. The solid lines denote the inner and outer wall of the annulus. The dashed line denotes the mean perimeter.

high pressure blasts that occur close to the bottom plate. Here, CASE2 and CASE6 have irregular detonation cell patterns which are elaborated on in the enlarged sections in the middle of the images and are all concentrated close to the inner wall, emphasizing again the fact that the detonation only propagates in the inner half of the annulus where mixing occurs. Figure 11.12 a) 1-4 show detonation cells of various cell sizes λ_{cell} where the largest λ_{cell}

is of order of $\Delta_{CC}/2$. The same observation is made for Fig. 11.12 b) 1-3. A significant difference between Fig. 11.12 a) and b) is a low pressure area in the first quadrant of b), which is followed by a sudden increase of pressure in propagation direction. This corresponds to the locally quenched detonation wave in Fig. 11.10 bottom.

On the next level at $x = 0.0106m$ (Fig. 11.12 c) and d)), the same behavior is observed excpet for relatively larger cells, with the cell size remaining of the order of $\Delta_{CC}/2$.

A strong deviation between CASE2 and CASE6 occurs at $x = 0.0206$ Height-wise, Fig. 11.13 b) corresponds to the axial height where the low pressure/ quenched detonation area is located. One observes that the overall pressure in the inner span of the annulus is considerably higher in (CASE2 Fig. 11.13 a)) than in CASE6 (Fig. 11.13 b)) which highlights once more the instability of the detonation in CASE6. The soot foil in Fig. 11.13 a) keeps the same features as seen in Fig. 11.12 b): detonation cells with a cell size dominantly around $\lambda_{cell} = \Delta_{CC}/2$, which is displayed in detail in the sections 1-4. On the other hand CASE6 (Fig. 11.13 b)) hints at structures, which are shown in 1 and 2, but not over the full propagation distance depicted in this soot foil.

Figure 11.13 c) and d) depict the last set of cuts at $x = 0.0276m$. close to the detonation height (which is $35mm$ (CASE2) and $40mm$ (CASE6)). At this height, the detonation only propagates in a smaller portion of the annulus (much lower than the half span). This is in agreement with the effective refill width at $x = 0.0276m$ (see Fig. 11.11), showing hat in fact detonations occur only in areas with sufficient amount of mixed reactants.

The analysis of the different heights highlights two important points: the first information is that the stability of the detonation in radial direction is highly dependent on the span width filled with mixed fresh gases, in other words the detonation cell size in the current RDE configuration depends on the refill behavior. The second information is that the choice of $\delta_{1/2}$ has a significant impact on the detonation stability, since it directly influences the detonation cell formation in the annulus.

11.6 Conclusion

To investigate the influence of the chemical kinetics on the computations of RDEs, three different 1-step chemical schemes have been compared and their

performance analyzed:1S-Deto, 1S-Deto-II and 1S-Deto-III.

In all cases one detonation wave propagates in the domain and all waves propagate at different D, with CASE2 at $7620Hz$, CASE5 at $7575Hz$ and CASE6 at $7200Hz$. All three cases overestimate the experimental detonation rotation frequency $5800Hz$.

The different tests show that the detonation speed decreases for an increasing $\delta_{1/2,target}$ and the detonation propagates less stable. The difference in D between CASE2 and CASE6 was the highest in this set of runs, hence only CASE2 and CASE6 are compared in detail.

It has been shown that the refill height of CASE6 is higher ($0.04m$) than the one of CASE2 ($0.035m$), since a slower detonation wave allows for a longer refill period and consequently longer mixing time frame. This alters the mixing field considerably and the mixture in front of the detonation in CASE6 tends to be leaner than in CASE2. Additionally 1S-Deto-III is not able to consume all of the mixed reactants in a detonation, hereby increasing the losses due to less combustion in a detonation regime.

The unstable detonation propagation is investigated via numerical soot foils taken at the inner wall. They show that the reflection of triple points at the walls and the presence of local explosions at the interface of hot and cold gases, compressed by the local pressure wave (top of the detonation), are required for sustaining a detonation. Local quenching in CASE6 occurs in areas of low I_{mix}, pointing out that 1S-Deto-III is not able to sustain a detonation for lean mixtures. On the other hand CASE2, hence 1S-Deto is able to process such lean mixtures , showing that the choice of $\delta_{1/2,targer}$ significantly impacts the stability of the detonation. This has also been demonstrated by soot foils taken at various axial positions above the bottom plate. These cuts highlight that the detonation cell size is limited by the effective refill span width of the chamber and is not solely on the annular gap width Δ_{CC}. It stresses the necessity of an injection system capable of effectively flushing the full span width of the annulus, to improve the stabilization of the detonation wave.

PART II : Master setup and comparison to experimental data

Chapter 12

Design of a numerical master setup and comparison to experimental data

Contents

12.1 Introduction

The previous chapters have identified the effects of different numerical and physical sub-models on the computation of RDEs. They show that each sub-model (except the SGS model) has an impact on the detonation propagation, efficiency and overall flow field conditions. The current chapter aims to construct a numerical "master" setup, which incorporates the numerical and physical sub-models leading to the predicted detonation speed D closest to the experimentally obtained wave speed.

12.2 Setup of MASTER-CASE

The first step in the design of the numerical master setup is the choice of the numerical scheme, chemistry (represented by $\delta_{1/2,target}$), SGS-model and wall treatment for the master case, which is called MASTER-CASE in the following. The chosen models/ parameters are listed in Tab. 12.1:

Model parameter	choice
Numerical scheme	TTG4A
$\delta_{1/2,target}$	$180\mu m$
SGS-model	WALE
Wall treatment	Wall-Law

Table 12.1: Choice of sub-models for MASTER-CASE

The justifications for these parameters/models are:

1. Numerical scheme: Chapter 9.7.2 has shown that the choice of the numerical scheme has a significant influence on the detonation propagation as well as the detonation efficiency. The run performed with TTG4A led to a lower predicted D, compared to LW. Additionally, since TTG4A is a scheme of higher order, it leads to more accurate results in CFD simulations, hence TTG4A is the numerical scheme retained for MASTER-CASE.

2. $\delta_{1/2,target}$: The choice of $\delta_{1/2,target}$ (Chapter 11) has shown the biggest influence on the detonation speed as well as the detonation efficiency: $\delta_{1/2,target}$ impacts local quenching and the structure of the detonation

front. However, preliminary tests for running MASTER-CASE with 1S-Deto-III led to quenching of the detonation wave, which resulted in the application of 1S-Deto-II with $\delta_{1/2,target} = 180\mu m$.

3. SGS-model: WALE is chosen for the SGS model, since the other reasonable option SIGMA did not impact the detonation in a significant manner (Chapter 9).

4. Wall treatment: The application of a wall law (Chapter 10) impacts the refill height of fresh gases, the mixing field in the radial direction and the detonation structure. It also leads to a lower predicted D of the simulation, closer to the experimental value. These factors show that the application of a wall law is mandatory for the simulation.

12.3 Comparison of experimental data with MASTER-CASE

Performing experiments on RDEs is a difficult task and only a few data are available to validate the LES results. This work focuses on three of them: (1) the RDE wave speed, (2) the wall pressure signals and (3) the overall pressure gain.

12.3.1 Wave speed

As established, the first qualitative parameter to compare is the numerically obtained detonation wave speed (Tab. 12.2).

	MASTER-CASE	EXPERIMENT
Wave mode [-]	single	single
Rotation Frequency $[Hz]$	7050	5800
Detonation wave speed $[m/s]$	2000	1640
D/D_{cj} [-]	1.04	0.85

Table 12.2: Comparison of the predicted detonation frequencies of MASTER-CASE with respect to the experimentally obtained wave speed. $D_{CJ} = 1925m/s$, is based on the nominal $\phi = 0.9$, T_{init} and P_{init}

The performed LES of the rotating detonation has decreased to $7050m/s$, which corresponds to an over prediction of 21%. The choice of models in

Tab. 12.1 leads to the expected decrease of the computed detonation speed, however, the over prediction is still significant and one could not full decelerate the wave speed closer to the experimental value without detonation quenching.

12.3.2 Pressure measurements

Another variable which was measured by the TUB experiment is the axial pressure distribution along the combustor. This allows to investigate the peak pressures at the wall and the pressure development in the RDE in downstream direction. 7 Kulite sensors, which measure the dynamic pressure at are mounted on the outer wall of the combustor. Additionally one PCB sensor in a CTAP configuration is positioned to obtain an estimate of the mean pressure of the cold gases. The configuration is sketched in Fig. 12.1. The measured pressures from the PCB are used to correct the value of the Kulite sensors, which typically only gives the dynamic pressure. The correction has been performed by the Team of TUB. During all test runs, difficulties with the pressure measurements occurred, such as sensors breaking or malfunctioning. It resulted in the retrieval of data from of 3 of the 7 sensors, Kulite1, Kulite3 and Kulite4.

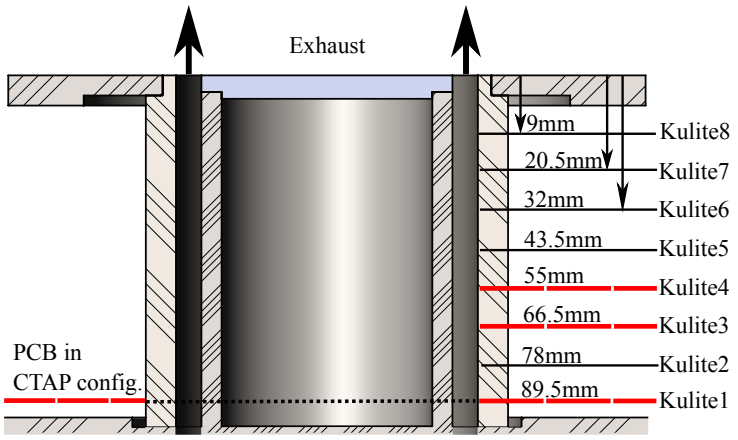

Figure 12.1: Sketch of the test rig with instrumentation: The red marked sensors are the ones the numerical data is compared with. The lengths are given as distance from the outlet.

Nevertheless numerical pressure signals at the probes in the chamber are

fully evaluated to obtain insight on the axial distribution in the combustor. To compare the pressures at the outer wall, 7 probes are placed along the height of the outer combustor wall, to record the static pressure in the computational domain at a frequency of $3.8MHz$.

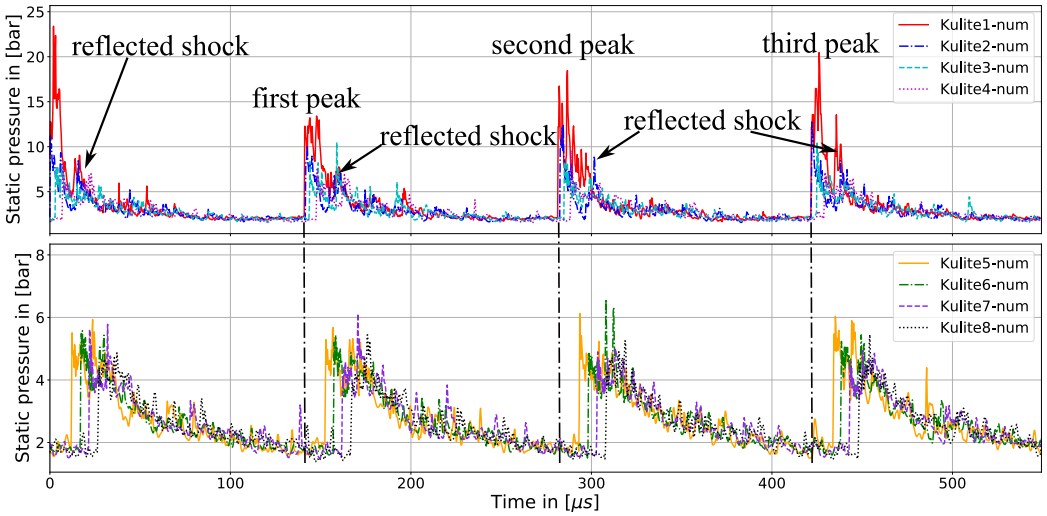

Figure 12.2: Numerical pressure probe signals for four exemplary cycles of MASTER-CASE.

Figure 12.2 signals display pressures of over $10bar$ at the outer wall for Kulite1-num. All lower Kulites-num display a second peak after the shock passage, showing the presence of a secondary, reflected shock propagating behind the detonation. The upper numerical Kulite5-num to Kulite8-num all show peak pressures of 4-6bar. However they all show an increasing delay with respect to Kulite1-num: the pressure jumps occur due to the passing of the oblique shock, who passes the probes with an increasing delay for an increasing axial distance from the bottom plate. To compare the LES and experimental pressure signals, the same filtering procedure applied to the experimental data is performed on the LES signals: the numerical data is re-sampled at $50kHz$ and a low pass filter with a cut-off frequency of $500kHz$ is applied to filter noise. The average detonation frequencies (Tab 12.2) are multiplied with the run time so that the detonation signals can be displayed normalized over the respective cycle, since a comparison over time is not very meaningful, due to the different cycle lengths. Instead the cycle normalized data is used to check if the numerical signals qualitatively

match the experimental ones.

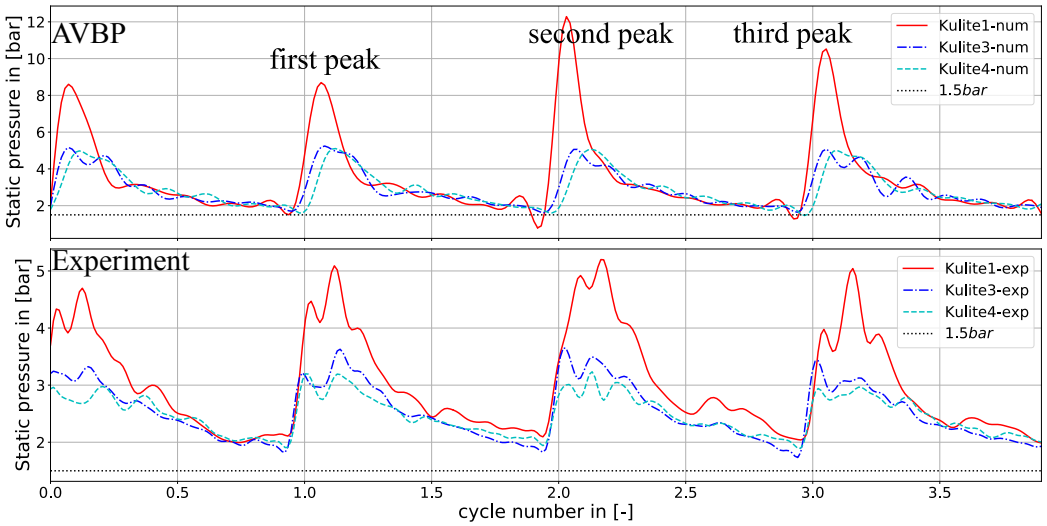

Figure 12.3: Numerical pressure probe signals over time for four exemplary cycles of MASTER-CASE after treatment (top) and corresponding experimental pressure signals (bottom).

The comparison between experimental data and the numerical is displayed in Fig. 12.3 and shows that the highest pressure occur at the bottom of the chamber due to the detonation wave passage. The relatively low pressure values in Fig. 12.2 and Fig. 12.3 further prove that at the outer wall gases are not detonated since only hot product gases, but no mixed fresh reactants are close to the outer walls. Further one can see a decrease in pressure downstream, pointing to an expansion of the gases towards the outlet. The slight phase shift between the pressure signals in the LES, is not observed in the experiments. The reason for this could be the fact that the detonation height in the experiment is higher than the one in MASTER-CASE. If it were signals from an oblique shock the data should display an offset between the curves due to the oblique shocks angle. This is plausible since the detonation wave in the experiment is significantly slower than in the simulation, allowing more fresh gases to enter the chamber and to mix. The downside of this would be the longer exposure time of the fresh gases to parasitic combustion, which could in turn create more losses to non detonative combustion, as well as increase the degree of dilution in the fresh gases.

12.3.3 Pressure gain

The final parameter, available from experiments, for the validation of the simulation is the validation of the pressure gain: the pressure gain can be calculated by different methods, e.g. introduce Kaemming and Paxson (2018) the so called EAP (Equivalent Available Pressure). Another option is the direct comparison of the outlet total pressure $P_{t,outlet}$ performed by e.g. Bach et al. (2020). In fact, Bach et al. (2020) performed various measurements for the TUB RDE, by measuring the total pressure close to the outlet via a Kiel-probe, with various geometry modifications, (e.g. varying outlet restrictions) and mass flow rates at a global $\phi = 1.0$. Although the exact point of operation in thesis is not specifically mentioned in Bach et al. (2022), they point out that the pressure gain does not show significant differences for changing equivalence ratios. Since the experimental data for the investigated point of operation ($\phi = 0.9$) in this thesis has not been measured, the results of Bach et al. (2020) at $\phi = 1.0$ will be used as reference and allow to further validate the results of the LES. The pressure gain is computed as

$$P_{GAIN} = \frac{P_{t,outlet}}{P_{t,Air-plenum}} - 1 \tag{12.1}$$

P_{GAIN} is a function of the outlet total pressure $P_{t,outlet}$ and the total pressure $P_{t,Air-plenum}$ of the air plenum following the method of Bach et al. (2020).

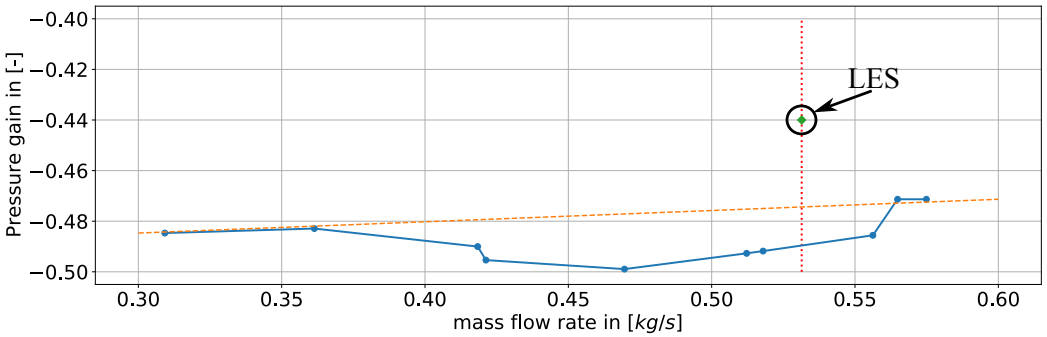

Figure 12.4: Measured pressure gain for different mass flow rates for $\phi = 1.0$ and $g = 1.76mm$. Adapted from Bach et al. (2020).

As a reference, the measured pressure gain from a set of experiments with the same ratio of air slot height $g = 1.76mm$ and chamber gap width $\Delta_{cc} = 7.6mm$ is taken. The pressure gain over the mass flow rate is shown in

Fig. 12.4. The total nominal mass flow rate of the experiment investigated in this work is $0.5314 kg/s$, hence the pressure gain can be estimated from Fig. 12.4 and reads $P_{GAIN,mean} \approx -0.49$ This is to be compared with the LES value $P_{GAIN,mean} = -0.44$, computed using a mean P_{tot}, $Air - plenum = 6.4 bar$ obtained from a pressure probe in the air plenum.

The first information obtained is that the numerically obtained pressure gain is negative. This in accordance with the measured data of e.g. Bach et al. (2020), and in fact, no pressure gain in any experimental devise has been reported yet. The second point is an overestimation of the mean P_{GAIN} by 0.03 - 0.05 in comparison to the expected range of P_{GAIN} by literature. There are various possible reasons for the overestimation such as loss mechanisms which are not included in the modeling of MASTER-CASE like heat losses. Another possible explanation could be the detonation efficiency: the measured detonation rotation frequency is significantly lower than in the LES, which, based on the results of this work, points to a significantly lower experimental E_{det}. This in turn leads to higher amounts of losses to parasitic combustion, which would introduce additional pressure losses. Lastly, the pressure losses in the air feeding slot are minimized due to the slip wall condition at the air feeding walls: applying a wall law or increasing the resolution to apply no-slip walls would introduce pressure losses in the air feeding slots, which decreases the pressure gain.

12.4 Analysis of MASTER-CASE

The validation process has shown that relevant features such as a significant negative pressure gain and downstream pressure distribution is captured in the LES, even though the detonation wave speed is over predicted and the pressure gain slightly higher than expected. In the next step the flow field is analyzed in 3D and 2D to analyze the inner flow structures.

12.4.1 Flow field analysis 3D

One interesting feature is the shock structures in an RDE. The visualization is performed with two quantities: the gradient of pressure normalized by pressure $\Delta P/P$ and an iso contour of I_{det} to visualize the distribution of the detonating mixture. Figure 12.5 left displays the detonation front and tailing shock structures. The iso contour of $\Delta P/P$ spans the full annular gap

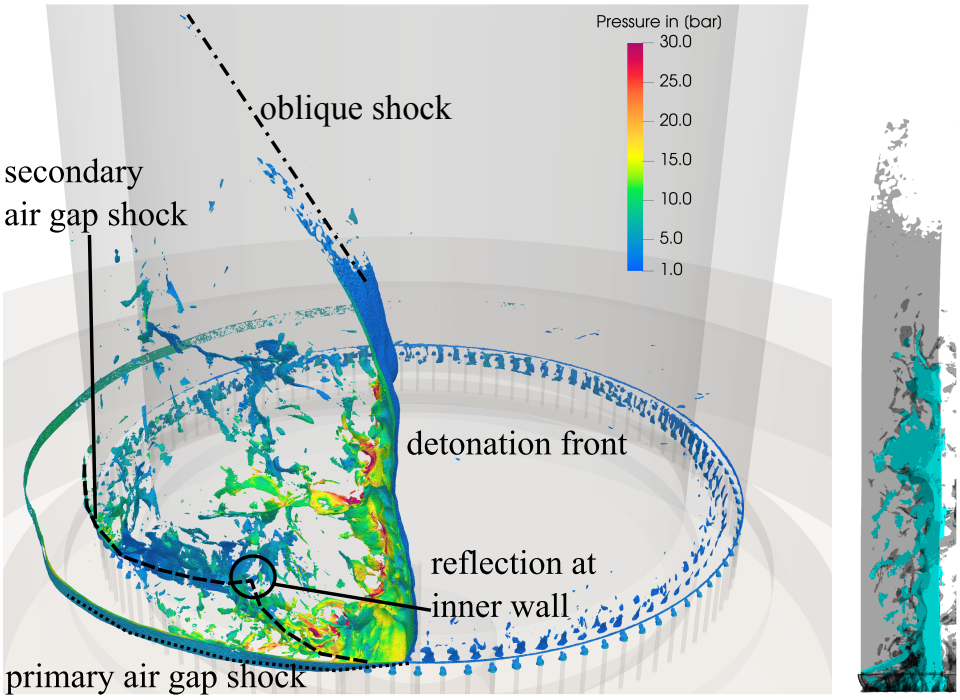

Figure 12.5: Left: Visualization of the detonation front and shock structures via an iso contour of $\Delta P/P$ at $2000m^{-1}$, colored by the static pressure P. Right: front view on the detonation front. In black the iso contour of $\Delta P/P$ at $2000m^{-1}$, partly transparent partially displayed and in turquoise an iso contour of $I_{det} = 1.0$.

width Δ_{cc}. The coloring by pressure allows to see the local strength of the shock front. At the outer detonation front, at the air inlet gap, a primary air gap shock (dotted line) originates from the detonation and propagates into the plenum. The detonation front is additionally followed by a shock, which is reflected at the inner wall and propagates towards the air inlet gap transitioning into a secondary air gap shock (dashed line). This reflected shock is seen as secondary peaks in Fig. 12.2. The air gap shocks are the reason for the blockage of the air feeding flow into the combustion chamber. On top of the detonation a dot-dashed line indicated the oblique shock that propagates to the chamber outlet. The right part of Fig. 12.5 shows that the actual detonation occurs close to the inner wall, emphasized by I_{det}, which is only seen at the inner wall. This explains the low pressures in Fig. 12.2 since effectively a detonation does not occur at the outer wall.

The next interesting feature is the instantaneous refill process: by regard-

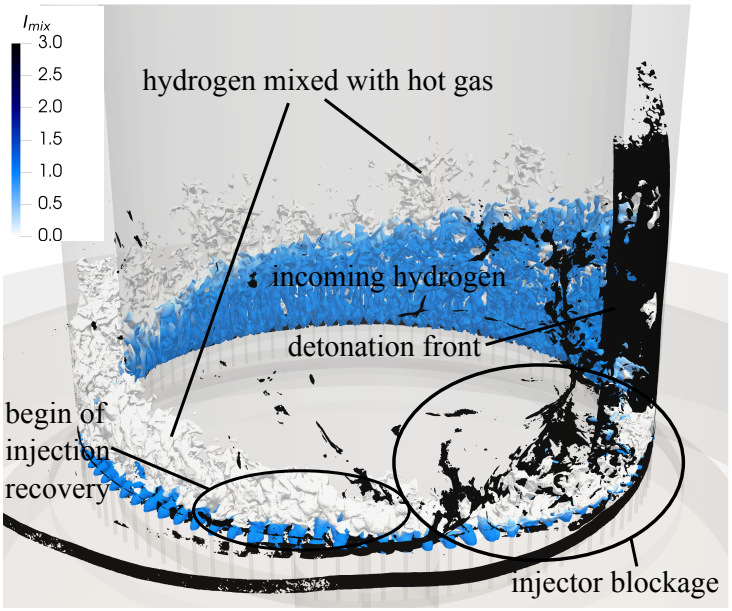

Figure 12.6: Detonation front and shock structures via an iso contour of $\Delta P/P$ at $2000m^{-1}$, colored in black. Colored by I_{mix}, an iso contour of $Y_{H_2} = 0.0258$ is shown to visualize the refill process and mixing losses due to not mixing with Air.

ing iso contours of Y_{H_2}, colored by I_{mix} one obtains a good characterization of the mixing field. The refill structure of a RDE is triangular and the Y_{H_2} fields show a linearly increasing axial height of the iso contour after recovery. The iso contour also illustrates, that a lot of fuel is mixed with hot gases instead of air, clearly showing mixing losses in the simulation. The blue colored part emphasizes that the fresh gases are best mixed at the inner wall/ inner span region of the annulus. The iso contour of Y_{H_2} persists after detonation passage close to the bottom wall in the blockage area, showing that the detonation does not consume all the fuel in front of it. The blockage and refill behavior is also depicted in Fig. 12.7. The detonation blocks the air mass flow into the chamber and induces even a slight back flow, which can be seen by the few instances of $\dot{m}_{air} < 0$. Only a slight blockage of H_2 occurs, introducing significant mixing losses due to the absence of air.

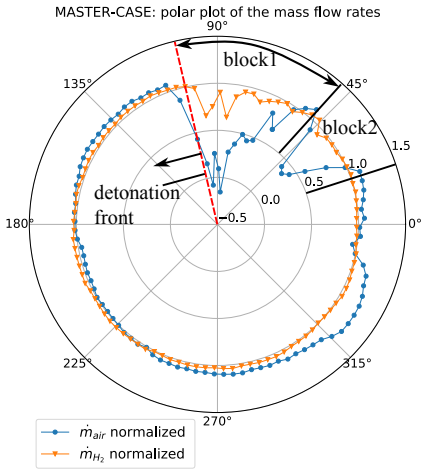

Figure 12.7: Polar plot of Master-CASE. The curves show the mass flow rates through the air gap and the H_2 injectors normalized by the nominal mass flow through the injectors. The detonation propagates counter clock-wise direction and is denoted by a red dashed line in each graph.

12.4.2 Flow field analysis 2D

MASTER-CASE combines different models that were originally tested separately, hence the detonation speed as well as the flow structure might have changed with regard to CASE2. The flow field is hence re-examined, but no comparison to the previous cases is performed. The analysis of the flow field is performed on a cylindrical cut at 33% span width.

The first row of Fig. 12.8, (a) and (b) show the instantaneous and phase averaged temperature field of MASTER-CASE. It highlights the presence of clear pockets of hot gas in front of the detonation wave (Fig. 12.8 (a)), which point to elevated parasitic combustion losses. These pockets result in elevated temperatures in front of the detonation wave in Fig. 12.8 (b).

The instantaneous Y_{H_2} field (Fig. 12.8 (c)) shows a strongly heterogeneous mixture in front of the detonation wave. Additionally a large number of unburnt fuel spots after detonation passage shows that the detonation does not process all of the available fuel: this behavior leads to the appearance of a band of unburnt fuel just after the detonation passage in the average field of Fig. 12.8. Just in front of the detonation, two dominant states of Y_{H_2} distribution can be found: (1) the rich layer at the bottom and (2) a lean layer resulting from the mixing of air and H_2. At the top of the refill height,

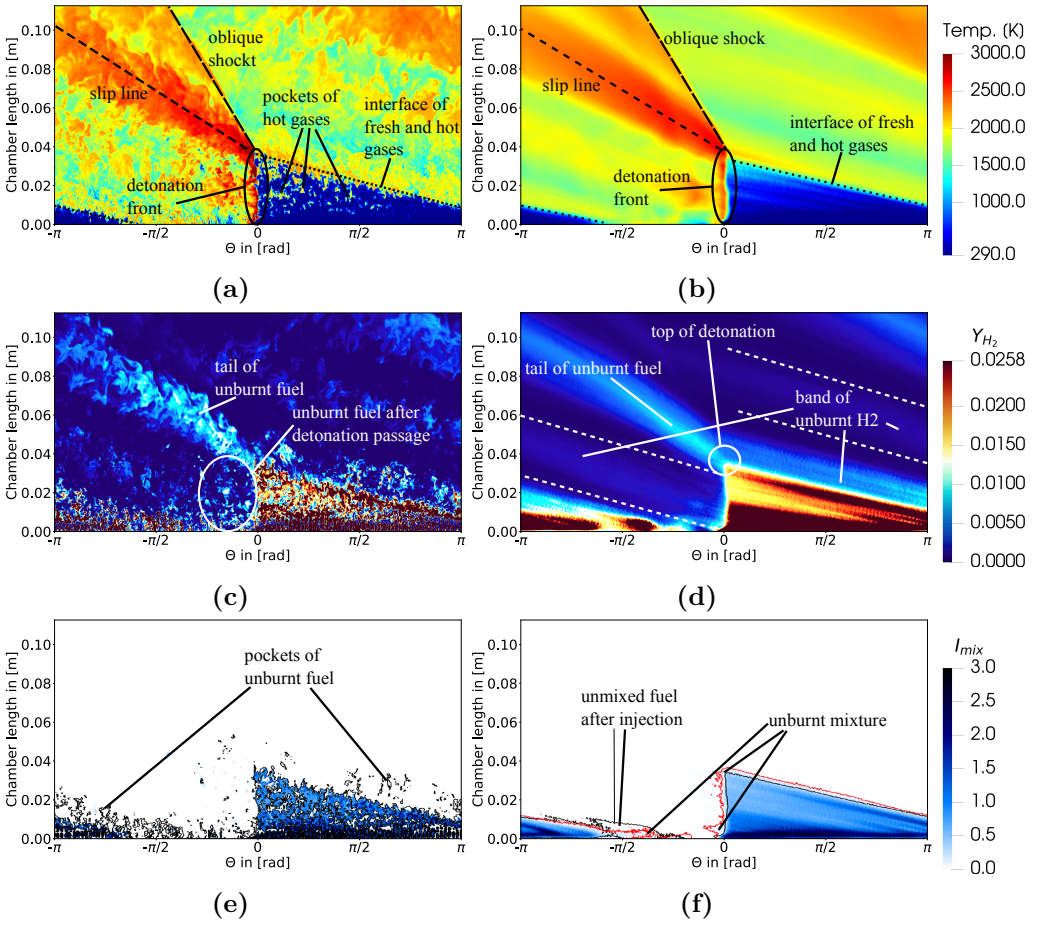

Figure 12.8: Instantaneous (a,c,e) and phase averaged (b,d,f) cut of MASTER-CASE at 33% depicting temperature (top row), Y_{H_2} (middle row)and I_{mix} (bottom row). An additional red iso contour of $I_{mix} = 0.1$ hints at the amount of consumed mixture.

the detonation is unable to burnt fuel efficienty, and a tail of unburnt H_2 emerges from the top of the detonation.

The fields of I_{mix} reveal the occurrence of high amounts of dilution and unmixed fresh gases as can seen in Fig. 12.8 (e). The highest value of I_{mix} occur again at the bottom due to the presence of the fuel injectors and pockets of unburnt fuel are found in Fig. 12.8 (e). The phase averaged solution reveals that the fresh gas mixture is highly diluted by the the pockets of hot gases, previously introduced. Around $\Theta = -\pi/2$ fuel is injected without mixing

with air, pointing out that the air recovery occurs later than the fuel injection recovery (see also Fig. 12.6).

To study the refill behavior of this particular setup the radial, phase averaged pre-and post detonation planes are once more plotted in Fig. 12.9. Two main differences compared to the cases shown in the last chapters are worth pointing out: (1) in the pre-detonation Y_{H_2} field (Fig. 12.9 (c)), high amount of fuel mixed with burnt gases from the previous cycel can be found in the outer half of the combustion chamber. (2) post-detonation, both Imix fields (Fig. 12.9 (b)) and Y_{H_2} fields (Fig. 12.9 (c)) show pockets of unburnt material in the inner half of the combustion chamber in accordance with the observations made in Fig. 12.8, in that the detonation is unable to process the reactive gases efficiently.

12.4.3 Detonation wave structure

The detonation structure can be investigated in more detail: first the instantaneous and phase averaged pressure fields and second numerically obtained soot foils, taken at 5 different span widths, is investigated to understand the stability of the detonation propagation and its structure.

Additionally the averaged detonation front is divided into different sections, which is highlighted in Fig. 12.10: first, the figure shows that the high pressure values at the bottom coincide with the presence of the hydrogen jets at the bottom of the chamber and on top of the rich area a stratified mixture. This emphasizes the influence of the mixing structures in the chamber on the detonation structure and by extension on the propagation behavior of the detonation.

The numerical soot foils (Fig. 12.11) allow to track the detonation stability at different span widths: Fig. 12.11 (a) reveals that for the displayed cycle the detonation propagates stably along the inner wall and reveals various detonation cell sizes. Interestingly the detonation does not stably propagate at 25% span width but quenches and reignites locally at different axial positions. Continuing at a span width of 50% the soot foil hints at local detonation passage via locally high pressures. Finally, at a span width of 75% and 100% the soot foils show that no detonation is propagating at the outer span, which is in agreement with Fig. 12.9, where only the outer half of the annulus is actually flushed. It also further illustrates, why the measured pressures at the outer wall, numerical or experimental (Fig. 12.3), are considerably lower than one would expected from a detonation.

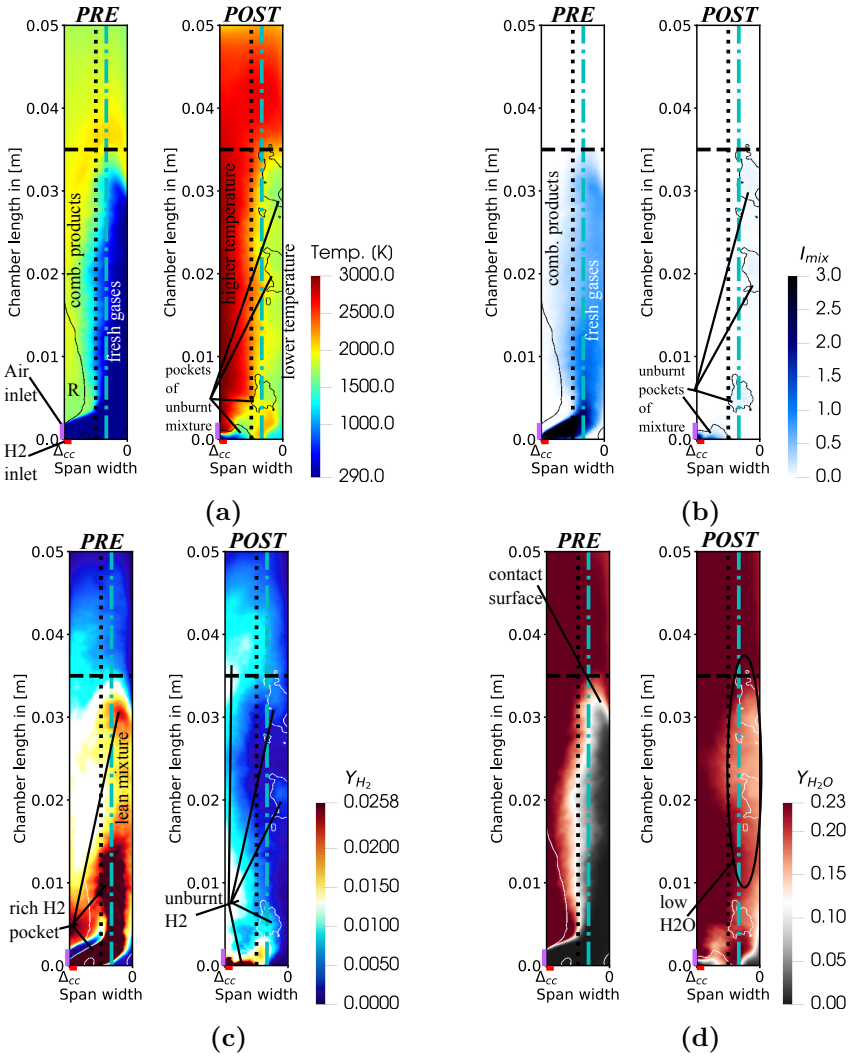

Figure 12.9: MASTER-CASE - Phase locked averaged cuts in front and after the detonation front in pairings pre-and post-detonation: the first pair shows the temperature fields (a), the second I_{mix} (b), the third H_2 (c) and the last the H_2O (d) fields. The dot-dashed line denotes the radial position of the previously displayed unwrapped cuts and the dotted line denotes 50% span width. A black (white in (d)) iso contour at $u = 0$ (axial downstream velocity) reveals a re-circulation zone R in front of the detonation. The colormaps are saturated as established. The x-axis goes from Δ_{cc}, the **outer wall** to 0, the **inner wall**.

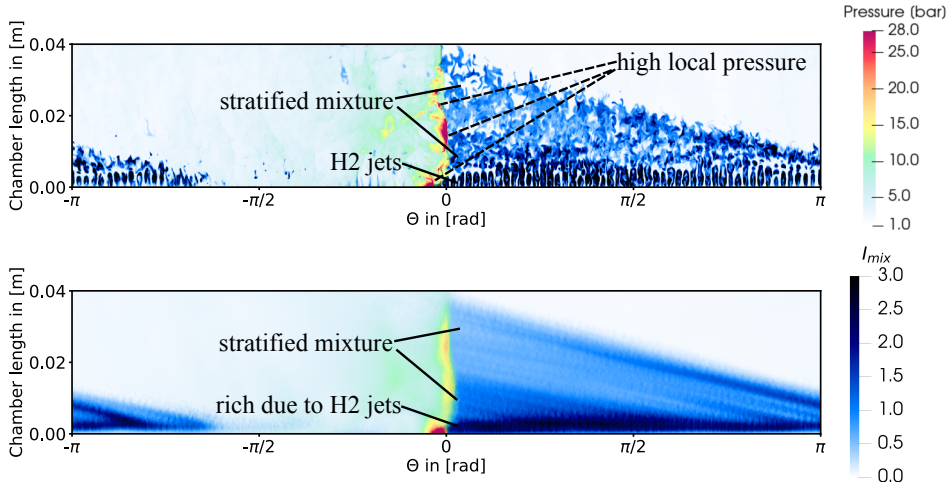

Figure 12.10: Top: exemplaric instantaneous pressure field of MASTER-CASE superimposed on the respective instantaneous I_{mix} field at a span width of 33%, showing the dependence of the detonation structure on the mixing field. Bottom: the same fields for a phase averaged solution.

12.4.4 Efficiencies

The resulting efficiencies (Fig. 12.12) show that the overall combustion efficiency E stays constant over the run time while the detonation efficiency E_{det} is oscillating and in fact dropping down to values of $< 35\%$. It shows that the detonation in MASTER-CASE is not propagating in a stable manner. The reason for the unstable propagation can be mainly attributed to the chosen $\delta_{1/2}$ and the numerical scheme. These results in Fig. 12.12 point out that the decrease in detonation efficiency and hence detonation speed can be considerably amplified by the choice of sub models.

12.5 Conclusion and Outlook

This chapter has designed a master case, where all previously investigated parameters have been optimized to obtain a simulation with a detonation wave speed close to the experimental one. The resulting detonation rotation frequency of $7050Hz$ is still significantly higher than the experimental one of $5800Hz$, but it is the lowest of the numerically obtained D.

The obtained average pressure gain -0.44 is slightly overestimated with

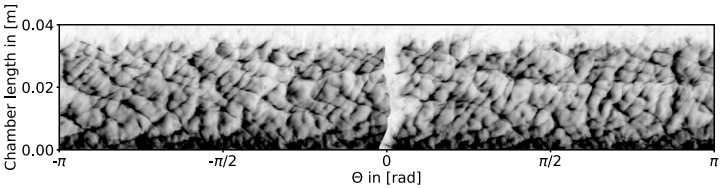

(a) 0% span width

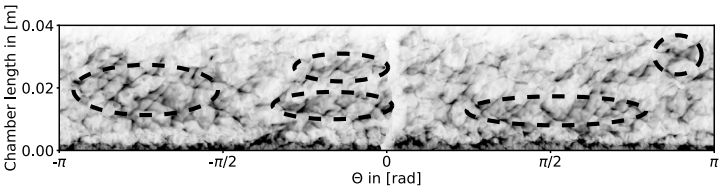

(b) 25% span width

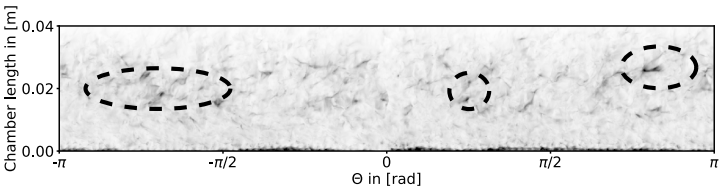

(c) 50% span width

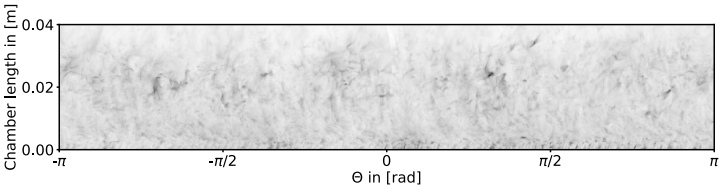

(d) 75% span width

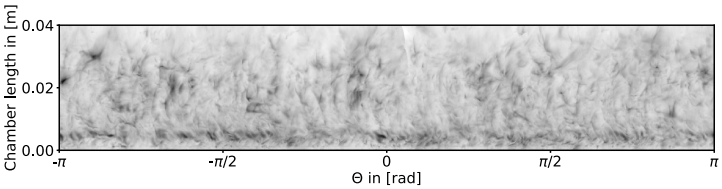

(e) 100% span width

Figure 12.11: Numerical soot foil of MASTER-CASE at different span widths. The dashed lines in (b) and (c) denote the locus of local detonation passage.

respect to the estimated one between -0.49 and -0.46. Since different loss mechanism such as losses in the air feeding slot or hear transfer are not

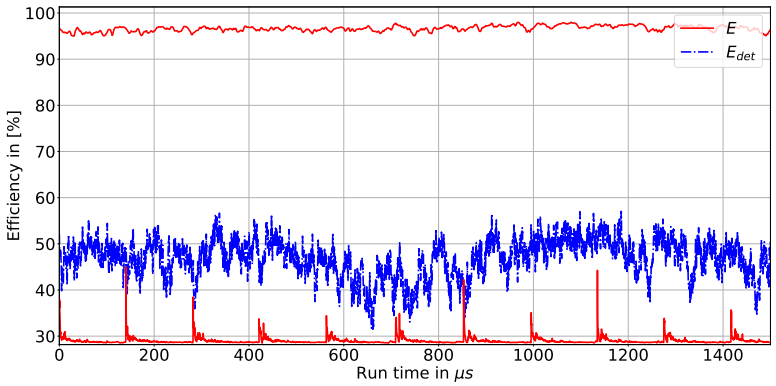

Figure 12.12: Combustion E and detonation efficiency E_{det} of MASTER-CASE for 11 cycles.

included, the numerically obtained pressure gain is a reasonable estimate of the real one. Overall MASTER-CASE reproduces the basic features found in the current setup of the TUB RDE. These LES clearly show that the TUB RDE, with the injection system considered in this thesis, suffers from far from ideal injection and mixing and also suggest that the considerably negative pressure gain is the result of a highly unstable detonation propagation and significant losses to parasistic combustion. The present results also emphasize that the LES methods need further improvement to accurately predict the propagation behavior inside RDEs, especially in these far from ideal setups.

Chapter 13

Global summary and conclusion

This thesis investigates LES of RDEs. It has shown that their applicability to RDEs is not straightforward and suffers from the lack of a reference LES setup for reliable RDE simulations. The current work aims to fill this gap by: first understanding the key features controlling these simulations and second, identifying the crucial modeling challenges that merits further investigations. The thesis abstains from relying on a 2D geometrical representation of the RDE chamber, a commonly applied simplification of the problem in literature. It only considers simulations of a realistic full three-dimensional RDE tested at TU Berlin. It includes fuel (hydrogen here), air plenums and their injection lines feeding an annular, cylindrical combustion chamber. Performing LES of RDEs poses multiple difficulties, some which were the subject of particular attention:

The geometrical meshing constraints of a full RDE configuration (chamber and injection systems) can be difficult to satisfy in LES, especially for the investigated TUB configuration where H_2 is injected through 100 small tubes resulting in 100 H_2 jets in cross-flow configuration with the main air stream. Hence, a dedicated meshing strategy has been developed to properly resolve the flow in the feeding lines (10 cells per H_2 tube diameter and air gap), the mixing process at the bottom of the RDE chamber and the detonation wave passing though the reactive mixture.

The presence of multiple shock waves necessitates proper numerical treatments which consisted in this work of a localized artificial diffusivity, which activates in regions of strong pressure gradients.

A one-step chemical scheme based on a reference mechanism (here Mevel) has been designed so that the correct D_{CJ} and a correct $\delta_{1/2,target}$ are repro-

duced. This chemical scheme has been validated in CERFACS' LES solver AVBP for canonical 1D and 2D detonation simulations. The scheme is designed to include the contribution of deflagration via targeting s_L , which is often overlooked when designing chemical schemes for RDE simulations despite its crucial importance.

Two new post processing parameters I_{mix} and I_{det} have been introduced to analyze combustion in the RDE: the mixing index I_{mix} allows to quantify the quality of mixed reactants and influence of residual gases. The detonation index I_{det} allows to split the combustion efficiency E into a part giving the amount of fuel burnt in a detonation regime and a part burnt in a deflagrative regime.

In the first simulation of the TUB RDE, a non reactive RDE simulation has been run, which reveals complicated shock structures reminiscent of typical jet in cross flow configurations and allows a first estimate of the mixing behavior of the system.

The main part of this work is dedicated to the influence of different modeling parameters. In particular the effects of 1. mixing assumptions and sub-grid scale modeling (Chapter 9), 2. numerical scheme (Chapter 9.7.2), 3. wall treatment (Chapter 10) and 4. chemical scheme via variations of the targeted half reaction thickness $\delta_{1/2}$ (Chapter 11) on the detonation speed D are checked. The specific influences of the different modeling approaches can be summarized as follows:

1. the mixing assumptions have shown that a perfectly premixed RDE results in a considerably faster wave than obtained by its non-premixed counterpart, resulting in wave speeds exceeding the experimentally obtained detonation wave speed. The influence of the sub-grid scale model has been shown to be negligible, in the prediction of the D, pointing out that as long a proper sub-grid scale model is chosen, the model itself (e.g. WALE or SIGMA) is not of importance. The results also stretch the necessity of an injection system that is capable of effectively mixing the reactants as well as properly flushing the hot gases towards the exhaust.

2. the LW scheme produced a faster detonation wave than TTG4A. The reason for these differences needs to be further explored, but it can be in part attributed to the differences in diffusivity for strong gradients: the LW scheme lead to a stronger mixing of fresh gases especially in the shear layers of the H_2 jets and the air cross flow.

3. the application of adiabatic wall laws instead of adiabatic slip walls for the chamber walls leads to a modification of the mixture quality and the fresh gas distribution during the refill process. Dilution in radial direction of the annular chamber increases when wall laws are used leading to a slightly decreased D compared to a slip wall case.

4. the chosen $\delta_{1/2}$ has a significant impact on the detonation speed, detonation efficiency and quenching behavior, if chosen large enough. In this work the maximum $\delta_{1/2} = 206\mu m$ has been chosen, since values where $\delta_{1/2} > 206\mu m$ lead to quenching during the first 2 cycles of the computation. The choice of $\delta_{1/2} = 206\mu m$ has shown to produce quenching in areas containing a low amount of well mixed reactants and overall larger detonation cells than for the reference $\delta_{1/2} = 149.6\mu m$. Numerical soot foils show that the flushing of only half of the inner span results in detonation cells which are naturally limited by the inner wall and the interface of fresh and hot gases, stretching the need for a proper flushing of the combustion chamber. The influence of $\delta_{1/2}$ is significant for the prediction of D and needs to be taken into account when designing a reduced chemical scheme for the computation of RDEs.

Based on the influence of the different numerical and physical sub-models, a numerical master setup has been designed to optimize the prediction of D and has been further compared to experimental pressure and pressure gain measurements for validation. The master setup, named MASTER-CASE was run with TTG4A, adiabatic wall law for the combustion chamber walls, a $\delta_{1/2,target} = 180\mu m$ and WALE as sub-grid scale model. Results show that MASTER-CASE delivers the slowest detonation wave speed with $7050Hz$ and the numerically obtained pressure gain of -0.44 results in a reasonable approximation of the expected experimental one of -0.49 to -0.46. A comparison between experimentally obtained pressure signals and numerically obtained pressure signals shows that the numerical signals deliver higher static pressures, but the overall trend in downstream direction is captured sufficiently.

This work shows that LES can be used to understand the dynamics and stabilization mechanisms as well as overall performance of RDE systems. However, further optimization is necessary: The near wall resolution requires improvement for better modeling the influence of walls and the losses due to boundary layers as well as heat losses. Another point is the optimization

of the chemical scheme especially for the prediction of the detonation cell sizes, including the contribution of dilution with hot gases of the previous cycle, which changes the mixture properties in front of the detonation in a considerable manner. Finally it is worth pointing out for the present results that the numerical scheme has an effect on the results and can lead to excess dissipation especially due to the interplay of shock dynamics, chemistry and mixing structures. The outlet boundary condition and its effect were not fully tested and they might significantly influence the result. It also begs the question if the addition of an exhaust plenum might alter the obtained results.

13.1 Publications

The presented studies in this work have resulted in the following publication:

Strempfl, P., Dounia, O., Laera, D. and Poinsot, T. (2024). Effects of mixing assumptions and models for LES of Hydrogen-fueled Rotating Detonation Engines, *International Journal of Hydrogen Energy, 62*, 1-16. https://doi.org/10.1016/j.ijhydene.2024.03.033

Bibliography

Adamson, T. (1967). "Performance analysis of a rotating detonation wave rocket engine (Rotating detonation wave rocket engine performance analyzed and compared to conventional rocket engines)" (cited on p. 20).

Akpan, J. and Olanrewaju, O. (2023). "Sustainable Energy Development: History and Recent Advances". *Energies*, 16(20) (cited on p. 17).

Alekseev, V. A., Christensen, M., and Konnov, A. A. (2015). "The effect of temperature on the adiabatic burning velocities of diluted hydrogen flames: A kinetic study using an updated mechanism". *Combustion and Flame*, 162(5), pp. 1884–1898 (cited on p. 75).

Anand, V., St. George, A., and Gutmark, E. (2017). "Amplitude modulated instability in reactants plenum of a rotating detonation combustor". *International Journal of Hydrogen Energy*, 42(17), pp. 12629–12644 (cited on p. 24).

Athmanathan, V., Braun, J., Ayers, Z. M., Fugger, C. A., Webb, A. M., Slipchenko, M. N., Paniagua, G., Roy, S., and Meyer, T. R. (2022). "On the effects of reactant stratification and wall curvature in non-premixed rotating detonation combustors". *Combustion and Flame*, 240, p. 112013 (cited on p. 152).

Ayers, Z. M., Athmanathan, V., Meyer, T. R., and Paxson, D. E. (2023). "Variably Premixed Rotating Detonation Engine for Evaluation of Detonation Cycle Dynamics". *Journal of Propulsion and Power*, 39(3), pp. 351–364 (cited on p. 127).

Bach, E., Bohon, M. D., Paschereit, C. O., and Stathopoulos, P. (2019). "Impact of Outlet Restriction on RDC Performance and Stagnation Pressure Rise". In: *AIAA Scitech 2019 Forum* (cited on p. 32).

Bach, E., Paschereit, C. O., Stathopoulos, P., and Bohon, M. (2022). "Advancement of Empirical Model for Stagnation Pressure Gain in RDCs". In: *AIAA SCITECH 2022 Forum* (cited on p. 188).

Bach, E., Stathopoulos, P., Paschereit, C. O., and Bohon, M. D. (2020). "Performance analysis of a rotating detonation combustor based on stagnation pressure measurements". *Combustion and Flame*, 217, pp. 21–36 (cited on pp. 188, 189).

Bai, Q., Han, J., Qiu, H., Zhang, S., and Weng, C. (2024). "Study on initiation characteristics of rotating detonation by auto-initiation and predetonation method with high-temperature hydrogen gas". *International Journal of Hydrogen Energy*, 49, pp. 450–461 (cited on p. 103).

Batista, A., Ross, M. C., Lietz, C., and Hargus, W. A. (2021). "Descending Modal Transition Dynamics in a Large Eddy Simulation of a Rotating Detonation Rocket Engine". *Energies*, 14(12) (cited on pp. 26, 29, 98, 152).

Baurle, R. A., Alexopoulos, G. A., and Hassan, H. A. (1994). "Assumed joint probability density function approach for supersonic turbulent combustion". *Journal of Propulsion and Power*, 10(4), pp. 473–484 (cited on p. 29).

Bellenoue, M., Boust, B., Vidal, P., Zitoun, R., Gaillard, T., Davidenko, D., Leyko, M., and Le Naour, B. (2016). "New Combustion Concepts to Enhance the Thermodynamic Efficiency of Propulsion Engines". *Aerospace Lab*, (11), 13 pages (cited on p. 18).

Bluemner, R. (2020). "Operating Mode Dynamics in Rotating Detonation Combustors". URL: https://depositonce. tu- berlin.de/handle/11303/11517. PhD thesis. Technical University Berlin (cited on pp. 31, 103).

Bluemner, R., Bohon, M. D., Paschereit, C. O., and Gutmark, E. J. (2018). "Single and Counter-Rotating Wave Modes in an RDC". In: *2018 AIAA Aerospace Sciences Meeting* (cited on p. 23).

Bluemner, R., Bohon, M. D., Paschereit, C. O., and Gutmark, E. J. (2020). "Effect of inlet and outlet boundary conditions on rotating detonation combustion". *Combustion and Flame*, 216, pp. 300–315 (cited on pp. 23, 24, 28, 30, 31).

Bluemner, R., Gutmark, E. J., Paschereit, C. O., and Bohon, M. D. (2021). "Stabilization mechanisms of longitudinal pulsations in rotating detonation combustors". *Proceedings of the Combustion Institute*, 38(3), pp. 3797–3806 (cited on p. 28).

Bohon, M., Bluemner, R., Paschereit, C., and Gutmark, E. (2019). "High-speed imaging of wave modes in an RDC". *Experimental Thermal and Fluid Science*, 102, pp. 28–37 (cited on pp. 23, 31).

Boivin, P., Jiménez, C., Sánchez, A., and Williams, F. (2011). "An explicit reduced mechanism for H2–air combustion". *Proceedings of the Combustion Institute*, 33(1), pp. 517–523 (cited on pp. 74, 75).

Briscoe, M. G. and Kovitz, A. A. (1968). "Experimental and theoretical study of the stability of plane shock waves reflected normally from perturbed flat walls". *Journal of Fluid Mechanics*, 31(3), pp. 529–546 (cited on p. 62).

Browne, S., Ziegler, J, and Shepherd, J. (2008). "Numerical solution methods for shock and detonation jump conditions". *GALCIT report FM2006*, 6, p. 90 (cited on p. 75).

Burke, R., Rezzag, T., Dunn, I., Flores, W., and Ahmed, K. (2021). "The effect of premixed stratification on the wave dynamics of a rotating detonation combustor". *International Journal of Hydrogen Energy*, 46(54), pp. 27816–27826 (cited on p. 127).

Candel, S. M. and Poinsot, T. (1990). "Flame stretch and the balance equation for the flame surface area". *Combustion Science and Technology*, 70, pp. 1–15 (cited on p. 48).

Chacon, F. and Gamba, M. (2018). "Development of an optically accessible continuous wave Rotating Detonation Engine". In: *2018 Joint Propulsion Conference* (cited on pp. 21, 23).

— (2019). "Study of Parasitic Combustion in an Optically Accessible Continuous Wave Rotating Detonation Engine". In: *AIAA Scitech 2019 Forum* (cited on p. 97).

Chai, X., Iyer, P. S., and Mahesh, K. (2015). "Numerical study of high speed jets in crossflow". *Journal of Fluid Mechanics*, 785, pp. 152–188 (cited on pp. 97, 117).

Chen, H., Si, C., Wu, Y., Hu, H., and Zhu, Y. (2023). "Numerical investigation of the effect of equivalence ratio on the propagation characteristics and performance of rotating detonation engine". *International Journal of Hydrogen Energy*, 48(62), pp. 24074–24088 (cited on p. 127).

Ciccarelli, G., Ginsberg, T., Boccio, J., Finfrock, C., Gerlach, L., Tagawa, H., and Malliakos., A. (1997). *Detonation cell size measurements in high-temperature hydrogen-air-steam mixtures at the bnl high-temperature combustion facility*. Technical Report NUREG/CR-6391, BNL-NUREG-52482, Brookhaven National Laboratory (cited on p. 63).

Clavin, P. (1985). "Dynamic behavior of premixed flame fronts in laminar and turbulent flows". *Progress in Energy and Combustion Science*, 11, pp. 1–59 (cited on p. 48).

Clavin, P and Denet, B (2002). "Diamond patterns in the cellular front of an overdriven detonation." *Phys Rev Lett*, 88(4), p. 044502 (cited on p. 63).

Clavin, P. and Williams, F. A. (1982). "Effects of molecular diffusion and of thermal expansion on the structure and dynamics of premixed flames in turbulent flows of large scales and low intensity". *Journal of Fluid Mechanics*, 116, pp. 251–282 (cited on p. 48).

Clavin, P. and He, L. (1996). "Acoustic effects in the nonlinear oscillations of planar detonations". *Phys. Rev. E*, 53 (5), pp. 4778–4784 (cited on p. 62).

Clavin, P. and Searby, G. (2016). *Combustion Waves and Fronts in Flows: Flames, Shocks, Detonations, Ablation Fronts and Explosion of Stars*. Cambridge University Press (cited on pp. 52, 56, 57, 63).

Clavin, P. and Williams, F. A. (2002). "Dynamics of planar gaseous detonations near Chapman-Jouguet conditions for small heat release". *Combustion Theory and Modelling*, 6(1), pp. 127–139 (cited on p. 62).

Cocks, P. A., Holley, A. T., and Rankin, B. A. (2016). "High Fidelity Simulations of a Non-Premixed Rotating Detonation Engine". In: *54th AIAA Aerospace Sciences Meeting* (cited on pp. 26, 29, 98, 99, 116, 126, 152, 164).

Colin, O. (2000). "Simulations aux grandes échelles de la combustion turbulente prémélangée dans les statoréacteurs". PhD Thesis. INP Toulouse (cited on p. 68).

Colin, O., Ducros, F., Veynante, D., and Poinsot, T. (2000). "A thickened flame model for large eddy simulations of turbulent premixed combustion". *Physics of Fluids*, 12(7), pp. 1843–1863 (cited on pp. 71, 98).

Colin, O. and Rudgyard, M. (2000). "Development of high-order Taylor-Galerkin schemes for unsteady calculations". *Journal of Computational Physics*, 162(2), pp. 338–371 (cited on p. 68).

Cook, A. W. (2007). "Artificial fluid properties for large-eddy simulation of compressible turbulent mixing". *Physics of Fluids*, 19(5), p. 055103 (cited on p. 69).

Cook, A. W. and Cabot, W. H. (2004). "A high-wavenumber viscosity for high-resolution numerical methods". *Journal of Computational Physics*, 195(2), pp. 594–601 (cited on p. 97).

Davidenko, D., Gokalp, I, and Kudryavtsev, A. (2010). "Numerical simulation of continuous detonation in a layer of hydrogen-oxygen mixture with periodic conditions". In: *Deflagrative and detonative combustion*, pp. 407–422 (cited on p. 29).

Dickmann, D. A. and Lu, F. K. (2009). "Shock/Boundary-Layer Interaction Effects on Transverse Jets in Crossflow over a Flat Plate". *Journal of Spacecraft and Rockets*, 46(6), pp. 1132–1141 (cited on p. 118).

Dionne, J., Duquette, R., YOSHINAKA, A., and LEE, J. (2000). "Pathological Detonations in H2-CI2". *Combustion Science and Technology*, 158(1), pp. 5–14 (cited on p. 57).

Donea, J, Quartapelle, L, and Selmin, V (1987). "An analysis of time discretization in the finite element solution of hyperbolic problems". *Journal of Computational Physics*, 70(2), pp. 463–499 (cited on p. 68).

Dounia, O., Vermorel, O., Misdariis, A., and Poinsot, T. (2019). "Influence of kinetics on DDT simulations". *Combustion and Flame*, 200, pp. 1–14 (cited on p. 74).

Dounia, O. (2018). "Numerical investigation of gas explosion phenomena in confined and obstructed channels". 2018INPT0031. PhD thesis (cited on pp. 59, 61).

Driscoll, R., Aghasi, P., St George, A., and Gutmark, E. J. (2016). "Three-dimensional, numerical investigation of reactant injection variation in a H2/air rotating detonation engine". *International Journal of Hydrogen Energy*, 41(9), pp. 5162–5175 (cited on p. 113).

Dubrovskii, A. V., Ivanov, V. S., and Frolov, S. M. (2015). "Three-dimensional numerical simulation of the operation process in a continuous detonation combustor with separate feeding of hydrogen and air". *Russian Journal of Physical Chemistry B*, 9(3), pp. 104–119 (cited on pp. 26, 29).

Duff, R. E. (1961). "Investigation of Spinning Detonation and Detonation Stability". *The Physics of Fluids*, 4(11), pp. 1427–1433 (cited on p. 59).

Echekki, T. and Ferziger, J. (1993). "A simplified reaction rate model and its application to the analysis of premixed flames". *Combustion Science and Technology*, 89, pp. 293–351 (cited on p. 46).

Elasrag, H. A, Hoke, J, Rankin, B, and Schumaker, S. A (2022). "A Local criterion for distinguishing detonation and deflagration for pressure gain combustion". *Proceedings of the Summer Program, CTI, Stanford University*, pp. 279–288 (cited on p. 107).

European Commission (2020). *COMMUNICATION FROM THE COMMISSION TO THE EUROPEAN PARLIAMENT, THE COUNCIL, THE EUROPEAN ECONOMIC AND SOCIAL COMMITTEE AND THE COMMITTEE OF THE REGIONS - A hydrogen strategy for a climate-neutral Europe*. European Commision (cited on p. 16).

Fickett, W. and Davis, W. C. (2000). *Detonation: Theory and Experiment*. Courier Corporation (cited on p. 52).

Fotia, M., Kaemming, T. A., Hoke, J., and Schauer, F. (2015). "Study of the Experimental Performance of a Rotating Detonation Engine with Nozzled Exhaust Flow". In: *53rd AIAA Aerospace Sciences Meeting* (cited on p. 21).

Franzelli, B., Riber, E., and Cuenot, B. (2013). "Impact of the chemical description on a Large Eddy Simulation of a lean partially premixed swirled flame". *Comptes Rendus. Mécanique*, 341(1-2), pp. 247–256 (cited on p. 75).

Frolov, S. M., Dubrovskii, A. V., and Ivanov, V. S. (2013). "Three-dimensional numerical simulation of the operation of a rotating-detonation chamber with separate supply of fuel and oxidizer". *Russian Journal of Physical Chemistry B*, 7, pp. 35–43 (cited on pp. 26, 29).

Gaillard, T., Davidenko, D., and Dupoirieux, F. (2017). "Numerical Simulation of a Rotating Detonation under Conditions of Premixed and Separate Injection of H2-O2". *EUCASS*, 6, pp. 1–14 (cited on pp. 26, 29).

Gallier, S., Le Palud, F., Pintgen, F., Mével, R., and Shepherd, J. (2017). "Detonation wave diffraction in H2–O2–Ar mixtures". *Proceedings of the Combustion Institute*, 36(2), pp. 2781–2789 (cited on p. 75).

Gavrikov, A., Efimenko, A., and Dorofeev, S. (2000). "A model for detonation cell size prediction from chemical kinetics". *Combustion and Flame*, 120(1), pp. 19–33 (cited on p. 64).

Gicquel, L. Y. M. and Roux, A. (2011). "LES to Ease Understanding of Complex Unsteady Combustion Features of Ramjet Burners". *Flow, Turbulence and Combustion*, 87, pp. 449–472 (cited on pp. 71, 99).

Global Hydrogen Review (2023). IEA (cited on p. 17).

Goodwin, D. G., Moffat, H. K., Schoegl, I., Speth, R. L., and Weber, B. W. (2023). *Cantera: An Object-oriented Software Toolkit for Chemical Kinetics, Thermodynamics, and Transport Processes*. https://www.cantera.org. Version 3.0.0 (cited on p. 75).

Goto, K., Matsuoka, K., Matsuyama, K., Kawasaki, A., Watanabe, H., Itouyama, N., Ishihara, K., Buyakofu, V., Noda, T., Kasahara, J., Matsuo, A., Funaki, I., Nakata, D., Uchiumi, M., Habu, H., Takeuchi, S., Arakawa, S., Masuda, J., Maehara, K., Nakao, T., and Yamada, K. (2023). "Space Flight Demonstration of Rotating Detonation Engine Using Sounding Rocket S-520-31". *Journal of Spacecraft and Rockets*, 60(1), pp. 273–285 (cited on p. 21).

Gourdain, N, Gicquel, L, Montagnac, M, Vermorel, O, Gazaix, M, Staffelbach, G, Garcia, M, Boussuge, J., and Poinsot, T (2009). "High performance parallel computing of flows in complex geometries: I. Methods". *Comput. Sci. Disc.*, 2(1), p. 015003 (cited on p. 67).

Gritsch, M., Schulz, A., and Wittig, S. (1998). "Discharge Coefficient Measurements of Film-Cooling Holes With Expanded Exits". *Journal of Turbomachinery*, 120(3), pp. 557–563 (cited on p. 116).

Effect of Crossflows on the Discharge Coefficient of Film Cooling Holes With Varying Angles of Inclination and Orientation (2001). Vol. Volume 3: Heat Transfer; Electric Power; Industrial and Cogeneration (cited on p. 117).

Guo, L., Yan, Y., and Maltson, J. (2011). "Numerical study on discharge coefficients of a jet in crossflow". *Computers and Fluids*, 49(1), pp. 323–332 (cited on pp. 116, 117).

Hassan, E., Boles, J., Aono, H., Davis, D., and Shyy, W. (2013). "Supersonic jet and crossflow interaction: Computational modeling". *Progress in Aerospace Sciences*, 57, pp. 1–24 (cited on pp. 97, 117).

Heiser, W. H. and Pratt, D. T. (2002). "Thermodynamic Cycle Analysis of Pulse Detonation Engines". *Journal of Propulsion and Power*, 18(1), pp. 68–76 (cited on p. 18).

Hirsch, C. (2007). "Finite Volume Method and Conservative Discretization with an Introduction to Finite Element Method". In: *Numerical Computation of internal & external flows: Fundamentals of Computational Fluid Dynamics, second edition*. New York: John Wiley & Sons. Chap. 5, pp. 203–248 (cited on p. 38).

Hirschfelder, J. O., Curtiss, C. F., and Bird, R. B. (1969). *Molecular theory of gases and liquids*. New York: John Wiley & Sons (cited on p. 35).

Ishii, K., Morita, K., Okitsu, Y., Sayama, S., and Kataoka, H. (2013). "Cellular pattern formation in detonation propagation". *Proceedings of the Combustion Institute*, 34(2), pp. 1903–1911 (cited on p. 60).

Ishii, K., Ohno, K., Kawana, H., Kawasaki, K., Hayashi, A. K., and Tsuboi, N. (2023). "Operation characteristics of a disk-type rotating detonation engine". *Shock Waves*, 33, pp. 267–274 (cited on pp. 21, 23).

Ivanov, M., Kiverin, A., and Liberman, M. (2011). "Flame acceleration and DDT of hydrogen-oxygen gaseous mixtures in channels with no-slip walls". *International Journal of Hydrogen Energy*, 36(13). Hysydays, pp. 7714–7727 (cited on p. 74).

Ivanova, D. and Wood, R. (2020). "The unequal distribution of household carbon footprints in Europe and its link to sustainability". *Global Sustainability*, 3, e18 (cited on p. 14).

Iwata, K., Suzuki, S., Kai, R., and Kurose, R. (2023). "Direct numerical simulation of detonation–turbulence interaction in hydrogen/oxygen/argon mixtures with a detailed chemistry". *Physics of Fluids*, 35(4), p. 046107 (cited on p. 71).

Jaravel, T., Riber, E., Cuenot, B., and Bulat, G. (2017). "Large Eddy Simulation of an industrial gas turbine combustor using reduced chemistry with accurate pollutant prediction". *Proceedings of the Combustion Institute*, 36(3), pp. 3817–3825 (cited on p. 75).

Jones, W. and Prasad, V. (2010). "Large Eddy Simulation of the Sandia Flame Series (D-F) using the Eulerian stochastic field method". *Combustion and Flame*, 157(9), pp. 1621–1636 (cited on p. 75).

Kaemming, T. A. and Paxson, D. E. (2018). "Determining the Pressure Gain of Pressure Gain Combustion". In: *2018 Joint Propulsion Conference* (cited on p. 188).

Kailasanath, K. (2011). "The Rotating Detonation-Wave Engine Concept: A Brief Status Report". In: *49th AIAA Aerospace Sciences Meeting including the New Horizons Forum and Aerospace Exposition* (cited on pp. 18, 20).

Kantrowitz, A. et al. (1945). *Preliminary investigation of supersonic diffusers*. National Advisory Committee for Aeronautics (cited on p. 24).

Karagozian, A. R. (2014). "The jet in crossflow". *Physics of Fluids*, 26(10), p. 101303 (cited on p. 97).

Katta, V. R., Cho, K. Y., Hoke, J. L., Codoni, J. R., Schauer, F. R., and Roquemore, W. M. (2019). "Effect of increasing channel width on the structure of rotating detonation wave". *Proceedings of the Combustion Institute*, 37(3), pp. 3575–3583 (cited on pp. 26, 29).

Kawai, S. and Lele, S. (2008). "Localized artificial diffusivity scheme for discontinuity capturing on curvilinear meshes". *Journal of Computational Physics*, 227(22), pp. 9498–9526 (cited on pp. 69, 97).

Kessler, D., Gamezo, V., and Oran, E. (2010). "Simulations of flame acceleration and deflagration-to-detonation transitions in methane-air systems". *Combustion and Flame*, 157(11), pp. 2063–2077 (cited on pp. 74, 76).

Khokhlov, A. M. and Oran, E. S. (1999). "Numerical simulation of detonation initiation in a flame brush: the role of hot spots". *Combustion and Flame*, 119(4), pp. 400–416 (cited on p. 74).

Kudo, Y., Nagura, Y., Kasahara, J., Sasamoto, Y., and Matsuo, A. (2011). "Oblique detonation waves stabilized in rectangular-cross-section bent tubes". *Proceedings of the Combustion Institute*, 33(2), pp. 2319–2326 (cited on p. 65).

Kuo, K. K. (2005 Second Edition). *Principles of combustion*. Hoboken, New Jersey: John Wiley & Sons, Inc. (cited on p. 33).

Larsson, J., Bermejo-Moreno, I., and Lele, S. K. (2013). "Reynolds- and Mach-number effects in canonical shock–turbulence interaction". *Journal of Fluid Mechanics*, 717, pp. 293–321 (cited on p. 62).

Lax, P. D. and Wendroff, B. (1960). "Systems of conservation laws". *Communications on Pure and Applied Mathematics*, 13, pp. 217–237 (cited on pp. 68, 145).

Lee, J. H. S. (2008). *The Detonation Phenomenon*. Cambridge: Cambridge University Press (cited on pp. 52, 53, 56, 62).

Liberman, M., Ivanov, M., Kiverin, A., Kuznetsov, M., Chukalovsky, A., and Rakhimova, T. (2010). "Deflagration-to-detonation transition in highly reactive combustible mixtures". *Acta Astronautica*, 67(7), pp. 688–701 (cited on p. 74).

Liu, E., Liu, X., Zhao, M., Zheng, H., Lu, J., and Zhang, Z. (2020). "Turbulent fuel-air mixing study of jet in crossflow at different velocity ratios using LES". *International Journal of Heat and Fluid Flow*, 85, p. 108633 (cited on p. 117).

Liu, W., Kelley, A., and Law, C. (2010). "Flame propagation and counterflow nonpremixed ignition of mixtures of methane and ethylene". *Combustion and Flame*, 157(5), pp. 1027–1036 (cited on p. 107).

Liu, Z., Braun, J., and Paniagua, G. (2023). "Integration of a transonic high-pressure turbine with a rotating detonation combustor and a diffuser". *International Journal of Turbo & Jet-Engines*, 40(1), pp. 1–10 (cited on p. 24).

Lu, F. K. and Braun, E. M. (2014). "Rotating Detonation Wave Propulsion: Experimental Challenges, Modeling, and Engine Concepts". *Journal of Propulsion and Power*, 30(5), pp. 1125–1142 (cited on p. 22).

Lu, T. F., Yoo, C. S., Chen, J. H., and Law, C. K. (2010). "Three-dimensional direct numerical simulation of a turbulent lifted hydrogen jet flame in heated coflow: a chemical explosive mode analysis". *Journal of Fluid Mechanics*, 652, 45–64 (cited on p. 107).

Luan, Z., Huang, Y., Gao, S., and You, Y. (2022). "Formation of multiple detonation waves in rotating detonation engines with inhomogeneous methane/oxygen mixtures under different equivalence ratios". *Combustion and Flame*, 241, p. 112091 (cited on pp. 24, 113).

Ma, F., Choi, J.-Y., and Yang, V. (2006). "Propulsive Performance of Airbreathing Pulse Detonation Engines". *Journal of Propulsion and Power*, 22(6), pp. 1188–1203 (cited on p. 29).

Massa, L., Chauhan, M., and Lu, F. (2011). "Detonation-turbulence interaction". *Combustion and Flame*, 158(9), pp. 1788–1806 (cited on p. 71).

Matalon, M. and Matkowsky, B. J. (1982). "Flames as gasdynamic discontinuities". *Journal of Fluid Mechanics*, 124, p. 239 (cited on p. 48).

Melguizo-Gavilanes, J., Rodriguez, V., Vidal, P., and Zitoun, R. (2021). "Dynamics of detonation transmission and propagation in a curved chamber: a numerical and experimental analysis". *Combustion and Flame*, 223, pp. 460–473 (cited on p. 126).

Metrow, C., Mozhdehe, V. Y. A., and Ciccarelli, G. (2021). "Detonation propagation across a stratified layer with a diffuse interface". *Proceedings of the Combustion Institute*, 38(3), pp. 3565–3574 (cited on p. 127).

Mével, R., Javoy, S., and Dupré, G. (2011). "A chemical kinetic study of the oxidation of silane by nitrous oxide, nitric oxide and oxygen". *Proceedings of the Combustion Institute*, 33(1), pp. 485–492 (cited on p. 75).

Mével, R., Javoy, S., Lafosse, F., Chaumeix, N., Dupré, G., and Paillard, C.-E. (2009). "Hydrogen–nitrous oxide delay times: Shock tube experimental study and kinetic modelling". *Proceedings of the Combustion Institute*, 32(1), pp. 359–366 (cited on p. 75).

Michalski, Q., Boust, B., and Bellenoue, M. (2018a). "Toward a cyclic self-ignited constant-volume combustion for airbreathing propulsion applications". In: *2018 Joint Propulsion Conference* (cited on p. 18).

Michalski, Q., Kha, K., Boust, B., Robin, V., Bellenoue, M., and Mura, A. (2018b). "Joint Numerical and Experimental Characterization of the Turbulent Reactive Flow within a Constant Volume Vessel". In: *2018 Joint Propulsion Conference* (cited on p. 18).

Mikoshiba, K., Sardeshmukh, S. V., and Heister, S. D. (2019). "Two Dimensional Simulation of RDE Combustor with a Dynamic Injection Model". In: *AIAA Scitech 2019 Forum* (cited on p. 26).

Moen, I., Murray, S., Bjerketvedt, D., Rinnan, A., Knystautas, R., and Lee, J. (1982). "Diffraction of detonation from tubes into a large fuel-air explosive cloud". *Symposium (International) on Combustion*, 19(1). Nineteenth Symposium (International) on Combustion, pp. 635–644 (cited on pp. 63, 64).

Monnier, V. (2023). "Aspects tridimensionnels de la détonation cellulaire : des observations expérimentales et un modèle". Thèse de doctorat dirigée par Vidal, PierreRodriguez, Vincent et Zitoun, Ratiba Energétique, thermique, combustion Chasseneuil-du-Poitou, Ecole nationale supérieure de mécanique et d'aérotechnique 2023. PhD thesis (cited on p. 64).

Mueller, M. A., Kim, T. J., Yetter, R. A., and Dryer, F. L. (1999). "Flow reactor studies and kinetic modeling of the H2/O2 reaction". *International Journal of Chemical Kinetics*, 31(2), pp. 113–125 (cited on p. 29).

Mushtaq, N., Colella, G., and Gaetani, P. (2022). "Design and parametric analysis of a supersonic turbine for rotating detonation engine applications". *International Journal of Turbomachinery, Propulsion and Power*, 7(1), p. 1 (cited on p. 24).

Mushtaq, N. and Gaetani, P. (2023). "Understanding and modeling unstarting phenomena in a supersonic inlet cascade". *Physics of Fluids*, 35(10) (cited on p. 24).

Nair, A. P., Lee, D. D., Pineda, D. I., Kriesel, J., Hargus, W. A., Bennewitz, J. W., Bigler, B., Danczyk, S. A., and Spearrin, R. M. (2021). "Methane-oxygen rotating detonation exhaust thermodynamics with variable mixing, equivalence ratio, and mass flux". *Aerospace Science and Technology*, 113, p. 106683 (cited on p. 23).

Nakagami, S., Matsuoka, K., Kasahara, J., Kumazawa, Y., Fujii, J., Matsuo, A., and Funaki, I. (2017). "Experimental Visualization of the Structure of Rotating Detonation Waves in a Disk-Shaped Combustor". *Journal of Propulsion and Power*, 33(1), pp. 80–88 (cited on p. 21).

Nakayama, H., Kasahara, J., Matsuo, A., and Funaki, I. (2013). "Front shock behavior of stable curved detonation waves in rectangular-cross-section curved channels". *Proceedings of the Combustion Institute*, 34(2), pp. 1939–1947 (cited on p. 65).

Nakayama, H., Moriya, T., Kasahara, J., Matsuo, A., Sasamoto, Y., and Funaki, I. (2012). "Stable detonation wave propagation in rectangular-cross-section curved channels". *Combustion and Flame*, 159(2), pp. 859–869 (cited on pp. 65, 66).

Naples, A., Hoke, J., Karnesky, J., and Schauer, F. (2013). "Flowfield Characterization of a Rotating Detonation Engine". In: *51st AIAA Aerospace Sciences Meeting including the New Horizons Forum and Aerospace Exposition* (cited on p. 26).

Nassini, P. C. (2022). "High-fidelity Numerical Investigations of a Hydrogen Rotating Detonation Combustor". URL: http://hdl.handle.net/2158/1276841. PhD thesis. University of Florence (cited on p. 115).

Nassini, P. C., Andreini, A., and Bohon, M. D. (2023). "Characterization of refill region and mixing state immediately ahead of a hydrogen-air rotating detonation using LES". *Combustion and Flame*, 258, p. 113050 (cited on pp. 26, 28, 29, 75, 98, 99, 126, 127, 133, 152, 164).

Ng, H., Radulescu, M. I., Higgins, A. J., Nikiforakis, N., and Lee, J. H. S. (2005). "Numerical investigation of the instability for one-dimensional Chapman-Jouguet detonations with chain-branching kinetics". *Combustion Theory and Modelling*, 9(3), pp. 385–401 (cited on p. 62).

Nicholls, J. A. and Cullen, R. E. (1964). "THE FEASIBILITY OF A ROTATING DETONATION WAVE ROCKET MOTOR" (cited on p. 20).

Nicoud, F. and Ducros, F. (1999). "Subgrid-scale stress modelling based on the square of the velocity gradient". *Flow, Turbulence and Combustion*, 62(3), pp. 183–200 (cited on p. 69).

Nicoud, F., Toda, H. B., Cabrit, O., Bose, S., and Lee, J. (2011). "Using singular values to build a subgrid-scale model for large eddy simulations". *Physics of Fluids*, 23(8), p. 085106 (cited on p. 69).

Olson, A., Fotia, M., Stevens, C., and Heyne, J. S. (2020). "Propagation of Gaseous Detonations in 2D Curved Channels". In: *AIAA Propulsion and Energy 2020 Forum* (cited on p. 66).

Our World in Data (2023). https://ourworldindata.org. Accessed: 2024-03-14 (cited on pp. 14, 16).

Paniagua, G, Iorio, M., Vinha, N, and Sousa, J (2014). "Design and analysis of pioneering high supersonic axial turbines". *International Journal of Mechanical Sciences*, 89, pp. 65–77 (cited on p. 24).

Paris Agreement (2015) (cited on p. 14).

Perkins, H. D. and Paxson, D. E. (2018). *Summary of Pressure Gain Combustion Research at NASA*. Glenn Research Center, Cleveland, Ohio (cited on p. 18).

Poinsot, T. and Lele, S. (1992). "Boundary conditions for direct simulations of compressible viscous flows". *Journal of Computational Physics*, 101(1), pp. 104–129 (cited on pp. 67, 101).

Poinsot, T. and Veynante, D. (2011). *Theoretical and Numerical Combustion*. Third Edition (www.cerfacs.fr/elearning) (cited on pp. 33, 38, 40–42, 45, 47, 49, 50, 107).

Pope, S. B. (2000). *Turbulent flows*. Cambridge University Press (cited on p. 69).

Population based on various sources (2023) – with major processing by Our World in Data (2023). Global Carbon Budget (cited on p. 14).

Prakash, S., Raman, V., Lietz, C. F., Hargus, W. A., and Schumaker, S. A. (2021). "Numerical simulation of a methane-oxygen rotating detonation rocket engine". *Proceedings of the Combustion Institute*, 38(3), pp. 3777–3786 (cited on pp. 26, 29, 97, 98, 152).

Rankin, B. A., Fotia, M. L., Naples, A. G., Stevens, C. A., Hoke, J. L., Kaemming, T. A., Theuerkauf, S. W., and Schauer, F. R. (2017a). "Overview of Performance, Application, and Analysis of Rotating Detonation Engine Technologies". *Journal of Propulsion and Power*, 33(1), pp. 131–143 (cited on p. 21).

Rankin, B. A., Richardson, D. R., Caswell, A. W., Naples, A., Hoke, J., and Schauer, F. (2015). "Imaging of OH* Chemiluminescence in an Optically Accessible Nonpremixed Rotating Detonation Engine". In: *53rd AIAA Aerospace Sciences Meeting* (cited on pp. 24, 113).

Rankin, B. A., Richardson, D. R., Caswell, A. W., Naples, A. G., Hoke, J. L., and Schauer, F. R. (2017b). "Chemiluminescence imaging of an optically accessible non-premixed rotating detonation engine". *Combustion and Flame*, 176, pp. 12–22 (cited on pp. 24, 113).

RANZI, E., FRASSOLDATI, A., STAGNI, A., PELUCCHI, M., CUOCI, A., and FARAVELLI, T. (2014). "Reduced Kinetic Schemes of Complex Reaction Systems: Fossil and Biomass-Derived Transportation Fuels". *International Journal of Chemical Kinetics*, 46(9), pp. 512–542 (cited on p. 75).

Ren, Z., Sun, Y., and Wang, B. (2023). "Propagation Behaviors of the Rotating Detonation Wave in Kerosene-Air Two-Phase Mixtures with Wide Equivalence Ratios". *Flow, Turbulence and Combustion*, 110, pp. 735–753 (cited on p. 26).

Reynaud, M., Taileb, S., and Chinnayya, A. (2020). "Computation of the mean hydrodynamic structure of gaseous detonations with losses". *Shock Waves*, 30, 645–669 (cited on p. 96).

Ritchie, H., Rosado, P., and Roser, M. (2020). "CO2 emissions by fuel". *Our World in Data*. https://ourworldindata.org/emissions-by-fuel (cited on p. 15).

Roser, M. (2020). "The world's energy problem". *Our World in Data*. https://ourworldindata.org/wo energy-problem (cited on p. 14).

Ruiz, A. M., Lacaze, G., and Oefelein, J. C. (2015). "Flow topologies and turbulence scales in a jet-in-cross-flow". *Physics of Fluids*, 27(4), p. 045101 (cited on p. 117).

Sato, T., Chacon, F., White, L., Raman, V., and Gamba, M. (2021). "Mixing and detonation structure in a rotating detonation engine with an axial air inlet". *Proceedings of the Combustion Institute*, 38(3), pp. 3769–3776 (cited on pp. 26, 29, 97, 127).

Sato, T. and Raman, V. (2020). "Detonation Structure in Ethylene/Air-Based Non-Premixed Rotating Detonation Engine". *Journal of Propulsion and Power*, 36(5), pp. 752–762 (cited on pp. 23, 26, 29, 126).

Saxena, P. and Williams, F. A. (2006). "Testing a small detailed chemical-kinetic mechanism for the combustion of hydrogen and carbon monoxide". *Combustion and Flame*, 145(1), pp. 316–323 (cited on p. 74).

Schott, G. L. (1965). “Observations of the Structure of Spinning Detonation”. *The Physics of Fluids*, 8(5), pp. 850–865 (cited on p. 60).

Schulz, O., Jaravel, T., Poinsot, T., Cuenot, B., and Noiray, N. (2017). “A criterion to distinguish autoignition and propagation applied to a lifted methane–air jet flame”. *Proceedings of the Combustion Institute*, 36(2), pp. 1637–1644 (cited on p. 75).

Schwer, D. and Kailasanath, K. (2013). “Fluid dynamics of rotating detonation engines with hydrogen and hydrocarbon fuels”. *Proceedings of the Combustion Institute*, 34(2), pp. 1991–1998 (cited on p. 23).

Schwer, D. A., Corrigan, A. T., and Kailasanath, K. (2014). “Towards Efficient, Unsteady, Three-Dimensional Rotating Detonation Engine Simulations”. In: *52nd Aerospace Sciences Meeting* (cited on pp. 26, 29).

Schwer, D. A. and Kailasanath, K. (2014). “Effect of Low Pressure Ratio on Exhaust Plumes of Rotating Detonation Engines”. In: *50th AIAA/ASME/SAE/ASEE Joint Propulsion Conference* (cited on pp. 26, 29).

Shank, J. C. (2012). “Development and Testing of a Rotating Detonation Engine Run on Hydrogen and Air”. MA thesis. AIR FORCE INST OF TECH WRIGHT-PATTERSON AFB OH GRADUATE SCHOOL OF ENGINEERING and MANAGEMENT (cited on p. 28).

Shi, L., Shen, H., Zhang, P., Zhang, D., and Wen, C. (2017). “Assessment of Vibrational Non-Equilibrium Effect on Detonation Cell Size”. *Combustion Science and Technology*, 189(5), pp. 841–853 (cited on p. 74).

Shimizu, K., Hibi, A., Koshi, M., Morii, Y., and Tsuboi, N. (2011). “Updated Kinetic Mechanism for High-Pressure Hydrogen Combustion”. *Journal of Propulsion and Power*, 27(2), pp. 383–395 (cited on p. 29).

Short, M., Chiquete, C., and Quirk, J. J. (2019). “Propagation of a stable gaseous detonation in a circular arc configuration”. *Proceedings of the Combustion Institute*, 37(3), pp. 3593–3600 (cited on p. 66).

GPU-Accelerated High-Fidelity Rotating Detonation Engine Simulations Using an Extended Flamelet Progress Variable Approach (2023). Vol. Volume 3A: Combustion, Fuels, and Emissions. Turbo Expo: Power for Land, Sea, and Air, V03AT04A031 (cited on p. 71).

Smith, S. H. and Mungal, M. G. (1998). "Mixing, structure and scaling of the jet in crossflow". *Journal of Fluid Mechanics*, 357, pp. 83–122 (cited on p. 97).

Starken, H., Yongxing, Z., and Schreiber, H.-A. (1984). *Mass flow limitation of supersonic blade rows due to leading edge blockage*. Vol. 79467. American Society of Mechanical Engineers (cited on p. 24).

Stathopoulos, P. (2018). "Comprehensive Thermodynamic Analysis of the Humphrey Cycle for Gas Turbines with Pressure Gain Combustion". *Energies*, 11(12) (cited on p. 18).

Statistical Review of World Energy (2023); Smil (2017) - with major processing by Our World in Data. "Primary energy from other renewables" [dataset]., "Energy Transitions: Global and National Perspectives" [dataset]. Energy Institute, "Statistical Review of World Energy"; Smil, "Energy Transitions: Global and National Perspectives" [original data] (2023). Energy Institute, "Statistical Review of World Energy"; Smil, "Energy Transitions: Global and National Perspectives" [original data] (cited on p. 15).

Strehlow, R. A. (1968). "Gas pase detonations: Recent developments". *Combustion and Flame*, 12(2), pp. 81–101 (cited on p. 60).

Suchocki, J., Yu, S.-T., Hoke, J., Naples, A., Schauer, F., and Russo, R. (2012). "Rotating Detonation Engine Operation". In: *50th AIAA Aerospace Sciences Meeting including the New Horizons Forum and Aerospace Exposition* (cited on pp. 23, 24).

Sugiyama, Y., Nakayama, Y., Matsuo, A., Nakayama, H., and Kasahara, J. (2014). "Numerical Investigations on Detonation Propagation in a Two-Dimensional Curved Channel". *Combustion Science and Technology*, 186(10-11), pp. 1662–1679 (cited on p. 126).

Sun, J., Zhou, J., Liu, S., Lin, Z., and Cai, J. (2017). "Effects of injection nozzle exit width on rotating detonation engine". *Acta Astronautica*, 140, pp. 388–401 (cited on p. 26).

Sutherland, W. (1893). "The viscosity of gases and molecular force". *Philosophical Magazine*, 5(36), pp. 507–531 (cited on p. 38).

Taileb, S., Melguizo-Gavilanes, J., and Chinnayya, A. (2020). "Influence of the chemical modeling on the quenching limits of gaseous detonation waves confined by an inert layer". *Combustion and Flame*, 218, pp. 247–259 (cited on p. 96).

Tanaka, R., Matsuo, A., Eiji, S., Watanabe, H., Kawasaki, A., Matsuoka, K., and Kasahara, J. (2022). "Numerical Investigation of the Effect of Ozone Addition on Detonation in the Two-dimensional RDE Chamber". In: *28th International Colloquium on the Dynamics of Explosions and Reactive Systems* (cited on p. 26).

Taylor, B., Kessler, D., Gamezo, V., and Oran, E. (2013). "Numerical simulations of hydrogen detonations with detailed chemical kinetics". *Proceedings of the Combustion Institute*, 34(2), pp. 2009–2016 (cited on p. 74).

Thomas, G. and Williams, R. (2002). "An eddy-viscosity subgrid-scale model for turbulent shear flow: Algebraic theory and applications". *Shock Waves*, 11(10), pp. 481–492 (cited on p. 65).

Tieszen, S., Sherman, M., Benedick, W., and Berman, M. (1987). *Detonability of H2-air-diluent mixtures*. Technical Report NUREG/CR-4905, SAND85-1263, Sandia National Laboratories (cited on p. 63).

Tonello, N. A., Sichel, M., and Oran, E. S. (1996). "Numerical simulations of the diffraction of planar detonations in H2-O2 mixtures". *Symposium (International) on Combustion*, 26(2), pp. 3033–3039 (cited on p. 74).

Tsuboi, N., Eto, S., Hayashi, A. K., and Kojima, T. (2017). "Front Cellular Structure and Thrust Performance on Hydrogen–Oxygen Rotating Detonation Engine". *Journal of Propulsion and Power*, 33(1), pp. 100–111 (cited on pp. 26, 29, 152).

Tsuboi, N., Watanabe, Y., Kojima, T., and Hayashi, A. K. (2015). "Numerical estimation of the thrust performance on a rotating detonation engine for a hydrogen–oxygen mixture". *Proceedings of the Combustion Institute*, 35(2), pp. 2005–2013 (cited on pp. 26, 29).

Turns, S. R. et al. (1996). *Introduction to combustion*. Vol. 287 (cited on p. 45).

Uhl, G., Taileb, S., Odier, N., Zurbach, S., Poinsot, T., and Bellenoue, M. (2024). "Numerical Analysis of an Ejector under Pulsating Inflow Characteristic of RDC Exhaust Conditions". In: *AIAA SCITECH 2024 Forum* (cited on p. 24).

Van Driest, E. R. (1951). "Turbulent Boundary Layer in Compressible Fluids". *Journal of the Aeronautical Sciences*, 18(3), pp. 145–160 (cited on p. 72).

Varatharajan, B. and Williams, F. A. (2002). "Ethylene Ignition and Detonation Chemistry, Part 2: Ignition Histories and Reduced Mechanisms". *Journal of Propulsion and Power*, 18(2), pp. 352–362 (cited on p. 29).

Vignat, G., Brouzet, D., Bonanni, M., and Ihme, M. (2024). "Analysis of weak secondary waves in a rotating detonation engine using large-eddy simulation and wavenumber-domain filtering". *Combustion and Flame*, 263, p. 113387 (cited on pp. 26, 29, 98, 152).

Voitsekhovskii, B. V. (1960). "Stationary spin detonation". *Soviet Journal of Applied Mechanics and Technical Physics*, 3(6), pp. 157–164 (cited on p. 20).

Voitsekhovskii, B., Mitrofanov, V., and Topchian, M. (1963). "Structure of a detonation front in gases. Novosibirsk: Siberian Branch of the USSR Academy Science" (cited on p. 20).

von Neumann, J. (1942). *Theory of detonation waves*. Tech. rep. Princeton NJ: Institute For Advanced Study (cited on p. 57).

Vreman, A. W. (2004). "An eddy-viscosity subgrid-scale model for turbulent shear flow: Algebraic theory and applications". *Physics of Fluids*, 16(10), pp. 3670–3681 (cited on p. 29).

Wang, C. J., Wen, J., Lu, S. X., and Guo, J. (2012). "Single-step chemistry model and transport coefficient model for hydrogen combustion". *Science China Technological Sciences*, 55(8), pp. 2163–2168 (cited on p. 74).

Wang, G., Boileau, M., and Veynante, D. (2011). "Implementation of a dynamic thickened flame model for large eddy simulations of turbulent premixed combustion". *Combustion and Flame*, 158(11), pp. 2199–2213 (cited on p. 71).

Wang, Y. and Le, J. (2021). "A rotating detonation engine using methane-ethylene mixture and air". *Acta Astronautica*, 188, pp. 25–35 (cited on p. 23).

Wang, Y., Le, J., Wang, C., and Zheng, Y. (2018). "A non-premixed rotating detonation engine using ethylene and air". *Applied Thermal Engineering*, 137, pp. 749–757 (cited on pp. 21, 23).

Weiss, S., Bohon, M. D., Paschereit, C. O., and Gutmark, E. J. (2020). "Computational Study of Reactants Mixing in a Rotating Detonation Combustor Using Compressible RANS". *Flow, Turbulence and Combustion*, 105, pp. 267–295 (cited on pp. 99, 113).

Wen, H., Wei, W., Fan, W., Xie, Q., and Wang, B. (2022). "On the propagation stability of droplet-laden two-phase rotating detonation waves". *Combustion and Flame*, 244, p. 112271 (cited on p. 26).

White, D. R. (1961). "Turbulent Structure of Gaseous Detonation". *The Physics of Fluids*, 4(4), pp. 465–480 (cited on p. 59).

Williams, D. N., Bauwens, L., and Oran, E. S. (1996). "Detailed structure and propagation of three-dimensional detonations". *Symposium (International) on Combustion*, 26(2), pp. 2991–2998 (cited on p. 74).

Williams, F. A. (1985). *Combustion Theory*. Menlo Park, CA: Benjamin Cummings (cited on p. 46).

Wolański, P. (2013). "Detonative propulsion". *Proceedings of the Combustion Institute*, 34(1), pp. 125–158 (cited on p. 18).

WON-WOOK KIM, S. M. and MONGIA, H. C. (1999). "Large-Eddy Simulation of a Gas Turbine Combustor Flow". *Combustion Science and Technology*, 143(1-6), pp. 25–62 (cited on p. 29).

Wu, D., Liu, Y., Liu, Y., and Wang, J. (2014). "Numerical investigations of the restabilization of hydrogen–air rotating detonation engines". *International Journal of Hydrogen Energy*, 39(28), pp. 15803–15809 (cited on pp. 26, 27, 29).

Xu, R., Wang, K., Banerjee, S., Shao, J., Parise, T., Zhu, Y., Wang, S., Movaghar, A., Lee, D. J., Zhao, R., Han, X., Gao, Y., Lu, T., Brezinsky, K., Egolfopoulos, F. N., Davidson, D. F., Hanson, R. K., Bowman, C. T., and Wang, H. (2018). "A physics-based approach to modeling real-fuel combustion chemistry - II. Reaction kinetic models of jet and rocket fuels". *Combustion and Flame*, 193, pp. 520–537 (cited on p. 29).

Yokoo, R., Goto, K., Kasahara, J., Athmanathan, V., Braun, J., Paniagua, G., Meyer, T. R., Kawasaki, A., Matsuoka, K., Matsuo, A., and Funaki, I. (2021). "Experimental study of internal flow structures in cylindrical rotating detonation engines". *Proceedings of the Combustion Institute*, 38(3), pp. 3759–3768 (cited on p. 21).

Yu, J., Yao, S., Li, J., Huang, Y., Guo, C., and Zhang, W. (2023). "Effects of inlet and secondary flow conditions on the flow field of rotating detonation engines with film cooling". *International Journal of Hydrogen Energy*, 48(24), pp. 9082–9094 (cited on pp. 26, 28, 29).

Yuan, L. L., Street, R. L., and Ferzinger, J. H. (1999). "Large-eddy simulations of a round jet in crossflow". *Journal of Fluid Mechanics*, 379, pp. 71–104 (cited on p. 97).

Zel'dovich, Y., Librovich, V., Makhviladze, G., and Sivashinsky, G. (1970). "On the development of detonation in a non-uniformly preheated gas". *Astronautica Acta*, 15(5-6), pp. 313–321 (cited on p. 74).

Zeldovich, Y. B. (1992). *Chemical Physics and Hydrodynanics*. Ed. by G. I. Barenblatt and R. A. Sunyaev. Princeton: Princeton University Press (cited on p. 57).

Zhao, M., Li, J.-M., Teo, C.-J., Khoo, B.-C., and Zhang, H. (2020). "Effects of Variable Total Pressures on Instability and Extinction of Rotating Detonation Combustion". *Flow, Turbulence and Combustion*, 104, pp. 261–290 (cited on pp. 24, 26).

Zhao, M. and Zhang, H. (2020). "Large eddy simulation of non-reacting flow and mixing fields in a rotating detonation engine". *Fuel*, 280, p. 118534 (cited on p. 113).

Zhou, R. and Wang, J.-P. (2013). "Numerical investigation of shock wave reflections near the head ends of rotating detonation engines". *Shock Waves*, 23, pp. 461–472 (cited on pp. 26, 29).

Zhou, R. and Wang, J.-P. (2012). "Numerical investigation of flow particle paths and thermodynamic performance of continuously rotating detonation engines". *Combustion and Flame*, 159(12), pp. 3632–3645 (cited on p. 127).

Öberg, S., Odenberger, M., and Johnsson, F. (2022). "Exploring the competitiveness of hydrogen-fueled gas turbines in future energy systems". *International Journal of Hydrogen Energy*, 47(1), pp. 624–644 (cited on p. 17).

RÉPUBLIQUE FRANÇAISE
Liberté
Égalité
Fraternité

Université de Toulouse

Titre : LES des moteurs à détonation rotative: Sensibilité et physique

Mots clés : Moteur à détonation rotative, LES, Détonation, Combustion, Mécanique des fluides

Résumé : Afin d'accroître l'efficacité des moteurs thermiques, de nouveaux systèmes de combustion à gain de pression ont fait l'objet d'études approfondies au cours des dernières années. Les moteurs à détonation rotative (RDE) constituent un exemple de ces systèmes, où une détonation auto-entretenue consomme continuellement du carburant dans une chambre de combustion typiquement annulaire. L'étude expérimentale de ces moteurs est extrêmement difficile, c'est pourquoi des méthodes numériques sont utilisées pour explorer davantage les processus régissant ces types de moteurs. Les simulations de grandes turbulences (LES) constituent un outil puissant pour analyser l'écoulement dans les moteurs à détonation rotatifs, mais la littérature a montré que leur mise en œuvre n'est pas simple. Différents groupes utilisent des simplifications (par exemple, prémélange parfait, représentations géométriques en 2D de la chambre) et l'analyse numérique de haute fidélité comparant les hypothèses de mélange, les schémas numériques ou les schémas chimiques dans des configurations à échelle réelle n'est pas couramment trouvée dans la littérature.
Cette thèse étudie les stratégies de LES 3D d'un RDE complet testé à l'Université technique de Berlin et l'influence de divers paramètres de modélisation sur les résultats de la simulation. Pour ce faire, un schéma chimique fiable en une étape est d'abord élaboré pour la prédiction correcte des propriétés de détonation et de déflagration. Ensuite, une procédure d'initialisation fiable est développée et deux indices de post-traitement pour évaluer la qualité du mélange (I_mix) et l'efficacité de la détonation (I_det) sont introduits pour quantifier davantage les résultats des simulations.
Les résultats confirment que le mélange joue un rôle important dans la performance des RDE et qu'il doit être reproduit avec précision dans les LES afin de capturer les caractéristiques essentielles des RDE. Le manuscrit met également en évidence l'impact que les schémas chimiques et numériques peuvent avoir sur la dynamique de détonation à l'intérieur des RDE. Enfin, les simulations montrent l'importance de la déflagration dans l'ensemble de la chambre de combustion RDE, ce qui implique que les modèles chimiques doivent tenir compte des propriétés de déflagration ainsi que de la détonation pour capturer l'efficacité des RDE et révèlent que tous les cas perdent une grande quantité de carburant dans la combustion non-détonante.
Sur la base de l'étude de sensibilité, une configuration numérique principale est conçue et des simulations sont effectuées. Les résultats sont validés en comparant la vitesse expérimentale de l'onde de détonation et le gain de pression estimé. La LES surestime la vitesse de l'onde de détonation expérimentale de 21 %. La LES confirme également l'absence de gain de pression dans la configuration TUB.
Cette thèse montre que la LES peut être utilisée pour comprendre la dynamique et les mécanismes de stabilisation ainsi que la performance globale des systèmes RDE. Cependant, elle met également en évidence les limites actuelles de la méthode et les nombreux domaines sur lesquels la communauté LES doit se concentrer pour la LES prédictive des RDE.

Title: LES of Rotating Detonation Engines: Sensitivity and Physics

Key words: Rotating Detonation Engine (RDE), LES, Detonation, Combustion, Fluid mechanics

Abstract: To increase the efficiency of thermal engines, new pressure-gain combustion systems are the subject of extensive studies over the last years. Rotating Detonation Engines (RDE) constitute an example of such systems, where a self-sustained detonation continuously consumes fuel in a typically annular combustion chamber. Experimental investigation of these engines is extremely difficult, hence numerical methods are used to further explore the processes governing these types of engines. A powerful tool to analyse the flow in Rotating Detonation Engines are Large Eddy Simulations (LES), but literature has shown that their implementation is not straightforward. Various groups use simplifications (e.g. perfect premixing, geometrical 2D representations of the chamber) and numerical high-fidelity analysis comparing mixing assumptions, numerical schemes or chemical schemes in full scale configurations are not commonly found in literature.
This thesis investigates strategies for 3D LES of a full RDE tested at TU Berlin and the influence of various modelling parameters on the simulation results. This is done by first deriving a reliable 1-step chemical scheme for the correct prediction of detonation and deflagration properties. Second a reliable initialization procedure is developed and two postprocessing indices for evaluating the mixture quality (I_mix) and the detonation efficiency (I_det) are introduced to further quantify the results of the simulations.
Results confirm that mixing plays a significant role in the performance of RDEs and must be accurately reproduced in LES the capture the essential features of RDEs. The manuscript also highlights the impact that the chemical and numerical schemes can have on the detonation dynamics inside RDEs. Finally, the simulations show the importance of deflagration in the overall RDE combustor, implying that chemistry models need to account for deflagration properties as well as for detonation to capture the efficiency of RDEs and reveal that all cases lose a high amount of fuel to non-detonative combustion.
Based on the sensitivity study, a numerical master setup is designed and simulations are performed. The results are validated by comparing the experimental detonation wave speed and estimated pressure gain. The LES overpredicts the experimental detonation wave speed by 21%. The LES also confirms the absence of pressure gain in the TUB configuration.
This thesis shows that LES can be used to understand the dynamics and stabilization mechanisms as well as overall performance of RDE systems. However, it also highlights the current limitations of the method and the many areas where the LES community has to shift the focus on for predictive LES of RDEs.